MAGNETOELECTRIC SMART CURRENT SENSORS FOR WIRELESS CONDITION MONITORING APPLICATIONS

LEUNG CHUNG MING

Ph.D

The Hong Kong Polytechnic University

2012

The Hong Kong Polytechnic University

Department of Electrical Engineering

Magnetoelectric Smart Current Sensors for Wireless Condition Monitoring Applications

LEUNG CHUNG MING

A thesis submitted in partial fulfillment of the requirements for the degree of Doctor of Philosophy

September 2011

CERTIFICATE OF ORIGINALITY

I hereby declare that this thesis is my own work and that, to the best of my knowledge and belief, it reproduces no material previously published or written, nor material that has been accepted for the award of any other degree or diploma, except where due acknowledgment has been made in the text.

(Signed)

LEUNG CHUNG MING (Name of Student)

Abstract

Studies on the structure, working principle, physical modeling, fabrication, characterization, and performance of magnetoelectric (ME) sensing elements as well as investigations on the design, fabrication, and evaluation of ME passive current sensors and multichannel wireless communication units for wireless condition monitoring of electrical assets are presented and discussed in this thesis. Explorations of the fabrication, characterization, and physical properties of magnetostrictive and piezoelectric materials constituting the ME sensing elements are performed. Conclusions and suggestions for future work are also included. Original contributions reported in this research are stated as follows.

(1) $Tb_{0.3}Dy_{0.7}Fe_{1.92}$ (Terfenol-D) alloy plates and Terfenol-D short-bar–NdFeB magnet–epoxy composite rings were used as the magnetostrictive constituent materials, while $0.7Pb(Mg_{1/3}Nb_{2/3})O_3$–$0.3PbTiO_3$ (PMN–PT) single-crystal plates/bars, PMN–PT single-crystal transformers, and $Pb(Zr, Ti)O_3$ (PZT) ceramic rings were employed as the piezoelectric constituent materials, in the ME sensing elements. These constituent materials were fabricated into three characteristic types of ME sensing elements, including: (i) plate-shaped sensing elements with a PMN–PT single-crystal plate having a thickness polarization sandwiched between two Terfenol-D alloy plates having a length

magnetization; (ii) ring-shaped sensing elements with an inner Terfenol-D short-bar–NdFeB magnet–epoxy composite ring having a circumferential magnetization and an internal magnetic biasing concentric to an outer PZT ceramic ring having a wall-thickness polarization; and (3) bar-shaped sensing elements with a Rosen-type or long-type PMN–PT single-crystal transformer with its input part sandwiched between two Terfenol-D alloy plates having a length magnetization.

(2) An existing physical model was applied to describe the working principle and to predict the ME voltage coefficient ($\alpha_V=dV/dH$) of the plate-shaped sensing elements, while novel physical models were developed for the ring-shaped and bar-shaped sensing elements. Good agreements were obtained between the theoretical and experimental results in all cases. The plate-shaped and ring-shaped sensing elements were found to be suitable for broadband nonresonance sensing, while the bar-shaped sensing elements were good for narrowband resonance sensing with increased sensitivity.

(3) Novel surface mount-type and clamp-type ME passive current sensors with magnetic field biasing, electric field shielding, and thermal insulation capabilities were developed based on the plated-shaped and ring-shaped sensing elements, respectively. The effects of magnetic field biasing, electric field shielding, and thermal insulation on the performance of the current

sensors were evaluated, both analytically and experimentally. The fabrication and performance of the current sensors were reported.

(4) A short-range, 4-channel, 2.4 GHz wireless communication unit and a long-range, 3-channel, 3G/2G wireless communication unit were developed for integration with the ME passive current sensors. The hardware and software developments were described and the design features are highlighted. The performance of the two units was evaluated and disclosed in the laboratory using direct signals generated by an arbitrary waveform generator and indirect signals detected by ME passive current sensors.

(5) Three distinct sets of wireless condition monitors were formed and deployed in three different field tests by suitably combining the developed ME passive current sensors and wireless communication units. In the first field test, four surface mount-type current sensors were integrated with the 2.4 GHz wireless communication unit for monitoring the electrical motor drives of the train traction system of a 12-cabin mainline train operated by MTR Corporation Limited and running between Hong Kong and Shenzhen, China on the East Rail Line. In the second field test, three surface mount-type current sensors were connected with the 3G/2G wireless communication unit for monitoring an ABB 400 V, 1,000 A, 3-phase electrical switchgear located in the Electrical Machines Laboratory (EF001a) of the Department of Electrical

Engineering at PolyU. In the third field test, a clamp-type current sensor was inputted to the 2.4 GHz wireless communication unit for monitoring a 220 V, 13 A switching mode power supply used for driving personal computers. For all tests, the application background, field installation and implementation as well as test results and analysis were disclosed.

A number of publications (please refer to the list of publications) were produced during four years of PhD studies, further elucidating the originality, significance, and excellence of the present work. In addition, the present work was led to the award of the Li Po Chun Charitable Trust Fund Scholarship 2011.

List of Publications

SCI Journals (11 Items):

1) Yuan-Feng Duan, Chung Ming Leung, Shengyao Zhang, Long Zhang, and Siu Wing Or, "High magnetoelectric tuning effect in a polymer-based magnetostrictive-piezoelectric laminate under resonance drive", *Journal of Applied Physics*, Vol. 111, No. 7, Article 07C717 (April 1, 2012). *[Impact Factor=2.064; Grade A]*

2) Fang Yang, Chung Ming Leung, Siu Wing Or, Wei Liu, Zhidong Zhang, and Yuan-Feng Duan, "Dynamic magnetoelastic properties of epoxy-bonded $Sm_{0.88}Nd_{0.12}Fe_{1.93}$ pseudo-1–3 negative magnetostrictive particulate composite", *Journal of Applied Physics*, Vol. 111, No. 7, Article 07A940 (April 1, 2012). *[Impact Factor=2.064; Grade A]*

3) Chung Ming Leung, Siu Wing Or, Feifei Wang, and S. L. Ho, "Dual-resonance converse magnetoelectric and voltage step-up effects in laminated composite of long-type $0.71Pb(Mg_{1/3}Nb_{2/3})O_3$–$0.29PbTiO_3$ piezoelectric single-crystal transformer and $Tb_{0.3}Dy_{0.7}Fe_{1.92}$ magnetostrictive alloy bars", *Journal of Applied Physics*, Vol. 109, No. 10, Article 104103 (May 15, 2011). *[Impact Factor=2.064; Grade A]*

4) Fang Yang, Chung Ming Leung, Siu Wing Or, Wei Liu, Xiangke Lv, and Zhidong Zhang, "Magnetomechanical properties of epoxy-bonded $Sm_{1-x}Nd_xFe_{1.55}$ ($0 \leq x \leq 0.56$) pseudo-1–3 magnetostrictive particulate composites", *Journal of Alloys and Compounds*, Vol. 509, Issue 15, pp. 4954–4957 (April 14, 2011). *[Impact Factor=2.134; Grade A]*

5) Chung Ming Leung, Siu Wing Or, Feifei Wang, S. L. Ho, and Haosu Luo, "Enhanced magnetoelectric effect in heterostructure of magnetostrictive alloy bars and piezoelectric single-crystal transformer", *Review of Scientific Instruments*, Vol. 82, No. 1, Article 013903 (January 11, 2011). *[Impact Factor=1.598; Grade A]*

6) Chung Ming Leung, Siu Wing Or, and Siu Lau Ho, "DC magnetoelectric sensor based on direct coupling of Lorentz force effect in aluminum strip with transverse piezoelectric effect in $0.7Pb(Mg_{1/3}Nb_{2/3})O_3–0.3PbTiO_3$ single-crystal plate", *Journal of Applied Physics*, Vol. 107, Issue 9, Article 09E702 (May 1, 2010). *[Impact Factor=2.064; Grade A]*

7) Chung Ming Leung, Siu Wing Or, Shengyao Zhang, and S. L. Ho, "Ring-type electric current sensor based on ring-shaped magnetoelectric laminate of epoxy-bonded $Tb_{0.3}Dy_{0.7}Fe_{1.92}$ short-fiber/NdFeB magnet magnetostrictive composite and Pb(Zr, Ti)O_3 piezoelectric ceramic", *Journal of Applied Physics*, Vol. 107, Issue 9, Article 09D918 (May 1, 2010). *[Impact Factor=2.064; Grade A]*

8) Yaojin Wang, Xiangyong Zhao, Jie Jiao, Qinhui Zhang, Wenning Di, Haosu Luo, and Chung Ming Leung, and Siu Wing Or, "Lead-free magnetoelectric laminated composite of Mn-doped $Na_{0.5}Bi_{0.5}TiO_3–BaTiO_3$ single crystal and $Tb_{0.3}Dy_{0.7}Fe_{1.92}$ alloy", *Journal of Alloys and Compounds*, Vol. 496, Issues 1–2, pp. L4–L6 (April 30, 2010). *[Impact Factor=2.134; Grade A]*

9) Yaojin Wang, Chung Ming Leung, Siu Wing Or, Xiangyong Zhao, and Haosu Luo, "Resonance converse magnetoelectric effect in a dual-mode bilayered composite of $Pb(Mg_{1/3}Nb_{2/3})O_3–PbTiO_3$ and $Tb_{0.3}Dy_{0.7}Fe_{1.92}$, *Journal of Alloys and Compounds*, Vol. 487, Issues 1–2, pp. 450–452 (November 13, 2009). *[Impact Factor=2.135; Grade A]*

10) Yaojin Wang, Chung Ming Leung, Siu Wing Or, Xiangyong Zhao, Haosu Luo, Xiangke Lv, and Zhidong Zhang, "Magnetoelectric effect in laminates of polymer-based pseudo-1–3 $(Tb_{0.3}Dy_{0.7})_{0.5}Pr_{0.5}Fe_{1.55}$ composite and $0.3Pb(Mg_{1/3}Nb_{2/3})O_3–0.7PbTiO_3$ single crystal", *Applied Physics A: Materials Science and Processing*, Vol. 97, No. 1, pp. 201–204 (October 2009). *[Impact Factor=1.595; Grade B]*

11) Yaojin Wang, Chung Ming Leung, Feifei Wang, Siu Wing Or, Xiangyong Zhao, and Haosu Luo, "Dual-mode magnetoelectric effect in laminate composite of Terfenol-D alloy and PMN–PT transformer with double output ports", *Journal of Physics D: Applied Physics*, Vol. 42, No. 13, Article 135414 (July 7, 2009). *[Impact Factor=2.083; Grade B]*

International Conference Proceedings (3 Items):

1) Chung Ming Leung, Shengyao Zhang, Siu Wing Or, S. L. Ho, and K. Y. Lee, "Magnetoelectric smart current sensors for wireless condition monitoring of train traction systems", *Proceedings 1st International Workshop on High-speed and Intercity Railways (IWHIR 2011)*, 19–22 July 2011, Shenzhen and Hong Kong, China, Vol. 2, LNEE 148, pp. 319–327.

2) Wei Kuang, Siu Wing Or, Chung Ming Leung, and S. L. Ho, "Development of piezoelectric transformer-coupled solid state relays for electrical circuit control in railway systems", *Proceedings 1st International Workshop on High-speed and Intercity Railways (IWHIR 2011)*, 19–22 July 2011, Shenzhen and Hong Kong, China, Vol. 2, LNEE 148, pp. 329–338.

3) Chung Ming Leung, Siu Wing Or, and Helen Lai Wa Chan, "Development of an energy storage device for piezoelectric energy harvesters", *Proceedings International Symposium on Smart Materials and Devices and Workshop on Microfluidics and Its Applications*, 10–12 December 2007, The Hong Kong Polytechnic University, Article S2P.07p.

List of Award

(1) Li Po Chun Charitable Trust Fund Scholarship 2010/11
For local full-time UGC-funded postgraduate research students based on academic excellence

Acknowledgements

I would like to express my deep appreciation to my chief supervisor, Dr Derek Siu Wing Or, for his precious guidance and valuable advice throughout the course of my studies. I would also like to extend my warmest appreciation to my co-supervisor, Prof. Siu Lau Ho, for his constant encouragement, advice, and support.

Sincerely thanks are also due to: (1) Prof. Haosu Luo of the Shanghai Institute of Ceramics, Chinese Academy of Sciences for providing $0.7Pb(Mg_{1/3}Nb_{2/3})O_3–0.3PbTiO_3$) (PMN–PT) piezoelectric single crystals for this work; (2) Dr Tony Kar Yun Lee, the rolling stock fleet manager of MTR Corporation Limited, for authorizing the tests of magnetoelectric (ME) passive current sensors and their wireless condition monitors at mainline trains running between Hong Kong and Shenzhen, China; and (3) Mr. Micky Lo, Mr. Kevin Tse, and Mr. Jacky Lam of the Innovative Technology Research Syndicate (ITRS) of PolyU for their valuable advices and supports to the development of the 3G/2G multichannel wireless communication units.

To my research groupmates: Dr. Feifei Wang, Dr. Yaojin Wang, Mr. Chang Shen Wu, Mr. Kowk Fung Cheung, Mr. Shengyao Zhang, Mr. Ching Yin Lo, Ir. Terence Ho Chi Wong, and Ms. Sui Yin Wong, I owe special thanks for their contributing discussion and technical assistance.

I gratefully acknowledge the financial and technical supports from The Hong Kong Polytechnic University.

Last, but not the least, I would like to express my immense gratitude to my family for their understanding and encouragement over the four years of my studies.

Table of Contents

List of Figure Captions

List of Table Captions

List of Symbols and Their Units

Symbol	Meaning	Unit
A	Area	m^2
A_E	Absorption losses of the shield for electric fields and magnetic fields	dB
A_H	Absorption losses of the shield for electric fields and magnetic fields	dB
avg (superscript)	Average value	-
B (superscript)	At constant magnetic flux density	-
B_i	Magnetic flux density	T
B_H	Multiple-reflection correction factor of the shield for magnetic fields	dB
B_r	Residual magnetic flux density	T
c	Specific Heat capacity	J/kg·°C
c_{pq}	Elastic stiffness coefficient	Pa
C_i	Capacitance component	F
C_h	Heat capacity	kJ/kg·K
C_{lth}	Coefficient of linear thermal expansion	10^{-6} /°C
d	Detection distance	m
d_{pq}	Piezoelectric (charge) coefficient or magnetostrictive (strain) coefficient	m/V or C/N or m/A
D (superscript)	At constant electric displacement	-
D_i	Electric displacement	C/m^2
E (superscript)	At constant electric field	-
E_d	Energy density	kJ/m^3
E_i	Electric field	V/m
E_l	Electric field strengths of the transmitted wave as it emerges from the shield	dB
E_0	Incident electric strengths	dB
H_0	Incident magnetic field strengths	dB
E	Young's modulus	Pa
f	Frequency	Hz
f_a	Anti-resonance frequency	Hz
f_r	Resonance frequency	Hz
f_{op}	Operating frequency	Hz
F_i	Force	N
g_{pq}	Piezoelectric (voltage) coefficient or Magnetostrictive coefficient	Vm/N or mAm/V
H (superscript)	At constant magnetic field strength	-
H_i	Magnetic field strength	A/m or Oe
H_l	Magnetic field strengths of the transmitted wave as it emerges from the shield	dB

Symbol	Meaning	Unit
H_c	Coercive field	kA/m
H_{ci}	Intrinsic coercive field	kA/m
H_{Bias}	Magnetic bias field strength	A/m or Oe
I_i	Current component	A
k	Thermal Conductivity	W/m·°C
k_{pq}	Electromechanical coupling factor	-
lam (subscript)	laminate	
l_i	Length component	m
Δl	Change in length	m
m	Mass	kg
m (subscript)	Magnetostrictive phase	-
Mag (subscript)	Magnet phase	-
M_i	Magnetization	A/m
M_{iS}	Saturation magnetization	A/m
N	Frequency constant	Hz·m
p (subscript)	Piezoelectric phase	-
P	Polarization	C/m^2
Q_i	Charge component	C
QS (superscript)	Quasistatic component	-
R_E	Reflection losses of the shield for electric fields and magnetic fields	dB
R_H	Reflection losses of the shield for electric fields and magnetic fields	dB
R_{Ik}	Ratio of harmonic current to fundamental current	%
r_i	Radius component	m
r_C	Radius of the electrical cable	m
s_{pq}	Elastic compliance	m^2/N
S (superscript)	At constant strain	-
S_{ij}	Strain component	-
S_E	Shielding effectiveness for electric fields	dB
S_I	Current sensitivity	V/A
S_M	Shielding effectiveness for magnetic fields	dB
S_W	Wireless transmission strength	%
t	Times	s, min, h
t_r	Response time	μs
t_i	Thickness component	m
T (superscript)	At constant stress	-
T_{ij}	Stress component	Pa
T	Temperature	^oC or K
T_C	Curie temperature	^oC or K
T_{max}	Maximum operating temperature	°C
T_N	Néel temperature	^oC or K

Symbol	Meaning	Unit
T_{op}	Operating temperature	^{o}C or K
T_{hr}	Heat-resistant temperature	°C
TS	Tensile strength	MPa
v_i	Velocity component	m/s
v_l	Longitudinal wave velocity	m/s
v_s	Shear wave velocity	m/s
V_i	Voltage component	V
V_B	DC supply voltage of the battery	V
V_T	Generated sinusoidal voltage to transmitter	V
V_R	Received sinusoidal voltage from receiver	V
w_i	Width component	m
Z_i	Mechanical characteristic impedances component	N/m/s
α_E	Direct magnetoelectric field coefficient	V/cm·Oe
α_V	Direct magnetoelectric voltage coefficient	V/Oe
α_{the}	Thermal expansion coefficient	$\times 10^{-6}$/°C
σ_{th}	Thermal conductivity	J/°C/m/s
β	Constant	-
ε	Permittivity of material	F/m
ε_o	Permittivity of free space = 8.854×10^{-12}	F/m
ε_r	Relative permittivity or dielectric constant	-
λ	Magnetostriction	ppm
λ_s	Saturation magnetostriction	ppm
σ_r	relative conductivity of the shield	Ω·m
φ_i	Magnetomechanical or electromechanical transformation factors	-
μ	Permeability of material	H/m
μ_o	Permeability of free space = $4\pi \times 10^{-7}$	H/m
μ_{rij}	Relative permeability component	-
υ	Volume	m^3
ρ	Density	kg/m^3
ρ_a	Density of Terfenol-D short bars	kg/m^3
ρ_e	Density of epoxy	kg/m^3
ρ_c	Density of composite	kg/m^3
δ	Skin depth	m
τ	Dynamic viscosity	mPa·s

Chapter 1

Introduction

1.1 Asset Management

The concept of asset management tends to be broad in scope, covering a wide variety of areas such as general management, operations, services, production, maintenance, finance, human resources, real estate, etc. While the broader concept allows a multifaceted investigation of physical assets, the arenas constitute a multiplicity of spheres of activity. In general, the term "asset management" can be applied to any asset in which things of value to an entity or to a group are monitored and maintained [1].

In engineering, asset management is often referred to a total management of physical assets so that the term "engineering asset management" is more appropriate to describe asset management with specialism in engineering [1]. Accordingly, the term "electrical asset management" is adopted to specify engineering asset management in the field of electrical engineering, while the term "electrical assets" is employed to indicate electrical engineering assets to be managed [2]. The following sections further elaborate the two terms: electrical assets and electrical asset management.

1.1.1 Electrical Assets

The importance of using the term "assets" in engineering is to let the concept of engineering assets to be consistent with basics, every idea. Before looking at electrical assets, we need to differentiate "engineering assets" from "non-engineering assets". In fact, all assets fall into one of these two categories of assets. In non-engineering assets (e.g., financial assets), stocks, bonds, mortgages, loans, savings, deposits, etc. of various sorts exist as contracts between legal entities. In engineering assets, by contrast, things that are managed by engineering asset managers such as inventories, products, equipment, parts, components, materials, etc. may exist independent of any contract even though legal rights in them can be included in contracts as in non-engineering assets [2–5]. Figure 1.1 shows the fundamental nature of engineering assets. Like a pyramid, the non-engineering asset components can be built upon the base of engineering assets to enlarge the scope and scale as well as to achieve the multiplicity of functions and activities [2]. For example, engineering assets usually have a financial dimension that reflects their economic value.

With the above clarification, electrical assets are a subset of engineering assets used especially to describe worthy electrical engineering systems and their associated equipment, parts, components, materials, etc., which are capable of being owned or controlled to produce value in the field of electrical engineering [6]. In other words, electrical assets can be defined as valuable, influential, and essential facilities that are necessary to life of human. Hence, electrical assets are usually referred to huge electrical engineering systems, which would affect the crowd to a certain extent

although they only exhibit a small trouble. The said huge electrical engineering systems include electric power systems, renewable energy systems, nuclear energy systems, railway systems, aircrafts and aerospace systems, to name but a few.

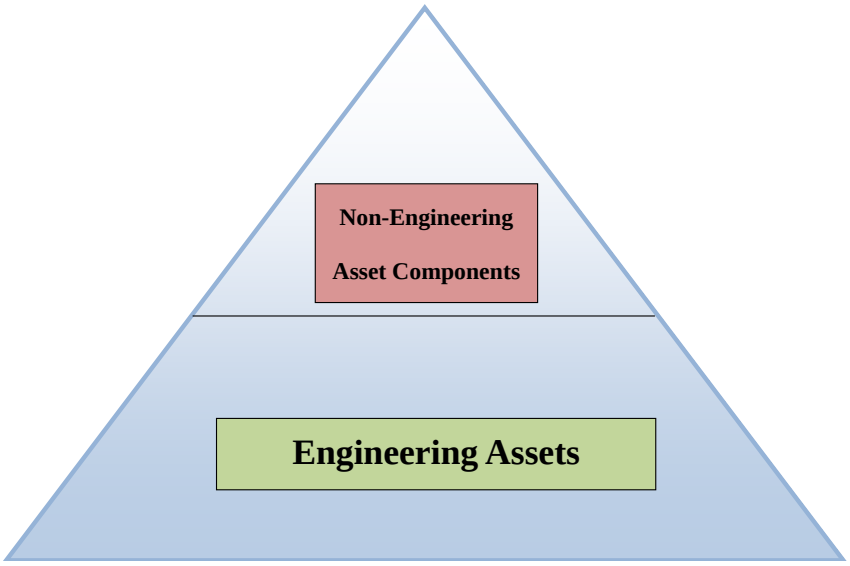

Fig. 1.1 Fundamental nature of engineering assets [2].

1.1.2 Electrical Asset Management

Electrical asset management is considered to be one of the most important general managements in electrical engineering. The applications are numerous and researchers tackle them from different aspects and viewpoints. Figure 1.2 illustrates the relationship between applications and base research of electrical assets in electrical asset management [2,7]. From a technical perspective, electrical asset management is an engineering asset management focused specifically on the maintenance and condition monitoring of electrical assets to support their infrastructures and to assure their safety, reliability, and availability. Condition monitoring is thus an important electrical asset management tool and can be applied to any maintenance plans in

electrical assets. Consequently, base research on condition monitoring technology has received considerable attention in recent years, which involves a number of new/advanced enabling technologies varying from new materials, sensors, etc. to advanced instruments, computers, microprocessors, software, wireless communications, etc. The review, technology trend, and challenges of condition monitoring are discussed in Section 1.2.

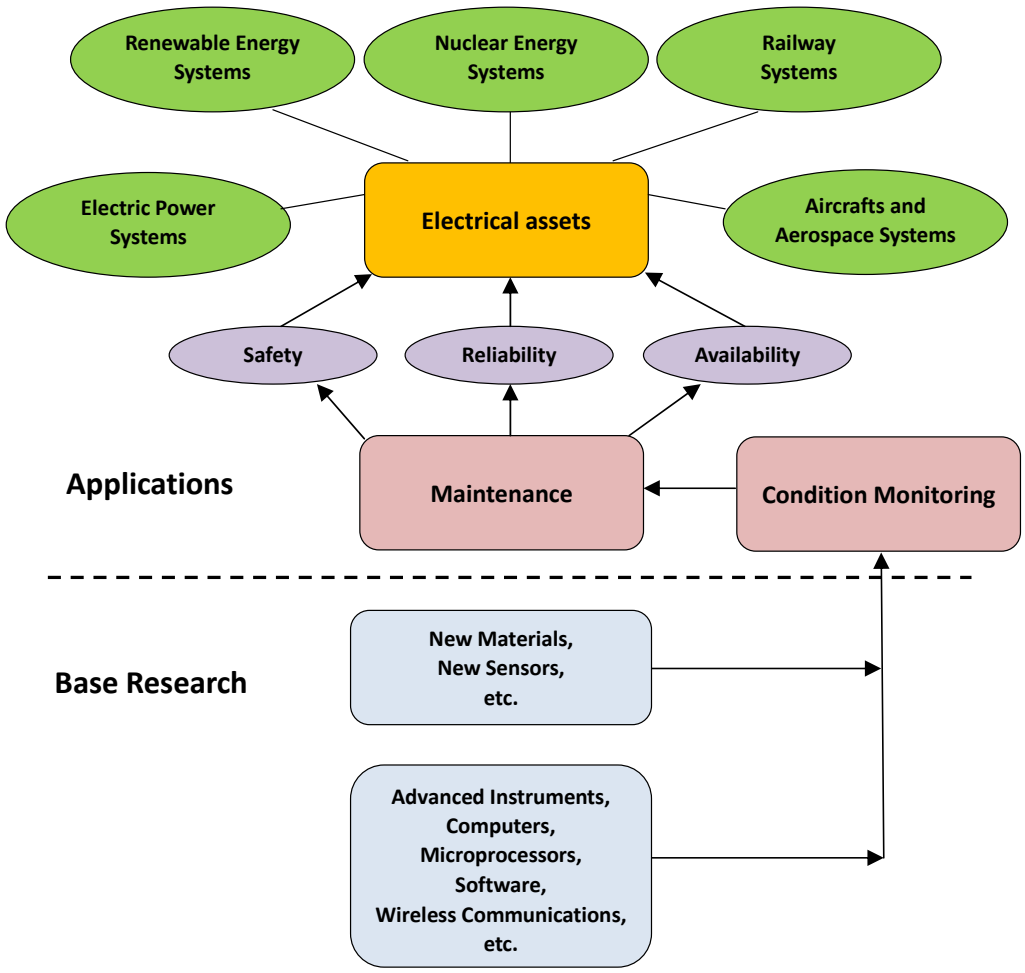

Fig. 1.2 Relationship between applications and base research of electrical assets in electrical asset management [2,7].

1.2 Condition Monitoring

1.2.1 Review of Condition Monitoring Technology

Condition monitoring is an essential electrical asset management tool to maintain a successful management of electrical assets against failures and therefore to increase the degrees of safety, reliability, and availability (Fig. 1.2) [2,7]. The historical development of condition monitoring has been intimately tied to two factors, including an industrial imperative towards effective maintenance and a technological improvement in condition monitors [8]. In fact, the demand for condition monitoring has increased greatly in recent years as electrical assets have aimed to utilize existing maintenance resources more effectively on the one hand, and to minimize the consequence of failures on the other hand.

Figure 1.3 shows the evolution of traditional "wired" condition monitoring technology from 1960 to 2000 [9]. The technology essentially went through four major evolutional stages as a result of the rapid development of the instrument, computer, microprocessor, and software technologies during those four decades. The four major evolutional stages included the emergence of human-oriented measurements in the early 1960s, analog instrument-based monitoring in the early 1970s, digital instrument-based monitoring in the mid-1980s, and software-integrated monitoring in the mid-1990s.

From Fig. 1.3, the early so-called condition monitoring was merely human-oriented measurements. The instruments employed were very elemental using deflecting pointers or some electro-/magneto-mechanical indicators as readout means,

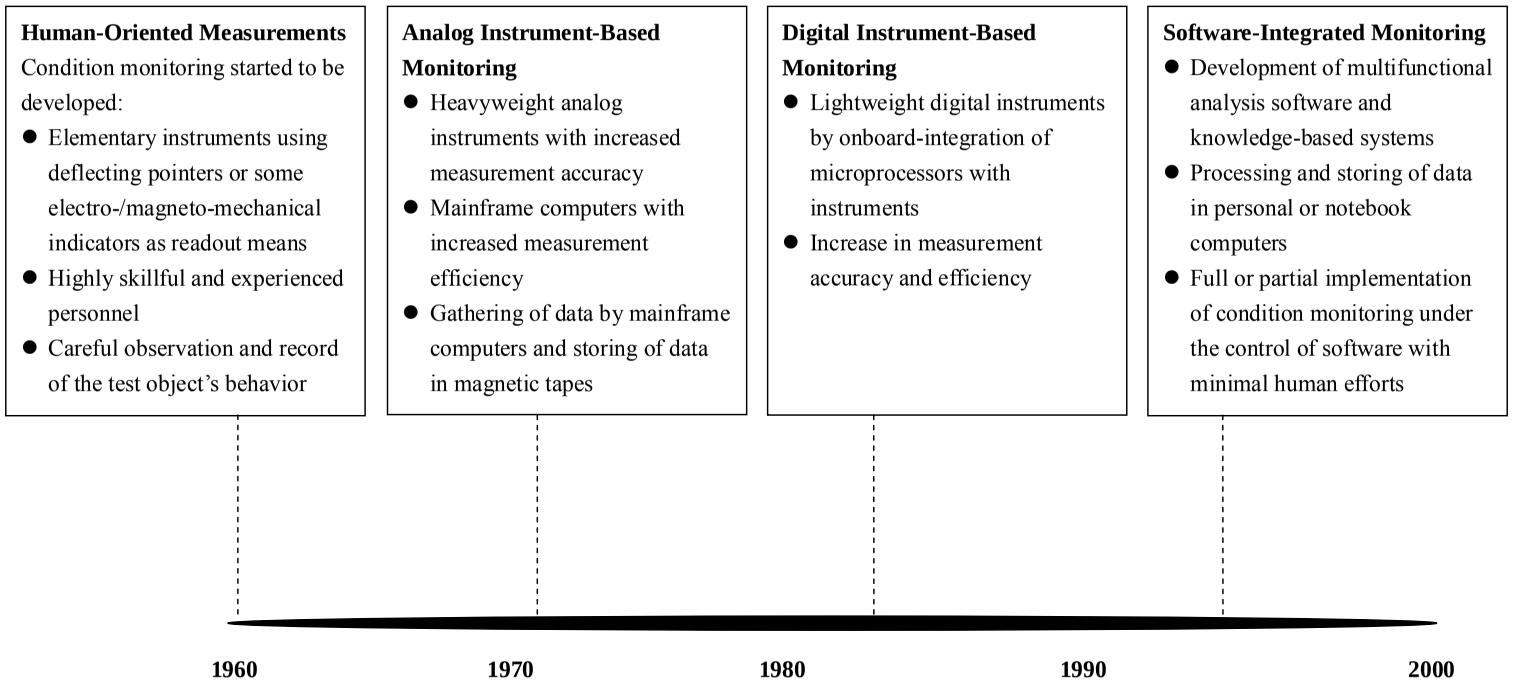

Fig. 1.3 Evolution of traditional "wired" condition monitoring technology from 1960 to 2000 [9].

and the measurements relied totally on highly skillful and experienced technical staff to carefully observe and record the behavior of the objects to be measured. Starting from the early 1970s, some heavyweight analog instruments (e.g., analog oscilloscopes) and mainframe computers were introduced into market and used in condition monitoring to increase the measurement accuracy and efficiency. The measured data were gathered by the mainframe computers and stored in magnetic tapes. The condition monitoring thus became analog instrument-based monitoring. Because of the successful development of microprocessors and onboard-integration of microprocessors with instruments, digital instrument-based monitoring was grown dynamically in the mid-1980s. The size and weight of digital instruments were much reduced, and the measurement accuracy and efficiency were much increased, in comparison with the analog instruments. With the rapid development of software technology in the 1990s, software-integrated monitoring started to appear in the mid-1990s. Multifunctional analysis software and knowledge-based systems were readily developed, and all monitored data were processed and stored in personal or notebook computers. Condition monitoring could be fully or partially implemented under the control of software with minimal human efforts.

Although condition monitoring has been undergone several evolutional improvements in the past several decades, all powering and signal-conditioning activities have been mainly based on electrical cables or wires. To this extent, the traditional condition monitoring technology described above is commonly referred to "wired" condition monitoring technology in order to make distinction from the modern

or desired "wireless" condition monitoring technology to be discussed in Section 1.2.2.

1.2.2 Technology Trend and Challenges of Condition Monitoring

Driven by the strategic development of smart electric grids, renewable energy systems, nuclear power plants, high-speed and intercity railways, electric vehicles, aircrafts and aerospace systems, transportation infrastructures, intelligent buildings, telecommunication systems, etc. in various nations in the past two decades, the ability to readily operate and maintain these infrastructures relies heavily on the support of advanced condition monitoring technologies to real-time monitor condition or health for performance optimization, utilization maximization, safety increment, reliability improvement, availability enhancement, and life cycle extension [8]. Hence, condition monitoring has taken on greater significance with the growing importance of the modern electrical asset management tool in recent times. Accordingly, the sensing device, condition monitoring equipment, and their service market holds tremendous potential and is poised to grow every year with market size in excess of US$2 billion by 2015 [3].

From the technological viewpoints, traditional "wired condition monitors" as pointed out in Section 1.2.1 and further illustrated in Fig. 1.4(a) involve the deployment of active sensors (e.g., active current sensors) in multiple locations (nodes) and the connections between the active sensors and their power supplies, signal conditioners, and base station (network) through electrical power and signal cables or wires. These wired condition monitors are not only bulky and complicated but also

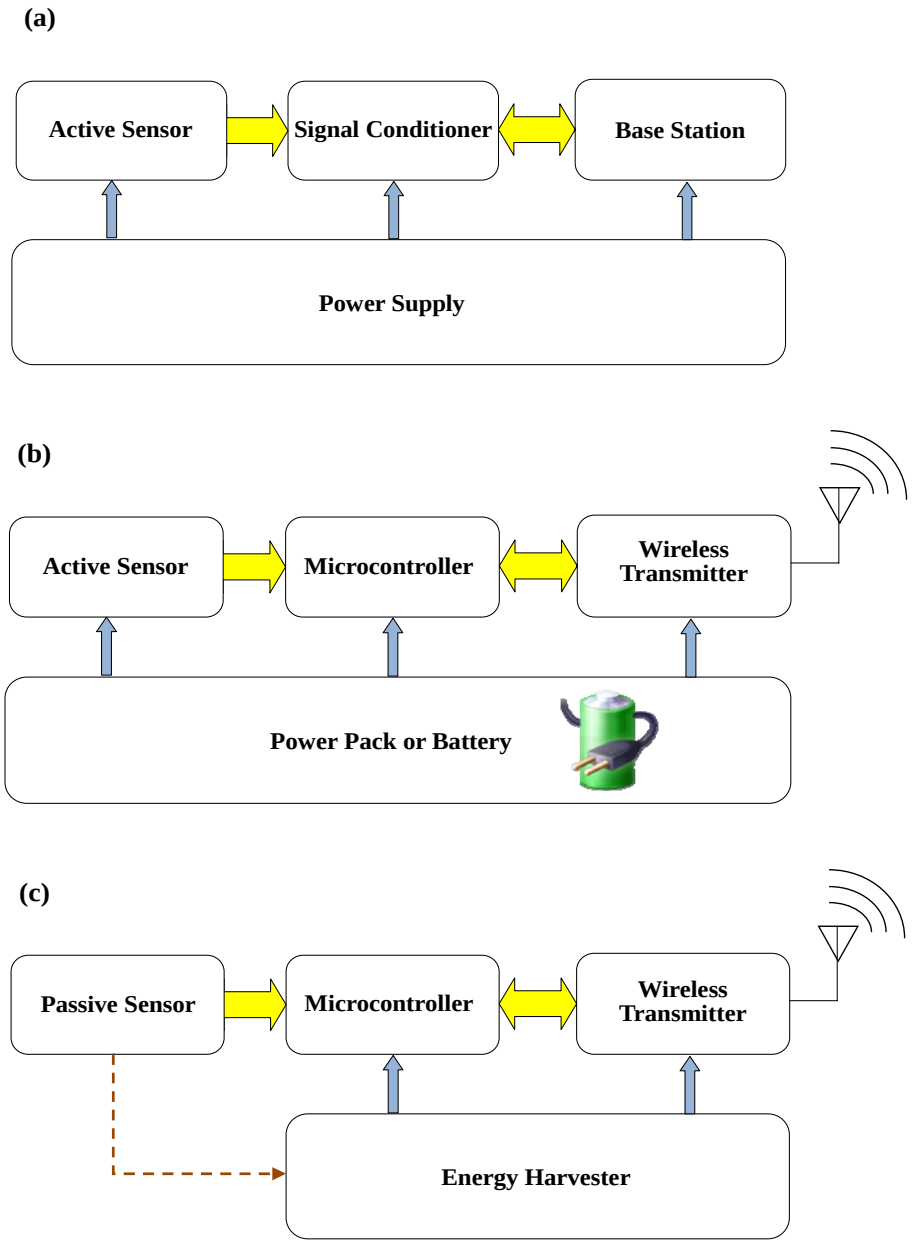

Fig. 1.4 **(a) Traditional "wired condition monitor" with wired active sensor, signal conditioner, power supply, and base station; (b) state-of-the-art "wireless condition monitor" integrating an active sensor with a microcontroller and a wireless transmitter, all powered by a power pack or a battery; and (c) next generation "self-powered wireless condition monitor" having a power supply-free, signal conditionerless, wideband passive sensor integrated with a microcontroller and a wireless transmitter powered by the electrical energy scavenged by an energy harvester.**

expensive in terms of installation and maintenance. In addition, the large spatial size, tough and complex arrangement, critical measuring locations, hazardous operating environment (e.g., high-voltage and heavy-current environment), etc. of the electrical assets always impose great difficulties in implementing these system-based wired condition monitors [1].

By contrast, state-of-the-art "wireless condition monitors" [Fig. 1.4(b)], which usually integrate active sensors with microcontrollers and wireless communication (transmitter and receiver) units, all powered by power packs or batteries, have emerged as a flexible alternative to the traditional system-based wired condition monitors due to the ease of installation, large scalability, and highly distributed nature. However, the major drawback of the wireless condition monitors is their limited battery life to sustain the operations of active sensors, microcontrollers, and wireless transmitters [1]. The powering of the densely populated active sensors and their associated electronics is indeed a critical problem in the light of wiring and replacing batteries. In practice, these battery-powered wireless condition monitors are unable to assure an autonomous and uninterrupted monitoring.

A possible solution that may be the most efficient and practical solution is to develop "self-powered wireless condition monitors" for realizing self-sustainable condition monitoring. However, this solution is not possible without the enabling of two levels of core technologies, namely: (1) the power supply-free, signal conditionerless, wideband passive sensor technology for the first level, and (2) the energy harvesting technology for the second level. As indicated in Fig. 1.4(c), since

the passive sensors in the new generation self-powered wireless condition monitors require no external power supplies to sustain their operation and produce sufficiently large and clear output signals in response to the input stimulus without the strong support (or even without the support) of the signal conditioners, they can truly serve as autonomous sensors for improved monitoring purposes. This suggests that the passive sensors can even act as energy converters to convert wasted environmental energy (e.g., electromagnetic energy, mechanical vibration energy, etc.) into electrical energy in the energy harvesters. In either way, the electrical energy scavenged by the energy harvesters can be fully supplied to the microcontrollers and the wireless transmitters. Another advantage of this design is that the condition monitors can evolve from the traditional format of bulky and complicated systems to the new generation format of portable devices at each node. Consequently, the successful development of the power supply-free, signal conditionerless, wideband passive sensor technology has the most determinative effect on realizing self-powered wireless condition monitors.

1.2.3 State-of-the-Art Current Sensors

Current sensors are electrical devices which measure currents in a cable or a wire and generate a signal of some sort in response to the currents [10]. Current monitoring is more meaningful compared to voltage monitoring in most electrical assets because current signals contain much valuable information such as harmonics and unbalanced loads in electric power distribution systems, unbalanced forces and motor/bearing irregularities in motor drives of train traction systems, etc. Nowadays, there are four main types of current sensors available in market; they are namely: Hall sensors, current transformers, Rogowski coils, and resistive shuts [10–15].

As shown in Fig. 1.5, Hall sensors, current transformers, and Rogowski coils are operated on the basis of measuring current-induced magnetic fields governed by Ampère's law [10], while resistive shunts work on the principle of Ohm's law to measure current-induced voltage drop across some precision shunt resistors of low resistances [10,11]. Hall sensors [Fig. 1.5(a)] feature real-time measurement capability for frequencies up to about 30 kHz at the expense of requiring high-quality constant-current supplies and signal conditioners to actively excite and gather the inherently weak Hall voltages (5–40 μV/Oe), respectively [11,12]. Current transformers [Fig. 1.5(b)] possess power supply-free real-time measurement nature, but this only happens at a low detection sensitivity (≥40 A) and in a very limited operating frequency range (40–60 Hz) due to the high relative permeability (≥1000) and increased magnetic losses at elevated frequencies in the ring-shaped ferromagnetic cores, respectively

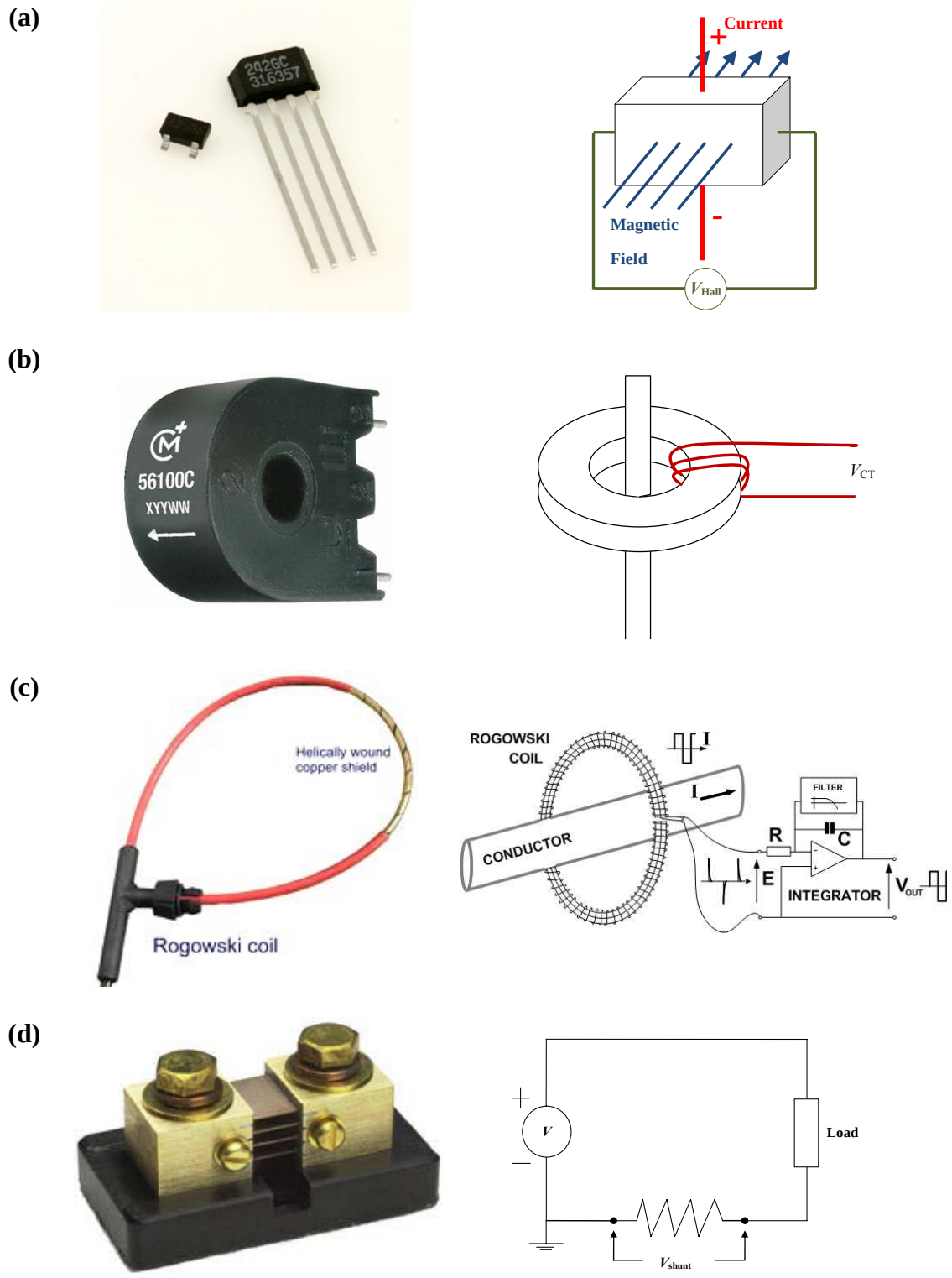

Fig. 1.5 Photographs and schematic diagrams of (a) Hall sensor [12], (b) current transformer [13], (c) Rogowski coil [14], and (d) resistive shut [15].

[10,13]. Rogowski coils [Fig. 1.5(c)] only allow real-time measurements at sufficiently high frequencies (>100 Hz) with the support of high-precision integrating fluxmeters [10,14]. Resistive shunts [Fig. 1.5(d)] enable real-time measurements over a broad range of frequencies without auxiliary equipment, but they suffer intrinsically from in-circuit current flow and hence voltage drop and power loss in the shunt resistors without any self-isolation [10,15].

Obviously, all these state-of-the-art current sensors do not contain the all-in-one features of power supply free, signal conditionerless (i.e., high signal strength and high detection sensitivity), and wide bandwidth (i.e., wide operating frequency range) necessarily for the realization of the desired self-powered wireless condition monitors. Hence, the development of such an advanced class of passive current sensors is physically interesting, technologically important, and commercially valuable.

1.3 Magnetoelectric Effect, Materials, and Applications

1.3.1 The Magnetoelectric Effect

The magnetoelectric (ME) effect, which is defined as an induced electric polarization in a material by an applied magnetic field [16,17], was first proposed by Pierre Curie in 1894. Curie stated that a material with asymmetric molecules produces a change in electric polarization when it is subject to an applied magnetic field [18]. However, the effect was not formally named until the first use of the term "magnetoelectric" by Peter Debeye in 1926 [17], and researchers started to use "magnetoelectric" to address the effect from then on. In 1961, D. N. Astrov reported the first observation of magnetic field-induced electric polarization in an antiferromagnetic single crystal – chromium oxide (Cr_2O_3) [19,20]. This observation attracted increasing research attention in the ME effect and ME materials in general.

Today, the ME research has become a hot research topic, partly due to the evolutional concept of multifunctionality in materials, and partly owing to the innovative application potential of the resulting smart sensors and smart systems such as power supply-free, signal conditionerless, wideband passive current sensors for self-powered wireless condition monitors. Figure 1.6 shows the number of SCI journal publications per half a decade in the topic of "magnetoelectric" recorded by ISI Web of Science from 1971 to 2010. In the early 1970s, the research on ME was quite warmly with a record of 50 publications. The number of publications increased rapidly from 150 publications in 1991–1995 to as many as 1600 publications in 2006–2010.

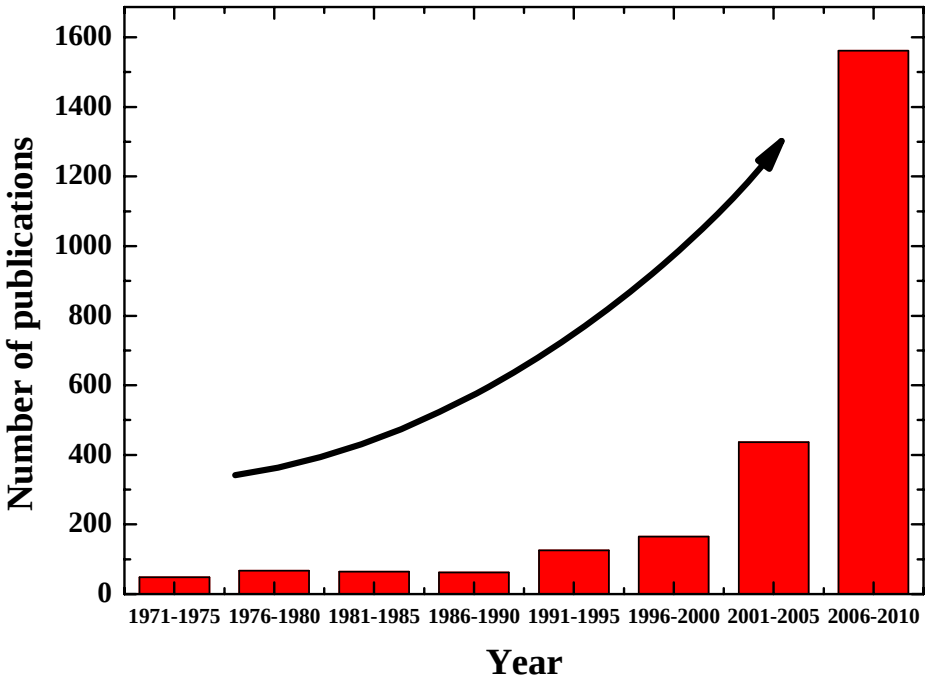

Fig. 1.6 Number of SCI journal publications per half a decade in the topic of "magnetoelectric" recorded by ISI Web of Science from 1971 to 2010 [21].

Figure 1.7 illustrates the evolution of ME materials technology from 1894 to 2006. This commenced with the first proposal of the ME effect in 1894, followed by the first discovery of single-phase materials in 1961, and then by the first introduction of multi-phase materials in 1974. The multi-phase materials, in turn, involved two-phase bulk composites introduced in 1974, two-phase laminated composites reported in 2001, and three-phase laminated composites disclosed in 2004. For all cases, the main development objective is to enhance the ME effect. The detailed development of ME materials is discussed in Section 1.3.2.

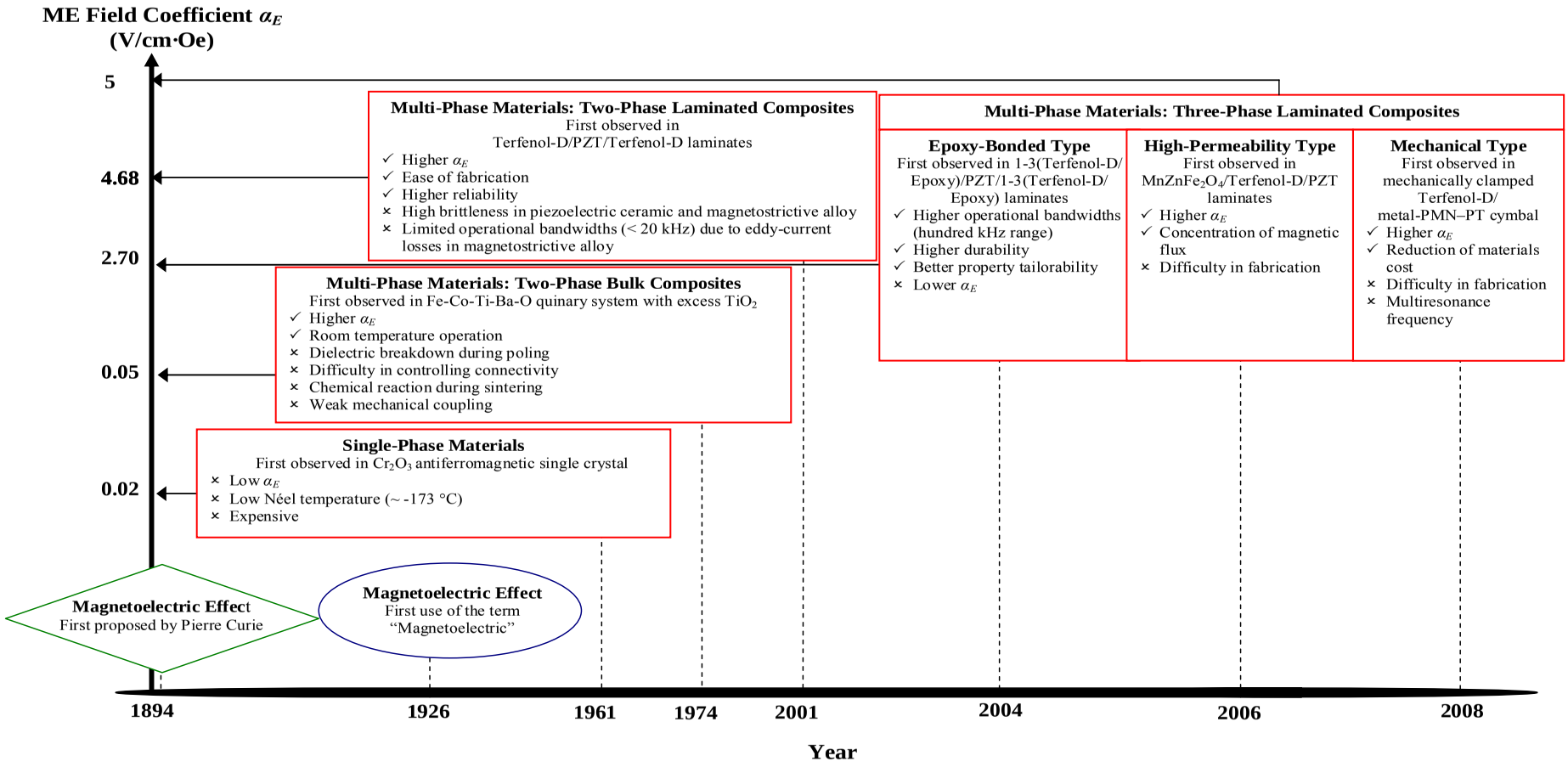

Fig. 1.7 Evolution of ME materials technology from 1894 to 2006 [18–24].

Before going through the details of ME materials, it is required to give a common quantification of the ME effect. In single-phase materials and bulk composite materials, it is preferable to characterize the materials using ME field coefficient (α_E), defined by an induced electric field (E) in response to an applied magnetic field (H), as follows:

$$\alpha_E = \frac{dE}{dH} \tag{1.1}$$

For laminated composite materials and practical devices such as magnetic field sensors and their associated current sensors, it is more appropriate to use ME voltage coefficient (α_V), defined by an induced electric voltage (V) in response to an applied magnetic field (H), expressed as follows:

$$\alpha_V = \frac{dV}{dH} \tag{1.2}$$

In Eqs. (1.1) and (1.2), α_E and α_V have units of V/cm·Oe and V/Oe, respectively.

It is noted that α_V is of the main consideration in this thesis as our current sensing elements and passive current sensors are essentially developed using ME laminated composite materials, which are presented in Chapters 3 and 4, respectively.

1.3.2 Magnetoelectric Materials

1.3.2.1 Single-Phase Materials

Single-phase materials with both antiferromagnetic and ferroelectric order in the same phase are the first discovered ME materials (Fig. 1.7). In 1961, D. N. Astrov observed the temperature dependence of the ME effect in an antiferromagnetic single-crystalline sample of Cr_2O_3 and found a sub-zero antiferromagnetic Néel temperature (T_N) of -173 °C above which the ME effect vanished [20]. In late 1961, Folen *et al*. measured an α_E of 20 mV/cm·Oe in a Cr_2O_3 single crystal [25]. Two years later, Foner and Hanabusa reported the ME effect in Cr_2O_3 and $(Cr_2O_3)_{0.8}(Al_2O_3)_{0.2}$ single crystals and showed the existence of a higher T_N of -13 °C in $(Cr_2O_3)_{0.8}(Al_2O_3)_{0.2}$ [26]. In the same year, Shtrikman and Terves demonstrated experimentally and theoretically that Cr_2O_3 polycrystalline powders also possess the ME effect when they are annealed in an electric field or a magnetic field environment [27].

Due to the fact that the weak ME effect with a small α_E of 20 mV/cm·Oe reported in Cr_2O_3 was considered to be inapplicable for many industrial use. Alshin and Astrov investigated Ti_2O_3 in 1963 [29], while Rado explored $GaFeO_3$ in 1964 [28]. In 1969, Hornreich provided a group of potential candidates based on the magnetic point group, including $DyAlO_3$, $GdAlO_3$, $TbCoO_3$, $DyFeO_3$, Fe_2TeO_6, Cr_2TeO_6, $FeCrWO_6$, Cr_2WO_6, V_2WO_6, $FeSb_2O_4$, Ca_2FeAlO_5, Eu_3O_4, and β-$FeNaO_2$ [29]. However, the observed ME effects were still weak and only available at low T_N levels.

In 1970, $BiFeO_3$, a commensurate ferroelectric material, was found to be unique amongst various ME multiferroics because of its exceptionally high

antiferromagnetic and ferroelectric transition temperatures well above room temperature [30]. This gave rise to a hope of developing the material into practical devices based on the intrinsic ME coupling at room temperature. As a result, $BiFeO_3$ has received tremendous research attention over the last few decades. In particular, the research efforts spent in the last couple of years have led to encouraging results on this compound in the pure and solid solution forms [30].

In 2004, high T_N dielectric anomalies of 42 and 60% were observed in $YMnO_3$ and $HoMnO_3$, respectively. In $YMnO_3$, antiferromagnetic and ferroelectric domain walls were seen in experiments. In $HoMnO_3$, an electrically driven magnetic phase transition was observed. This is a dramatic form of switching, suggesting a new approach for ME switching [30].

1.3.2.2 Multi-Phase Materials

To overcome the drawbacks of weak ME effect and low T_N intrinsic in single-phase materials, considerable research efforts have been put on multi-phase materials since the 1970s (Fig. 1.7). Bulk and laminated composite materials are the two main groups of multi-phase materials.

In practice, multi-phase materials are usually prepared by combining different magneto- and electro-active material phases together to form magnetoelectrically coupled composites in the bulk and laminated forms. These magnetoelectrically coupled composites have drawn significant research interest in recent years because of the greater availability in constituent material phases, the larger flexibility in

materials' design and fabrication, the stronger ME effect of several orders of magnitude higher than the single-phase materials, and the higher operational temperatures well above room temperature [16].

In multi-phase materials, "product property" or "product effect" is the physical origin of the ME interaction between the constituent phases. Therefore, multi-phase materials can exhibit ME effect extrinsic in the materials themselves. For example, the ME effect in a magnetostrictive-piezoelectric two-phase composite is the product effect of the magnetostrictive effect in the magnetostrictive material phase and the piezoelectric effect in the piezoelectric material phase, through the mechanical mediation between the two material phases [31]. In more details, a magnetic field applied to such a composite leads to magnetostrictive strains in the magnetostrictive material phase due to the magnetostrictive effect. These magnetostrictive strains are transferred through mechanical bonding to the piezoelectric material phase, resulting in mechanical stresses. These mechanical stresses, in turn, stress the piezoelectric material phase to produce piezoelectric voltages with amplitude proportional to and frequency the same as the applied magnetic field based on the piezoelectric effect. This type of ME effect, which is physically different from the "intrinsic" ME effect reported in single-phase materials in Section 1.3.2.1, is usually named as the "extrinsic" ME effect defined as follows:

$$\text{"Extrinsic" ME Effect} = \frac{\text{Electric Output}}{\text{Magnetic Input}} = \underbrace{\frac{\text{Mechanical Output}}{\text{Magnetic Input}}}_{\text{Magnetostrictive Effect}} \times \underbrace{\frac{\text{Electric Output}}{\text{Mechanical Input}}}_{\text{Piezoelectric Effect}} \quad (1.3)$$

Therefore, multi-phase materials are potential candidates for practical applications. Details of the magnetostrictive and piezoelectric constituent material phases used in the present study, together with the magnetostrictive and piezoelectric effects, are described in detail in Chapter 2.

(1) Bulk Composites

The exploration of bulk composites actually began in 1948 when B. D. H. Tellegen failed to synthesize bulk composites with the extrinsic ME effect by combining two different types of macroscopic particles having magnetic and electric dipole moments [31]. Though the original idea was fundamentally flawed, it created a new approach to prepare novel classes of ME materials in the multi-phase composite form.

In 1974, Boomgaard *et al*. prepared a quinary system Fe-Co-Ti-Ba-O using an unidirectional solidification technique (Fig. 1.7) [22,32]. A large α_E of 50 mV/cm·Oe was obtained at room temperature in an eutectic composition with an excess TiO_2 of 1.5 wt%. Their later work in 1976 demonstrated an improved α_E of 130 mV/cm·Oe in an eutectic composition of $CoFe_2O_4/BaTiO_3$ prepared by a modified unidirectional solidification technique [33]. This α_E is about 7 times larger than the singe-phase Cr_2O_3 of 20 mV/cm·Oe (Fig. 1.7). Another work by Boomgaard *et al.*, also in 1976, reported an α_E of 25 mV/cm·Oe in sintered composites of $NiFe_2O_4/BaTiO_3$ doped with Co and Mn [34]. Two years later, they acquired a larger

α_E of 80 mV/cm·Oe in sintered composites of $Ni(Co,Mn)Fe_2O_4/BaTiO_3$ [35]. These composites belonged to the same system as their previous work but with excess TiO_2.

Ismailzade *et al.* in 1980 and 1981 found that bulk composites of $BiFeO_3$ and $Pb(Fe_{0.5}Nb_{0.5})O_3$, $BaTiO_3$, or $PbTiO_3$ show the ME effect [36,37]. Bunget and Raetchi investigated the ME effect in Ni-Zn ferrite/Pb(Zr, Ti)O_3 (PZT) bulk composites and found in 1981 and 1982 that α_E is dependent upon the applied magnetic field [38,39]. Rottenbacher *et al.* reported an observation of ferromagnetic and ferroelectric hystereses in bulk composites of Mg-Mn ferrite and $BaTiO_3$, having 30:70, 50:50, 70:30, and 90:10 wt% ratios of Mg-Mn ferrite to $BaTiO_3$, in 1981 [40]. In 1988, Gelyasin and Laletin found that the piezoelectric resonance frequencies in bulk composites of ferromagnetic ferrite and piezoelectric ceramic have the dependent effect on applied magnetic field with the maximum change of ~0.2 at ~11 kOe [41].

The Newnham's group and Russia scientists prepared bulk composites of ferrites and $BaTiO_3$ or PZT by a conventional sintering process in the early 1990s [42]. Patankar *el al.* performed extended experiments on several doped ferrite/titanate bulk composites such as $CuFe_{1.8}Cr_{0.2}O_4/Ba_{0.8}Pb_{0.2}TiO_3$ in 2001 [42]. Table 1.1 lists some other common bulk composites, including their compositions, synthesis techniques and conditions, and α_E values [42].

Table 1.1 List of some common ME bulk composites [42].

Composition	Synthesis Technique and Condition	α_E (mV/cm·Oe)
0.38 $CoFe_2O_4$/0.62 $BaTiO_3$	Bridgman under 1 atm at O_2/50 cm^3 h^{-1}	50
0.40$Ni_{0.97}Co_{0.03}Mn_{0.1}Fe_{1.90}O_4$/0.60 $BaTiO_3$	Sintered at 1,300 °C for 24 h	80
0.3 $CuFe_2O_4$/0.7 $PbZr_{0.53}Ti_{0.47}O_3$	Sintered at 950 °C for 2 h	421
$Ni_{0.8}Zn_{0.2}Fe_2O_4$/0.41 vol% PZT	Hot-pressed at 1,000 °C under 7 MPa	45
CoO-FeO/BaO-TiO_2 solution	Sintered at 1,000–1,200 °C for 3 h	5.58
20 wt% $NiCo_{0.02}Cu_{0.02}Mn_{0.1}Fe_{1.8}O_4$/PZT	Sintered at 1,250 °C	115
0.25 $CuFe_2O_4$/0.75 $BaTiO_3$	Sintered at 1,200 °C for 12h	~0.52
0.45 $CuFe_{1.6}Cr_{0.4}O_4$/0.55$BaTiO_3$	Sintered at 1,200 °C for 24h	~0.1

Researchers have been persisting in the study of bulk composites for 25 years, and different sintering methods, particulate sizes, and volume fractions have been studied to improve the performance of bulk composites. However, the observed maximum α_E is still limited to 100 mV/cm·Oe. In fact, there are several reproducibility and reliability problems crucially remained unsolvable to date [43]. These problems include: (1) difficulty in controlling the connectivity of the constituent phases; (2) chemical reaction between phases during the sintering process; (3) dielectric breakdown through the low-resistive magnetostrictive phase during poling of the piezoelectric phase; and (4) weak mechanical coupling between phases due to processing-induced mechanical defects such as pores, cracks, etc. All these problems tend to weakening of the ME effect for practical applications.

(2) Laminated Composites

In view of the drawbacks of bulk composites, researchers have further adjusted their focus from bulk composites to laminated composites of magnetostrictive and piezoelectric materials since 2000 (Fig. 1.7). In fact, the fabrication of laminated composites is relatively simple. It basically involves a combination of magnetostrictive and piezoelectric material phases arranged along the desired direction(s) and an addition of adhesion in forms of conductive or passive adhesives to the interfaces for mechanical bonding. There are two major types of laminated composites: namely, two-phase laminated composites and three-phase laminated composites. The α_V values are from several times to several tens of times larger (30–1600 mV/Oe) compared to the bulk composites (10 mV/Oe maximum).

(2a) Two-Phase Laminated Composites

Two-phase laminated composites are typically made of one or more magnetostrictive material layers bonded with one or more piezoelectric material layers with different arrangements of the magnetization (*M*) and polarization (*P*) directions as shown in Fig. 1.8. The possible magnetostrictive materials include: $Tb_{0.3}Dy_{0.7}Fe_{1.92}$ (Terfenol-D) alloy, Metglas alloy, Permendur alloy, Ni metal, etc., while the possible piezoelectric materials include: Pb(Zr, Ti)O_3 (PZT) ceramics, $Pb(Mg_{1/3}Nb_{2/3}O_3)$–$PbTiO_3$ (PMN–PT) single crystals, PVDF polymers, etc. [23,24,43–45].

The first two-phase laminated composite, which was a Terfenol-D /PZT/Terfenol-D sandwich with a transverse magnetization–transverse polarization

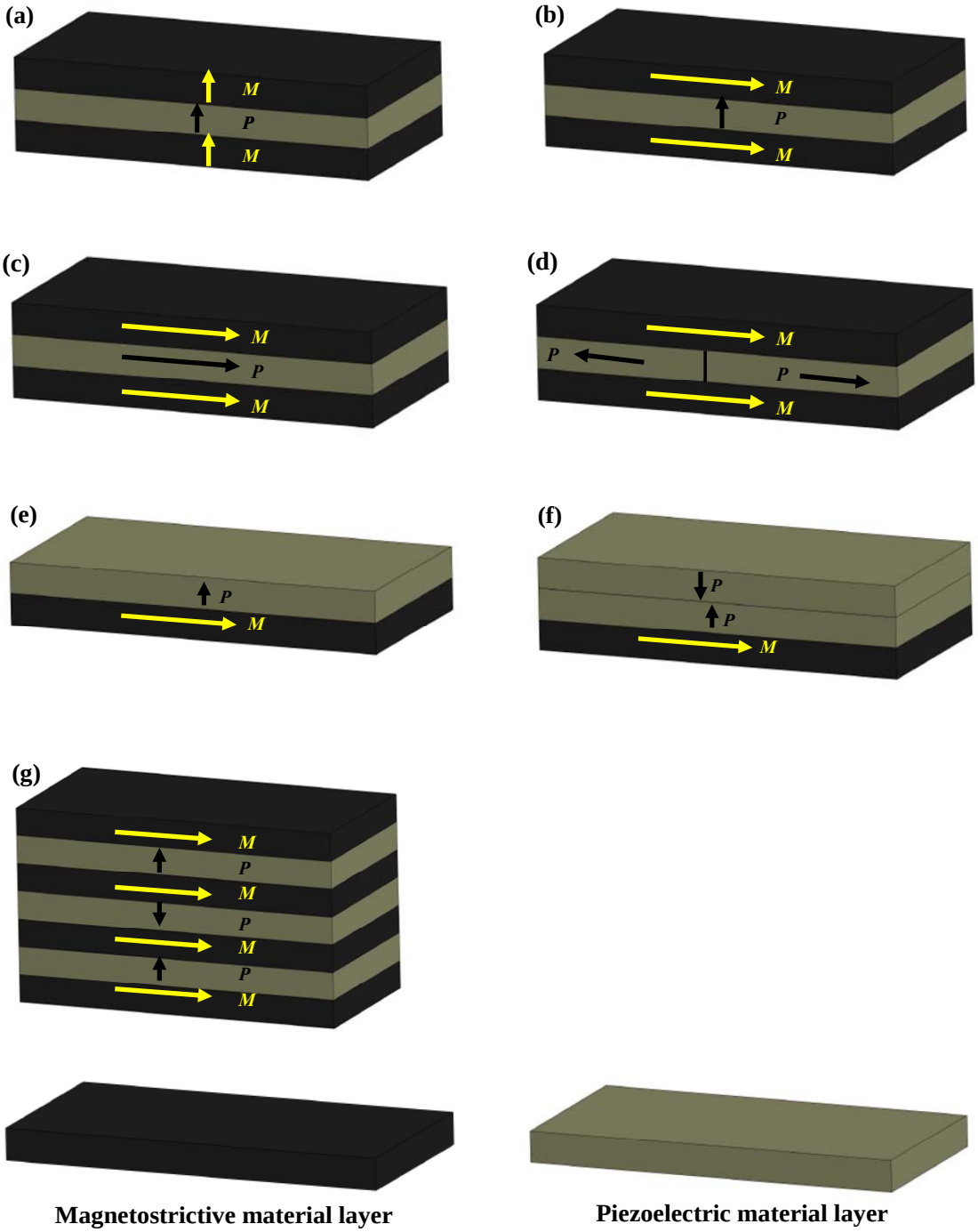

Fig. 1.8 **Some common ME two-phase laminated composites with different arrangements of the magnetization (*M*) and polarization (*P*) directions: (a) transverse–transverse (*T*–*T*) sandwich, (b) longitudinal–transverse (*L*–*T*) sandwich, (c) longitudinal–longitudinal (*L*–*L*) sandwich, (d) *L*–double-half-*L* sandwich, (e) *L*–*T* bilayer, (f) *L*–double-*T* bilayer, and (g) *L*–*T* multilayer [23,24,43–52].**

(*T–T*) arrangement [Fig. 1.8(a)], was reported by Ryu *et al.* in 2001 [23,24]. A large α_V of 30 mV/Oe was found at a magnetic bias field (H_{Bias}) of 4.2 kOe at 1 kHz. One year later, they further enhanced α_V to 41 mV/Oe at an optimal H_{Bias} of 4 kOe at 1 kHz by replacing the PZT layer by a PMN–PT layer with the same *T–T* arrangement [46]. Dong *et al.* prepared Terfenol-D/PZT/Terfenol-D and Terfenol-D/PMN–PT/Terfenol-D sandwiches, both with a longitudinal magnetization–transverse polarization (*L–T*) arrangement, in 2003 and 2004, respectively [Fig. 1.8(b)] [51,43]. The significantly reduced demagnetization factor in the longitudinally magnetized Terfenol-D resulted in a large reduction in H_{Bias} required for achieving the maximal α_V. The Terfenol-D/PZT/Terfenol-D and Terfenol-D/PMN–PT/Terfenol-D sandwiches were measured to have much enhanced α_V of 85 and 110 mV/Oe at much lower H_{Bias} levels of 0.5 and 0.4 kOe at 1 kHz, respectively. Dong *et al.*, also in 2004, demonstrated a superlarge α_V of 430 mV/Oe at an H_{Bias} of 0.5 kOe at 1 kHz in a Terfenol-D/PMN–PT/Terfenol-D sandwich with a longitudinal magnetization–longitudinal polarization (*L–L*) arrangement [Fig. 1.8(c)] [44]. Although, the *L–L* sandwich had a superlarge α_V, its associated charge was quite low because of the reduced capacitance in the PMN–PT layer associated with an increase in length. To facilitate the simultaneous high voltages and high charges, a Terfenol-D/PMN–PT/Terfenol-D sandwich with a *L*–double-half-*L* arrangement was developed in 2005 [Fig. 1.8(d)] [47]. This design took the advantages of the high ME voltage of the *L–L* arrangement [Fig. 1.8(c)] and the high ME charge of the *L–T* arrangement [Fig. 1.8(b)] with an extremely high α_V of 1.6 V/Oe. To study the bending resonance effect, *L–T* bilayers consisting of one or two PZT

layers bonded on a Terfenol-D layer were proposed in 2005 and 2008, respectively [Fig. 1.8(e) and (f)] [48,49]. The observed α_V based on the bending mode of operation was generally 3 times smaller than those based on the longitudinal and/or transverse modes of operation [Fig. 1.8(a)–(d)]. However, these *L–T* bilayers showed improved low-frequency (<20 kHz) responses to applied magnetic fields, making them useful for low-frequency (<100 Hz) magnetic field sensor applications. *L–T* multilayers of Terfenol-D layers and PMN–PT layers were developed in 2005 [Fig. 1.8 (g)] to exhibit a low working frequency of ~0.01 Hz and a large α_V of 100 mV/Oe [50]. Wang *et al.* in 2008 studied the effect of crystallographic orientation of PMN–PT crystals on the ME effect in the Terfenol-D/PMN–PT/Terfenol-D sandwiches with a *L–T* arrangement [Fig. 1.8 (b)] and found the existence of a giant α_V of 302 mV/Oe at an H_{Bias} of 0.4 kOe at 1 kHz in a sandwich having a preferred [001] crystallographic orientation along the length of the PMN–PT crystal compared to the previously reported [001] crystallographic orientation along the thickness direction [52].

(2b) Three-Phase Laminated Composites

In the two-phase laminated composites described in (2a), eddy-current losses in monolithic Terfenol-D become significant at high frequencies, which limit the applications of the composites in high-frequency sensing. In addition, Terfenol-D, PZT, and PMN–PT are all mechanically brittle. In order to overcome these two major difficulties, three-phase laminated composites were readily developed. They involved: epoxy-bonded-type, high-permeability-type, and mechanical-type three-phase

laminated composites.

Nersessian *at al*. fabricated epoxy-bonded-type three-phase laminated composites by sandwiching a thickness-polarized PZT plate between two length-magnetized epoxy-bonded Terfenol-D particulate composite plates of different Terfenol-D volume fractions in 2004 [Fig. 1.9(a)] [53]. This type of composite had a maximum α_V of 70 mV/Oe under an optimal H_{Bias} of 0.6 kOe at 8 Hz. In 2006, Dong *at al.* combined high-permeability ferromagnetic ($MnZnFe_2O_4$) bases with a two-phase Terfenol-D/PZT *L*–double-*T* bilayer to form a high-permeability-type three-phase laminated composite as shown in [Fig. 1.9(b)] [54]. The effective permeability in the composite was significantly increased as a result of the concentration of magnetic flux in the composite. The measured α_V was as high as 300 mV/Oe. In 2008, Wang *at al.* fabricated a mechanical-type three-phase laminated composite which was essentially a cymbal-type metal-PMN–PT piezoelectric transducer bonded with a Terfenol-D alloy bar and then clamped mechanically by two platforms [Fig. 1.9(c)] [55]. This design enhanced the piezoelectric effect and improved mechanical coupling between the magnetostrictive and piezoelectric phases, giving raise to an extremely large α_V of 440 mV/Oe at 1 kHz.

(a)

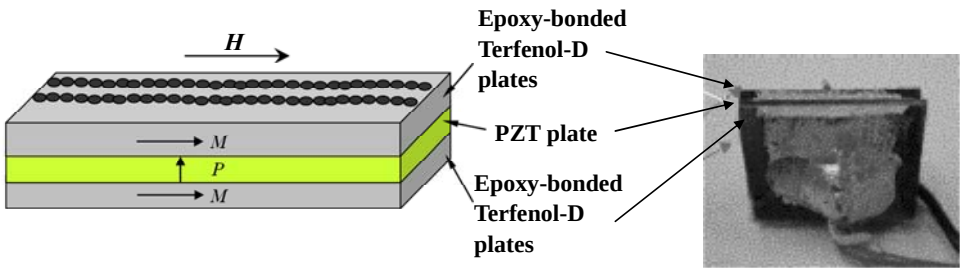

(b)

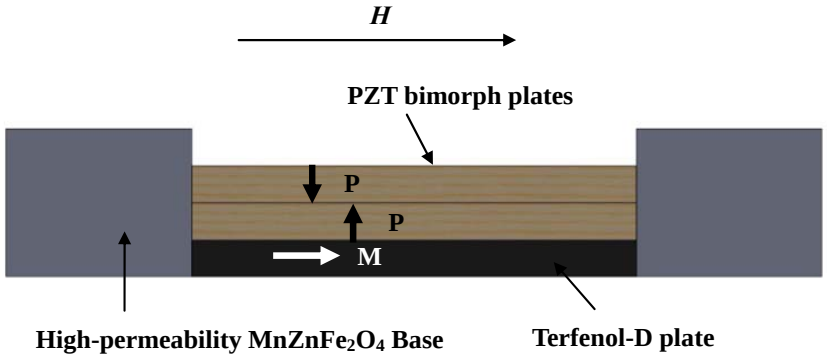

(c)

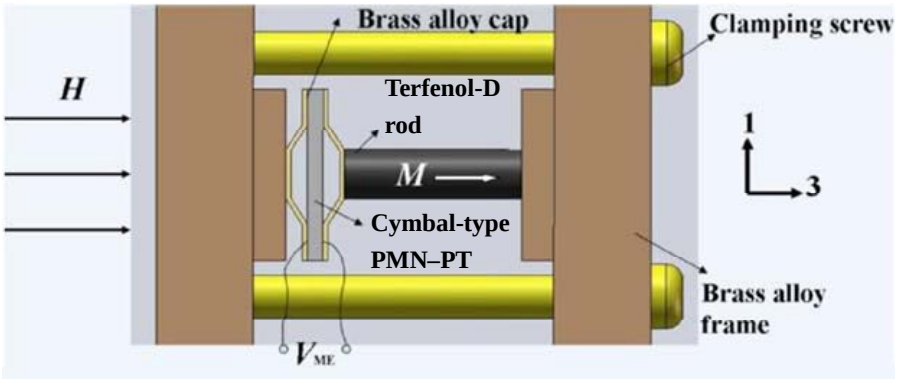

Fig. 1.9 **Some common three-phase laminated materials: (a) epoxy-bonded type; (b) high-permeability type, and (c) mechanical type [53–55].**

1.3.3 Magnetoelectric Applications

So far only bulk and laminated composites exhibit practically useful ME effect above room temperature. In fact, most of the bulk and laminated composites are ready for technological applications, and scientists start to change the research direction from materials research to device applications. Nowadays, there are two main promising device applications, including ME sensors and ME transformers.

1.3.3.1 Magnetoelectric Sensors

The working principle of magnetic field sensing in ME composites is simple and direct. Highly sensitive magnetic field sensors can be obtained using ME composites with high ME coefficients (α_E or α_V). The schematic diagrams of some magnetic field sensors are shown in Fig. 1.10. Viehland *et al.* in 2006 proposed a passive magnetic field sensor using a two-phase laminated composite with a *L–T* arrangement (i.e., a *L–T* sandwich) as illustrated in Fig. 1.10(a) [56]. A pair of permanent magnets was placed at the two ends of the sandwich to provide an optimal H_{Bias} to the sandwich. This H_{Bias} was capable of enhancing α_V of the sandwich and hence the detection sensitivity of the sensor. The maximum α_V of the sensor was evaluated to be 55 mV/Oe. One year later, Or and Chan invented another types of passive magnetic field sensors based on a variety of epoxy-bonded-type three-phase laminated composites with different arrangements of the magnetization and polarization directions similar to the illustrations in Fig. 1.8(a)–(g) [57]. Moreover, a

number of three-phase laminated composites can be arranged in a single housing to provide multichannel magnetic field detections as shown in Fig. 1.10(b) [57,58].

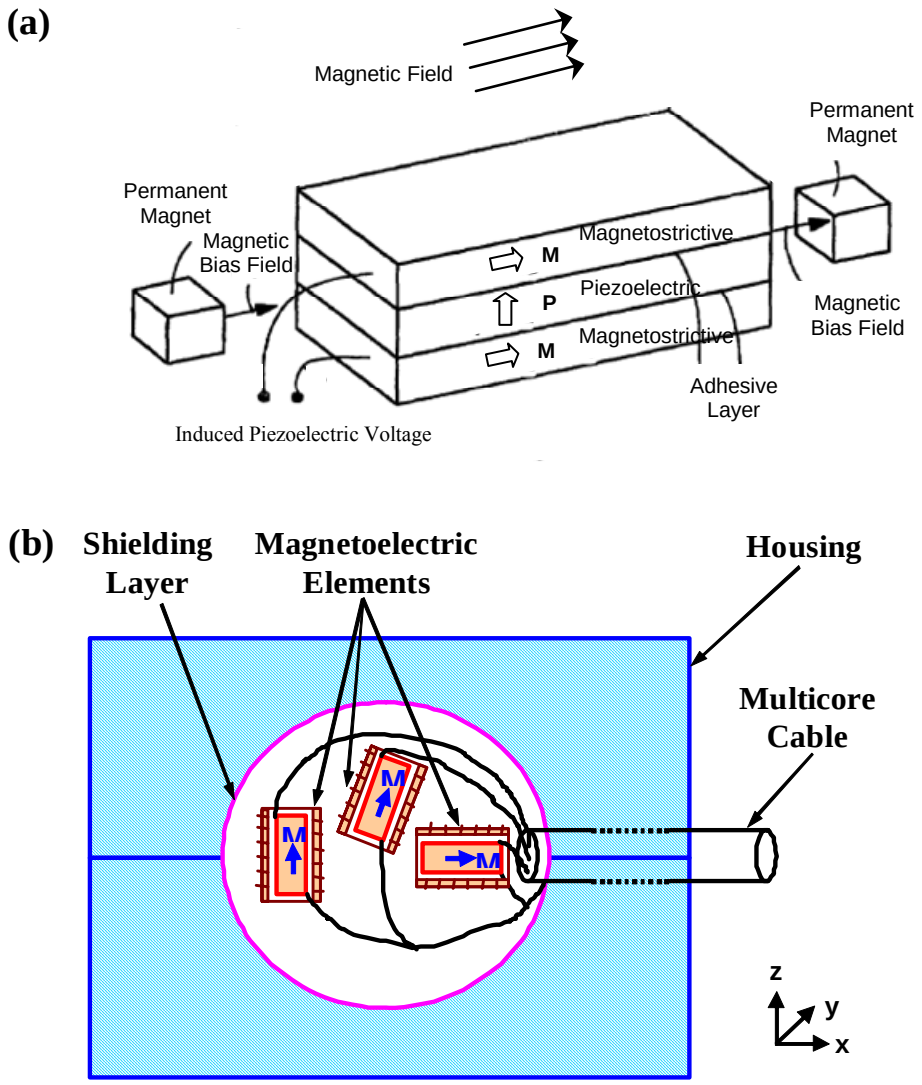

Fig. 1.10 Schematic diagrams of passive magnetic field sensors: (a) a magnetic field sensor using a two-phase laminated composite with a *L–T* arrangement (i.e., a *L–T* sandwich) [56]; (b) a magnetic field sensor using three epoxy-bonded-type three-phase laminated composites in a single housing to provide multichannel magnetic field detections [57,58].

1.3.3.2 Magnetoelectric Transformers

Wang *at al*. investigated an ME transformer based on the combination of a coil-wound, length-magnetized Terfenol-D magnetostrictive layer with a length-polarized PMN–PT piezoelectric layer along the longitudinal direction as shown in Fig. 1.11 [59]. The working principle is as follows. An ac magnetic field (H_{ac}), which is excited by an ac electric current (I_i) associated with an ac electric voltage (V_i) in a coil of N turns wrapped around the Terfenol-D layer, is applied along the longitudinal direction of the transformer. This H_{ac} induces an ac magnetostrictive strain in the Terfenol-D layer based on the magnetostrictive effect which, in turn, is transferred dynamically to stress the PMN–PT layer. As a result of the piezoelectric effect, the transferred dynamic stress produces an ac electric voltage (V_o) across the length of PMN–PT layer. When the frequency of V_i is equal to the resonance frequency of the transformer, the ME effect will be greatly enhanced, giving a much amplified V_o from a given V_i. Thus, the transformer will exhibit a large voltage gain due to the resonance ME effect. A maximum voltage gain of 130 was found at a resonance frequency of 36 kHz under an optimal H_{Bias} of 0.4 kOe.

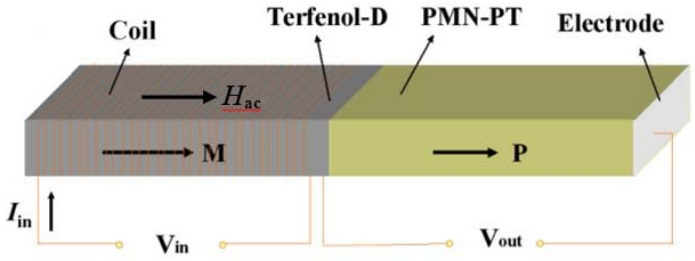

Fig. 1.11 Schematic diagram of an ME transformer based on the combination of a coil-wound, length-magnetized Terfenol-D magnetostrictive layer with a length-polarized PMN–PT piezoelectric layer along the longitudinal direction [59].

1.4 Aim and Objectives of Project

As discussed in Section 1.2, while state-of-the-art wireless condition monitors have emerged as a flexible alternative to the traditional wired condition monitors due to the ease of installation, large scalability, and highly distributed nature, the need for powering the active current sensors with limited power pack/battery life through power cables still constrains their applicability in modern electrical assets. As addressed in Section 1.3, magnetic field sensors based on the extrinsic ME effect in magnetostrictive-piezoelectric ME sensing elements not only eliminate the need of external power supplies to sustain their operations, but also produce significantly larger output voltages and higher sensitivities in wider operating frequency ranges compared to the state-of-the-art active current sensors. These make these ME-based passive sensors suitable for a broad domain of magnetic field sensing applications.

Therefore, the aim of this study is to develop a new generation of wireless condition monitors consisting of novel ME passive current sensors and multichannel wireless communication units for an improved real-time wireless monitoring of current signatures governed by electrical assets. To accomplish the research aim, the project objectives are set as follows.

(1) Study of the fabrication, characterization, and physical properties of magnetostrictive and piezoelectric constituent materials for ME sensing elements.

(2) Development of characteristic types of ME sensing elements for ME passive current sensors.

(3) Development of novel surface mount-type and clamp-type ME passive current sensors with magnetic field biasing, electric field shielding, and thermal insulation capabilities.

(4) Development of short-range and long-range multichannel wireless communication units for integration with the developed ME passive current sensors.

(5) Establishment and deployment of distinct sets of wireless condition monitors for monitoring of current signatures in electrical assets by suitably combining the developed ME passive current sensors and multichannel wireless communication units.

1.5 Scope of Project

In order to realize the improved wireless condition monitors comprising novel ME passive current sensors and specific multichannel wireless communication units for electrical engineering applications, the following work sequence is followed:

(1) In Chapter 1, an introduction to asset management, condition monitoring as well as ME effect, materials, and applications are provided, together the aim, objectives, and scope of the project.

(2) In Chapter 2, two types of magnetostrictive materials, including: (1) Terfenol-D alloy plates and (2) Terfenol-D short-bar–NdFeB magnet–epoxy composite rings, are identified in addition to three types of piezoelectric materials, involving: (1) PMN–PT single-crystal plates/bars, (2) PMN–PT single-crystal

transformers, and (3) PZT ceramic rings. The fabrication, characterization, and physical properties of the magnetostrictive and piezoelectric materials are studied.

(3) In Chapter 3, three characteristic types of ME sensing elements, including: (1) plate-shaped sensing elements, (2) ring-shaped sensing elements, and (3) bar-shaped sensing elements, are developed through the investigation of their structures, working principles, physical modeling, fabrication, characterization, and performance.

(4) In Chapter 4, two novel types of ME passive current sensors, including: (1) surface mount-type current sensors and (2) clamp-type current sensors, are developed with magnetic field biasing, electric field shielding, and thermal insulation capabilities based on the plated-shaped and ring-shaped sensing elements, respectively.

(5) In Chapter 5, two specific types of multichannel wireless communication units, including: (1) a short-range, 4-channel, 2.4 GHz unit and (2) a long-range, 3-channel, 3G/2G unit, are developed for integration with the ME passive current sensors.

(6) In Chapter 6, three distinct sets of wireless condition monitors are formed and deployed in three different field tests to implement wireless condition monitoring. These include: (1) the integration of four surface mount-type current sensors with a 2.4 GHz wireless communication unit for monitoring the electrical motor drives of the train traction system of a 12-cabin mainline

train operated by MTR Corporation Limited on the East Rail Line, (2) the integration of three surface mount-type current sensors with a 3G/2G wireless communication unit for monitoring an ABB 400 V, 1,000 A, 3-phase electrical switchgear located in the Electrical Machines Laboratory (EF001a) of the Department of Electrical Engineering at PolyU, and (3) the integration of a clamp-type current sensor with a 2.4 GHz wireless communication unit for monitoring a 220 V, 13 A switching mode power supply used for driving personal computers.

(7) In Chapter 7, conclusions and suggestions for future work are given.

Chapter 2

Physical Properties of Magnetostrictive and Piezoelectric Materials

2.1 Introduction

As mentioned in Chapter 1, magnetoelectric (ME) passive current sensors are required for self sustainable condition monitoring of electrical assets in order to eliminate the major shortcomings of powering, signal-conditioning, and bandwidth issues intrinsic in conventional active current sensors. To enable the interesting characteristics of power supply free, signal conditionerless (i.e., high signal strength and high detection sensitivity), and wide bandwidth (i.e., wide operating frequency range) in the ME passive current sensors, it is deemed necessary to develop characteristic types of ME sensing elements. As magnetostrictive and piezoelectric materials are the constituent functional phases of the ME sensing elements, they have critical influences on the performance of the resulting ME sensing elements and hence the resulting ME passive current sensors.

In this chapter, the fabrication, characterization, and material properties of five different types of magnetostrictive and piezoelectric constituent functional phases of the ME sensing elements are described. The magnetostrictive constituent functional phase includes: Terfenol-D alloy plates and Terfenol-D short-bar−epoxy composite

plates, while the piezoelectric constituent functional phase involves PMN–PT single-crystal plates/bars, PMN–PT single-crystal transformers, and PZT ceramic rings. The room-temperature data (25 ± 1 °C) are summarized and will be used for designing ME sensing elements in Chapter 3.

2.2 Magnetostrictive Materials

2.2.1 Terfenol-D Alloy Plates

$Tb_{0.3}Dy_{0.7}Fe_{1.92}$ (Terfenol-D) magnetostrictive alloy plates supplied by Baotou Rare Earth Research Institute, Inner Mongolia, China were used as the basic magnetostrictive material for our ME sensing elements. They were delivered in the form of a rectangular plate with dimensions of 12 ± 0.15 mm in length, 6 ± 0.1 mm in width, and 1 ± 0.1 mm in thickness. They had highly magnetostrictive [112] crystallographic axis oriented along the longitudinal direction as shown in Fig. 2.1. In fact, Terfenol-D was named based on the combination of the four keywords: terbium (Ter), iron (fe), Naval Ordnance Laboratory (nol), and dysprosium (D) [60]. The manufacturer data are summarized in Table 2.1 [61]. The as-supplied Terfenol-D has a giant positive magnetostriction in excess of 700 ppm at an applied magnetic field of 100 kA/m under zero prestress condition. This giant magnetostriction (≥700 ppm) at such relatively low applied magnetic field (~100 kA/m) makes Terfenol-D a good magnetmechanical actuator in the ME sensing elements. The high magnetomechaincal coupling coefficient (≥0.65) permits the efficient conversion between magnetic and

mechanical energies. The high operating temperature (~150 °C) ensures a high thermal stability in the ME sensing elements.

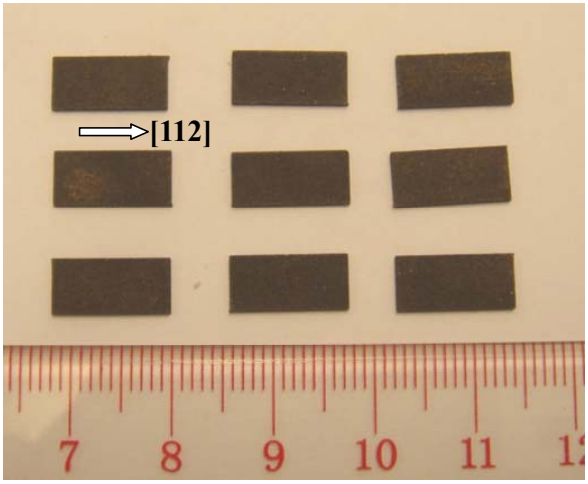

Fig. 2.1 Photograph of Terfenol-D alloy plates with dimensions of 12 mm in length, 6 mm in width, 1 mm in thickness, and having the highly magnetostrictive [112] crystallographic axis oriented along the longitudinal direction.

Table 2.1 Material properties of Terfenol-D alloy plates supplied by Baotou Rare Earth Research Institute, Inner Mongolia, China [1].

	Symbol	Terfenol-D alloy plates
Magnetic and Electric Properties		
Relative permeability	μ_{r33}	5−10
Saturation magnetization (T)	M_s	1
Electrical resistivity ($\mu\Omega$·m)	ρ_e	0.6
Magnetomechanical Properties		
Magnetomechaincal coupling coefficient	k	0.65–0.75
Magnetostriction (ppm)	λ	≥700*
Saturation magnetostriction (ppm)	λ_s	1000–1200**
Response time (μs)	t_r	<1
Operating frequency (kHz)	f_{op}	1−10
Energy density (kJ/m^3)	E_d	14–25
Mechanical Proprieties		
Density (kg/m^3)	ρ	9150–9250
Young's modulus (GPa)	E	25−65
Tensile strength (MPa)	TS	≥25
Sound velocity (m/s)	v	1700–2600
Thermal Properties		
Thermal expansion coefficient (×10^{-6}/°C)	α_{the}	8–12
Thermal conductivity (J/°C/m/s)	σ_{th}	10.5–10.8
Curie temperature (°C)	T_C	380
Operating temperature (°C)	T_{op}	-40–150
Heat capacity (kJ/kg·K)	C_h	0.35

* Measured at 79.6 kA/m magnetic field and with 10 MPa prestress.
** Measured at 100 kA/m magnetic field and with 10 MPa prestress.

2.2.2 Terfenol-D Short-Bar–Epoxy Composite Plates

2.2.2.1 Preparation of Terfenol-D Short Bars

Terfenol-D short bars with dimensions of 2−4 mm in length and 1 × 1 mm^2 in cross-section (Fig. 2.2) were prepared by cutting the as-supplied Terfenol-D alloy plates along the highly magnetostrictive [112] crystallographic direction (Fig. 2.1) using a wire electrical discharge machining (WEDM) technique [3].

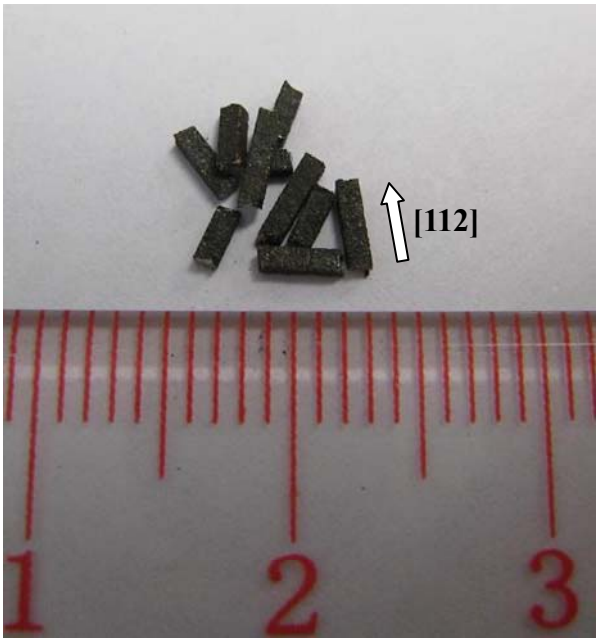

Fig. 2.2 Photograph of [112]-oriented Terfenol-D short bars of 2–4 mm long and 1×1 mm^2 cross-section prepared by cutting monolithic Terfenol-D alloy plates along the highly magnetostrictive [112] crystallographic direction using a WEDM technique.

WEDM is a non-contract, stress-free, and burr-free precision cutting process which uses wire erosion to obtain a desired shape from an electrically conductive workpiece [3]. The cutting mechanism is essentially based on the removal of the material from the workpiece by a series of rapidly recurring current-induced

discharges between the wire and the workpiece washed by a dielectric liquid when subjected to an applied electrical voltage. Fig. 2.3 shows the photograph of the WEDM equipment used to prepare the [112]-oriented Terfenol-D short bars in Fig. 2.2 (Dophen DW-250 CNC wirecut EDM and EDM drilling machine). The Terfenol-D alloy plate to be cut was placed on the worktable of the WEDM equipment and washed continuously by the hydrocarbon-oil (dielectric liquid). The wire, which was energized by an applied voltage of 90 V, was moved adjacent to, but not in touch with, the Terfenol-D alloy plate. This created a sufficiently high electric field stress to overcome the resistance of the hydrocarbon-oil, leading to a series of rapidly recurring current-induced discharges between the wire and the Terfenol-D alloy plate and thus resulting in the removal of Terfenol-D alloy plate material through erosion. By setting the cutting speed to be 2 mm/min and the cutting direction to be along the [112] crystallographic direction of the Terfenol-D alloy plate, Terfenol-D continuous bars with dimensions of 12 mm in length and 1×1 mm^2 cross-section were obtained. The as-prepared Terfenol-D continuous bars were cleaned and stored in a temperature- and humility-controlled chamber. They were bended into short bars of 2−4 mm long (Fig. 2.2) for the fabrication of Terfenol-D short-bar−epoxy composite plates in Section 2.2.2.3.

Fig. 2.3 Photograph of WEDM equipment used to prepare our [112]-oriented Terfenol-D short bars in Fig. 2.2.

2.2.2.2 Description of Epoxy

Epoxy of Araldite LY564 resin and Araldite HY2954 hardener supplied by Ciba-Geigy Hawthorne, New York, USA was chosen as the matrix material for the Terfenol-D short-bar–epoxy composite plates. The material properties of the epoxy are summarized in Table 2.2 [63]. This epoxy has a low dynamic viscosity of 620 mPa·s at room temperature and a high heat-resistant temperature of 180–200 °C with a low

coefficient of linear thermal expansion of 60×10^{-6} /°C. The low dynamic viscosity makes the liquid epoxy to be easily filled into gaps between the Terfenol-D short bars, while the high heat-resistant temperature and the low coefficient of linear thermal expansion ensure the temperature stability of the resulting composite plates.

Table 2.2 Material properties of Ciba-Geigy Araldite LY564/HY2954 epoxy at room temperature [63].

	Symbol	Araldite LY564/HY2954 Epoxy
Electrical Properties		
Relative permittivity at 1 kHz	ε	3.27
Thermal Properties		
Coefficient of linear thermal expansion (10^{-6} /°C)	C_{lth}	60
Heat-resistant temperature (°C)	T_{hr}	180−200
Mechanical Proprieties		
Density (kg/m^3)	ρ	1097
Young's modulus (GPa)	E_{y}	2.600
Longitudinal wave velocity (m/s)	v_{l}	1874
Shear wave velocity (m/s)	v_{s}	943
Longitudinal stiffness coefficients (GPa)	$c_{11} = c_{22} = c_{33}$	3.852
Shear stiffness coefficients (GPa)	$c_{44} = c_{55} = c_{66}$	0.970
Cross-plane stiffness coefficients (GPa)	$c_{12} = c_{21} = c_{23} = c_{32} = c_{13} = c_{31}$	1.898
Longitudinal compliance coefficients (pm^2/N)	$s_{11} = s_{22} = s_{33}$	384.6
Shear compliance coefficients (pm^2/N)	$s_{44} = s_{55} = s_{66}$	977.0
Cross-plane compliance coefficients (pm^2/N)	$s_{12} = s_{21} = s_{23} = s_{32} = s_{13} = s_{31}$	127.0
Dynamic viscosity (mPa·s)	τ	620

2.2.2.3 Fabrication of Composite Plates

Terfenol-D short bars and Araldite LY564/HY2954 epoxy were used as the active and passive phases of the Terfenol-D short-bar–epoxy composite plates, respectively. The fabrication process is presented in Fig. 2.4. Araldite LY564 resin and Araldite HY2954 hardener were weighted with a mass ratio of 10:2 and mixed in a paper cup for 5 min. The mixed Araldite LY564/HY2954 epoxy was degassed under vacuum for 30 min to eliminate air bubbles. Predetermined quantities of Terfenol-D short bars and the degassed Araldite epoxy were transferred into a bronze mold with a rectangular cavity of length 12 mm, width 6 mm, and thickness 1 mm. These dimensions were the same as those of the Terfenol-D alloy plates in Fig. 2.1. The slurry of Terfenol-D short bars and Araldite epoxy slurry was degassed inside the bronze mold under vacuum for 15 min to further eliminate air bubbles. The mold was sealed and placed between a pair of Nd−Fe−B permanent magnets to experience a uniform magnetic field of about 150 kA/m along the length direction. Due to the large length-to-width aspect ratio of the Terfenol-D short bars, the shape anisotropy of the Terfenol-D short bars caused them to lengthwise-align with the magnetic flux lines in the Araldite epoxy matrix, thereby producing short-bar chains. The entire mold-magnetic assembly was placed in a temperature-controlled chamber at 70 °C for 8 h to ensure a proper cure of the Araldite epoxy for achieving a certainly high degree of crosslinking as well as to impact an average axial residual compressive stress of about 3 MPa to the Terfenol-D short-bar chains through the thermal shrinkage of the Araldite epoxy in the composite plate. This built-in residual compressive stress was

showed to be effective in creating a preferred non-180° domain state in the as-prepared composite plate similar to the case of applying an external prestress to assert an initial non-180° domain state in monolithic Terfenol-D alloy [60]. In fact, magnetostrictive materials with an enhanced motion of non-180° domain walls were found to have an increased deformation contribution and hence an enhanced magnetostrictive strain capability [64,65]. The volume fraction of Terfenol-D short bars in the composite plate was determined to be 0.52 based on Archimedes' principle and rule-of-mixture formulation for density expressed below:

$$\rho_c = v_f \rho_a + (1 - v_f)\rho_e , \tag{2.1}$$

where ρ_c, ρ_a, and ρ_e are the densities of the composite plate, Terfenol-D short bars (= 9200 kg/m^3), and Araldite epoxy (= 1097 kg/m^3), respectively; and v_f is the volume fraction of Terfenol-D short bars in the composite plate.

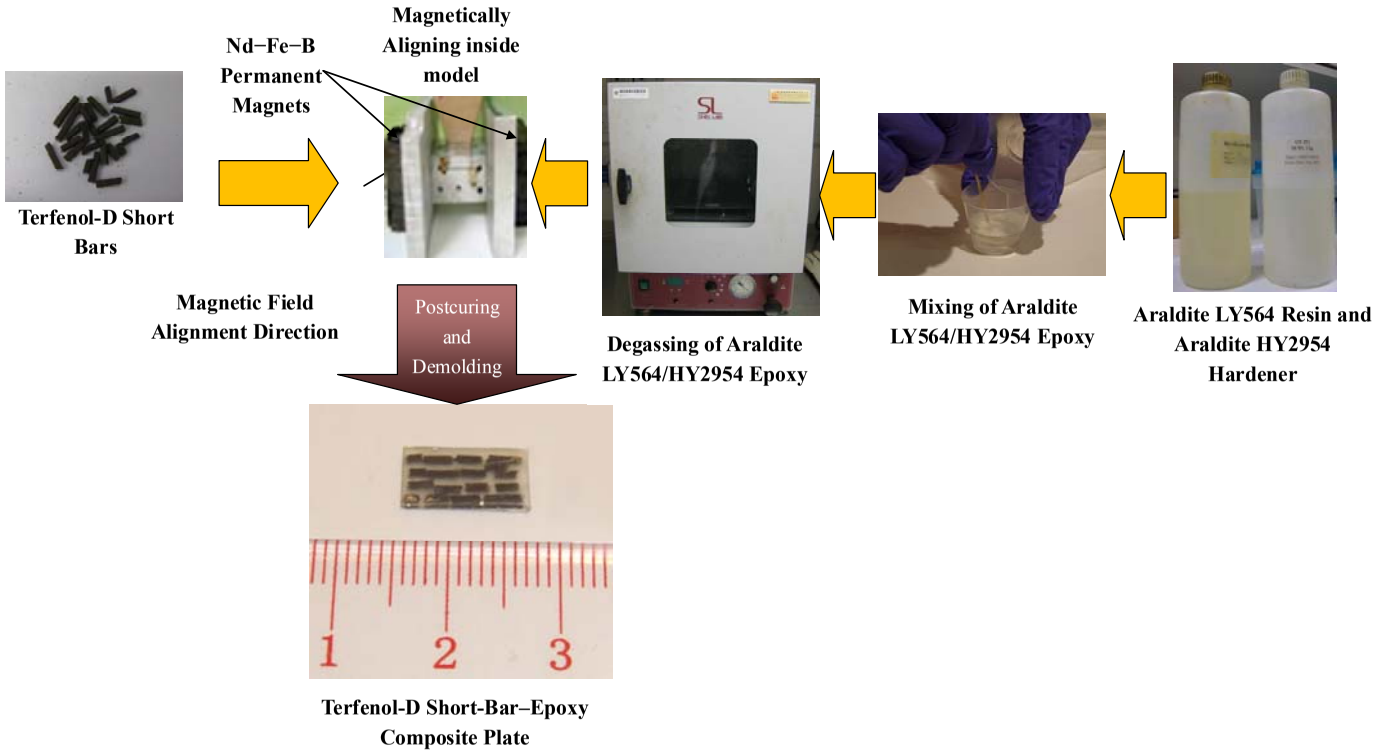

Fig. 2.4 Fabrication process of Terfenol-D short-bar–epoxy composite plates.

2.2.3 Magnetomechanical Measurements

An in-house automated magnetomechanical measurement system (Fig. 2.5) was used to measure both quasistatic and dynamic magnetomechanical properties of the Terfenol-D alloy plates in Fig. 2.1 and the Terfenol-D composite plates in Fig. 2.4. This system consisted of three basic sections (Fig. 2.5): (1) a magnetic field generation section, (2) a signal detection section, and (3) a data acquisition and system control section. The magnetic field generation section contained an arbitrary waveform generator (Agilent 33210A), a constant-current supply amplifier (AE Techron 7796HF), a dc current supply (Sorensen DHP200-15), a water-cooled, C-shaped electromagnet (Myltem PEM-8005K), and a pair of Helmholtz coils. The signal detection section included a transverse Hall-effect probe (STA99-0404), a Gaussmeter (F. W. Bell 7030), a strain gauge (Measurement Group EA-06-031CF-120-P), a strain amplifier (DACELL AM-310), a laser vibrometer (Graphtec AT0042) with a laser signal demodulator (Graphtec AT3700), a pick-up coil, and a search coil. The data acquisition and system control section comprised a data acquisition unit (Nation Instruments BNC-2110 and NI-PCI6132) and a Labview-based interface and control program.

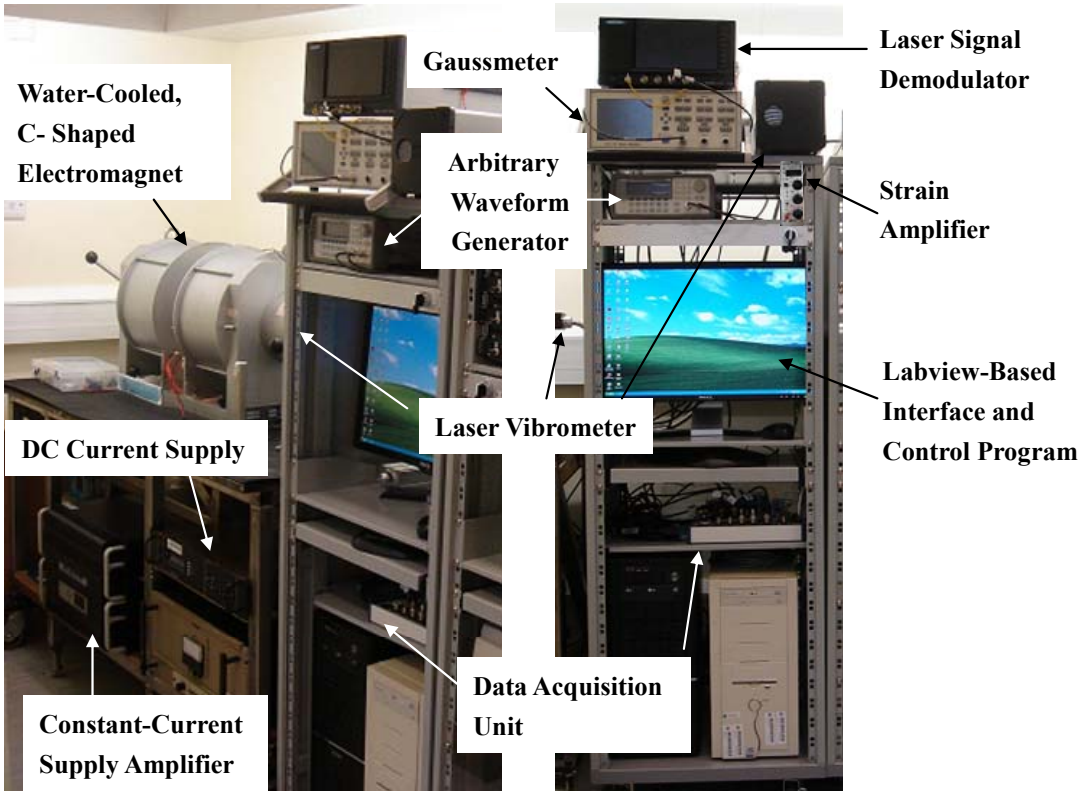

Fig. 2.5 Photographs of the in-house automated magnetomechanical measurement system.

2.2.3.1 Quasistatic Measurement

The quasistatic magnetomechanical properties of the Terfenol-D alloy plates and the Terfenol-D composite plates were measured in the longitudinal (or the 3-) direction at room temperature and with zero prestress by using the in-house automated magnetomechanical measurement system in Fig. 2.5. For the schematic diagram shown in Fig. 2.6, a low-frequency (f = 0.1 Hz) cyclic sinusoidal magnetic field (H_3^{QS}) with a maximum amplitude of 460 kA/m was provided by the electromagnet driven by the arbitrary waveform generator via the constant-current supply amplifier. The

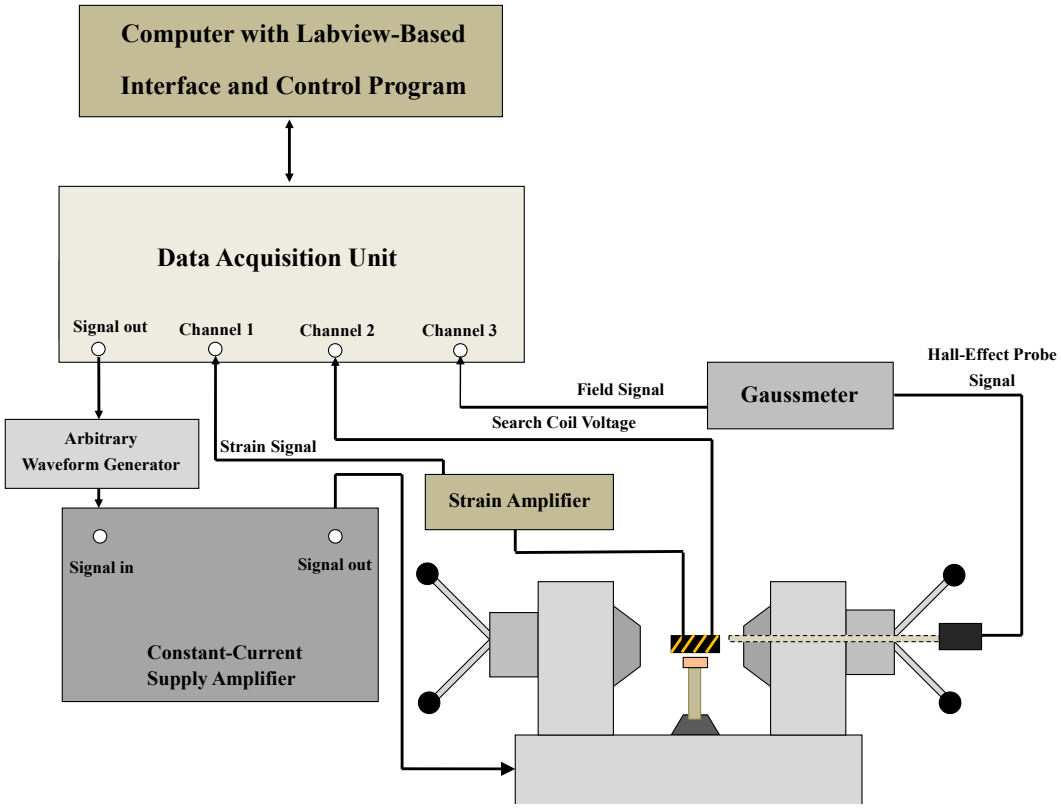

Fig. 2.6 Schematic diagram of the experimental setup for the quasistatic magnetomechanical measurement.

magnetostrictive strain (λ) was measured by the strain gauge attached to the center of the sample and connected to the strain amplifier. The quasistatic magnetic flux density (B_3^{QS}) was acquired by the search coil wrapped around the sample, while the magnetic field strength (H_3^{QS}) was detected by the transverse Hall-effect probe with the Gaussmeter. All quantities were sampled and measured by the data acquisition and system control section of the system. Fig. 2.7 shows how a Terfenol-D alloy plate and a Terfenol-D composite plate were wrapped with a search coil and attached with a

strain gauge for the quasistatic magnetomechanical measurement. The quasistatic relative permeability (μ_{r33}^{QS}) of the samples was found by

$$\mu_{r33}^{QS} = \frac{1}{\mu_0}\frac{\partial B_3^{QS}}{\partial H_3^{QS}}, \tag{2.2}$$

where $\mu_0 = 4\pi\times10^{-7}$ H/m is the permeability of free space. The magnetization (M_3^{QS}) was calculated from

$$M_3^{QS} = \frac{B_3^{QS}}{\mu_o} - H_3^{QS}. \tag{2.3}$$

The quasistatic (or differential) strain coefficient (d_{33}^{QS}) was determined by

$$d_{33}^{QS} = \frac{\partial \lambda}{\partial H_3^{QS}}. \tag{2.4}$$

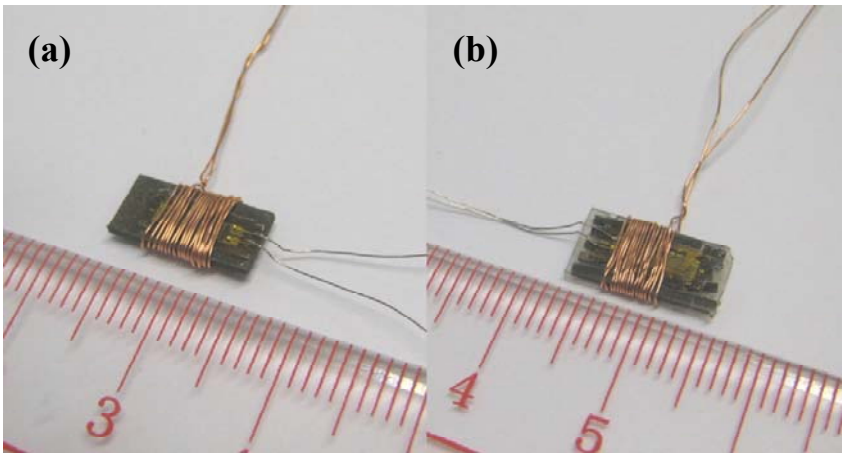

Fig. 2.7 Photographs of a Terfenol-D alloy plate and a Terfenol-D composite plate wrapped with a search coil and attached with a strain gauge for the quasistaic magnetomechanical measurement.

2.2.3.2 Dynamic Measurement

The dynamic magnetomechanical properties of the Terfenol-D alloy plates and the Terfenol-D composite plates were also measured in the longitudinal (or the 3-) direction at room temperature and with zero prestress by using the automated magnetomechanical measurement system in Fig. 2.5. For the schematic diagram shown in Fig. 2.8, a swept sinusoidal magnetic drive field (H_3) of 1 kA/m peak was generated over a prescribed frequency range (f) of 1–140 kHz by a pair of Helmholtz coils driven by the arbitrary waveform generator and the constant-current supply amplifier. Magnetic bias fields (H_{Bias}) of 5–100 kA/m were produced by the electromagnet under the energization of the dc current supply. H_3 and H_{Bias} were monitored in-situ by the pick-up coil and the Gaussmeter, respectively. The magnetic flux density (B_3) and the dynamic strain (S_3) were measured using the search coil wrapped around the sample and the laser vibrometer, respectively. All quantities were sampled and measured by the data acquisition and system control section of the system. The dynamic relative permeability (μ_{r33}) was determined from

$$\mu_{r33} = \frac{B_3}{\mu_o H_3}, \tag{2.5}$$

where $\mu_o = 4\pi \times 10^{-7}$ H/m is the permeability of free space. The elastic modulus at constant magnetic field strength (E_3^H) and that at constant magnetic flux density (E_3^B) were determined from the resonance frequency (f_r) and anti-resonance frequency (f_a) of the μ_{r33} spectrum, respectively, using the relations:

$$E_3^H = 4\rho(lf_r)^2, \tag{2.6}$$

$$E_3^B = 4\rho(lf_a)^2, \tag{2.7}$$

where ρ and l are the density and length of the sample, respectively. The dynamic strain coefficient (d_{33}) was calculated by

$$d_{33} = \frac{S_3}{H_3}. \tag{2.8}$$

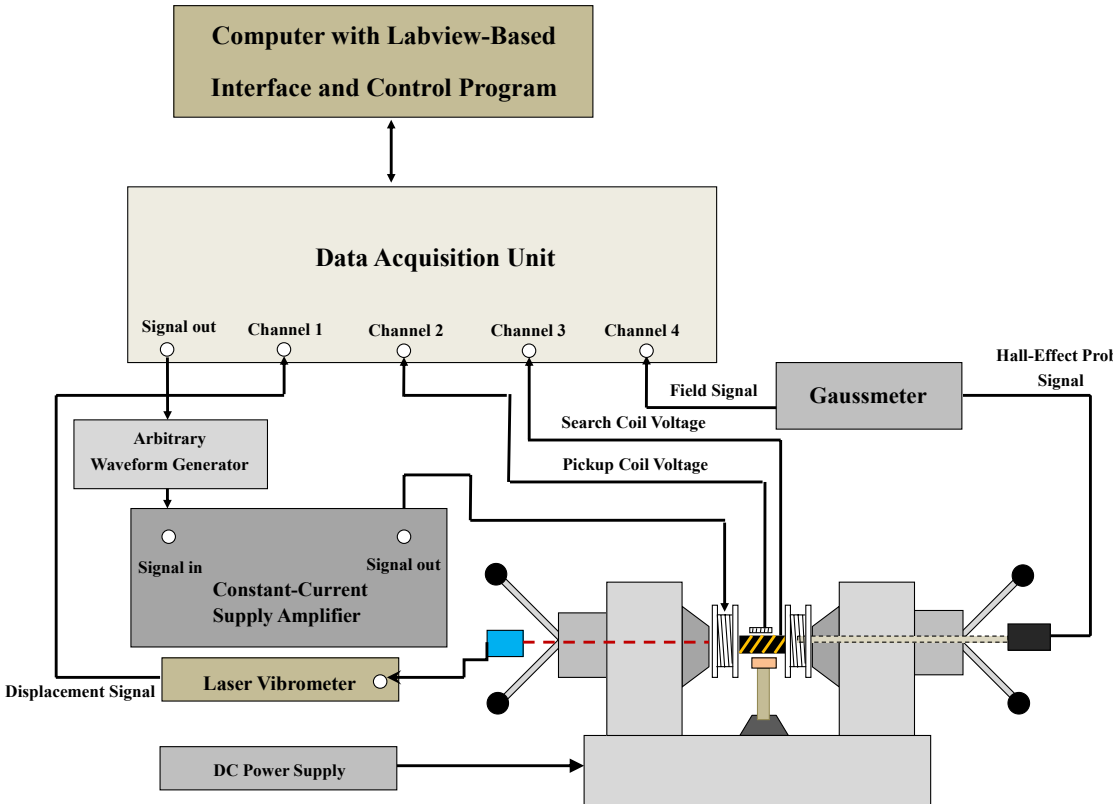

Fig. 2.8 Schematic diagram of the experimental setup for the dynamic magnetomechanical measurement.

2.2.4 Results and Discussion

2.2.4.1 Quasistatic Properties

Figure 2.9 shows the measured quasistatic $B_3^{QS} - H_3^{QS}$ curves for the Terfenol-D alloy plates and the Terfenol-D composite plates. Using Eq. 2.3, the corresponding quasistatic $M_3^{QS} - H_3^{QS}$ curves were calculated and shown in Fig. 2.10. It is clear that the magnetization process occurs with the initial motion of the available 180^o domain walls followed by the later motion of the non-180^o domain walls and domain saturation. For both types of samples, they possess quite similar $B_3^{QS} - H_3^{QS}$ curves.

The Terfenol-D alloy plates have higher B_3^{QS} and M_3^{QS} values than the Terfenol-D composite plates. In fact, the B_3^{QS} and M_3^{QS} values are approximately linearly proportional to the volume fraction of Terfenol-D short bars, elucidating that the magnetization process only relates to the contribution of the active Terfenol-D phase in the composite plates. The saturated magnetizations (M_{3s}^{QS}) of the Terfenol-D alloy plates and the Terfenol-D composite plates are found to be about 0.822 and 0.393 T at H_3^{QS}=350 kA/m, respectively. This further indicates that the behavior of the Terfenol-D composite plates is mainly dependent on the intrinsic magnetic properties of Terfenol-D and also the volume fraction of Terfenol-D short bars.

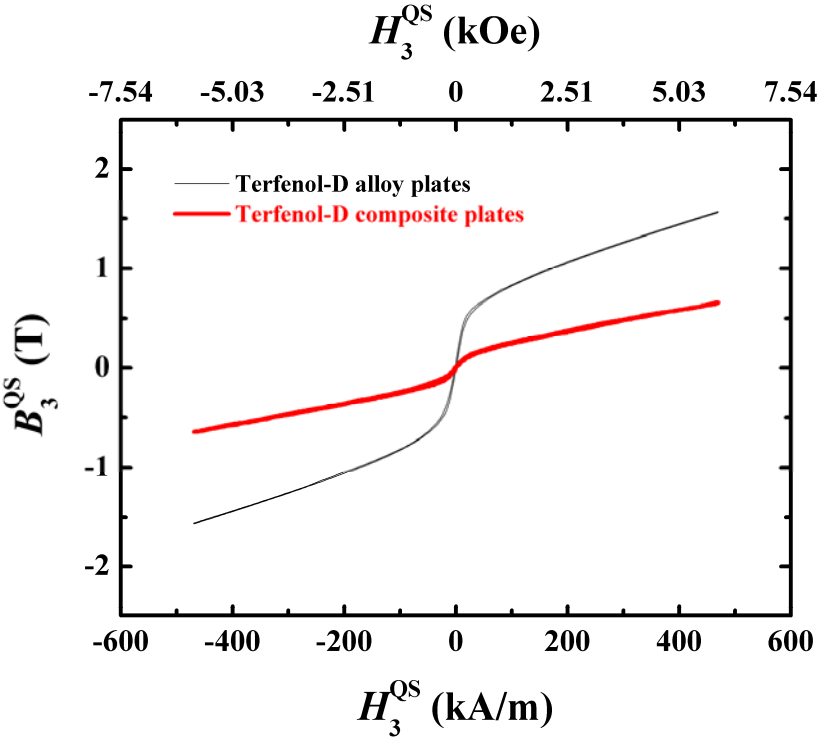

Fig. 2.9 $B_3^{QS} - H_3^{QS}$ **curves for Terfenol-D alloy plates and Terfenol-D composite plates.**

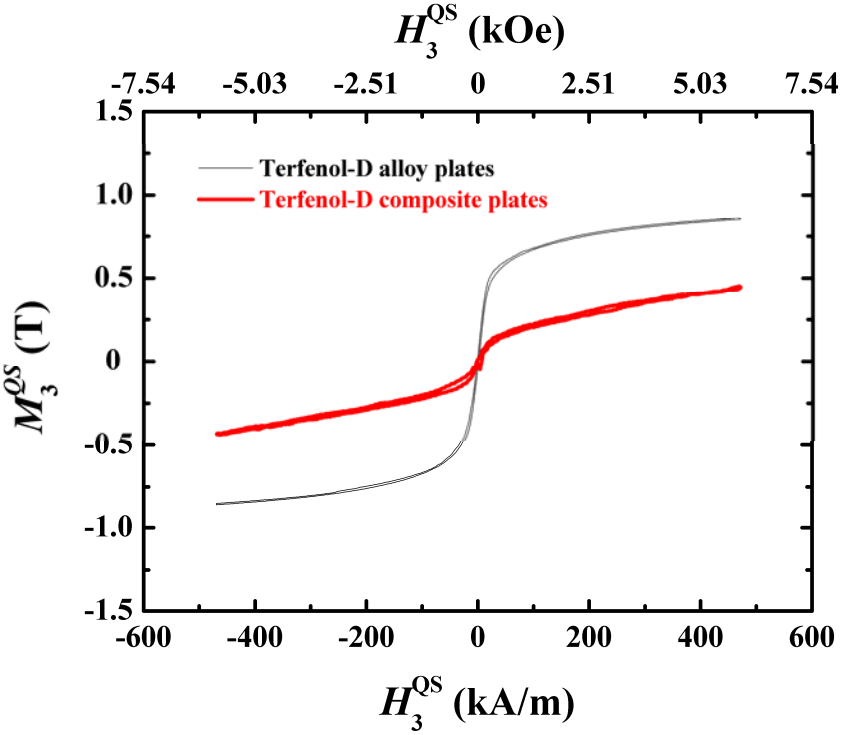

Fig. 2.10 $M_3^{QS} - H_3^{QS}$ **curves for Terfenol-D alloy plates and Terfenol-D composite plates.**

Figure 2.11 plots μ_{r33}^{QS} as a function of H_3^{QS} for the Terfenol-D alloy plates and the Terfenol-D composite plates. For both types of samples, when H_3^{QS} is small (<60 kA/m), μ_{r33}^{QS} attains its maximum value and then decreases sharply with increasing H_3^{QS} due to the relatively easy motion of the 180° domain walls. When H_3^{QS} is sufficiently large (≥100 kA/m), the motion of most of the 180° domain walls is complete. However, there often remain domains with nonzero components of magnetization at certain angles to the H_3^{QS} direction, and the magnetization in these domains must be aligned along the H_3^{QS} direction to minimize the potential energy described by $-M_3^{QS} \cdot B_3^{QS}$. This process generally requires more energy than the domain-wall motion because it involves displacing the magnetization away from an "easy" direction. When H_3^{QS} is increased beyond 200 kA/m, the samples are in the magnetic saturation state.

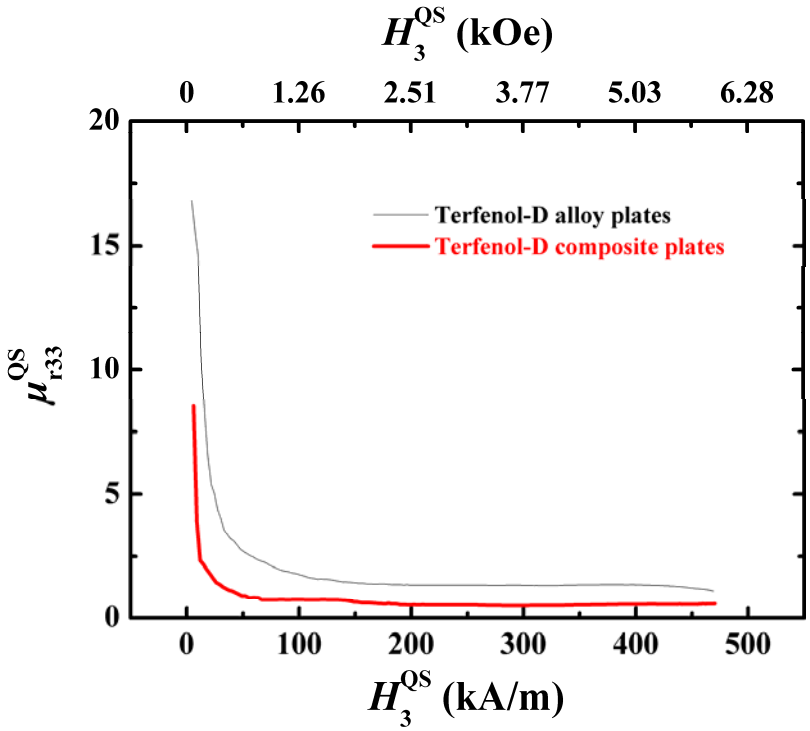

Fig. 2.11 μ_{r33}^{QS} **as a function of** H_3^{QS} **for Terfenol-D alloy plates and Terfenol-D composite plates.**

Figure 2.12 plots λ as a function of H_3^{QS} for the Terfenol-D alloy plates and the Terfenol-D composite plates. It is seen that the samples readily reach their saturation magnetostriction (λ_s) at 460 kA/m. As expected, V-shaped curve with relatively small hysteresis is observed in all samples. The small hysteresis indicates the existence of a lossy magnetization process in the samples. Below 50 kA/m, there is a magnetization jumping region (i.e., λ increases rapidly and linearly with H_3^{QS}) in which switching of 180° domains to non-180° domains is relatively easy by using a relatively small magnetic field. In the elevated H_3^{QS} region of ≥250 kA/m, the available non-180° domains are relatively immobile and they can only be rotated by a high H_3^{QS}. The saturation magnetostrictive strain (λ_s) is observed to be 1026 ppm for

the Terfenol-D alloy plates and 720 ppm for the Terfenol-D composite plates at 460 kA/m, respectively.

Figure 2.13 shows the values of d_{33}^{QS} as a function of H_3^{QS} for the Terfenol-D alloy plates and the Terfenol-D composite plates. d_{33}^{QS} was calculated by differentiating λ with respect to H_3^{QS} in Fig. 2.12 using Eq. 2.4. The maximum values of d_{33}^{QS} are ~9.5 nm/A at 15 kA/m for the Terfenol-D alloy plates and 3.8 nm/A at 50 kA/m for the Terfenol-D composite plates. At these maxima, the deformation due to the non-180^o domain-wall motion is maximized.

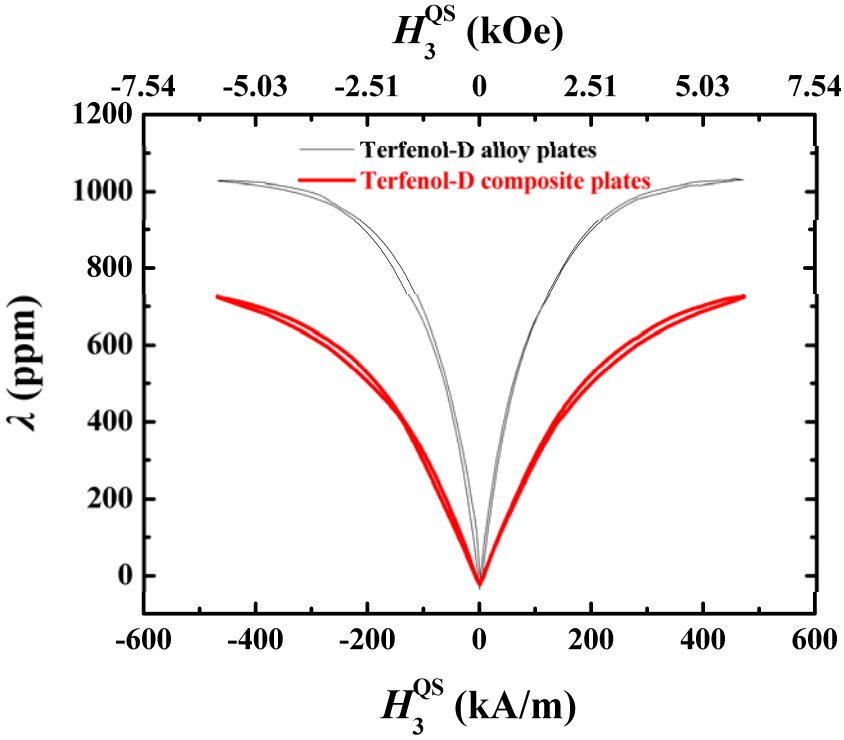

Fig. 2.12 $\lambda - H_3^{QS}$ **curves for Terfenol-D alloy plates and Terfenol-D composite plates.**

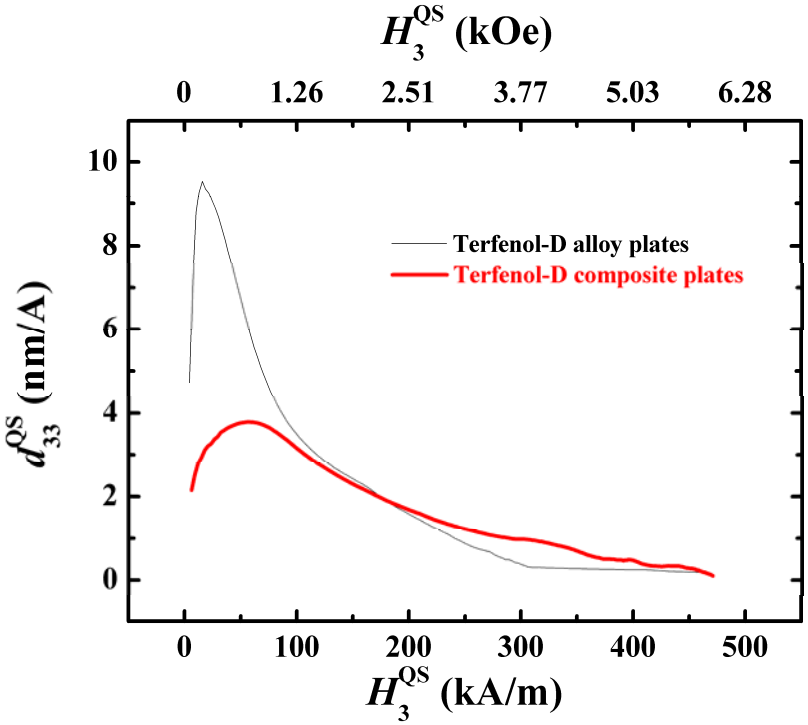

Fig. 2.13 $d_{33}^{QS} - H_3^{QS}$ **curves for Terfenol-D alloy plates and Terfenol-D composite plates.**

By extracting the related data from the $M_3^{QS} - H_3^{QS}$ curves in Fig. 2.10 and the $\lambda - H_3^{QS}$ curves in Fig. 2.12, the relationship between the magnetostriction and magnetization processes in the samples can be established. Figs. 2.14 and 2.15 show the $\lambda - M_3^{QS}$ and $\lambda/\lambda_s - M_3^{QS} / M_{3s}^{QS}$ plots, respectively. It is observed from Fig. 2.15 that the λ/λ_s values of the Terfenol-D composite plates are generally larger than those of the Terfenol-D alloy plates. Since the 180° domain-wall motion results in changes in magnetization without accompanying strain, while the non-180° domain-wall motion leads to changes in strain rather than those in magnetization. It is believed that the enhanced $\lambda/\lambda_s - M_3^{QS} / M_{3s}^{QS}$ response in the Terfenol-D composite plates compared to the Terfenol-D alloy plates originates from the increased non-180° domain-wall motion in the Terfenol-D composite plates. Moreover, this increased non-180° domain-wall motion is a result of the axial residual compressive stress developed through the cure of the epoxy matrix in the Terfenol-D composite plates.

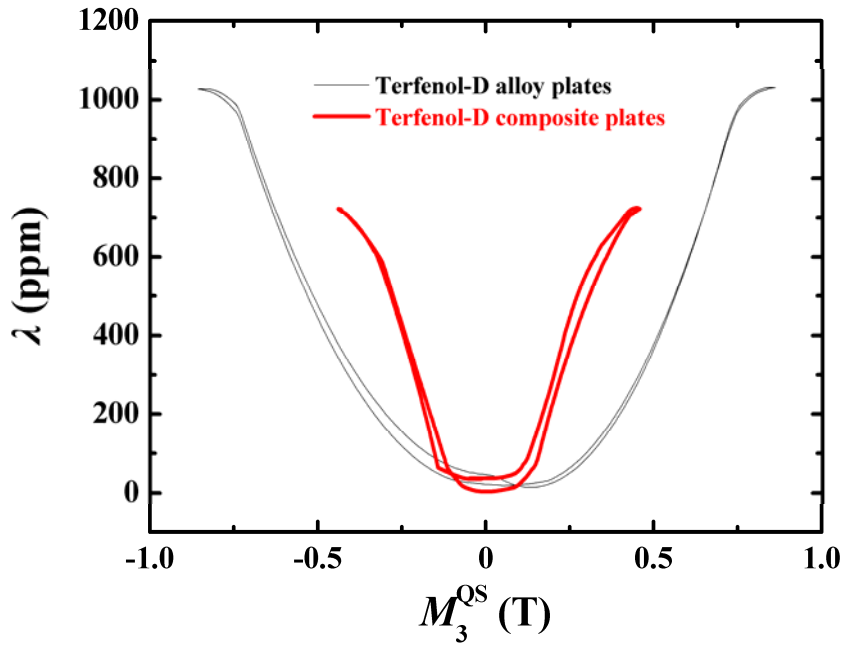

Fig. 2.14 $\lambda - M_3^{QS}$ **curves for Terfenol-D alloy plates and Terfenol-D composite plates.**

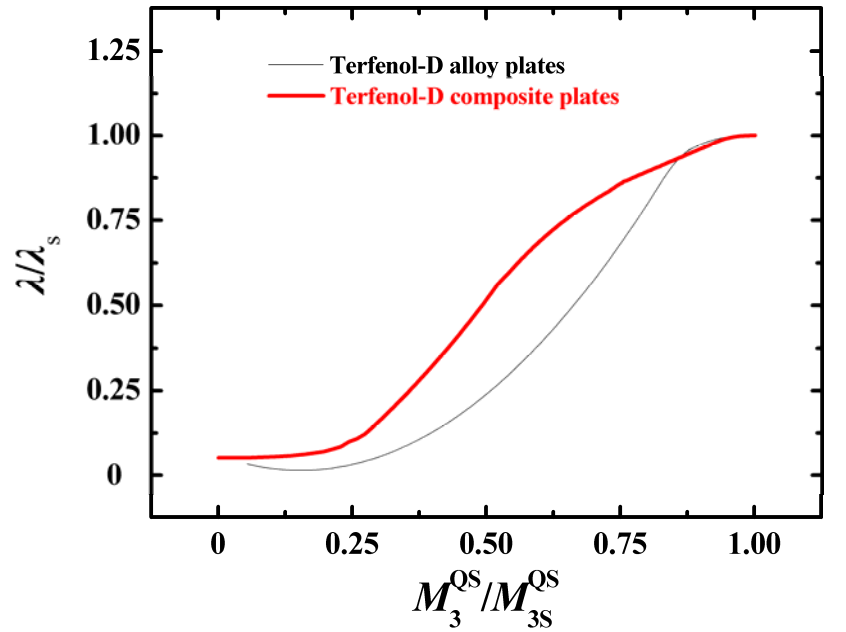

Fig. 2.15 $\lambda/\lambda_S - M_3^{QS} / M_{3S}^{QS}$ **curves for Terfenol-D alloy plates and Terfenol-D composite plates.**

2.2.4.2 Dynamic Properties

The dependence of μ_{r33} as a function of f at various H_{Bias} for the Terfenol-D alloy plates and the Terfenol-D composite plates are shown in Fig. 2.16. The fundamental longitudinal mode resonances of the Terfenol-D alloy plates and the Terfenol-D composite plates occur in the frequency range of 60–100 kHz, depending on the levels of H_{Bias}. The frequency responses for μ_{r33} are essentially flat over the measured frequency range, except for the variations associated with resonances. It implies the existence of an insignificant eddy-current-loss effect in both types of samples.

Figure 2.17 shows μ_{r33}^{T} and μ_{r33}^{S} as a function of H_{Bias} for the Terfenol-D alloy plates and the Terfenol-D composite plates. The data of μ_{r33}^{T} and μ_{r33}^{S} correspond to the 1 and 140 kHz values of the μ_{r33} spectra in Fig. 2.16. Both μ_{r33}^{T} and μ_{r33}^{S} attain their maximum values at $H_{Bias} \leq 15$ kA/m and decrease with increasing H_{Bias} before leveling off for $H_{Bias} > 50$ kA/m. The initial maximum values in μ_{r33}^{T} and μ_{r33}^{S} at $H_{Bias} \leq 15$ kA/m are mainly attributed to the relatively easy 180° domain-wall motion. As H_{Bias} is increased beyond this level, the reduced 180° domain-wall motion competes with the increased non-180° domain-wall motion, resulting in a decrease in μ_{r33}. For $H_{Bias} > 50$ kA/m, the contributions to μ_{r33}^{T} and μ_{r33}^{S} from the motion of 180° domain walls are negligible. This effect, together with the constraint of non-180° domain-wall motion under H_{Bias}, tends to level off μ_{r33}^{T} and μ_{r33}^{S}. In detail, the Terfenol-D composite plates exhibit lower μ_{r33}^{T} and μ_{r33}^{S} values than the Terfenol-D alloy plates

because the reduced Terfenol-D volume fraction in the composite plates tends to increase the demagnetizing fields which, in turn, require a larger magnetic energy to magnetize the composite plates.

Figure 2.18 plots the dependence of E_3^H and E_3^B on various H_{Bias} for the Terfenol-D alloy plates and the Terfenol-D composite plates. The values of E_3^H and E_3^B were calculated from the resonance frequency (f_r) and anti-resonance frequency (f_a) values of the μ_{r33} spectra in Fig. 2.16 using Eqs. (2.6) and (2.7), respectively. All samples show an initial drop in E_3^H with an increase in H_{Bias} because of the H_{Bias}-induced motion of the available non-180^o domain walls. As H_{Bias} is increased to about 30 kA/m for Terfenol-D alloy plates and 50 kA/m for Terfenol-D composite plates, the compliance associated with the increased deformation contribution from this non-180^o domain-wall motion is maximized, leading to a minimum in both E_3^H and E_3^B. Beyond this H_{Bias} level, E_3^H and E_3^B as a function of H_{Bias} displays an increasing trend. The effect is ascribed to the constraint of the non-180^o domain-wall motion by the increased H_{Bias}.

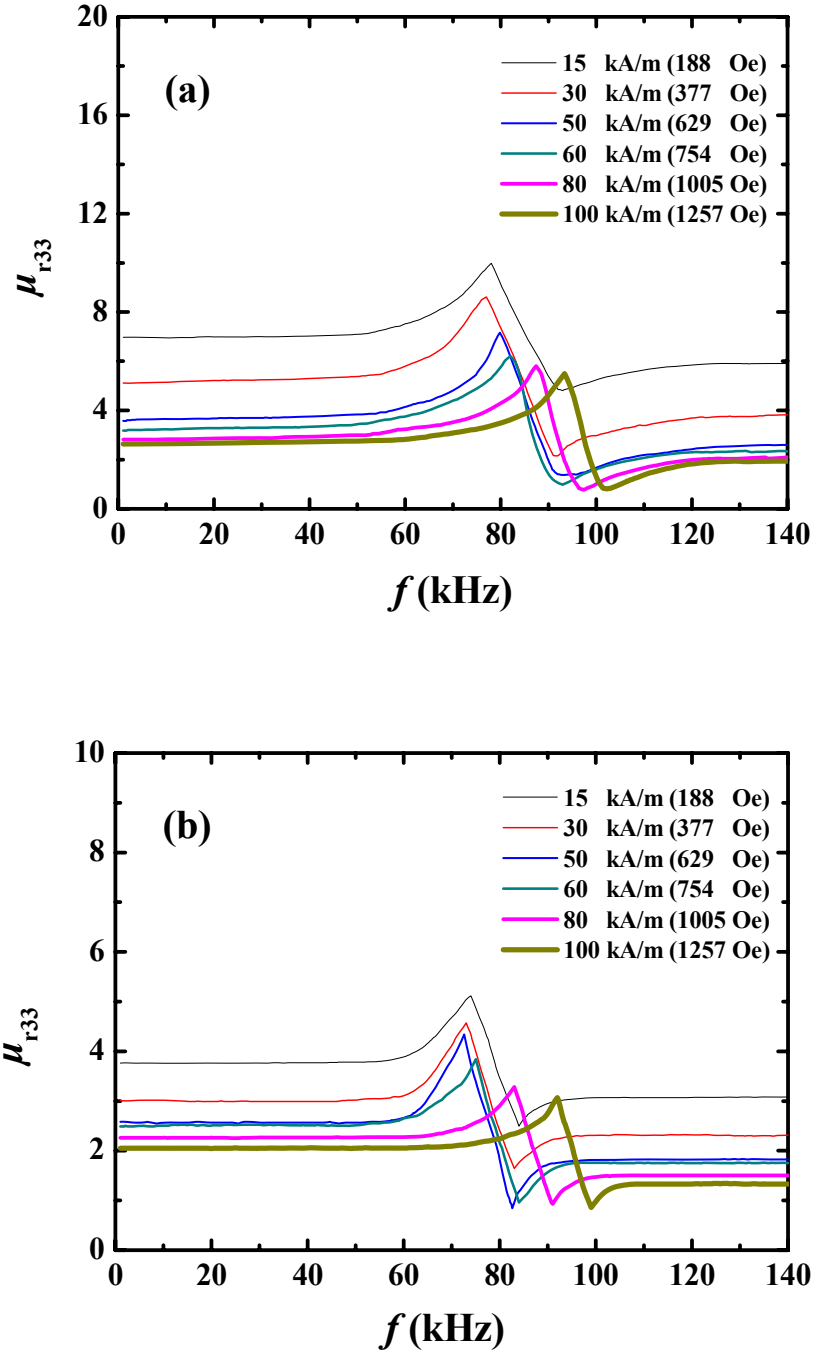

Fig. 2.16 μ_{r33}–H_3 **curves for (a) Terfenol-D alloy plates and (b) Terfenol-D composite plates.**

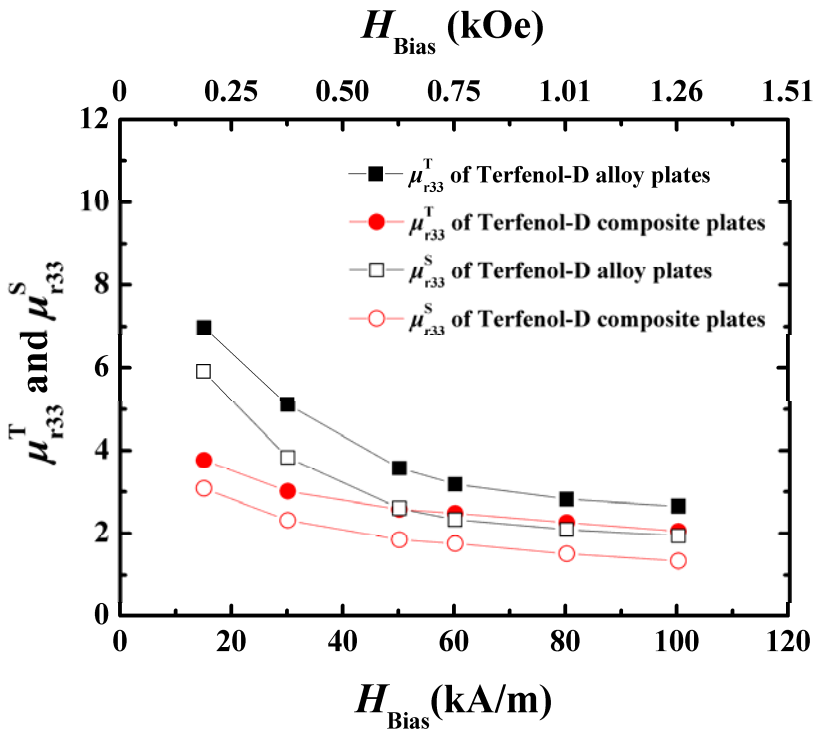

Fig. 2.17 μ_{r33}–H_3 curves for Terfenol-D alloy plates and Terfenol-D composite plates.

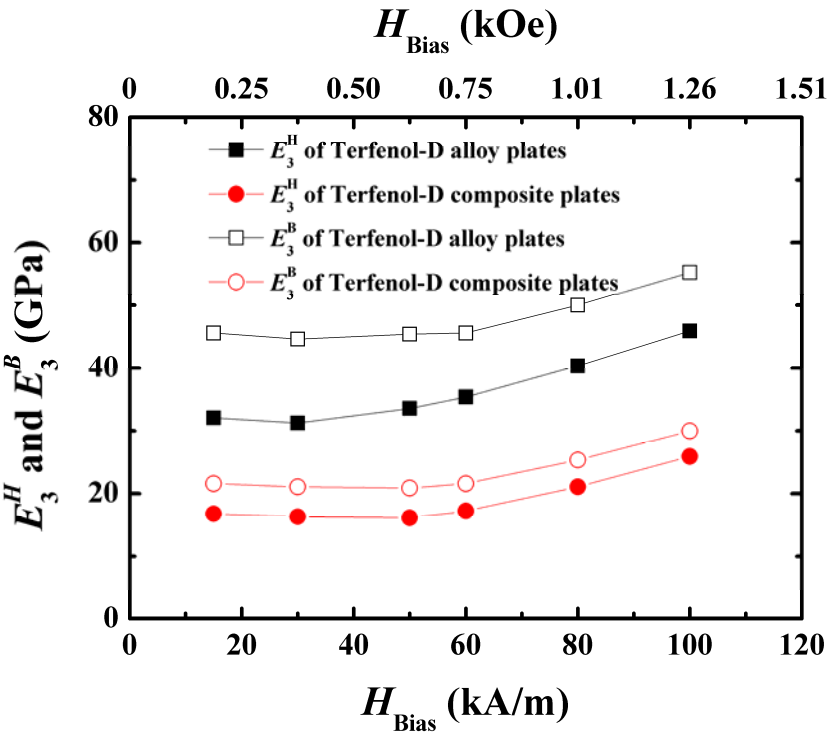

Fig. 2.18 E_3^H –H_3 and E_3^B –H_3 curves for Terfenol-D alloy plates and Terfenol-D composite plates.

Figure 2.19 shows the dependence d_{33} as a function of f for various H_{Bias} for the Terfenol-D alloy plates and Terfenol-D composite plates. Again, flat frequency responses are observed in the low frequency region of ≤40 kHz, and the fundamental resonances are detected in the resonance frequency range of 60–100 kHz depending on the levels of H_{Bias}. The observations are consistent with those of the μ_{r33} spectra shown in Fig. 2.16. In addition, insignificant eddy-current effects are seen in the d_{33} spectra.

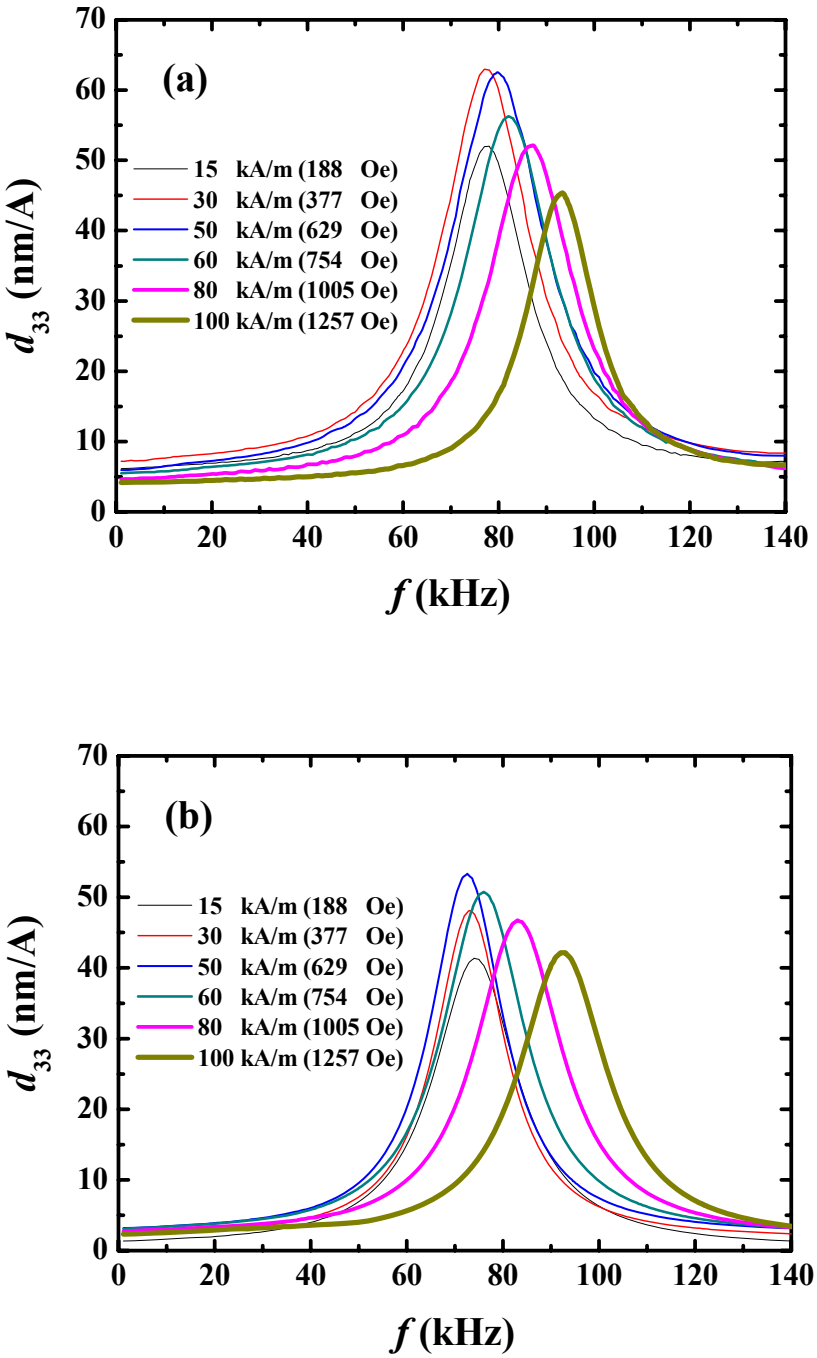

Fig. 2.19 d_{33}–H_3 curves for (a) Terfenol-D alloy plates and (b) Terfenol-D composite plates.

The dependences of d_{33} on H_{Bias} at 1 kHz for the Terfenol-D alloy plates and the Terfenol-D composite plates are shown in Fig. 2.20. It is clear that the d_{33} curves for both samples increase initially and attain the maximum values of 7.2 nm/A at H_{Bias} = 30 kA/m and 3.2 nm/A at H_{Bias} = 50 kA/m, respectively. This is a result of increasing and maximizing S_3 contribution from the non-180° domain-wall motion, respectively. In particular, the occurrence of maximum d_{33} at the respective H_{Bias} levels suggests that the samples are biased in the center of the magnetization jumping region of the quasistatic $\lambda - H_3^{QS}$ curves in Fig. 2.12 about which d_{33}^{QS} is also maximized (Fig. 2.13).

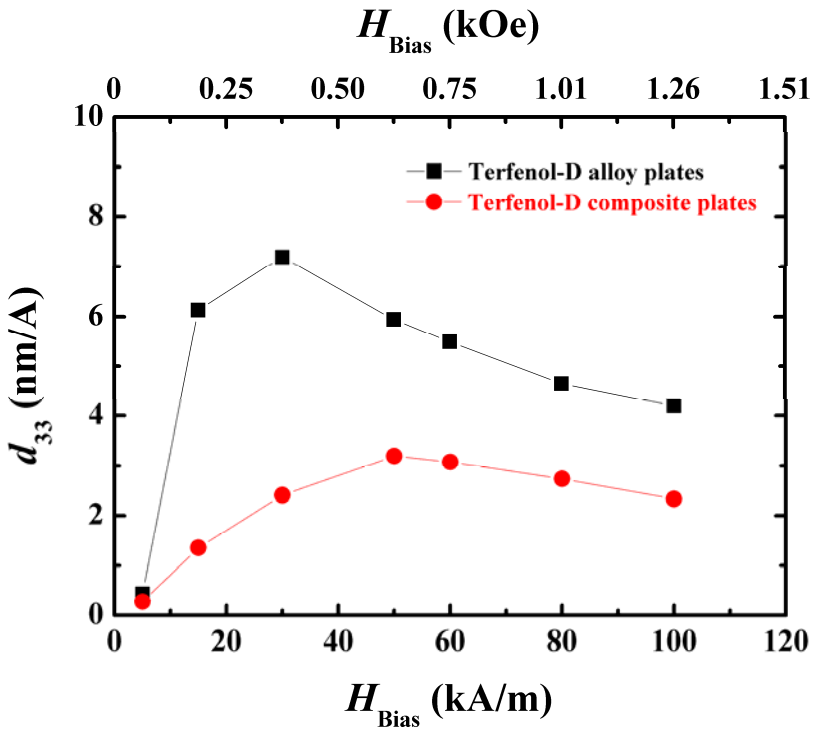

Fig. 2.20 d_{33}–H_{Bias} curves for Terfenol-D alloy plates and Terfenol-D composite plates.

2.2.5 Summary of Useful Material Properties

The measured material properties of the Terfenol-D alloy plates and the Terfenol-D composite plates are summarized in Table 2.3. The dynamic strain coefficients (d_{33} = 7.19 nm/A for Terfenol-D alloy plates and 3.19 nm/A for Terfenol-D composite plates) are reasonable high for the production of large mechanical strain in response to small magnetic fields. The saturation of magnetostrictions (λ_s = 1028 ppm for Terfenol-D alloy plates and 718 ppm for Terfenol-D actuator composite plates) are also very high for widening the operating sensitivity range. All these properties ensure the role of both Terfenol-D alloy plates and Terfenol-D composite plates in the ME sensing elements. These values will be used in Chapter 3 for designing ME sensing elements.

Table 2.3 Material properties of Terfenol-D alloy plates and Terfenol-D composite plates [61].

	Symbol	Terfenol-D Alloy Plate	Terfenol-D Short-Bar–Epoxy Composite Plate	Terfenol-D Alloy Plate
		Measured Data	Measured Data	Manufacturer's Data
Physical Properties				
Density (kg/m^3)	ρ	9200	5310	9250
Quasistatic Properties				
Saturation magnetization (kA/m)	M_s	0.84*	0.385*	1
Saturation magnetostriction (ppm)	λ_s	1028*	718*	1500–2000**
Relative permeability	μ_{r33}^{QS}	1-17*	0.5-9*	5–10
Dynamic Properties				
Dynamic relative permeability at 1 kHz	μ_{r33}^{T}	5.11***	2.58****	–
Dynamic relative permeability at 140 kHz	μ_{r33}^{S}	3.83***	2.32****	
Dynamic strain coefficient (nm/A)	d_{33}	7.19***	3.19****	–
Elastic modulus at constant magnetic field strength (GPa)	E_3^H	31.25*****	16.12******	–
Elastic modulus at constant magnetic flux density (GPa)	E_3^B	44.61*****	20.87******	–

* Measured at 100 Hz frequency.
** Measured at 79.6 kA/m magnetic field and with 10 MPa prestress.
*** Measured at 30 kA/m bias field.
**** Measured at 50 kA/m bias field.
***** Measured at 30 kA/m bias field.
****** Measured at 50 kA/m bias field.

2.3 Piezoelectric Materials

2.3.1 PMN–PT Single-Crystal Plates/Bars

Lead magnesium niobate-lead tiranate single-crystal plates and bars with the chemical composition of $0.71(Mg_{1/3}Nb_{2/3})O_3$–$0.29PbTiO_3$ (PMN–PT) (Fig. 2.21) were used in the fabrication of the ME sensing elements. The plated-shaped samples had dimensions of 12 ± 0.15 mm in length, 6 ± 0.1 mm in width, 1 ± 0.1 mm in thickness, and with the preferred [001] crystallographic axis oriented in the length direction and the electric polarization in the thickness direction. The bar-shaped samples had dimensions of 18 ± 0.1 mm in length, 2.5 ± 0.05 mm in width, 2.5 ± 0.05 mm in thickness, and with the preferred [001] crystallographic axis and the electric polarization oriented in the longitudinal direction.

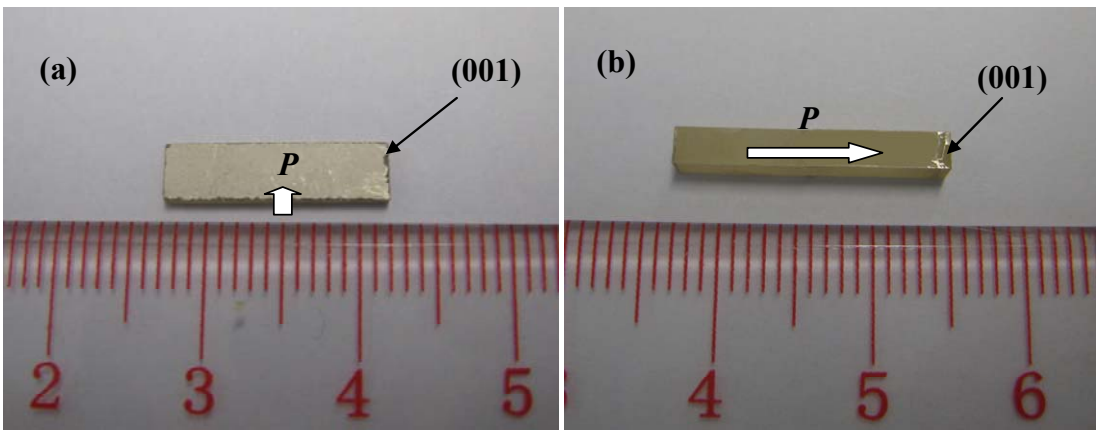

Fig. 2.21 Photographs of PMN–PT single-crystal samples. (a) Plate-shaped sample and (b) bar-shaped sample. *P* denotes the electric polarization direction.

To fabricate the samples with high performance, single crystals with composition near the rhombothedral-tetragonal morphotropic phase boundary (MPB) were chosen [66]. The single crystals were synthesized by a modified Bridgman technique and the procedures were as follows [67,68]: The high-purity (>99.99%) raw powders of PbO, MgO, Nb_2O_5, and TiO_2 were commercially acquired. They were weighted and mixed in a specified stoichiometric composition of 0.71PMN–0.29PT near the rhombothedral-tetragonal MPB (Fig. 2.22). The PMN–PT single crystals were grown in a sealed platinum crucible of a Bridgman furnace at ~1380 °C to prevent the evaporation of PbO. The orientation of the as-grown single crystals was chosen along the [111] direction for the crystal growth (Fig. 2.23). After the single crystals were soaked for 10 h, the crucible was dropped downward at a rate of 0.5 mm/hr. The temperature of the Bridgman furnace was cooled to room temperature (25 °C) at a rate of 25 °C/hr. The crystallographic orientation of the as-grown single-crystal boules was confirmed by a X-ray diffraction (XRD) technique, and the single-crystal boules were cut into the desired shape and dimensions along the [001] crystallographic direction using an annular saw. To impart the piezoelectric effect to the single-crystal samples, silver paste was painted on the sample surfaces and sintered at 700 °C for 30 min. The plate-shaped samples were polarized in a silicone oil bath at an electric field of 1 kV/mm and a temperature of 120 °C for 10 min, while the bar-shaped samples were polarized at 0.3 kV/mm and 120 °C for 10 min.

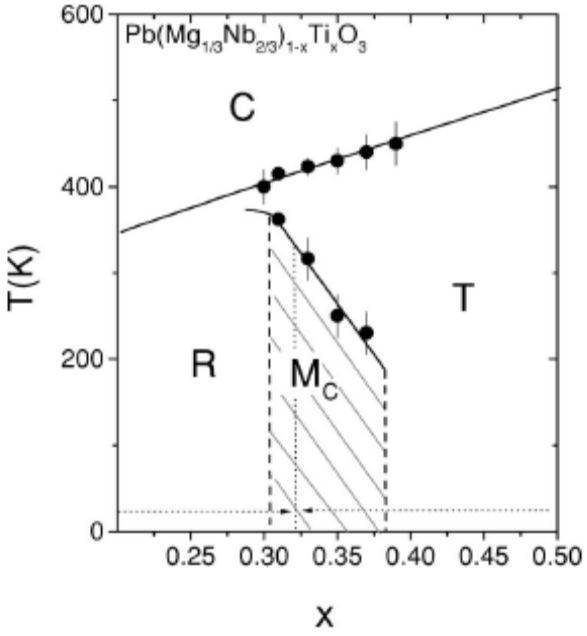

Fig. 2.22 Modified phase diagram of (1-*x*)PMN–*x*PT around the rhombothedral-tetragonal MPB [66].

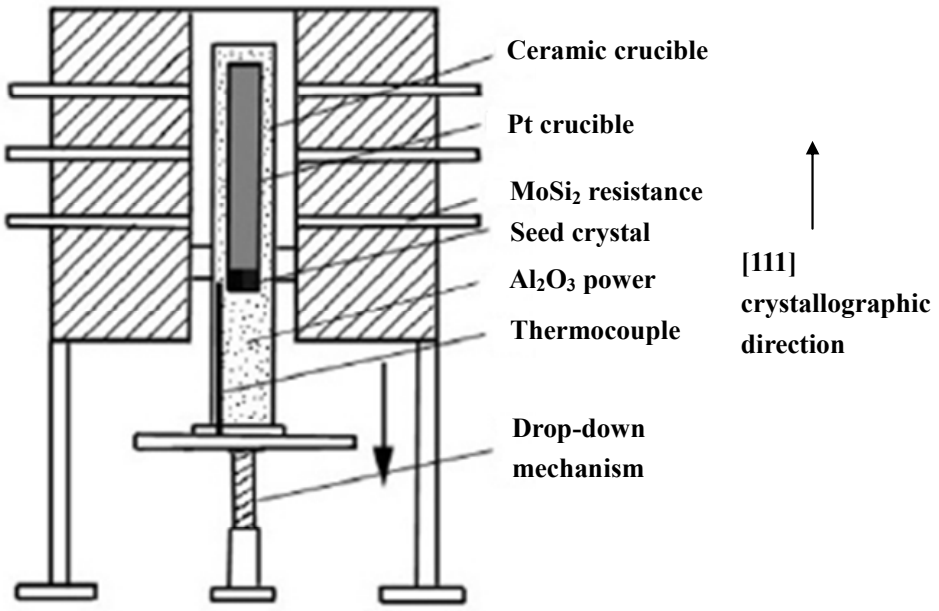

Fig. 2.23 Schematic diagram of Bridgman furnace used to grow PMN−PT single crystals [67,68].

2.3.1.1 Electromechanical Measurements

The electromechanical resonance method stated in the ANSI/IEEE standard was used for evaluating piezoelectric material properties [69]. The method was based on the electrical impedance (or admittance) equations for different resonance modes derived from the observed resonance and anti-resonance frequencies for the corresponding resonance modes. Determination of piezoelectric properties was achieved by using different piezoelectric samples with specific shapes; aspect ratios; and directions of polarization. By recording the corresponding resonance frequency (f_r) and anti-resonance frequency (f_a), various piezoelectric material parameters can be evaluated. Different resonance modes excited in various samples were measured, leading to the determination of the electromechanical coefficients of the PMN–PT single crystals used in the subsequent design and development of the ME sensing elements in Chapter 3.

A piezo d_{33} meter (Model ZJ-4B, Institute of Acoustics, Academia Sinica) shown in Fig. 2.24(a) was used to measure the piezoelectric charge coefficient (d_{33}). An impedance analyzer (Agilent 4294A) equipped with a test fixture (Agilent 16034E) and shown in Fig. 2.24(b) was employed to measure f_r and f_a, free capacitance (C_T) at 1 kHz, and clamped capacitance (C_s) at a frequency well above all pronounced resonances (i.e., 5 MHz). From the measured f_r and f_a, the electromechanical coupling coefficients (k) and elastic compliance constants (s) were determined. The relative free and clamped dielectric permittivities (ε_r^T and ε_r^S) were also found from the measured C_T and C_S values, respectively.

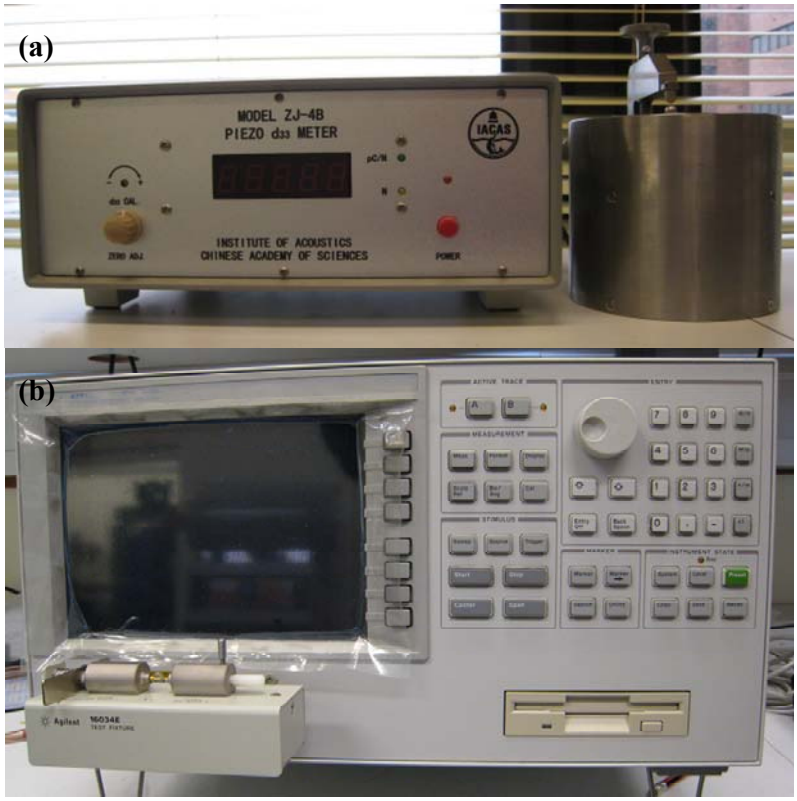

Fig. 2.24 Photographs of (a) piezo d_{33} meter and (b) impedance analyzer with test fixture.

The longitudinal−length (3−3) resonance mode states that the sample has its electric polarization and mechanical motion in the longitudinal (3-) direction. The relative free permittivity (ε_{33}^{T}) at 1 kHz and relative clamped permittivity ($\varepsilon_{33}^{\mathrm{S}}$) at 5 MHz were determined by:

$$\varepsilon_{33}^{T} = \frac{C_{\mathrm{p}} l}{\varepsilon_0 A} \tag{2.14}$$

and

$$\varepsilon_{33}^{\mathrm{S}} = \frac{C_{\mathrm{S}} l}{\varepsilon_{\mathrm{o}} A}, \tag{2.15}$$

where l and A are the length and electrode area of the sample, respectively, and C_p and C_s are the capacitances at 1 kHz and 5 MHz, respectively. The electromechanical coupling coefficient (k_{33}) was evaluated by

$$k_{33} = \sqrt{\frac{\pi}{2}\frac{f_r}{f_a}\tan[\frac{\pi}{2}\frac{(f_a - f_r)}{f_a}]} \quad . \tag{2.16}$$

The elastic compliance at constant electric field (s_{33}^E) and that at constant electric displacement (s_{33}^D) were determined, respectively, by

$$s_{33}^D = \frac{1}{4\rho f_a^2 l^2} \tag{2.17}$$

and

$$s_{33}^E = \frac{s_{33}^D}{1 - k_{33}^2} , \tag{2.18}$$

where the superscripts E and D denote the conditions of constant electric field and dielectric displacement, respectively; and ρ and l are the density and length of the sample, respectively. The piezoelectric voltage coefficient (g_{33}) was calculated by

$$g_{33} = \frac{d_{33}}{\varepsilon_{33}^T} \quad . \tag{2.19}$$

The transverse−length (3−1) resonance mode implies that the piezoelectric sample has its electric polarization in the thickness (3-) direction and its mechanical motion along the longitudinal (1-) direction. The electromechanical coupling coefficient (k_{31}) was calculated by

$$k_{31} = \sqrt{\frac{\pi}{2}\frac{f_a}{f_r}\frac{1}{\frac{\pi}{2}\frac{f_a}{f_r} - \tan\left(\frac{\pi}{2}\frac{f_a}{f_r}\right)}}. \tag{2.9}$$

The elastic compliance at constant electric field (s_{11}^E) and that at constant electric displacement (s_{11}^D) were determined by

$$s_{11}^E = \frac{1}{4\rho f_r^2 l^2} \tag{2.10}$$

and

$$s_{11}^D = s_{11}^E\left(1 - k_{31}^2\right), \tag{2.11}$$

where the superscripts E and D denote the conditions of constant electric field and dielectric displacement, respectively; and ρ and l are the density and length of the sample, respectively. The piezoelectric charge coefficient (d_{31}) and piezoelectric voltage coefficient (g_{31}) were obtained, respectively, by

$$d_{31} = k_{31} \cdot \sqrt{s_{11}^E \cdot \varepsilon_{33}^T} \tag{2.12}$$

and

$$g_{31} = \frac{d_{31}}{\varepsilon_0 \varepsilon_{33}^T}. \tag{2.13}$$

where $\varepsilon_0 = 8.854 \times 10^{-12}$ F/m is the permittivity of free space and ε_{33}^T is the relative free permittivity.

2.3.1.2 Summary of Useful Material Properties

The measured material properties of the PMN–PT single crystals are summarized in Table 2.4. The piezoelectric charge coefficients (d_{31} = -1238 pC/N and d_{33} = -1465 pC/N) are very high for the production of large electrical signals in response to small mechanical stresses. The electromechanical coupling coefficients (k_{31} = 0.74 and k_{33} = 0.88) are also high for the efficient conversion between mechanical and electrical energies in the transverse−length and longitudinal−length resonance modes, respectively. All these properties are crucial to the application of the PMN−PT single crystals as magnetoelectric sensors in the ME sensing elements. These values will be used in Chapter 3 for designing the ME sensing elements.

Table 2.4 Measured material properties of PMN–PT single crystals.

	Symbol	PMN-PT
Dielectric Properties		
Relative dielectric permittivity at 1 kHz	ε_{33}^{T}	6453
Electromechanical Properties		
Electromechanical coupling coefficients	k_{31}	0.74
	k_{33}	0.88
Piezoelectric charge coefficients (pC/N)	d_{31}	-1238
	d_{33}	1465
Piezoelectric voltage coefficients (mV·m/N)	g_{31}	-21.68
	g_{33}	25.65
Mechanical Proprieties		
Density (kg/m^3)	ρ	8092
Elastic compliance coefficients (pm^2/N)	s_{11}^{E}	49.04
	s_{33}^{E}	57.71
	s_{11}^{D}	22.18
	s_{33}^{D}	13.02

2.3.2 PMN–PT Single-Crystal Transformers

PMN–PT single-crystal transformers are devices used to step-up or step-down electrical voltages by the direct and converse piezoelectric effects between their input and output sides. The PMN–PT transformers, in this study, were fabricated by the $0.71(Mg_{1/3}Nb_{2/3})O_3$–$0.29PbTiO_3$ (PMN–PT) singe crystals described in Section 2.3.1. Two different types of PMN−PT transformers were prepared, including Rosen-type and long-type transformers. Their operating principles and photographs are shown in Fig. 2.25 and 2.26, respectively. As shown in Fig. 2.25(a), Rosen-type transformers are operated under a longitudinal resonance and suited for use as step-up transformers because of their voltage gains and high output impedances [70,71]. The displacement and stress distributions along the length of the Rosen-type transformers for the half-wavelength and full-wavelength longitudinal resonances are shown in Fig. 2.25(c). Long-type transformers produce lower voltage gains compared to the Rosen-type transformers, but they show distinct advantages of smaller size, simpler structure, no spurious vibration, and no acoustic mismatch [72]. The displacement and stress distributions along the longitudinal direction of the long-type transformers are the same as the Rosen-type transformers in Fig.2.25(c).

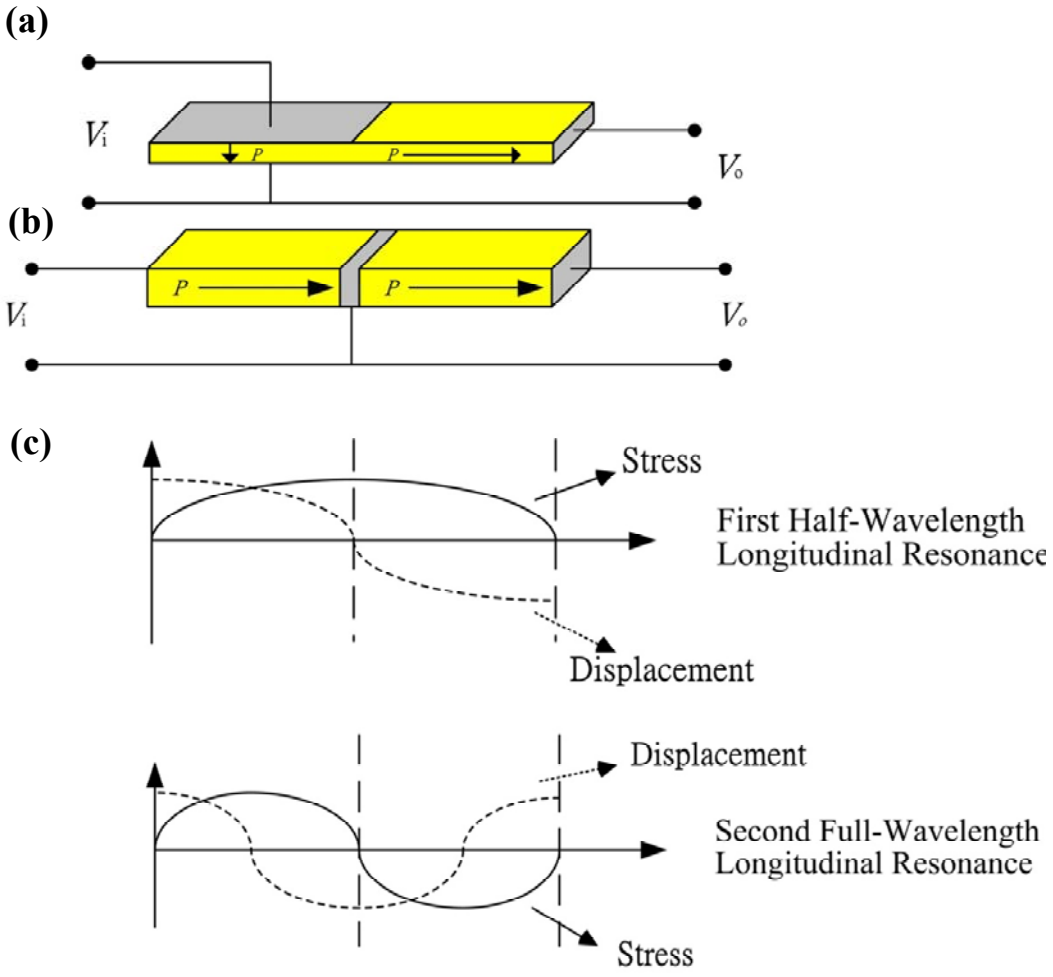

Fig. 2.25 (a) Schematic diagram of (a) Rosen-type transformer, (b) long-type transformer, and (c) the displacement and stress distributions along the length of the transformer for the first (half-wavelength) and second (full-wavelength) longitudinal resonances. The labels V_i and V_o denote the input and output voltages of the transformers, respectively.

As shown in Fig. 2.26, the Rosen-type transformers were prepared in a plate shape with dimensions of 26 ± 0.05 mm in length, 6 ± 0.05 mm in width, and 1 ± 0.05 mm in thickness, while the long-type transformers were made in a bar shape with dimensions of 16 ± 0.05 mm in length, 2 ± 0.05 mm in width, and 2 ± 0.05 mm in

thickness. Both types of transformers were oriented in such way that their preferred [001] crystallographic orientation were along the length direction. For the Rosen-type transformers, sliver pastes were painted on the half of two main surfaces of the input section in the thickness direction and the two main surfaces of the output section in the length direction before being fired at 600 °C for 1 h as electrodes. In order to prevent the transformers from temperature-induced depolarization, they were polarized twice in a silicon oil bath: the first times along the length direction using the output electrodes and the second times along the thickness direction using the input electrodes, both under an electric field of 1000 kV/mm at 110 °C for 15 min and then at a reduced electric field of 700 V/mm in the cooling run until room temperature. For the long-type transformers, sliver pastes were painted on the two main surfaces of the input and output electrodes in the length direction and the four side surfaces covering the central 2 mm portion normal to the length direction to form the ground electrode before being fired at 600 °C for 1 h. The same poling process was adopted.

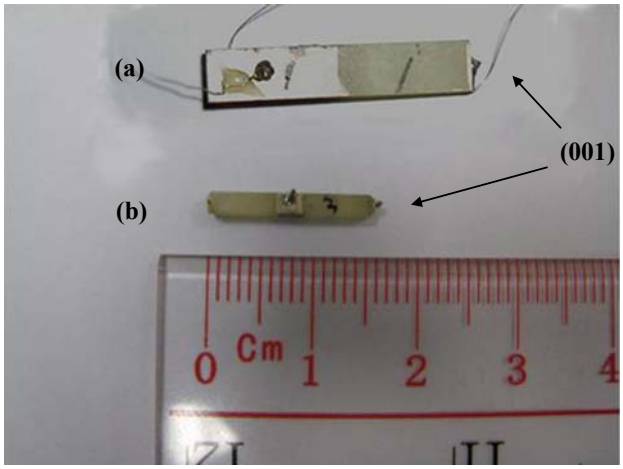

Fig. 2.26 Photograph of PMN−PT single-crystal transformers: (a) Rosen-type and (b) long-type transformers.

2.3.2.1 Step-Up Ratio Measurement

The step-up ratio properties of the Rosen-type and long-type PMN−PT single-crystal transformers were measured at room temperature by an automated measurement system as shown in Fig. 2.27. A swept sinusoidal electrical input voltage (V_i) of 1 V peak was generated over a prescribed frequency range (f) of 1−175 kHz by an arbitrary waveform generator (Agilent 33210A) via a constant-voltage supply amplifier (AE Techron 7796HF). The corresponding step-up voltage (V_o) was sampled and measured by a data acquisition unit (Nation Instruments NBC-2110 and NI-PCI6132) under the control of a computer with a Labview program.

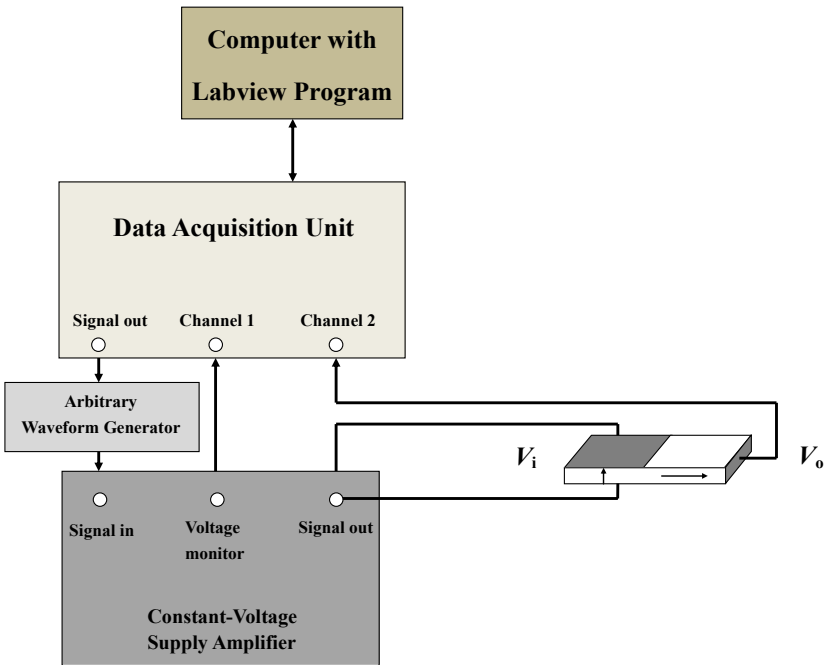

Fig. 2.27 Schematic diagram of the experimental setup for the step-up ratio measurement of piezoelectric transformers.

2.3.2.2 Results and Discussion

Figure 2.28 shows the step-up voltage ratio (V_o/V_i) as a function of frequency (f) of the Rosen-type and long-type PMN−PT single-crystal transformers. For the Rosen-type transformer in Fig. 2.28(a), two giant sharp V_{out}/V_{in} of 103 and 115, are observed at 33.2 and 62.5 kHz, representing the half-wavelength ($\lambda/2$) and full-wavelength (λ) longitudinal resonance, respectively. In the long-type transformers in Fig. 2.28(b), two sharp V_{out}/V_{in} of 28 and 29.5 are found at 60.1 and 122 kHz, indicating the half-wavelength ($\lambda/2$) and full-wavelength (λ) longitudinal resonances, respectively.

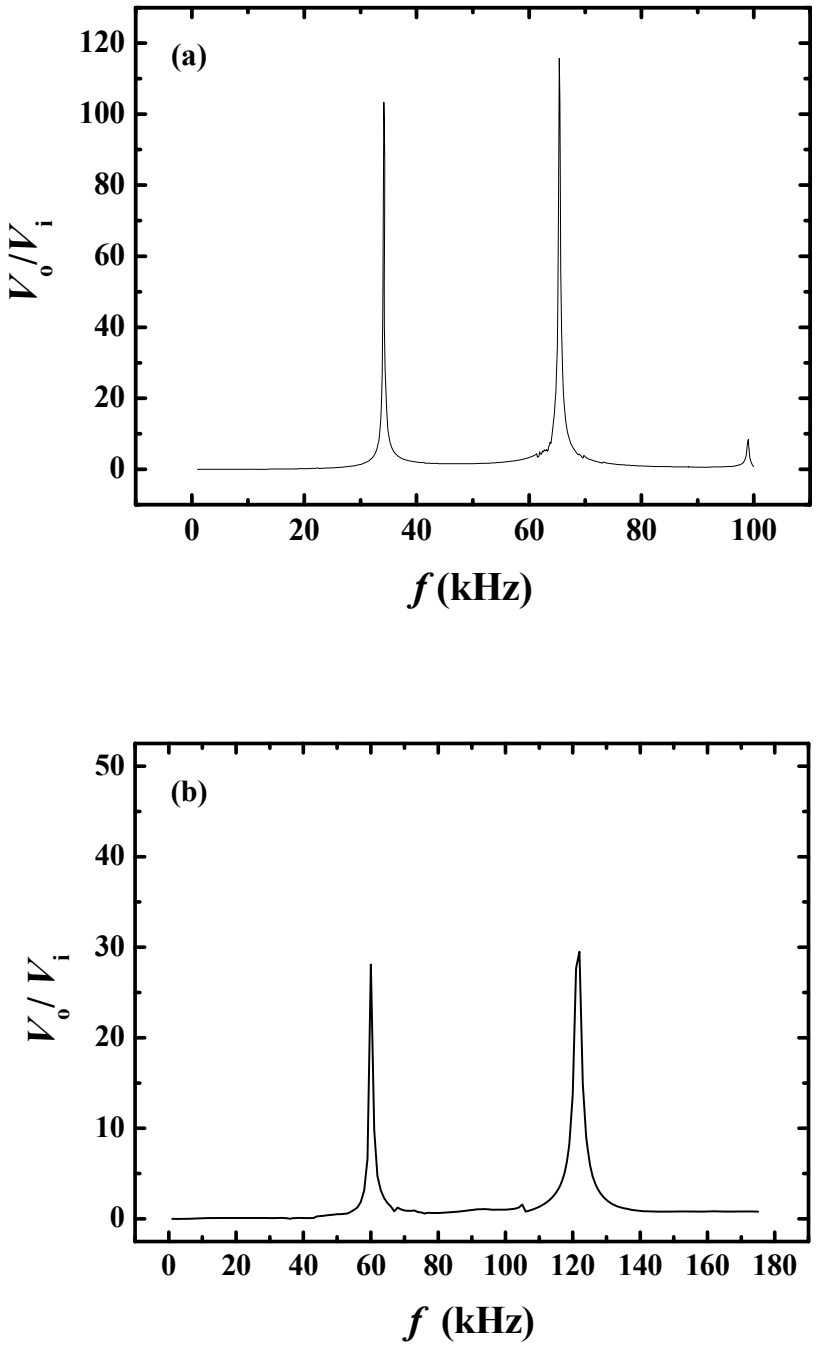

Fig. 2.28 V_o/V_i–f **curves for (a) Rosen-type and (b) long-type PMN−PT single-crystal transformers.**

2.3.3 PZT Ceramic Rings

Figure 2.29 shows the photograph of a PZT ceramic ring, Pz27, supplied by Ferroperm Piezoceramics in Demark [13]. This PZT ceramic ring will be used to fabricate ring-shaped ME sensing elements in Chapter 3. Different from the PMN−PT single crystals, PZT ceramics have polycrystalline structures. The PZT ceramic ring acquired had an outer diameter of 11.9 ± 0.05 mm, an inner diameter of 9.9 ± 0.05 mm, and a thickness of 1 ± 0.1 mm. It had full-fired silver electrodes on the two major inner and outer circumferential surfaces normal to the wall-thickness (or *r*-) direction and an electric polarization along the wall-thickness direction.

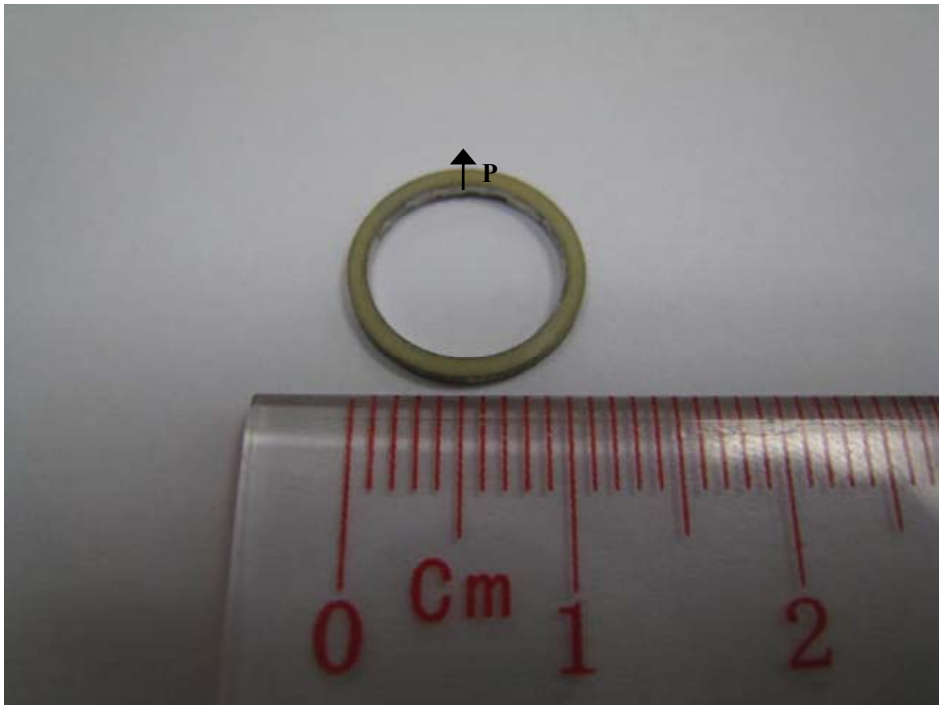

Fig. 2.29 Photograph of a PZT ceramic ring from Ferroperm Piezoceramics in Dermark.

2.3.3.1 Summary of Useful Material Properties

The materials properties of the piezoelectric ceramic ring, Pz 27, are summarized in Table 2.5. The piezoelectric ceramic ring exhibits a high Curie temperature of 350 °C, giving a high maximum operating temperature of 250 °C. This makes the resulting ME sensing elements workable at high operating temperatures. The piezoelectric charge coefficients (d_{31} = -170 pC/N and d_{33} = 425 pC/N) are reasonable high for the production of electrical signals in response to mechanical stresses. The electromechanical coupling coefficients (k_{31} = 0.33 and k_{33} = 0.70) are sufficiently high for the efficient conversion between mechanical and electrical energies in the transverse and longitudinal modes of operation, respectively. All these properties make the Pz 27 PZT ceramic ring a good sensing candidate for the ME sensing elements. These values will be used in Chapter 3 for designing the ring-shaped ME sensing elements.

Table 2.5 Material properties of piezoelectric ceramic ring Pz27, provided by FRRROPERM Piezoceramics in Demark.

	Symbol	Pz 27
Dielectric Properties		
Relative dielectric permittivity at 1 kHz	ε_{33}^{T}	1800
Dielectric dissipation factor at 1 kHz	$\tan\delta$	0.017
Curie temperature (°C)	$T_c>$	350
Maximum operating temperature (°C)	$<$	250
Electromechanical Properties		
Electromechanical coupling coefficients	k_{31}	0.33
	k_{33}	0.70
Piezoelectric charge coefficients (pC/N)	d_{31}	-170
	d_{33}	425
Piezoelectric voltage coefficients (mV·m/N)	g_{31}	-11
	g_{33}	27
Mechanical Proprieties		
Density (kg/m^3)	ρ	7700
Elastic compliance coefficients (pm^2/N)	s_{11}^{E}	17
	s_{33}^{E}	23
	s_{11}^{D}	15
	s_{33}^{D}	12

Chapter 3

Development of Magnetoelectric Sensing Elements

3.1 Introduction

A novel class of passive current sensors based on the magnetoelectric (ME) effect has been proposed and outlined in Chapter 1. The fabrication, characterization, and physical properties of the five different types of magnetostrictive and piezoelectric materials which constitute the ME sensing elements in the ME passive current sensors have been disclosed in Chapter 2. These materials include: Terfenol-D alloy plates and Terfenol-D short-bar−epoxy composite plates on the magnetostrictive side and PMN−PT single-crystal plates/bars, PMN−PT single-crystal transformers, and PZT ceramic rings on the piezoelectric side. The next step is to develop ME sensing elements based on the magnetostrictive and piezoelectric materials disclosed in Chapter 2.

In this chapter, three characteristic types of ME sensing elements are developed and reported. They are:

(1) Plate-shaped sensing elements with a PMN–PT piezoelectric single-crystal plate having a thickness polarization sandwiched between two Terfenol-D magnetostrictive alloy plates having a length magnetization;

(2) Ring-shaped sensing elements with an inner Terfenol-D short fiber–NdFeB magnet–epoxy three-phase magnetostrictive composite ring having a circumferential magnetization and an internal magnetic biasing concentric to an outer PZT piezoelectric ceramic ring having a wall-thickness polarization; and

(3) Bar-shaped sensing elements with a Rosen-type or a long-type PMN−PT piezoelectric single-crystal transformer sandwiched between two Terfenol-D magnetostrictive alloy plates having a length magnetization.

Physical models for describing the working principles of the sensing elements and for predicting their ME voltage coefficients (α_V) under different combinations of dimensions and material properties are established. The theoretical predications are confirmed by experimental investigations. Details of the fabrication processes and characterization methods are also provided.

3.2 Plate-Shaped Sensing Elements

3.2.1 Structure and Working Principle

Figure 3.1 shows the schematic diagram of the proposed plate-shaped sensing element having a thickness-polarized PMN–PT single-crystal plate sandwiched between two length-magnetized Terfenol-D alloy plates arranged in the Cartesian coordinate system and used to detect an ac magnetic field (H_3) along the length (or the 3-) direction of the sensing element (also along the length direction of the Terfenol-D alloy plates). The magnetization direction of the Terfenol-D alloy plates and the polarization direction of the PMN−PT single-crystal plate are marked as arrows *M* and *P* in the figure, respectively. It is noted that the length direction of the Terfenol-D alloy plates and the thickness direction of the PMN−PT single-crystal plate are taken as the main (or the 3-) direction because of the length magnetization in the Terfenol-D alloy plates and the thickness polarization in the PMN−PT single-crystal plate.

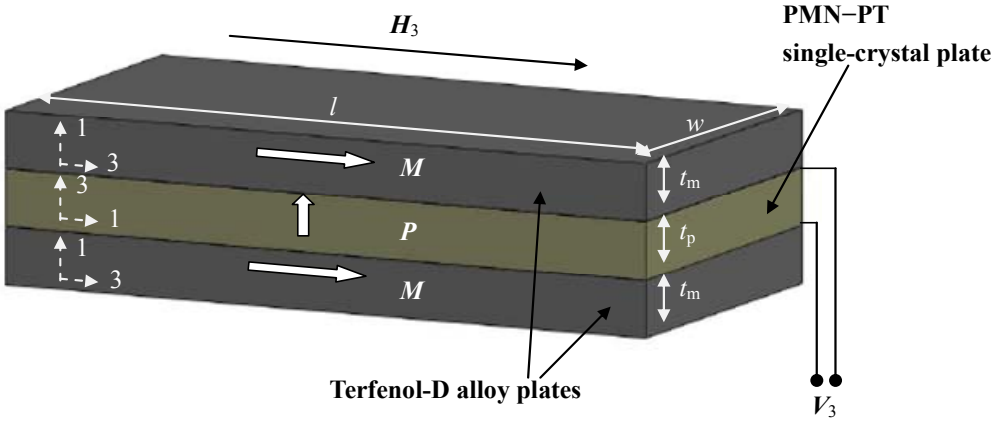

Fig. 3.1 Schematic diagram of the proposed plate-shaped sensing element arranged in the Cartesian coordinate system and used to detect an ac magnetic field (H_3). The arrows *M* and *P* denote the magnetization and polarization directions of the Terfenol-D alloy plates and the PMN−PT single-crystal plate, respectively.

The working principle of the plate-shaped sensing element is essentially based on the extrinsic ME effect realized using the mechanically mediated product effect of the magnetostrictive effect in the Terfenol-D alloy plates and the piezoelectric effect in the PMN−PT single-crystal plate. In more details, when such a sensing element is placed in an ac magnetic field (H_3) along the length (or the 3-) direction of the Terfenol-D alloy plates, an ac magnetostrictive strain ($S_{3,m}$) is induced in the length direction due to the magnetostrictive effect. This $S_{3,m}$ is mechanically coupled to the sandwiched PMN−PT single-crystal plate, leading to an ac piezoelectric voltage (V_3) across the thickness of the PMN−PT single-crystal plate in the 3-direction because of the piezoelectric effect. This mechanically mediated extrinsic ME effect in the sensing element results in an ME voltage coefficient ($\alpha_V = dV_3/dH_3$).

3.2.2 Physical Modeling

The ME effect in the plate-shaped sensing element operating at non-resonance frequencies well below its fundamental shape (length) resonance frequency can be described by the following quasistatic model. The sensing element is considered in such a way that its length (l) is much larger than its width (w) so that the physical modeling essentially involves the length and thickness (t) information as shown in Fig. 3.1. For the length-magnetized magnetostrictive material phase operating in the longitudinal-length (or the 33-) resonance mode, the piezoemagnetic constitutive equations can be expressed as follows [60]:

$$S_{3,\mathrm{m}} = s_{33}^{H} T_{3,\mathrm{m}} + d_{33,\mathrm{m}} H_3 , \tag{3.1}$$

$$B_3 = d_{33,\mathrm{m}} T_{3,\mathrm{m}} + \mu_{33}^{T} H_3 , \tag{3.2}$$

where H_3 and B_3 are the magnetic field and magnetic flux density along the length (or the 3-) direction, respectively; $S_{3,\mathrm{m}}$ and $T_{3,\mathrm{m}}$ are the mechanical strain and stress along the length direction, respectively; μ_{33}^{T} is the magnetic permeability at constant stress; $d_{33,\mathrm{m}}$ is the piezomagnetic strain coefficient; and s_{33}^{H} is the elastic compliance coefficient at constant magnetic field strength. For the thickness-polarized piezoelectric material phase operating in the transverse-length (or the 31-) resonance mode, the piezoelectric constitutive equations can be written as follows [73]:

$$S_{1,\mathrm{p}} = s_{11}^{E} T_{1,\mathrm{p}} + d_{31,\mathrm{p}} E_3 , \tag{3.3}$$

$$D_3 = d_{31,\mathrm{p}} T_{1,\mathrm{p}} + \varepsilon_{33}^{T} E_3 , \tag{3.4}$$

where E_3 and D_3 are the electric field and electric displacement along the thickness (or the 3-) direction, respectively; $S_{1,\mathrm{p}}$ and $T_{1,\mathrm{p}}$ are the mechanical strain and stress along the length (or the 1-) direction, respectively; ε_{33}^{T} is the dielectric permittivity at constant stress; $d_{31,\mathrm{p}}$ is the piezoelectric strain coefficient; and s_{11}^{E} is the elastic compliance coefficient at constant electric field strength.

Assuming a perfect mechanical coupling between the magnetostrictive and piezoelectric material phases, the mechanical boundary conditions of the strain and stress for the sensing element are as follows:

$$S_{3,\mathrm{m}} = S_{1,\mathrm{p}}, \tag{3.5}$$

$$2T_{3,\mathrm{m}}\upsilon_{\mathrm{m}} + T_{1,\mathrm{p}}\upsilon_{\mathrm{p}} = 0, \tag{3.6}$$

where υ_{m} and υ_{p} are the volumes of the magnetostrictive and piezoelectric material phases, respectively. Since the length (l) and width (w) of the two material phases are the same, Eq. (3.6) can be modified to depend on thickness (t) as follows:

$$2T_{3,\mathrm{m}}t_{\mathrm{m}} + T_{1,\mathrm{p}}t_{\mathrm{p}} = 0. \tag{3.7}$$

Under electrical open-circuit conditions, D_3 vanishes, giving

$$D_3 = 0. \tag{3.8}$$

Combining Eqs. (3.4), (3.7), and (3.8), $T_{3,\mathrm{m}}$ and $T_{1,\mathrm{p}}$ can be expressed, respectively, as

$$T_{3,\mathrm{m}} = \frac{\varepsilon_{33}^{T}E_3}{2d_{31,\mathrm{p}}}\cdot\frac{t_p}{t_{\mathrm{m}}} = \frac{E_3}{2g_{31,\mathrm{p}}}\cdot\frac{t_p}{t_m} \tag{3.9}$$

and

$$T_{1,\mathrm{p}} = -\frac{\varepsilon_{33}^{T} E_3}{d_{31,\mathrm{p}}} = -\frac{E_3}{g_{31,\mathrm{p}}}, \tag{3.10}$$

where $g_{31,\mathrm{p}}$ is the piezoelectric voltage coefficient.

Combining Eqs. (3.1), (3.3), (3.5), and (3.7)−(3.10), the ME field coefficient (α_E) is

$$\alpha_E = \left|\frac{dE_3}{dH_3}\right| = \left|\frac{2d_{33,\mathrm{m}} g_{31,\mathrm{p}} t_{\mathrm{m}}}{s_{33}^{H} t_{\mathrm{p}} + 2s_{11}^{E} t_{\mathrm{m}} - 2d_{31,\mathrm{p}} g_{31,\mathrm{p}} t_{\mathrm{m}}}\right|. \tag{3.11}$$

Then, the ME voltage coefficient (α_V) is

$$\alpha_V = \left|\frac{dV_3}{dH_3}\right| = \left|\frac{dE_3}{dH_3}\right| \cdot t_{\mathrm{p}} = \alpha_E \cdot t_{\mathrm{p}} = \left|\frac{2d_{33,\mathrm{m}} g_{31,\mathrm{p}} t_{\mathrm{m}} t_{\mathrm{p}}}{s_{33}^{H} t_{\mathrm{p}} + 2s_{11}^{E} t_{\mathrm{m}} - 2d_{31,\mathrm{p}} g_{31,\mathrm{p}} t_{\mathrm{m}}}\right|. \tag{3.12}$$

3.2.3 Practical Implication

Based on the physical modeling of the plate-shaped sensing element in Section 3.2.2, α_V can be predicted using Eq. (3.12). Table 3.1 shows the major roles of the material parameters of the magnetostrictive and piezoelectric material phases in α_V. The symbols ↑ and ↓ indicate, respectively, the need of increasing and decreasing a specific material parameter in order to increase the value of α_V. In fact, the magnetostrictive and piezoelectric material phases act as a magnetomechanical actuator and a mechanoelectric sensor in the sensing element, respectively. It is clear from Eq. (3.12) that $d_{33,\mathrm{m}}$ and s_{33}^{H} are the major material parameters in the determination of the actuation performance of the magnetostrictive material phase. It is also known from Figs. 2.18 and 2.20 in Section 2.4.2.2 of Chapter 2 that $d_{33,\mathrm{m}}$ and

s_{33}^{H} (= $1/E_3^H$) are strongly dependent upon the magnetic bias field (H_{Bias}). A larger $d_{33,\text{m}}$ leads to a larger magnetostrictive actuation strain, while a smaller s_{33}^{H} gives rise to a larger actuation force. On the other hand, $g_{31,\text{p}}$ and s_{11}^{E} are the major material parameters in the control of the sensing performance of the piezoelectric material phase. A higher $|g_{31,\text{p}}|$ means a larger piezoelectric voltage output, while a smaller s_{11}^{E} implies a better mechanical matching between the piezoelectric and magnetostrictive material phases for an improved strain transfer. As a result, the use of larger $d_{33,\text{m}}$ and $|g_{31,\text{p}}|$, together with smaller s_{33}^{H} and s_{11}^{E}, is capable of providing an enhanced α_V.

Table 3.1 Influence of material parameters on α_V in the plate-shaped sensing element.

Symbol / Material Phase	$d_{33,\text{m}}$	s_{33}^{H}	s_{11}^{E}	$\lvert g_{31,\text{p}}\rvert$
Magnetostrictive	↑	↓		
Piezoelectric			↓	↑

Figure 3.2 shows the modeled α_V versus thickness ratio (t_m/t_p) at various H_{Bias} for the plate-shaped sensing element shown in Fig. 3.1 and described in accordance with Eq. (3.12). The required material parameters of the Terfenol-D alloy plates (i.e., $d_{33,\text{m}}$ and s_{33}^{H}) and the PMN−PT single-crystal plate (i.e., $g_{31,\text{p}}$ and s_{11}^{E}) are extracted from Figs. 2.18 and 2.20 in Section 2.2.4.2 and Table 2.4 in Section 2.3.1.2 of

Chapter 2, respectively. It is found that α_V increases rapidly with the initial increase in t_m/t_p and tends to be stable for t_m/t_p >5. Since α_V is a function of both $d_{33,m}$ and s_{33}^H, the highest α_V is detected at H_{Bias} = 0.4 kOe due to the maximization of both $d_{33,m}$ and s_{33}^H in the Terfenol-D alloy plates at H_{Bias} = 0.4 kOe (Figs. 2.18 and 2.20) . As t_m/t_p becomes infinite, α_V at a given H_{Bias} level will attain its limit, and the limiting value can be expressed by

$$\lim_{\frac{t_m}{t_p}\to\infty} \alpha_V = \frac{d_{33,m} g_{31,p} t_p}{s_{11}^E - d_{31,p} g_{31,p}} . \tag{3.13}$$

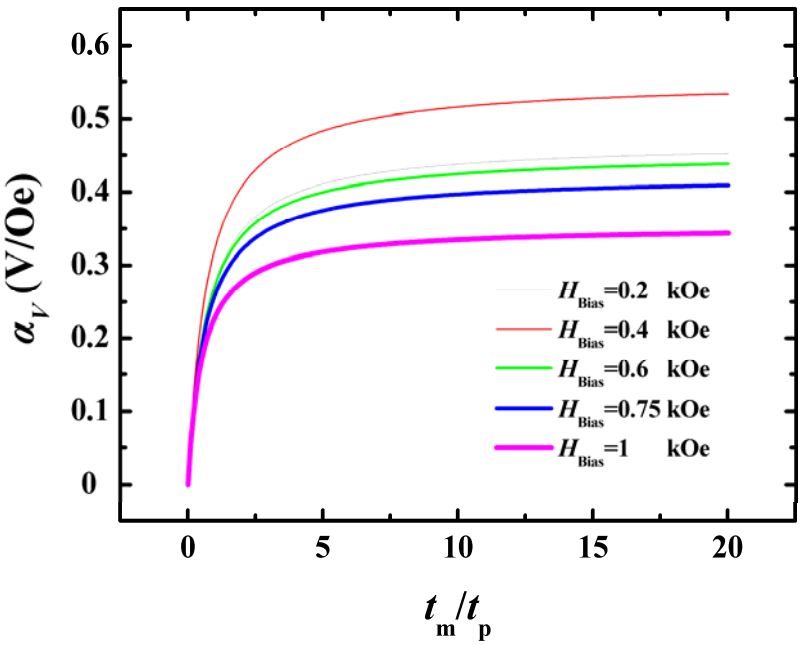

Fig. 3.2 Modeled α_V versus t_m/t_p at various H_{Bias} for the plate-shaped sensing element shown in Fig. 3.1 and described in accordance with Eq. (3.12).

Figure 3.3 shows the modeled α_V as a function of H_{Bias} at various t_m/t_p for the plate-shaped sensing element. The data of Fig. 3.3 is extracted from Fig. 3.2. For a given value of t_m/t_p, the highest α_V is observed at H_{Bias} = 0.4 kOe. This is the result of the maximization of $d_{33,m}$ and s_{33}^H in the Terfenol-D alloy plates at H_{Bias} = 0.4 kOe as explained in Fig. 3.2.

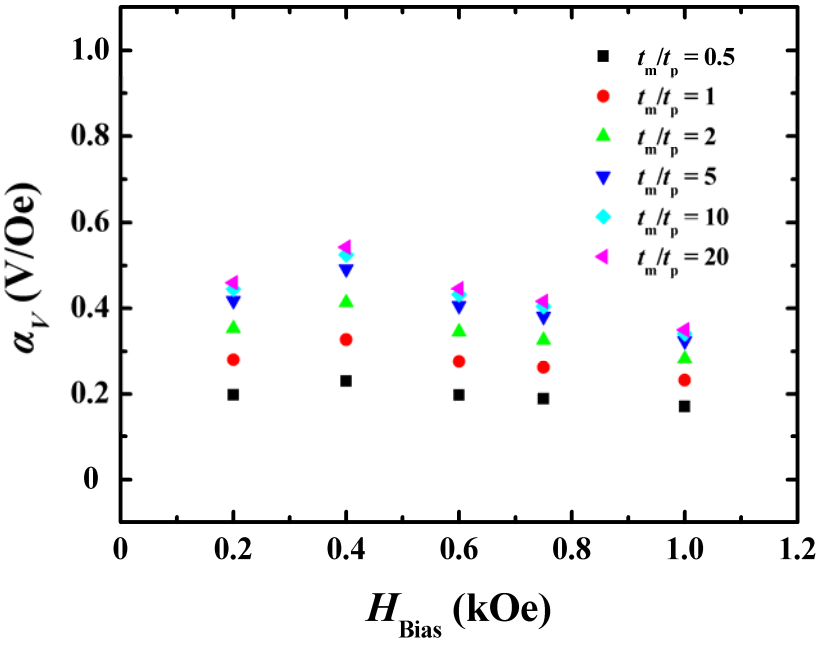

Fig. 3.3 Modeled α_V as a function of H_{Bias} at versus t_m/t_p for the plate-shaped sensing element shown in Fig. 3.1 and described in accordance with Eq. (3.12).

3.2.4 Fabrication

Terfenol-D alloy plates and PMN–PT single-crystal plates, having the same dimensions of 12 mm (length) × 6 mm (width) × 1 mm (thickness), were purchased/prepared, as described in Chapter 2. The fabrication process and photograph of a plate-shaped sensing element based on two Terfenol-D alloy plates and one PMN−PT single-crystal plate are shown in Fig. 3.4. The Terfenol-D alloy plates had an [112] crystallographic axis oriented along the length direction, while the PMN−PT single-crystal plate had an [001] crystallographic axis also oriented along the length direction. The PMN−PT single-crystal plate was sandwiched and bonded between the two Terfenol-D alloy plates using a silver-loaded epoxy adhesive (CHEMENCE IONACURE SL65). A mass of 10 kg was added on the sensing element during the cure of the adhesive at room temperature for 24 h to ensure good interface adhesion. The bonded sample had overall dimensions of 12 mm (length) × 6 mm (width) × 3 mm (thickness). Two electrical wires were connected to the Terfenol-D alloy plates as the leads for the ME signals.

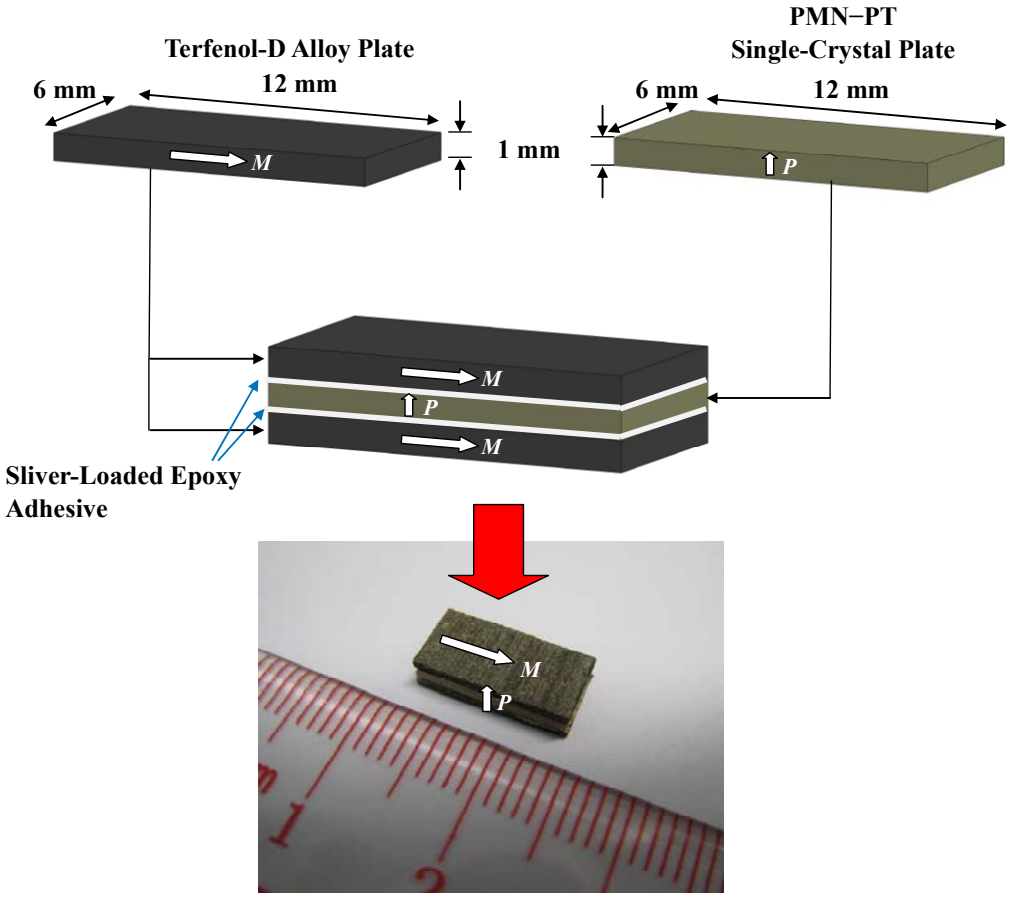

Fig. 3.4 Fabrication process and photograph of the proposed plate-shaped sensing element with a length of 12 mm, a width of 6mm, and a thickness of 3 mm.

3.2.5 Characterization

The quasistatic ME properties of the fabricated plate-shaped sensing element were measured in the length (or the 3-) direction at room temperature by using an in-house automated measurement system. The schematic diagram of the experimental setup is shown in Fig. 3.5. A low-frequency (f = 50 Hz) sinusoidal magnetic drive field (H_3) in the range of 0.1−10 Oe peak was provided by a pair of Helmholtz coils driven

by an arbitrary waveform generator (Agilent 33210A) via a constant-current supply amplifier (AE Techron 7796HF). A magnetic bias field (H_{Bias}) in the range of 0.02−1 kOe was produced by a water-cooled, C-shaped electromagnet (Mylten PEM-8005k) under the energization of a dc current supply (Sorensen DHP200-15). H_3 and H_{Bias} were monitored in-situ by a pick-up coil and an axial Hall-effect probe connected to a Gaussmeter (F. W. Bell 7030), respectively. The ME charge (Q_3) of the sensing element due to the applied H_3 was measured by a charge amplifier (Kistler 5015A). All quantities were sampled and measured by a data acquisition unit (Nation Instruments BNC-2110 and NI-PCI 6132) under the control of a computer with a Labview-based interface and control program. The ME voltage (V_3) at different combinations of H_3 and H_{Bias} was deduced by

$$V_3 = \frac{Q_3}{C}, \tag{3.14}$$

where C is the capacitance of the sensing element and was measured by an impedance analyzer (Agilent 4291A) equipped with a test fixture (Agilent 16034E) at the quasistatic frequency of 50 Hz. The ME voltage coefficient (α_V) at different levels of H_{Bias} was obtained by

$$\alpha_V = \frac{dV_3}{dH_3}. \tag{3.15}$$

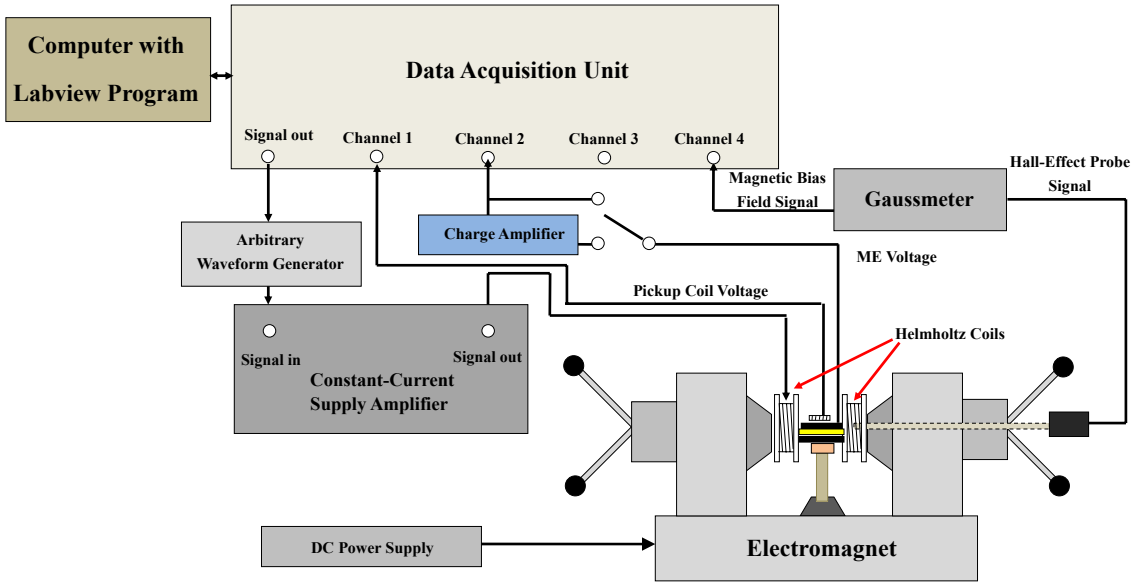

Fig. 3.5 Experimental setup for measuring the quasistatic and dynamic ME properties of the plate-shaped sensing elements.

The dynamic ME properties of the plate-shaped sensing element were also measured in the length (or the 3-) direction at room temperature by using the same set of in-house automated measurement system shown in Fig. 3.5 but with different operating parameters. A swept sinusoidal magnetic drive field (H_3) of 1 Oe peak was generated over a prescribed frequency (f) range of 1–150 kHz by the Helmholtz coils driven by the arbitrary waveform generator via the constant-current supply amplifier. A magnetic bias field (H_{Bias}) ranging from 0.02 to 1 kOe was provided by the electromagnet under the control of the dc current supply. H_3 and H_{Bias} were monitored in-situ by the pick-up coil and the axial Hall-effect probe connected to the Gaussmeter, respectively. All quantities were sampled and measured by the data acquisition unit

under the control of the computer and the Labview-based interface and control program. The dynamic ME voltage coefficient (α_V) was determined from

$$\alpha_V = \frac{V_3}{H_3}. \tag{3.16}$$

3.2.6 Results and Discussion

Figures 3.6 illustrates V_3 as a function of H_3 at 50 Hz under various H_{Bias} for the plate-shaped sensing element. It is clear that V_3 has a good linear response to H_3 for all H_{Bias}. Moreover, V_3–H_3 is found to depend on H_{Bias} because Terfenol-D is an H_{Bias}-dependent material (Section 2.2 of Chapter 2).

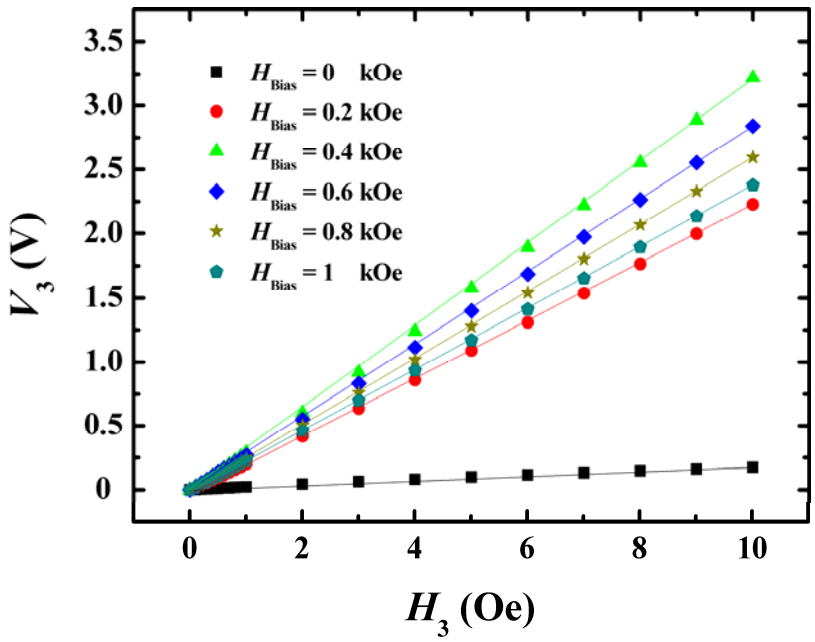

Fig. 3.6 Measured V_3 as a function of H_3 at 50 Hz under various H_{Bias} for the plate-shaped sensing element.

Figure 3.7 shows the measured α_V as a function of H_{Bias} at 50 Hz. The values of α_V are obtained from the slopes of the V_3–H_3 plot in Fig. 3.6. It is seen that α_V increases initially with increasing H_{Bias}. It is maximized at an optimal H_{Bias} of 0.4 kOe and then decreases with increasing H_{Bias}. This phenomenon can be explained by the negative-ΔE effect in the Terfenol-D alloy plates as described in Chapter 2. As H_{Bias} is increased towards 0.4 kOe, the non-180° domain-wall motion becomes easier so that both $d_{33,\text{m}}$ and s_{33}^{H} of the Terfenol-D alloy plates increase. At the optimal H_{Bias} of 0.4 kOe, the non-180° domain-wall motion is maximized and both $d_{33,\text{m}}$ and s_{33}^{H} are maximized at H_{Bias} = 0.4 kOe as well. After 0.4 kOe, both $d_{33,\text{m}}$ and s_{33}^{H} decrease due to the constrain of the non-180° domain-wall motion by the increased H_{Bias} levels.

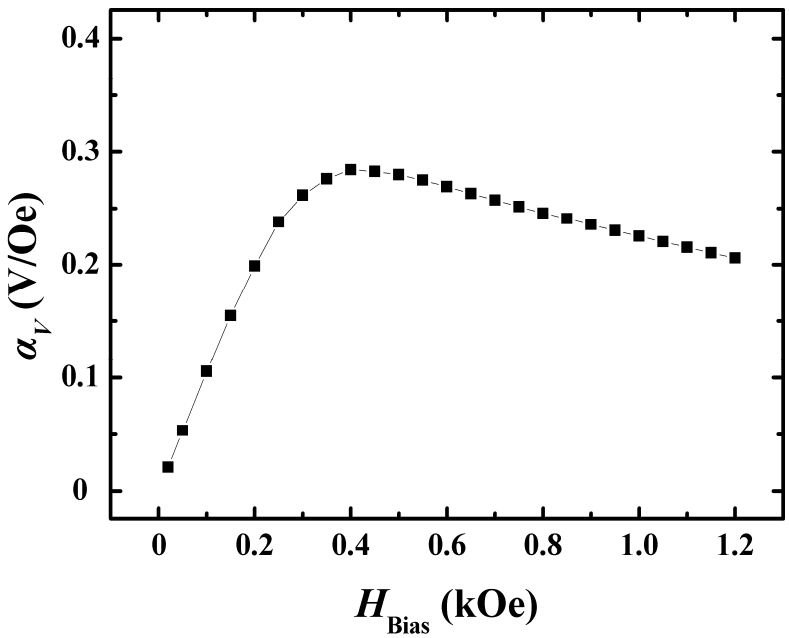

Fig. 3.7 Measured α_V as a function of H_{Bias} at 50 Hz for the plate-shaped sensing element.

Figure 3.8 shows the measured waveform of V_3 due to an applied H_3 of 1 Oe peak at an H_{Bias} of 0.4 kOe and a frequency of 50 Hz. The measured V_3 is very clear and has an amplitude of 0.28 V peak. This demonstrates the ability of stable signal conversion from H_3 to V_3 in our sensing element. V_3 has an opposite phase with H_3 since the piezoelectric voltage coefficient ($g_{31,p}$) carries a negative sign in Eq. (3.12).

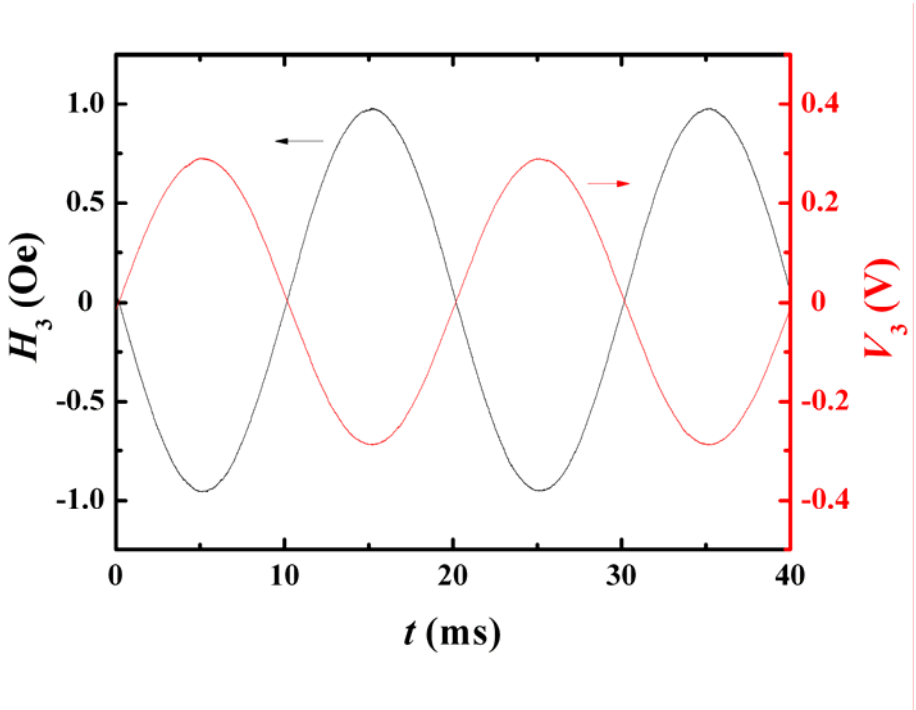

Fig. 3.8 Measured waveform of V_3 due to an applied H_3 of 1 Oe peak at an H_{Bias} of 0.4 kOe and a frequency of 50 Hz.

Figure 3.9 shows the measured α_V as a function of f at various H_{Bias} and with an H_3 of 1 Oe peak. The sensing element has an essentially flat response (i.e., the non-resonance region) for frequencies up to ~60 kHz. The resonance as seen at ~96 kHz is a result of the fundamental longitudinal-length (shape) resonance of the sensing element. The largest α_V is observed to be ~0.28 V/Oe at H_{Bias} = 0.4 kOe in the non-resonance frequency region (i.e., up to ~60 kHz). At the ME resonance frequency of 96.2 kHz, a greatly enhanced α_V is detected to be 3.22 V/Oe, being ~12 times enhanced from the non-resonance value.

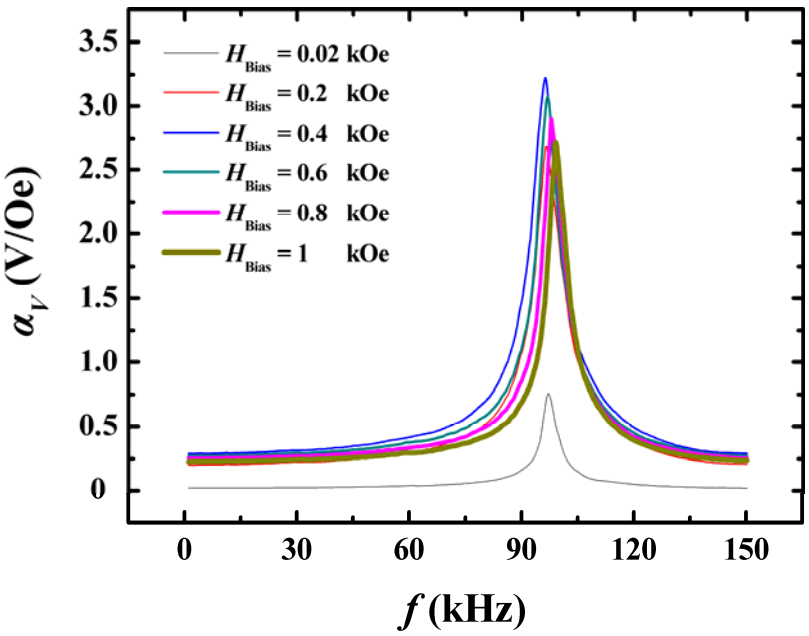

Fig. 3.9 Measured α_V as a function of f at various H_{Bias} and with an H_3 of 1 Oe peak for the plate-shaped sensing element.

3.3 Ring-Shaped Sensing Elements

3.3.1 Structure and Working Principle

Figure 3.10 shows the schematic diagram of the proposed ring-shaped sensing element with a vortex magnetic field detection mode configuration and intended to detect an ac vortex magnetic field (H_θ) governed by an ac current-carrying electrical cable having an ac current (I_z). This sensing element has a concentric magnetostrictive−piezoelectric ring structure in which the inner portion is a Terfenol-D short fiber–NdFeB magnet–epoxy three-phase magnetostrictive composite ring having a circumferential magnetization and an internal magnetic biasing in the θ-direction while the outer portion is a PZT piezoelectric ceramic ring having a wall-thickness polarization in the r-direction. The arrow P denotes the electric polarization direction of the PZT piezoelectric ceramic ring, while N and S indicate the north and south poles of the NdFeB magnet bars inside the magnetostrictive composite ring.

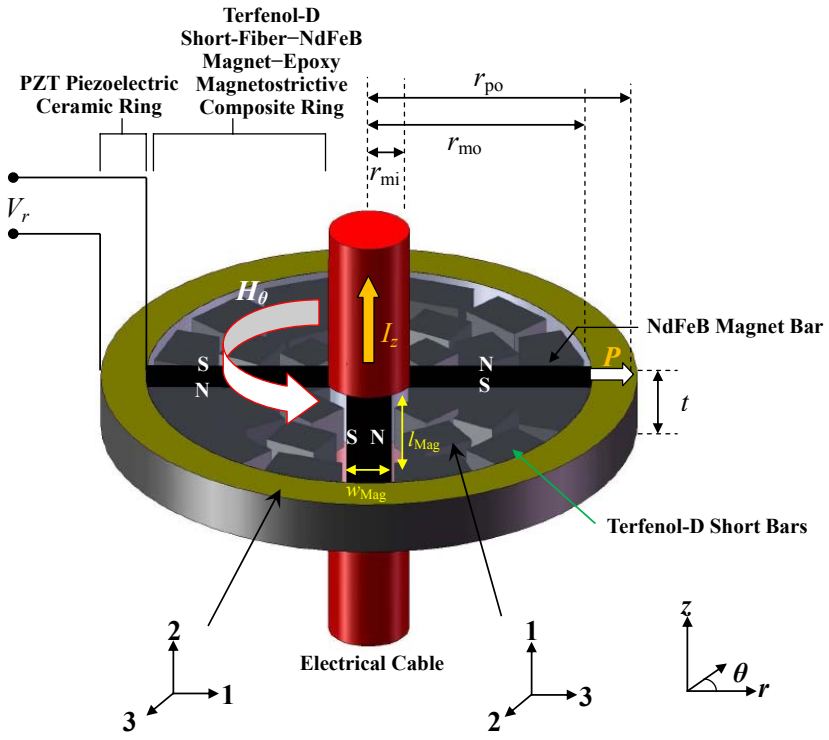

Fig. 3.10 Schematic diagram of the proposed ring-shaped sensing element with a vortex magnetic field detection mode configuration and intended to detect an ac vortex magnetic field (H_θ) governed by an ac current-carrying electrical cable having an ac current (I_z). The arrow *P* denotes the electric polarization direction, while N and S indicate the north and south poles of the NdFeB magnet bars.

The current sensing in the ring-shaped sensing element is essentially based on the direct coupling of vortex magnetic fields associated with current-carrying cables governed by Ampère's law with the extrinsic ME effect in the concentric magnetostrictive–piezoelectric ring structure. When an ac current (I_z) is applied to an electrical cable in the axial (or the z-) direction, an ac vortex magnetic field (H_θ) is induced about the length of the electrical cable in the circumferential (or the θ-) direction in accordance with Ampère's law. Because of the nonuniform distribution of H_θ over the volume (v_{vol}) of the sensing element, an average ac vortex magnetic field

($H_{\theta,\text{avg}}$) is detected instead, causing the inner magnetostrictive composite ring to produce circumferential (or the θ-) and also radial (or r-) motions due to the magnetostrictive effect. As the inner magnetostrictive composite ring is coupled mechanically to the outer piezoelectric ceramic ring, the magnetostrictive strains will subsequently stress the piezoelectric ceramic ring to generate an ac voltage (V_r) across the wall thickness of the piezoelectric ceramic ring in the r-direction owing to the piezoelectric effect.

3.3.2 Physical Modeling

The ME effect in the ring-shaped sensing element operating at non-resonance frequencies well below its fundamental shape (radial) resonance frequency can be described by the following quasistatic model. According to Ampère's law, the relation between I_z and $H_{\theta,\text{avg}}$ can be written as

$$H_{\theta,\text{avg}} = \frac{1}{v_{\text{vol}}}\int_{r_{\text{mi}}}^{r_{\text{mo}}} H_\theta dv_{\text{vol}} = \frac{I_z(r_{\text{mo}} - r_{\text{mi}})}{\pi(r_{\text{mo}}^2 - r_{\text{mi}}^2)}, \tag{3.17}$$

where r_{mi} and r_{mo} are the inner and outer radii of the magnetostrictive composite ring, respectively. Because the magnetostrictive composite ring is thin in the thickness (or the z-) direction and is magnetized along the circumferential (or the θ-) direction, the following piezomagnetic constitutive equations are used:

$$S_{3,\text{m}} = s_{33}^H T_{3,\text{m}} + d_{33,\text{m}} H_3, \tag{3.18}$$

$$B_3 = d_{33,\text{m}} T_{3,\text{m}} + \mu_{33}^T H_3, \tag{3.19}$$

where H_3 (= $H_{\theta,\text{avg}}$) and B_3 are the magnetic field and magnetic induction along the circumferential (or the θ-) direction, respectively; $T_{3,\text{m}}$ and $S_{3,\text{m}}$ are the mechanical stress and strain along the circumferential direction, respectively; μ_{33}^{T} is the magnetic permeability at constant stress; $d_{33,\text{m}}$ is the piezomagnetic strain coefficient; and s_{33}^{H} is the elastic compliance coefficient at constant magnetic field strength. For the piezoelectric ceramic ring with a wall-thickness polarization in the r-direction, and since it is thin in the thickness (or the z-) direction and small in the wall-thickness (or the r-) direction, the piezoelectric constitutive equations are as follows:

$$S_{1,\text{p}} = s_{11}^{E} T_{1,\text{p}} + d_{31,\text{p}} E_3 , \tag{3.20}$$

$$D_3 = d_{31,\text{p}} T_{1,\text{p}} + \varepsilon_{33}^{T} E_3 , \tag{3.21}$$

where E_3 (= E_r) and D_3 are the electric field and electric displacement along the wall-thickness (or the r-) direction, respectively; $T_{1,\text{p}}$ and $S_{1,\text{p}}$ are the mechanical stress and strain along the circumferential (or the θ-) direction, respectively; ε_{33}^{T} is the dielectric permittivity at constant stress; $d_{31,\text{p}}$ is the piezoelectric strain coefficient; and s_{11}^{E} is the elastic compliance coefficient at constant electric field strength.

Assuming a perfect mechanical coupling between the magnetostrictive and piezoelectric material phases, the mechanical boundaries for stress and strain are

$$T_{3,\text{m}}(r_{\text{mo}} - r_{\text{mi}}) + T_{1,\text{p}}(r_{\text{po}} - r_{\text{mo}}) = 0 \tag{3.22}$$

and

$$S_{3,\text{m}} = S_{1,\text{p}} , \tag{3.23}$$

respectively. Under electrical open-circuit conditions, D_3 vanishes, giving

$$D_3 = 0 . \tag{3.24}$$

Combining Eqs. (3.21), (3.22), and (3.24), $T_{3,\mathrm{m}}$ and $T_{1,\mathrm{p}}$ can be expressed as

$$T_{3,\mathrm{m}} = \frac{\varepsilon_{33}^{T} E_r}{d_{31,\mathrm{p}}} \cdot \frac{r_{\mathrm{po}} - r_{\mathrm{mo}}}{r_{\mathrm{mo}} - r_{\mathrm{mi}}} = \frac{E_r}{g_{31,\mathrm{p}}} \cdot \frac{r_{\mathrm{po}} - r_{\mathrm{mo}}}{r_{\mathrm{mo}} - r_{\mathrm{mi}}} \tag{3.25}$$

and

$$T_{1,\mathrm{p}} = -\frac{\varepsilon_{33}^{T} E_r}{d_{31,\mathrm{p}}} = -\frac{E_r}{g_{31,\mathrm{p}}} . \tag{3.26}$$

Combining Eqs. (3.20), (3.21), and (3.22)−(3.26), the ME voltage coefficient (α_V) of the ring-shaped sensing element is obtained as

$$\alpha_V = \left| \frac{dV_r}{dH_{\theta,\mathrm{avg}}} \right| = \frac{d_{33,\mathrm{m}} g_{31,\mathrm{p}} (r_{\mathrm{mo}} - r_{\mathrm{mi}})(r_{\mathrm{po}} - r_{\mathrm{mo}})}{s_{33}^{H}(r_{\mathrm{po}} - r_{\mathrm{mo}}) + s_{11}^{E}(r_{\mathrm{mo}} - r_{\mathrm{mi}}) - d_{31,\mathrm{p}} g_{31,\mathrm{p}} (r_{\mathrm{mo}} - r_{\mathrm{mi}})} . \tag{3.27}$$

Combining Eqs. (3.17) and (3.27), the current sensitivity (S_I) of the sensing element is

$$\begin{aligned} S_I &= \left| \frac{dV_r}{dI_z} \right| = \left| \frac{dV_r}{dH_{\theta,\mathrm{avg}}} \right| \cdot \left| \frac{dH_{\theta,\mathrm{avg}}}{dI_z} \right| \\ &= \alpha_V \cdot \left| \frac{dH_{\theta,\mathrm{avg}}}{dI_z} \right| \\ &= \frac{d_{33,\mathrm{m}} g_{31,\mathrm{p}} (r_{\mathrm{mo}} - r_{\mathrm{mi}})(r_{\mathrm{po}} - r_{\mathrm{mo}})}{[s_{33}^{H}(r_{\mathrm{po}} - r_{\mathrm{mo}}) + s_{11}^{E}(r_{\mathrm{mo}} - r_{\mathrm{mi}}) - d_{31,\mathrm{p}} g_{31,\mathrm{p}} (r_{\mathrm{mo}} - r_{\mathrm{mi}})]\pi(r_{\mathrm{mo}} + r_{\mathrm{mi}})} . \end{aligned} \tag{3.28}$$

It is noted that the terms (r_{mo}—r_{mi}) and (r_{po}—r_{mo}) in the above equations indicate the wall-thickness of the magnetostrictive composite ring and that of the piezoelectric ceramic ring, respectively.

3.3.3 Practical Implication

Table 3.2 shows the influence of material parameters on α_V and S_I in the ring-shaped sensing element. The symbols ↑ and ↓ indicate, respectively, the need of increasing and decreasing a specific parameter so as to elevate the values of α_V and S_I. Similar to the case of plate-shaped sensing element in Fig. 3.1, the inner magnetostrictive composite ring in this ring-shaped sensing element acts as a magnetomechnical actuator so that a large $d_{33,\mathrm{m}}$ and a small s_{33}^{H} are desirable. In addition, the outer piezoelectric ceramic ring functions as a mechanoelectric sensor, and a high $|g_{31,\mathrm{p}}|$ with a low s_{11}^{E} are important.

Table 3.2 Influence of material parameters on α_V and S_I in the ring-shaped sensing element.

Symbol / Material Phase	$d_{33,\mathrm{m}}$	s_{33}^{H}	s_{11}^{E}	$\lvert g_{31,\mathrm{p}}\rvert$
Magnetostrictive	↑	↓		
Piezoelectric			↓	↑

Figure 3.11 plots the modeled α_V and S_I versus r_{m} for two different ring-shaped sensing elements having the same piezoelectric ceramic ring's wall thickness ($r_{\mathrm{po}} - r_{\mathrm{mo}}$) of 1 mm but with different central hole radius (r_{mi}) of 1 and 5 mm. The values of $d_{33,\mathrm{m}}$ and s_{33}^{H} of the magnetostrictive composite ring are taken to be 1.05 nm/A and 61.2 pm^2/N at a reduced H_{Bias} of 90 Oe from Figs. 2.18 and 2.20 in

Section 2.4.2 of Chapter 2, respectively, because it is impossible to place large-size NdFeB magnet bars in the limited space of the magnetostrictive composite ring. The values of $d_{31,p}$, $g_{31,p}$, and s_{11}^{E} of the piezoelectric ceramic ring are obtained to be -170 pC/N, -11 mVm/N, and 17 pm^2/N, respectively, from Table 2.5 in Section 2.3.3.1 of Chapter 2. Nonetheless, it is seen that S_I increases with increasing r_{mo} and reaches its maximum value of 19.8 mV/A at r_{mo} = 3.8 mm for r_{mi} = 1 mm [Fig. 3.11(a)] and of 8.7 mV/A at r_{mo} = 11.5 mm for r_{mi} = 5 mm [Fig. 3.11(b)] before decreasing with further increasing r_{mo}. The observation is ascribed to an increase in $H_{\theta,avg}$ by an increase in r_{mo} as predicated by Eq. (3.17). For the ring-shaped sensing element with a smaller r_{mi} of 1 mm [Fig. 3.11(a)], $H_{\theta,avg}$ detected by the magnetostrictive composite ring is much more compared to that with a larger r_{mi} of 5 mm [Fig. 3.11(b)] under the same applied I_z. As a result, the use of a sensing element with a smaller r_{mi} can lead to an increased S_I under a given I_z. It is noted that α_V of both sensing elements increases obviously with the initial increase in r_{mo} and tends to be stable for r_{mo} > 50 mm because a larger r_{mo} causes a larger strain/stress transfer from the magnetostrictive composite ring to the piezoelectric ceramic ring. However, $H_{\theta,avg}$ decreases with increasing r_{mo} as stated by Eq. (3.17). Hence, the product effect of α_V and $dH_{\theta,avg}/dI_z$ in Eq. (3.28) results in an initial increase in S_I with small values of r_{mo} and a later decrease in S_I with big values of r_{mo}.

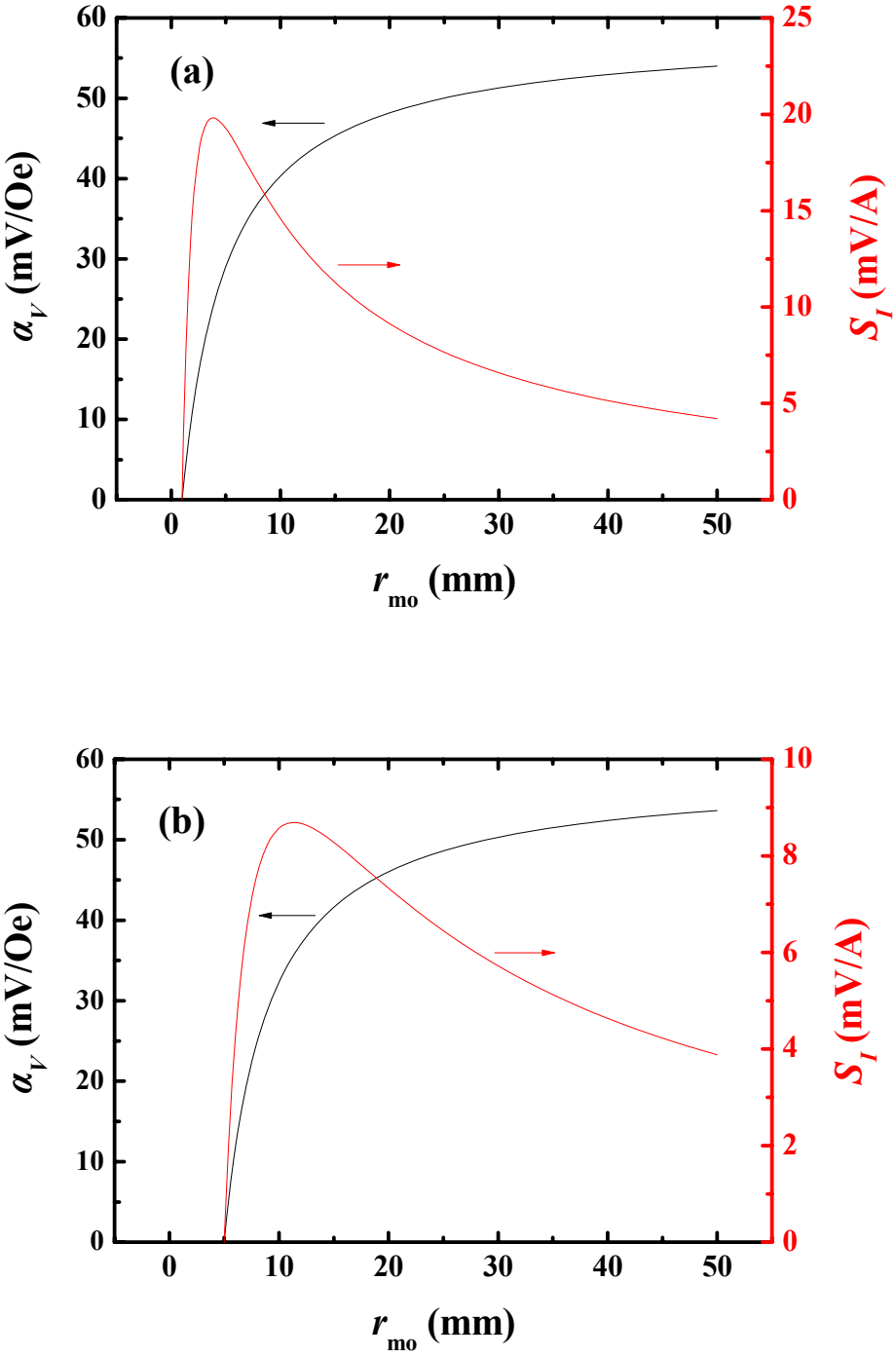

Fig. 3.11 Modeled α_V and S_I versus r_{mo} for two different ring-shaped sensing elements having the same piezoelectric ceramic ring's wall-thickness ($r_{po}-r_{mo}$) of 1 mm but with different central hole radius (r_{mi}) of (a) 1 and (b) 5 mm.

3.3.4 Fabrication

Figure 3.12 illustrates the fabrication process and photograph of the proposed ring-shaped sensing element. In the present study, two different dimensions of sensing elements were fabricated, namely: Ring A and Ring B. For Ring A, a PZT piezoelectric ceramic ring of 4.95 mm inner radius (r_{mo}), 5.95 mm outer radius (r_{po}), and 1 mm thickness (t) was used. For Ring B, a larger PZT ring of 8 mm inner radius (r_{mo}), 9 mm outer radius (r_{po}), and 1 mm thickness (t) was selected. This arrangement gave the same wall-thickness ($r_{po}-r_{mo}$) of 1 mm so that the model predication provided in Fig. 3.11 was applicable to describe their resulting sensing elements. Both PZT rings had full-fired silver electrodes on the two major inner and outer circumferential surfaces normal to the wall-thickness (or the r-) direction with an electric polarization (P) oriented along the wall-thickness direction. The magnetostrictive composite rings concentric to the piezoelectric ceramic rings were prepared in house. [112]-oriented Terfenol-D short bars with dimensions of 1−1.5 mm length and 0.8 mm wide were prepared by cutting the as-supplied Terfenol-D alloy plates along the highly magnetostrictive [112] crystallographic direction using a wire electrical discharge machining (WEDM) technique described in Chapter 2. Two different dimensions of NdFeB magnet bars were prepared, including the ones with 3.95 mm length (l_{Mag}), 1 mm width (w_{Mag}), and 1 mm thickness (t_{Mag}) for Ring A, and the ones with 3 mm length (l_{Mag}), 2 mm width (w_{Mag}), and 1 mm thickness (t_{Mag}) for Ring B. Both types of NdFeB magnet bars had the north (N) and south (S) poles normal to their major surfaces of cross-section defined by $l_{Mag} \times t_{Mag}$.

In fabrication, the four NdFeB magnet bars were arranged in the 0º, 90º, 180º, and 270º directions in the piezoelectric ceramic ring (acting as a mold here), and a predetermined quantity of Terfenol-D short bars was placed between the NdFeB magnet bars inside the piezoelectric ceramic ring mold. The dc magnetic field of ~90−150 Oe set up by the NdFeB magnet bars in the circumferential (or the θ-) direction not only caused the Terfenol-D short bars to align with the magnetic flux lines and to produce short-bar chains along the circumferential direction, but also imparted an internal magnetic bias field (H_{Bias}) to increase the magnetostrictive effect of the whole magnetostrictive composite ring. With the NdFeB magnet bars in place and the Terfenol-D short bars aligned, the predegrassed Araldite LY5210/HY2954 epoxy was transferred into the piezoelectric ceramic ring mold and degassed inside the mold again. The mold was then sealed and allowed the epoxy to cure at room temperature before being placed in an oven for postcuring at 80°C for 9 h. After that, a central hole of r_{mi} = 1 and 5 mm radius was opened in the magnetostrictive composite part for Ring A and Ring B, respectively, so as to form the magnetostrictive composite ring and hence the concentric ring structure for cable insertion.

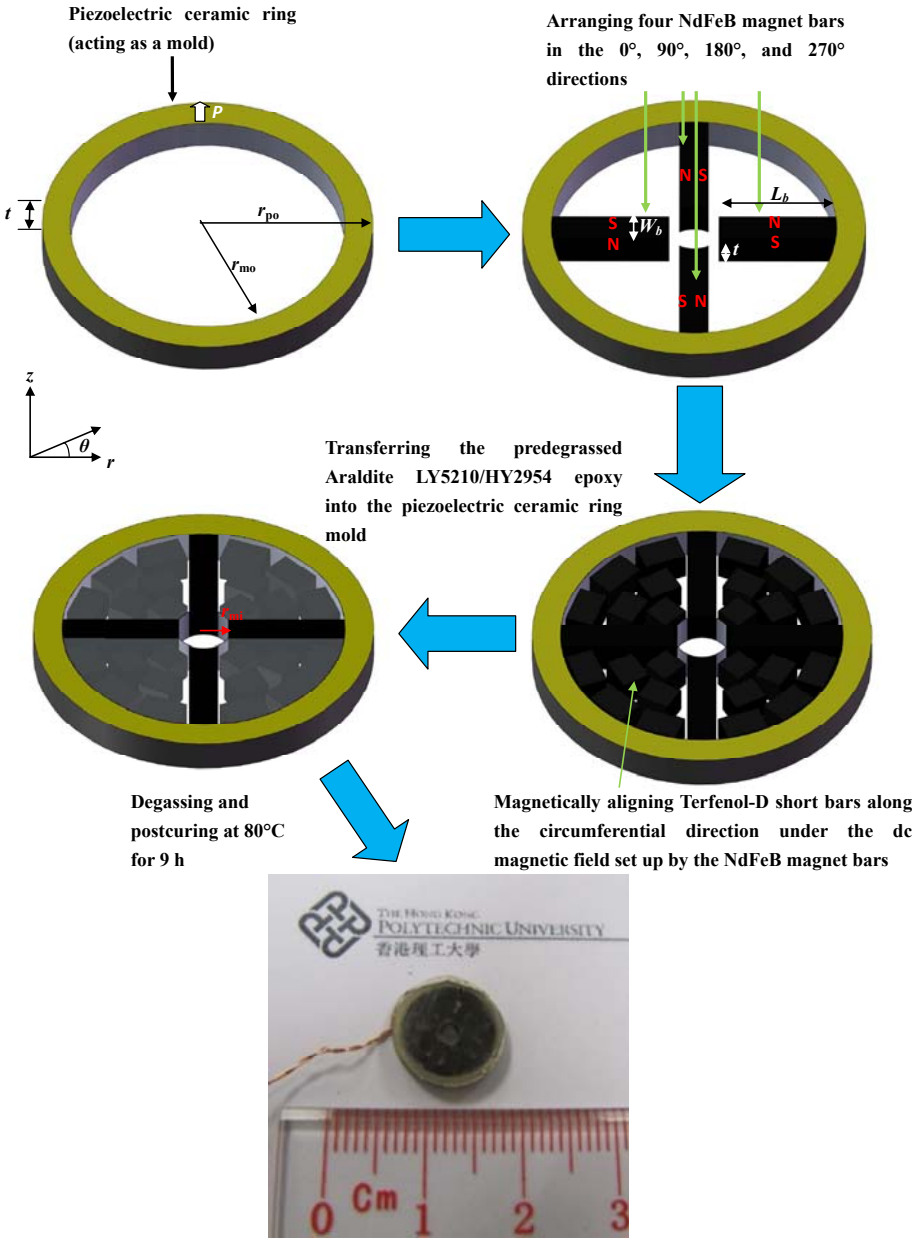

Fig. 3.12 Fabrication process and photograph of the proposed ring-shaped sensing elements.

3.3.5 Characterization

Figure 3.13 illustrates the experimental setup for measuring the quasistatic and dynamic ME properties of the ring-shaped sensing elements. The two ring-shaped sensing elements: Ring A and Ring B were inserted, respectively, in an electrical cable of diameter 1.8 mm for measurement. An arbitrary waveform generator (Agilent 33210A) and a constant-current supply amplifier (AE Techron 7796HF) were used to deliver an ac electric current (I_z) with predetermined amplitudes and frequencies to the electrical cable with a resistor load. A current probe (Hioki 9273) with a current amplifier (Hioki 3271) was employed to monitor I_z. For the quasistatic measurement, I_z was generated in the range of 0.01−3 A peak at 50 Hz, and the ac electric voltage (V_r) output from the sensing elements was acquired by measuring the associated electric charge (Q_r) using a charge meter (Kistler 5015A) according to the relation:

$$V_r = \frac{Q_r}{C}, \tag{3.29}$$

where C is the capacitance of the piezoelectric ceramic ring and was quantified using an impedance analyzer (Agilent 4294A) at 50 Hz. For the dynamic measurement, a constant I_z of 1 A peak was generated in the frequency range of 1−125 kHz, and the current sensitivity (S_I) was determined from

$$S_I = \frac{V_r}{I_z}. \tag{3.30}$$

For both types of measurement, I_z, Q_r, and V_r were recorded by a data acquisition unit (Nation Instruments BNC-2110 and NI-PCI6132) and controlled by a computer with a Labview-based program. It is noted that a reluctance coil with the turn number of 100

was wrapped around the electrical cable as a traditional current sensor for comparison with the dynamic performance of our ring-shaped sensing elements in Fig. 3.16.

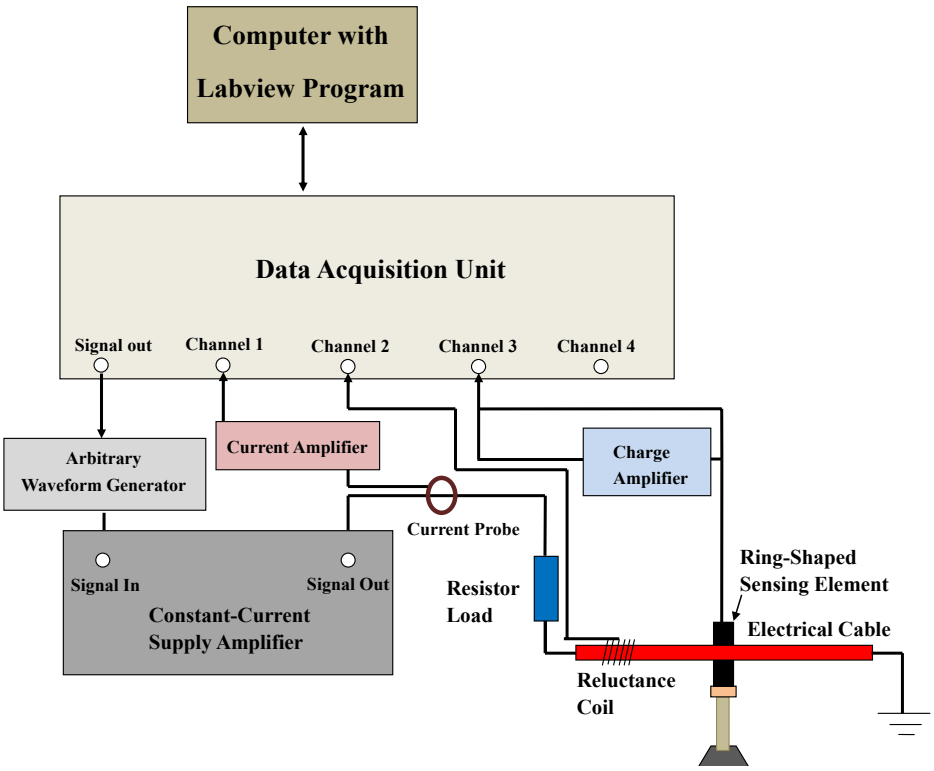

Fig. 3.13 Experimental setup for measuring the quasistatic and dynamic ME properties of the ring-shaped sensing elements.

3.3.6 Results and Discussion

Figure 3.14 plots the measured ac voltage (V_r) output from the two ring-shaped sensing elements: Ring A and Ring B over an applied ac current (I_z) of 0.01–3 A at 50 Hz. The values of the I_z-induced average ac vortex magnetic field ($H_{\theta,\text{avg}}$) are calculated based on Eq. (3.17). It is found that V_r varies essentially linearly with both I_z and $H_{\theta,\text{avg}}$ even at a very small I_z of 0.01 A. The good linearity between V_r and I_z as well as V_r and $H_{\theta,\text{avg}}$ confirms the operation of our sensing elements which is essentially based on the direct coupling of vortex magnetic fields associated with the current-carrying cable governed by Ampère's law with the extrinsic ME effect in the concentric magnetostrictive−piezoelectric ring structure. From the slopes of the plots, the current sensitivity (S_I) of Ring A is determined to be 14.7 mV/A, while the ME voltage coefficient (α_V) of its concentric ring structure is found to be 21.85 mV/Oe. For Ring B, slightly reduced S_I and α_V are obtained to be 5.8 mV/A and 18.8 mV/Oe, respectively. Both S_I and α_V of Ring A are higher than those of Ring B because $H_{\theta,\text{avg}}$ as detected by Ring A is larger than the Ring B [Eq. (3.17) and Fig. 3.11].

Figure 3.15 shows the waveforms of the measured V_r due to an applied I_z of 1 A peak and its associated $H_{\theta,\text{avg}}$ at 50 Hz for Ring A and Ring B. For both rings, V_r has an 180° phase reveal compared to I_z and $H_{\theta,\text{avg}}$. This is because the piezoelectric coefficient ($g_{31,\text{p}}$) carries a negative sign in Eqs. (3.27) and (3.28). Nevertheless, the strong and low-noise signals demonstrate the ability of stable signal conversion from I_z and hence $H_{\theta,\text{avg}}$ to V_r in the rings. It also proves that our sensing elements are good for further developing into clamp-type ME passive current sensors in Chapter 4.

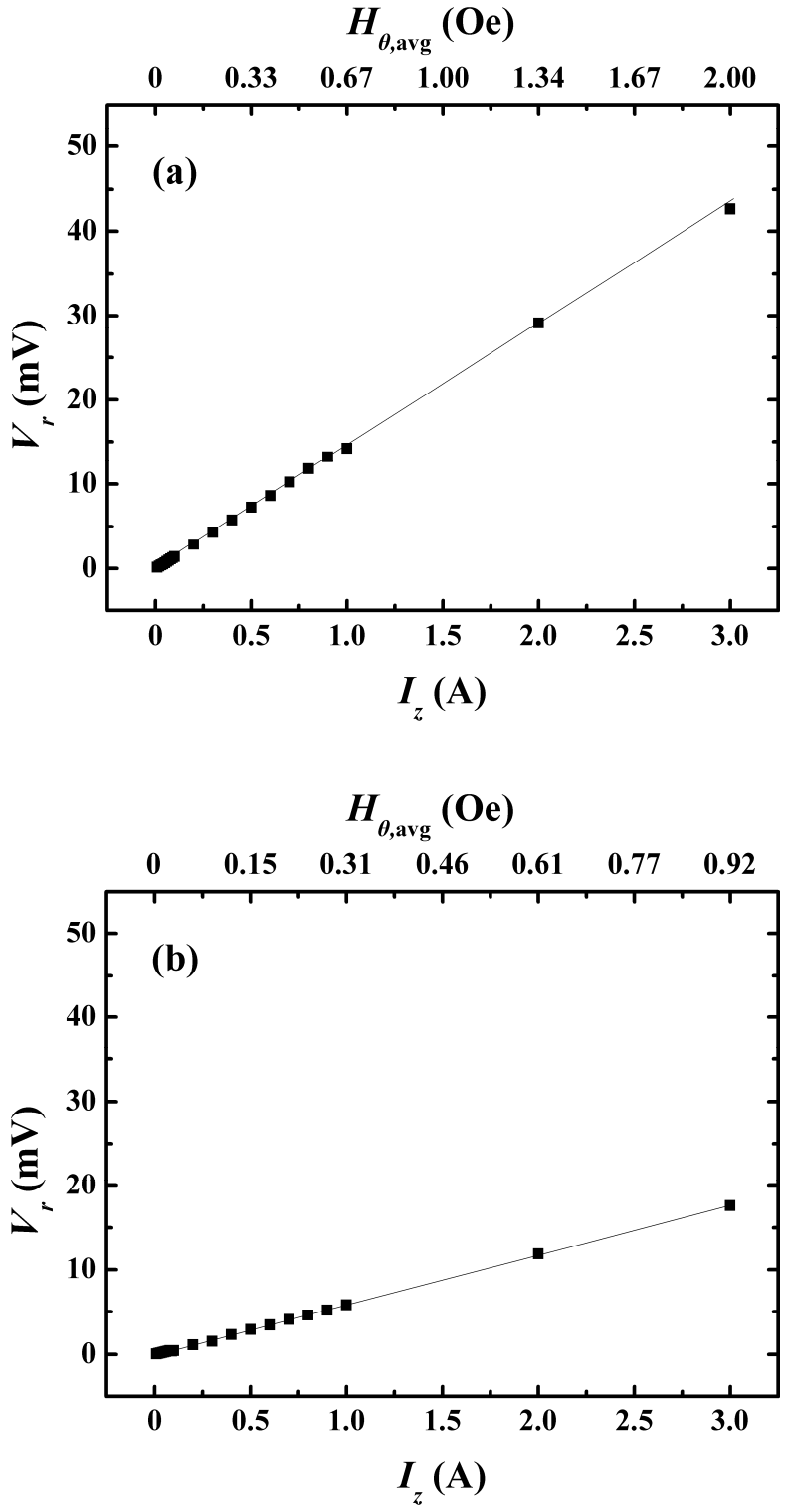

Fig. 3.14 Measured V_r as a function of I_z at 50 Hz for (a) Ring A and (b) Ring B. The I_z-induced $H_{\theta,avg}$ values are also calculated based on Eq. (3.17).

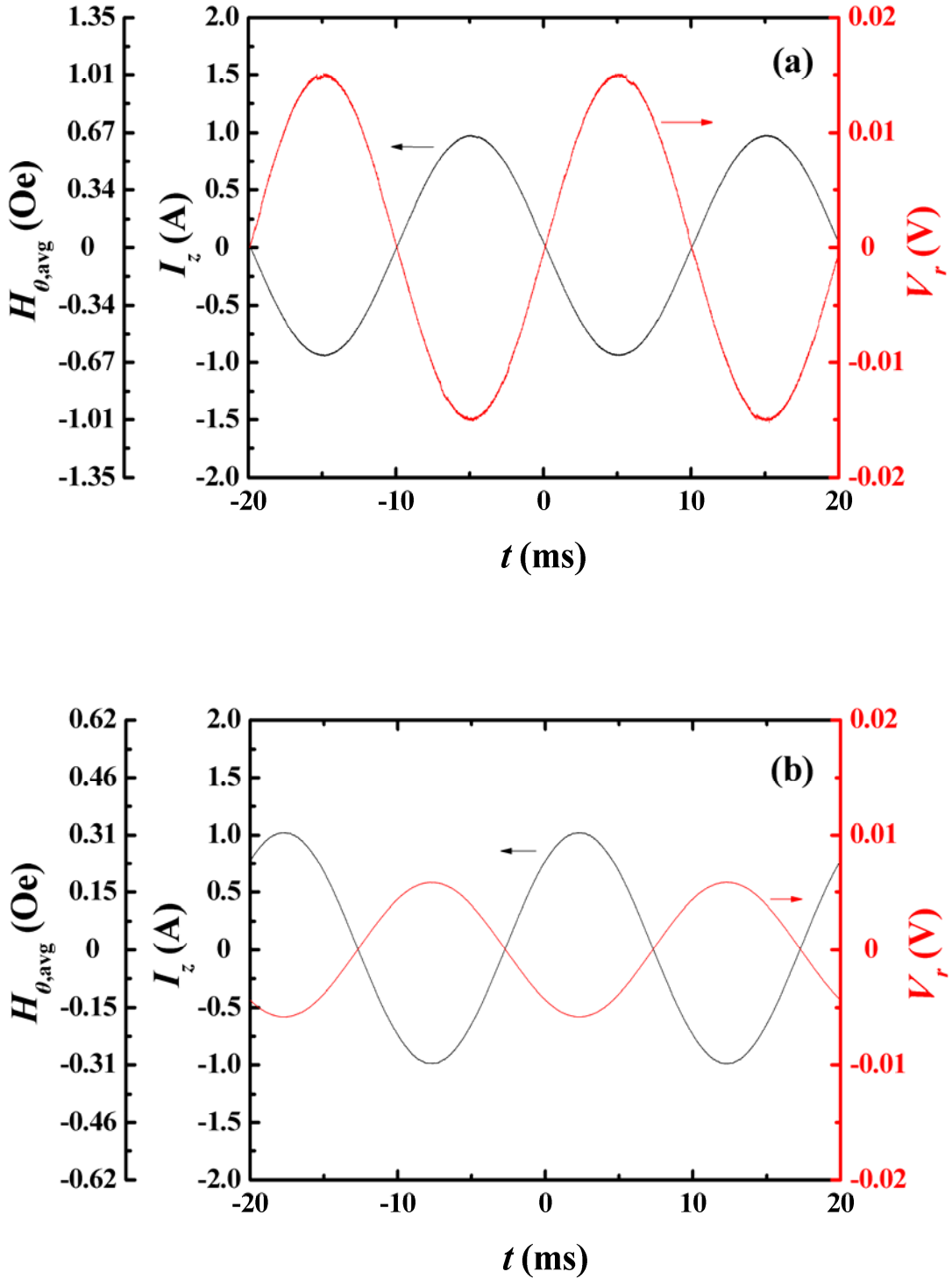

Fig. 3.15 Waveforms of V_r due to an applied I_z of 1 A peak and its associated $H_{\theta,avg}$ at 50 Hz for (a) Ring A and (b) Ring B.

Figure 3.16 shows S_I of Ring A and Ring B in the frequency (f) range of 50 Hz–125 kHz with a constant electric current (I_z) of 1 A peak applied to the electrical cable. For comparison, a reluctance coil with the turn number of 100 was wrapped around the electrical cable to detect I_z. It is obvious that S_I of Ring A has a high and flat response to f, which is ~15–17 mV/A, in the range of 50 Hz–50 kHz. A fundamental shape resonance, corresponding to the radial resonance mode of the sensing element, is observed at 96 kHz with a significantly high S_I of 185 mV/A. Nevertheless, this suggests that our sensing element has an essentially flat and usable detection bandwidth up to and beyond 50 kHz. S_I of Ring B has a reasonably high and flat response to f, which is ~5–6 mV/A, in the range of 50 Hz–25 kHz. The fundamental shape resonance is detected at a lower frequency of 63 kHz with a reasonably high S_I of 72 mV/A. For the reluctance coil, its S_I is strongly dependent on f with a typical inductive effect. For f below 50 Hz, the environmental noise level is larger than the voltage induced by the reluctance coil so that its S value decreases dramatically to ~7 μV/A.

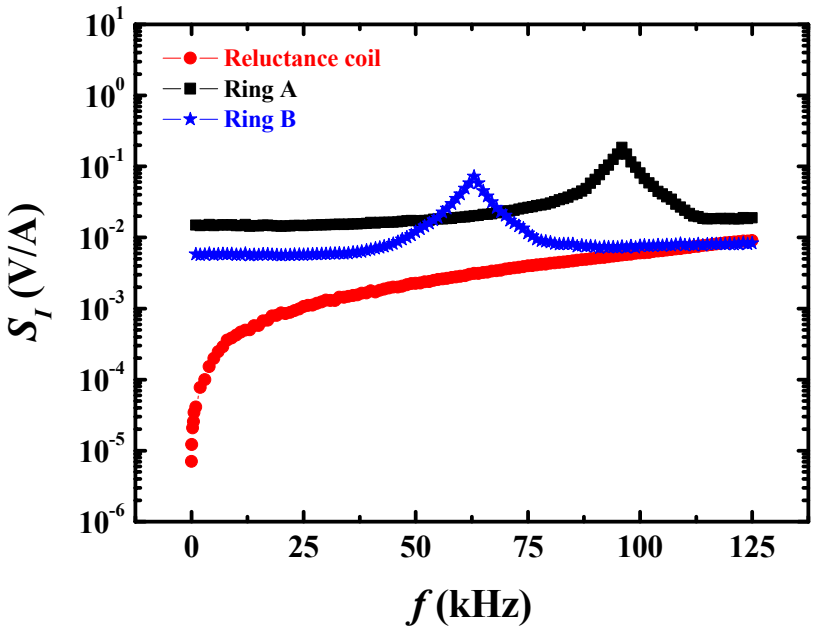

Fig. 3.16 Measured S_I as a function of f for Ring A and Ring B. The performance of a reluctance coil with the turn number of 100 and wrapped around the electrical cable as shown in Fig. 3.13 is included for comparison.

3.4 Bar-Shaped Sensing Elements

3.4.1 Structure and Working Principle

Figure 3.17 shows the schematic diagrams of two different types of bar-shaped sensing elements having a Rosen-type [Fig. 3.17(a)] and a long-type [Fig. 3.17(b)] PMN–PT single-crystal transformers with their input part sandwiched between two length-magnetized Terfenol-D alloy plates. These bar-shaped sensing elements give two interesting and independent operating modes, including the first ME sensing mode in the non-resonance region and the second ME transduction mode associated with the enhanced first and second shape (length) resonances by the PMN−PT single-crystal transformer.

In the ME sensing mode, the magnetostrictive effect in the Terfenol-D alloy plates is mediated mechanically with the piezoelectric effect in the input part of the PMN–PT single-crystal transformer. The configuration of the ME sensing mode in the bar-shaped sensing elements with a Rosen-type PMN−PT single-crystal transformer is an analogy to the combination of a length-magnetized, thickness-polarized plate-shaped sensing element (or a $L-T$ ME laminated composite) reported in Section 3.2 and a length-polarized piezoelectric plate. For the configuration with a long-type PMN−PT single-crystal transformer, it is an analogy to the combination of a length-magnetized, length-polarized ($L-L$) ME laminated composite shown in Fig. 1.8(c) and a length-polarized piezoelectric bar.

In the ME transduction mode, the working principles of the bar-shaped sensing elements with a Rosen-type and a long-type PMN−PT single-crystal

transformer are very similar. The resonance magnetostrictive effect in the Terfenol-D alloy plates is mediated mechanically with the resonance piezoelectric effect in the PMN–PT single-crystal transformer. In more details, an ac magnetic field (H_3) applied along the length (or the 3-) direction of the Terfenol-D alloy plates leads to longitudinal vibrations of the Terfenol-D alloy plates. These longitudinal vibrations, in turn, couple mechanically to the input part of the PMN–PT single-crystal transformer, causing it to produce a piezoelectric voltage ($V_{ME,S}$) at the ME sensing mode electrode with respect to the ground. In the meantime, this longitudinal vibrations are transferred to the output part of the PMN−PT single-crystal transformer and, under resonance conditions, gain an effective amplification, resulting in an amplified piezoelectric voltage ($V_{ME,T}$) at the ME transduction mode electrode with respect to the ground.

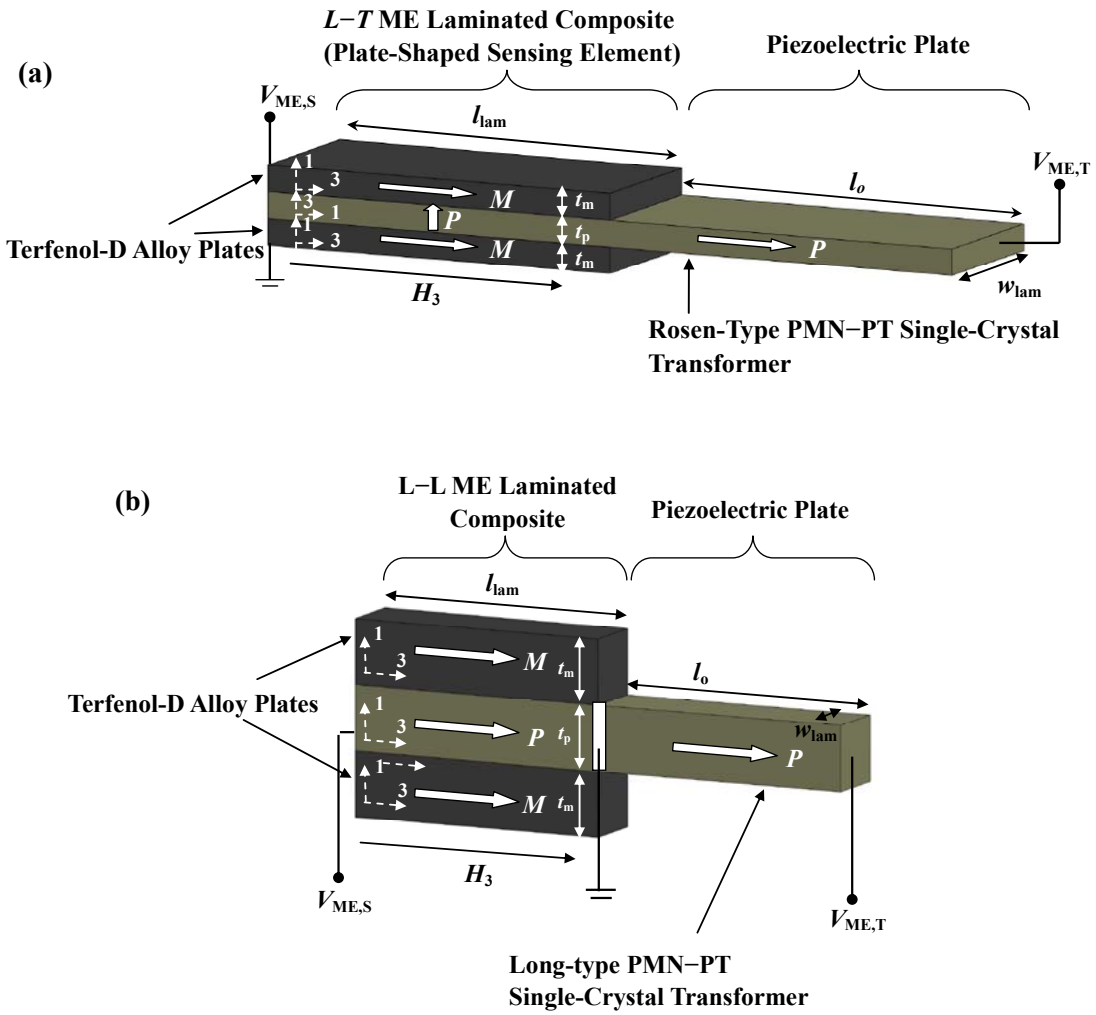

Fig. 3.17 Schematic diagrams of two different types of bar-shaped sensing elements with (a) a Rosen-type and (b) a long-type PMN−PT single-crystal transformer with its input part sandwiched between two length-magnetized Terfenol-D alloy plates. The arrows *M* and *P* denote the magnetization and polarization directions, respectively.

3.4.2 Physical Modeling

The ME effect in bar-shaped sensing elements operating in the ME sensing mode and the ME transduction mode can be described by an electrical equivalent circuit approach. In fact, the sensing elements with a Rosen-type piezoelectric transformer in Fig. 3.17(a) can be considered as a length-magnetized, thickness-polarized plate-shaped sensing element (i.e., a $L-T$ ME laminated composite) as in Fig. 3.1 combined with a length-polarized piezoelectric plate in the length direction. For the sensing elements with a long-type piezoelectric transformer, they can be treated as a length-magnetized, length-polarized ($L-L$) ME laminated composite as in Fig. 1.8(c) combined with a length-polarized piezoelectric plate in the length direction [Fig. 3.18(b)]. Thus, by deriving the electrical equivalent circuits of the $L-T$ ME laminated composite, the $L-L$ ME laminated composite, and the length-polarized piezoelectric plate, it is able to cascade the appropriate electrical equivalent circuits, and to form the electrical equivalent circuit for the bar-shaped sensing elements with a Rosen-type piezoelectric transformer and with a long-type piezoelectric transformer.

3.4.2.1 The Generic Electrical Equivalent Circuit

The electrical equivalent circuits of the $L-T$ ME laminated composite, $L-L$ ME laminated composite, and length-polarized piezoelectric plate have been derived in Appendix A. By cascading these electrical equivalent circuits, the generic electrical equivalent circuit of the bar-shaped sensing elements with a Rosen-type or a bar-type piezoelectric transformer can be constructed as shown in Fig. 3.18. The first and

second sections of Fig. 3.18 correspond to the ME laminated composite ($L-T$ or $L-T$) and the piezoelectric plate, respectively. X is the mechanical resistance of the ME laminated composite. $Z_1^{'}$, $Z_2^{'}$, and Z_1 , Z_2 are the mechanical characteristic impedances of the ME laminated composite and the piezoelectric plate, respectively; $C_0^{'}$ and C_0 are the clamped capacitances of the ME laminated composite and the piezoelectric plate, respectively; φ_{m} and φ_{p} are the magnetomechanical and electromechanical transformation factors of the ME laminated composite, respectively. N is the mechanoelectrical transformation factor of the piezoelectric plate; H_3 is the applied magnetic field; $V_{\mathrm{ME,S}}$ and $V_{\mathrm{ME,T}}$ are the induced voltages of the ME laminated composite and the piezoelectric plate, respectively; and $I_3^{'}$ and I_3 are the coupling currents of the ME laminated composite and the piezoelectric plate, respectively.

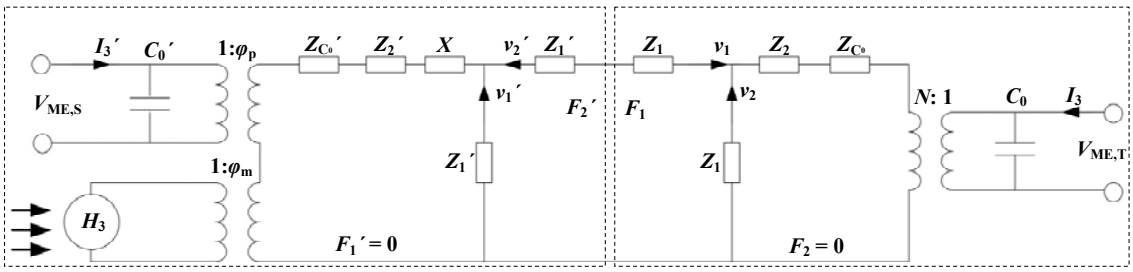

Fig. 3.18 Generic electrical equivalent circuit of the bar-shaped sensing elements with a Rosen-type or a long-type piezoelectric transformer.

According to the Fig. 3.18 and Appendix A, the solutions to the equations of motion of the bar-shaped sensing elements with a Rosen-type or a long-type piezoelectric transformer are given as

$$(Z_1^{'} + Z_2^{'} + Z_{C_0}^{'} + X)v_1^{'} + Z_2^{'}v_2^{'} + \varphi_{\mathrm{p}}V_{\mathrm{ME,S}} + \varphi_{\mathrm{m}}H_3 = 0\,, \tag{3.31}$$

$$Z_2 v_1 + (Z_1 + Z_2)v_2 + NV_{\mathrm{ME,T}} = 0\,, \tag{3.32}$$

$$(Z_2^{'} + Z_{C0}^{'} + X)v_1^{'} + (Z_1^{'} + Z_2^{'} + Z_{C0}^{'} + X)v_2^{'} + \varphi_p V_3^{'} + \varphi_m H_3 = (Z_1 + Z_2)v_1 + Z_2 v_2 + NV_3\,, \tag{3.33}$$

$$-v_2^{'} = v_1\,, \tag{3.34}$$

$$I_3^{'} = j\omega_0 C_0^{'} V_{\mathrm{ME,S}} - v_1^{'}\varphi_{\mathrm{p}} - v_2^{'}\varphi_{\mathrm{p}}\,, \tag{3.35}$$

$$I_3 = -N(v_1 + v_2) + j\omega C_0 V_{\mathrm{ME,A}}\,, \tag{3.36}$$

where v'_1, v'_2 and v_1, v_2 are the velocities at the two end surfaces of the ME laminated composite ($L-T$ or $L-L$) and the piezoelectric plate, respectively.

3.4.2.2 ME Sensing Mode

For the modeling of the ME sensing mode of the bar-shaped sensing elements with a Rosen-type or a long-type piezoelectric transformer, the electrical output port of the ME laminated composite ($L-T$ or $L-L$) is used as the signal output port ($V_{\mathrm{ME,S}}$), while that of the piezoelectric plate is assumed to be open circuit. The boundary conditions of $I_3^{'}$ and I_3 under the ME sensing mode can be written as

$$I_3^{'} = \frac{V_{\mathrm{ME,S}}}{R_{\mathrm{L}}}, \tag{3.37}$$

$$I_3 = 0. \tag{3.38}$$

where R_{L} is the electrical load of the sensing elements under measurement.

By solving Eqs. (3.31)−(3.28), the magnetoelectric voltage coefficient of of the bar-shaped sensing element operating in the ME sensing mode ($\alpha_{V,\mathrm{S}}$) can be expressed as

$$\alpha_{V,\mathrm{S}} = \frac{V_{\mathrm{ME,S}}}{H_3} = \frac{A}{N^2(B+C)}, \tag{3.39}$$

where

$A = -(\varphi_{\mathrm{m}}\varphi_{\mathrm{p}}R_L(2N^2(Z_1+Z_1^{'}) + j\omega C_0(2Z_2(Z_1+Z_1^{'}+Z_1(Z_1+2Z_1^{'}))))$;
$B = 2\varphi_{\mathrm{p}}^2R_{\mathrm{L}}(Z_1+Z_1^{'}) + W(2Z_1(Z_1^{'}+Z_2^{''}) + Z_1^{'}(Z_1^{'}+2Z_2^{''}))$;
$C = j\omega C_0(\varphi_{\mathrm{p}}^2R_{\mathrm{L}}(2Z_2(Z_1+Z_1^{'}) + Z_1(Z_1+2Z_1^{'})) + M)$;
$M = W(Z_1(Z_1(Z_1^{'}+Z_2^{''}) + Z_1^{'}(Z_1^{'}+2Z_2^{''})) + Z_2(2Z_1(Z_1^{'}+Z_2^{''}) + Z_1^{'}(Z_1^{'}+2Z_2^{''}))$;
$W = -1 + j\omega C_0^{'}R_{\mathrm{L}}$;
$Z_2^{''} = Z_2^{'} + Z_{C0}^{'} + X$.

3.4.2.3 ME Transduction Mode

To model the ME transduction mode of the bar-shaped sensing elements with a Rosen-type or a long-type piezoelectric transformer, the electrical output port of the ME laminated composite is assumed to be open circuit, while that of the piezoelectric plate is used as the signal output port ($V_{\mathrm{ME,T}}$). The boundary conditions of $I_3^{'}$ and I_3 under the ME transduction mode can be written as:

$$I_3^{'} = \frac{V_{\mathrm{ME,T}}}{R_{\mathrm{L}}}, \tag{3.40}$$

$$I_3 = 0. \tag{3.41}$$

By solving Eqs. (3.31)−(3.41) the magnetoelectric voltage coefficient of the bar-shaped sensing elements operating in the ME transduction mode ($\alpha_{V,\mathrm{T}}$) can be expressed as

$$\alpha_{V,\mathrm{T}} = \frac{V_{\mathrm{ME,T}}}{H_3} = \frac{A}{N^2(B+C)}, \tag{3.42}$$

where

$A = j\omega C_0^{'} N \varphi_{\mathrm{m}} R_L Z_1 Z_1^{'}$;
$B = R_{\mathrm{L}}(2\varphi_p^2(Z_1 + Z_1^{'}) + j\omega C_0^{'}(2Z_1(Z_1^{'} + Z_2^{'}) + Z_1^{'}(Z_1^{'} + 2Z_2^{''})))$;
$C = R_{\mathrm{L}}((-1 + j\omega C_0^{'} R_L)(\varphi_p^2(2Z_2(Z_1 + Z_1^{'}) + Z_1(Z_1 + 2Z_1^{'})) + M)$;
$M = j\omega C_0^{'}(Z_1(Z_1(Z_1^{'} + Z_2^{''}) + Z_1^{'}(Z_1^{'} + 2Z_2^{''}) + Z_2(2Z_1(Z_1^{'} + Z_2^{''}) + Z_1^{'}(Z_1^{'} + 2Z_2^{''})))$;
$Z_2^{''} = Z_2^{'} + Z_{C0}^{'} + X$.

3.4.3 Practical Implication

Table 3.3 shows the effective material parameters of the magnetostrictive and piezoelectric phases which can lead to an enhanced α_V. The symbols ↑ and ↓ indicate, respectively, the need of increasing and decreasing a specific parameter in order to increase the values of α_V. In the ME sensing mode, the magnetostrictive plates act as a magnetomechnical actuator so that a large $d_{33,\mathrm{m}}$ and a small s_{33}^{H} are preferred. Moreover, the input part of the piezoelectric transformer functions as a mechanoelectric sensor, while the output part becomes a load. Accordingly, a high $|g_{31,\mathrm{p}}|$ and a small s_{11}^{E} are desirable for the one with a Rosen-type piezoelectric transformer, while a high $d_{33,\mathrm{p}}$ and a small s_{33}^{E} are favorable for the one with a long-type piezoelectric transformer. In the ME transduction mode, the magnetostrictive plates still act as a magnetomechincal actuator as in the ME sensing mode. However, the piezoelectric transformer plays the role of a mechanoelectric transducer.

Table 3.3 Influence of material parameters on $\alpha_{V,\mathrm{S}}$ and $\alpha_{V,\mathrm{T}}$ in the bar-shaped sensing elements.

Symbol / Material Phase	$d_{33,\mathrm{m}}$ or $d_{33,\mathrm{p}}$	s_{33}^{H} or s_{33}^{E}	s_{11}^{E}	$\lvert g_{31,\mathrm{p}}\rvert$
Magnetostrictive	↑	↓		
Piezoelectric	↑	↓	↓	↑

Figures 3.19 and 3.20 show the modeled $\alpha_{V,S}$ and $\alpha_{V,T}$ as a function of f at various H_{Bias} for the two different bar-shaped sensing elements with a Rosen-type (Fig. 3.19) and a long-type PMN−PT single-crystal transformers (Fig. 3.20) working in the ME sensing mode and the ME transduction mode. The sensing element with a Rosen-type transformer is assumed to have dimensions of 13 mm (length) × 6 mm (width) × 1 mm (thickness) for the Terfenol-D alloy plates and of 26 mm (length) × 6 mm (width) × 1 mm (thickness) for the PMN−PT single-crystal transformer. The sensing element with a long-type transformer is taken to have smaller dimensions of 6 mm (length) × 2 mm (width) × 2 mm (thickness) for the Terfenol-D alloy plates and of 16 mm (length) × 2 mm (width) × 2 mm (thickness) for the PMN−PT single-crystal transformer. The material parameters of the Terfenol-D alloy plates (i.e., $d_{33,m}$ and s_{33}^{H}) and the PMN−PT single-crystal transformers (i.e., $d_{33,p}$, s_{33}^{E}, s_{11}^{E}, and $g_{31,p}$) are taken from Figs. 2.18 and 2.20 in Section 2.2.4.2 and Table 2.4 in Section 2.3.1.2 of Chapter 2, respectively.

For both types of sensing elements, it is observed that both $\alpha_{V,S}$ and $\alpha_{V,T}$ increase initially with increasing H_{Bias}, reach their maximum values at an optimal H_{Bias} of 0.4 kOe, and then decrease with increasing H_{Bias}. At the non-resonance region (e.g., up to 40 kHz), $\alpha_{V,S}$ is significantly larger than $\alpha_{V,T}$ in both types of sensing elements. For the sensing element with a Rosen-type transformer operating at resonance (Fig. 3.19), the two resonances detected for $\alpha_{V,S}$ at ~53 and 91 kHz and those seen in $\alpha_{V,T}$ at ~39 and 81 kHz are the half-wave and full-wave length resonance modes, respectively. For the sensing element with a long-type transformer in Fig. 3.20, the half-wave and

full-wave length resonance modes are found out at ~68 and 155 kHz, respectively, for $\alpha_{V,S}$ and at ~58 and 120 kHz, respectively, for $\alpha_{V,T}$. It is noted that $\alpha_{V,S}$ of the sensing element with a long-type transformer is larger than that with a Rosen-type transformer, The observation confirms the previous findings for the $L-T$ and $L-L$ laminated composites as pointed out in Chapter 1. However, $\alpha_{V,T}$ of the sensing element with a long-type transformer is smaller than that with a Rosen-type transformer due to the smaller step-up ratio in the long-type transformer compared to the Rosen-type transformer as addressed in Section 2.3.2.2 of Chapter 2.

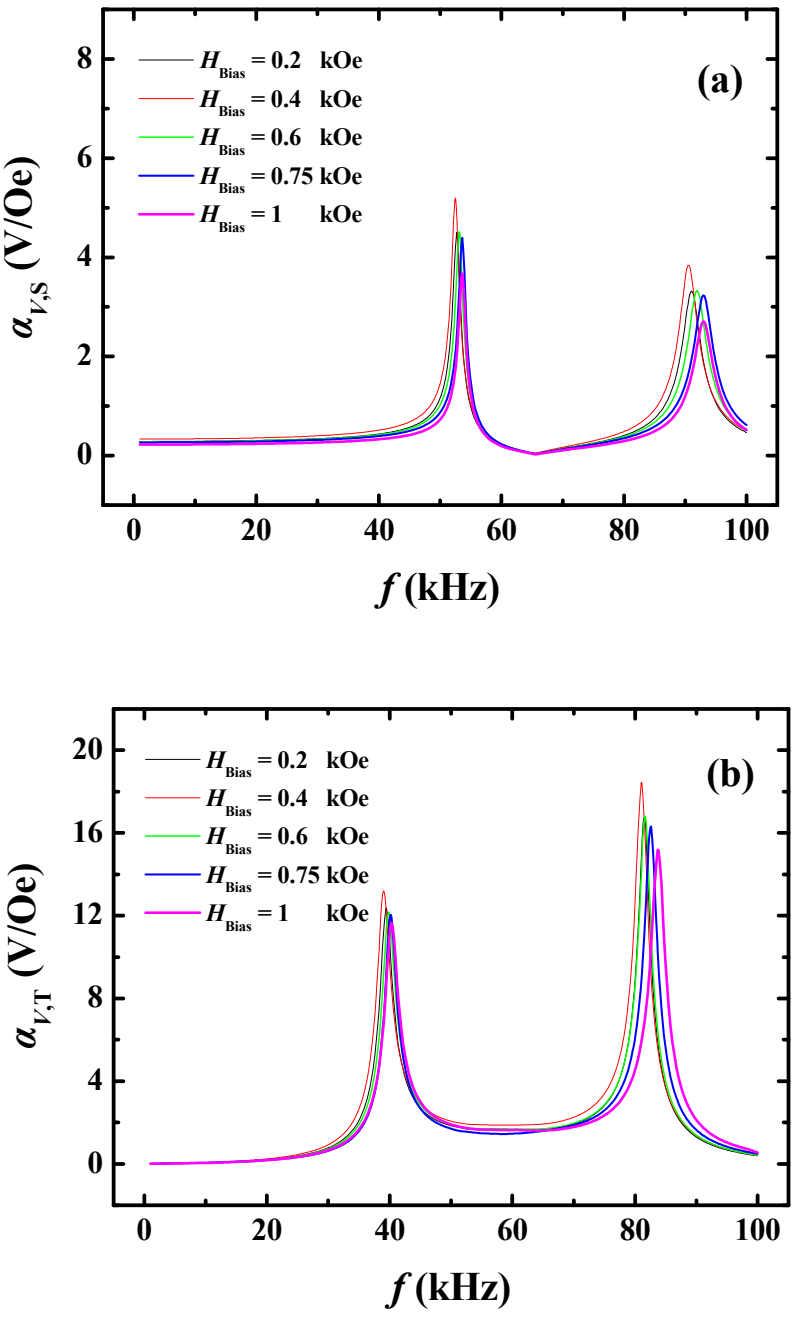

Fig. 3.19 Modeled (a) $\alpha_{V,S}$ and (b) $\alpha_{V,T}$ as a function of f at various H_{Bias} for the bar-shaped sensing element with a Rosen-type PMN−PT single-crystal transformers.

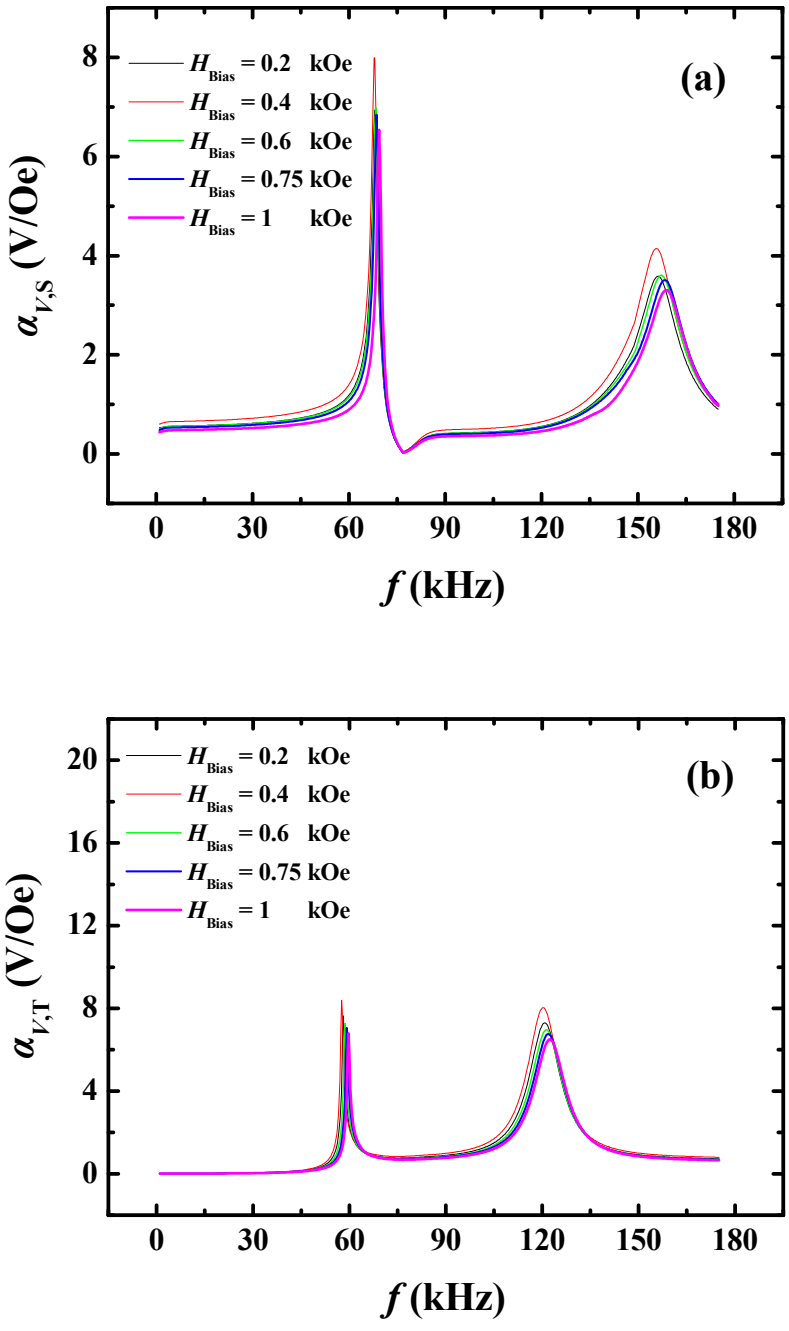

Fig. 3.20 Modeled (a) $\alpha_{V,S}$ and (b) $\alpha_{V,T}$ as a function of f at various H_{Bias} for the bar-shaped sensing element with a long-type PMN−PT single-crystal transformer.

3.4.4 Fabrication

The fabrication processes of the bar-shaped sensing elements with a Rosen-type and a long-type PMN−PT single-crystal transformers are illustrated in Fig. 3.21. Two Terfenol-D alloy plates of dimensions 13 mm (length) × 6mm (width) × 1 mm (thickness) were bonded on the top and bottom surfaces of the input part of a Rosen-type PMN−PT single-crystal transformer of dimensions 26 mm (length) × 6 mm (width) × 1 mm (thickness) to form the first bar-shaped sensing element [Fig. 3.21(a)]. Two Terfenol-D alloy plates of smaller dimensions 6 mm (length) × 2mm (width) × 2 mm (thickness) were bonded similarly on the input part of a long-type PMN−PT single-crystal transformer of smaller dimensions 16 mm (length) × 2 mm (width) × 2 mm (thickness) to form the second bar-shaped sensing element [Fig. 3.21(b)]. The photographs of the fabricated sensing elements are also shown in Fig. 3.21. The Terfenol-D alloy plates had an [112] crystallographic axis oriented along the length direction, while the Rosen-type and long-type PMN−PT single-crystal transformers had an [001] crystallographic axis oriented along the length direction. A silver-load epoxy adhesive (CHEMENCE IONACURE SL65) was used as the bonding agent, and a mass of ~ 10 kg was added on the sensing elements to ensure good surface adhesion at room temperature for 24 h. Three electrical wires were connected to the input, output, and ground of the PMN−PT single-crystal transformers as signal leads.

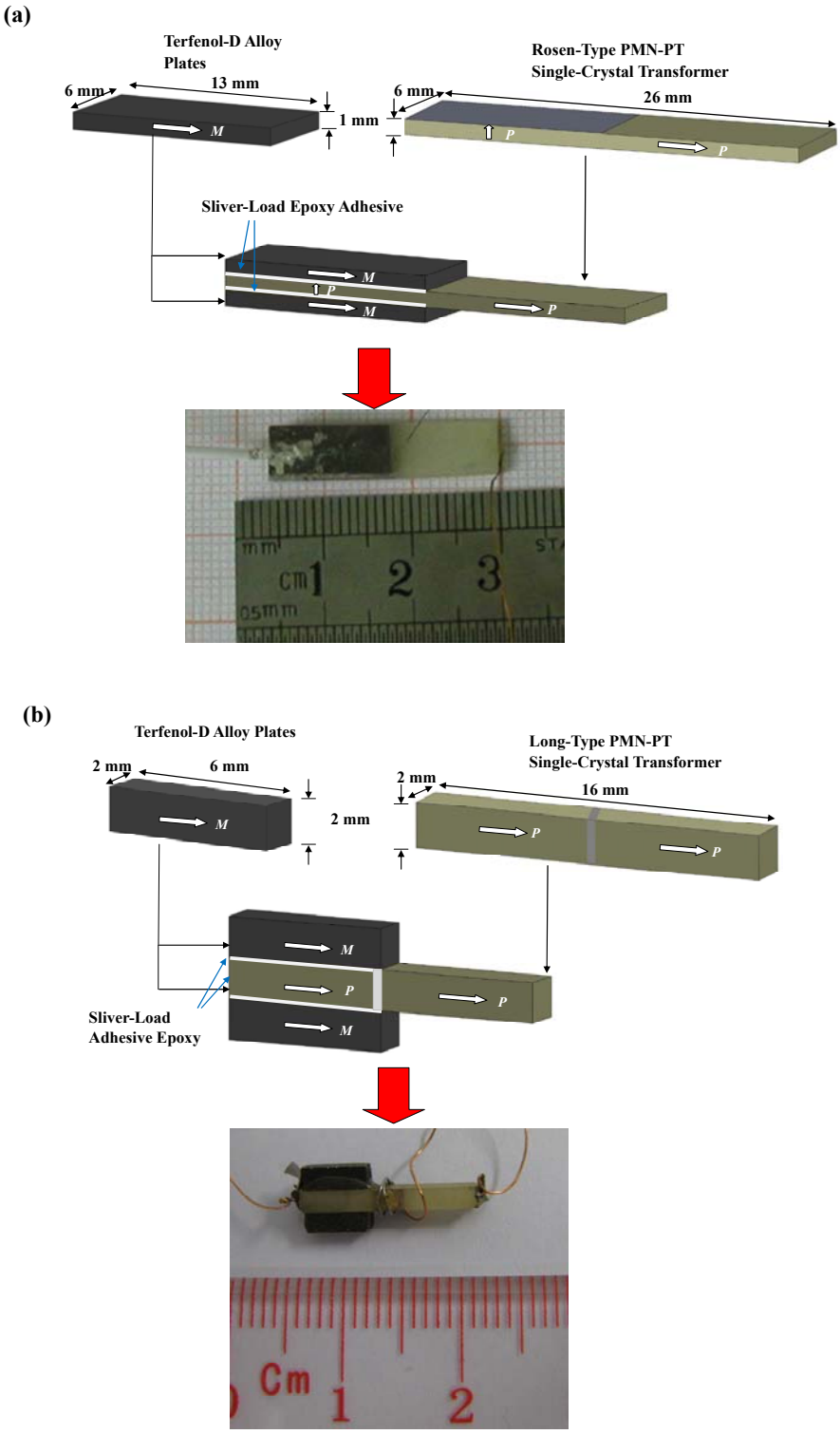

Fig. 3.21 Fabrication processes and photographs of the bar-shaped sensing elements having (a) Rosen-type and (b) long-type PMN−PT single-crystal transformers.

3.4.5 Characterization

The quasistatic and dynamitic ME properties of both types of sensing elements were measured in the length (or the 3-) direction at room temperature by using the in-house automated measurement system as shown in Fig. 3.5. The connections of each equipment in the measurement setup were the same as those used for the plate-shaped sensing elements presented in Section 3.2.5. For the quasistatic ME property measurement, a low-frequency (50 Hz) sinusoidal magnetic drive field (H_3) of 0.1−10 Oe peak, together with a magnetic bias field (H_{Bias}) of 0.02−1 kOe, were used. For the dynamic ME property measurement, a swept sinusoidal H_3 of 1 Oe peak varying from 1−180 kHz was utilized in conjunction with an H_{Bias} of 0.02−1 kOe.

3.4.6 Results and Discussion

Figure 3.22 plots the measured $V_{ME,S}$ as a function of H_3 at 50 Hz under various H_{Bias} for the bar-shaped sensing elements with a Rosen-type [Fig. 3.22(a)] and a long-type [Fig. 3.22(b)] PMN−PT single-crystal transformers. For both designs, $V_{ME,S}$ shows a good linear response to H_3 in the whole measured range for all H_{Bias} levels. The V_3−H_3 response is also found to depend on H_{Bias} with the largest response detected at H_{Bias} = 0.4 kOe. This is because Terfenol-D is an H_{Bias}-dependent material which has been described in the plate-shaped sensing elements in Section 3.2.

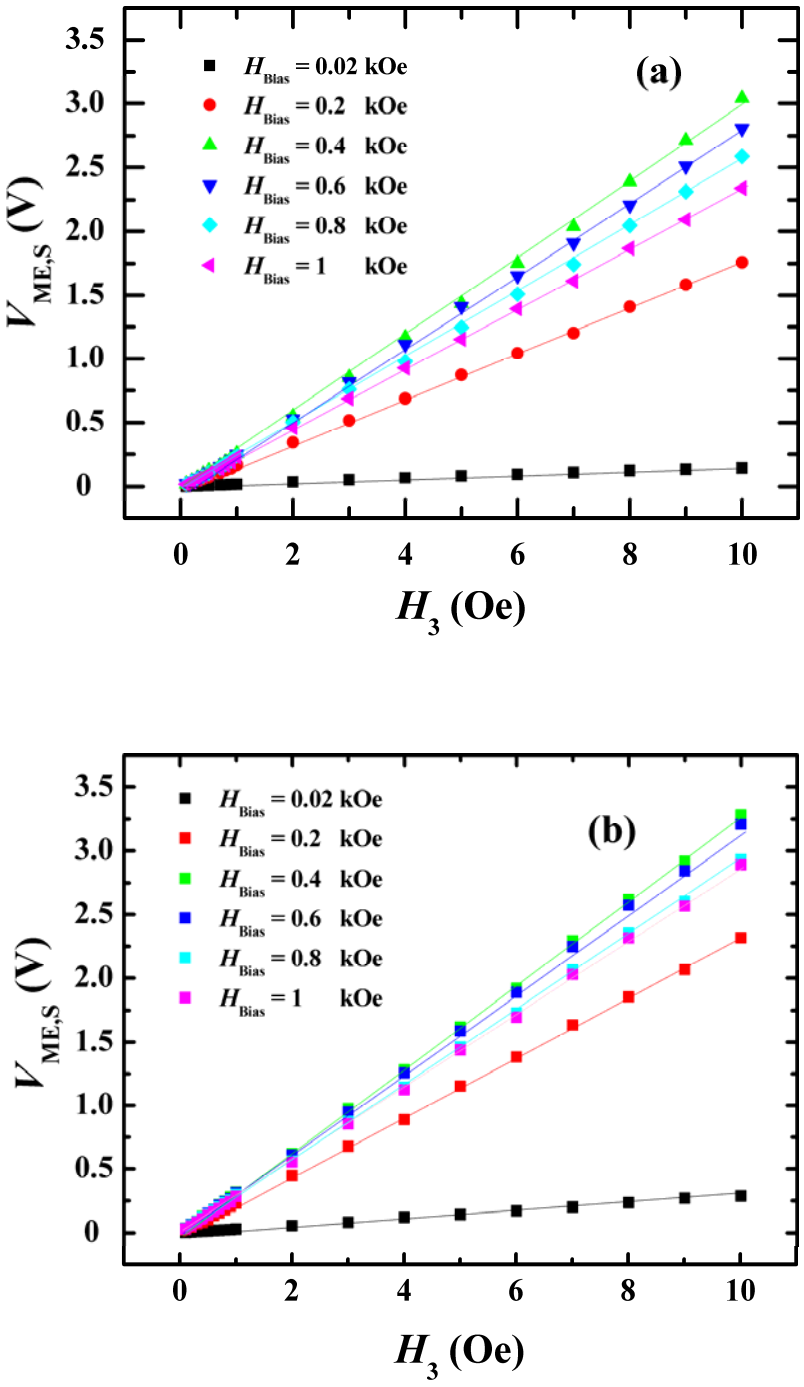

Fig. 3.22 Measured $V_{ME,S}$ as a function of H_3 at 50 Hz under various H_{Bias} for the bar-shaped sensing elements with (a) Rosen-type and (b) long-type PMN−PT single-crystal transformers operating in the ME sensing mode.

Figure 3.23 illustrates the measured $\alpha_{V,S}$ as a function of H_{Bias} at 50 Hz for the bar-shaped sensing elements with a Rosen-type [Fig. 3.23(a)] and a long-type [Fig. 3.23(b)] PMN−PT single-crystal transformers. The values of measured $\alpha_{V,S}$ are obtained from the slopes of the $V_{ME,S}$−H_3 plots in Fig. 3.22. It is seen that $\alpha_{V,S}$ of both sensing elements has a similar quantities trend to the plate-shaped sensing element in Fig. 3.7, and the similarity can be explained by the negative-ΔE effect in the Terfenol-D alloy plates as described in Chapter 2. In more details, $\alpha_{V,S}$ increases initially with increasing H_{Bias}; it reaches the maximum value at an optimal H_{Bias} of 0.4 kOe and then decreases with increasing H_{Bias}. While the sensing element with a long-type transformer is smaller in size, its $\alpha_{V,S}$ (=0.32 V/Oe) is larger than that with a Rosen-type transformer ($\alpha_{V,S}$ = 0.25 V/Oe).

Figures 3.24 shows the measured waveforms of $V_{ME,S}$ due to an applied H_3 of 1 Oe peak at an H_{Bias} of 0.4 kOe at a frequency of 50 Hz for the bar-shaped sensing elements with a Rosen-type [Fig. 3.24(a)] and a long-type [Fig. 3.24(b)] PMN−PT single-crystal transformers. It is noted that $V_{ME,S}$ in Fig. 3.24(a) has an opposite phase with H_3, but that in Fig. 3.24(b) has the same phase with H_3. The reason can be explained by the piezoelectric transverse (or the 31-) mode of operation (e.g., $g_{31,p}$, s_{11}^E, etc.) in the sensing element with a Rosen-type transformer and the piezoelectric length (or the 33-) mode of operation. (e.g., $d_{33,p}$, s_{33}^E, etc.) in the sensing element with a long-type transformer. Nonetheless, the measured $V_{ME,S}$ is very stable and has an amplitude of 0.25 and 0.32 V peak for sensing element with a Rosen-type and a long-type PMN−PT single-crystal transformers, respectively.

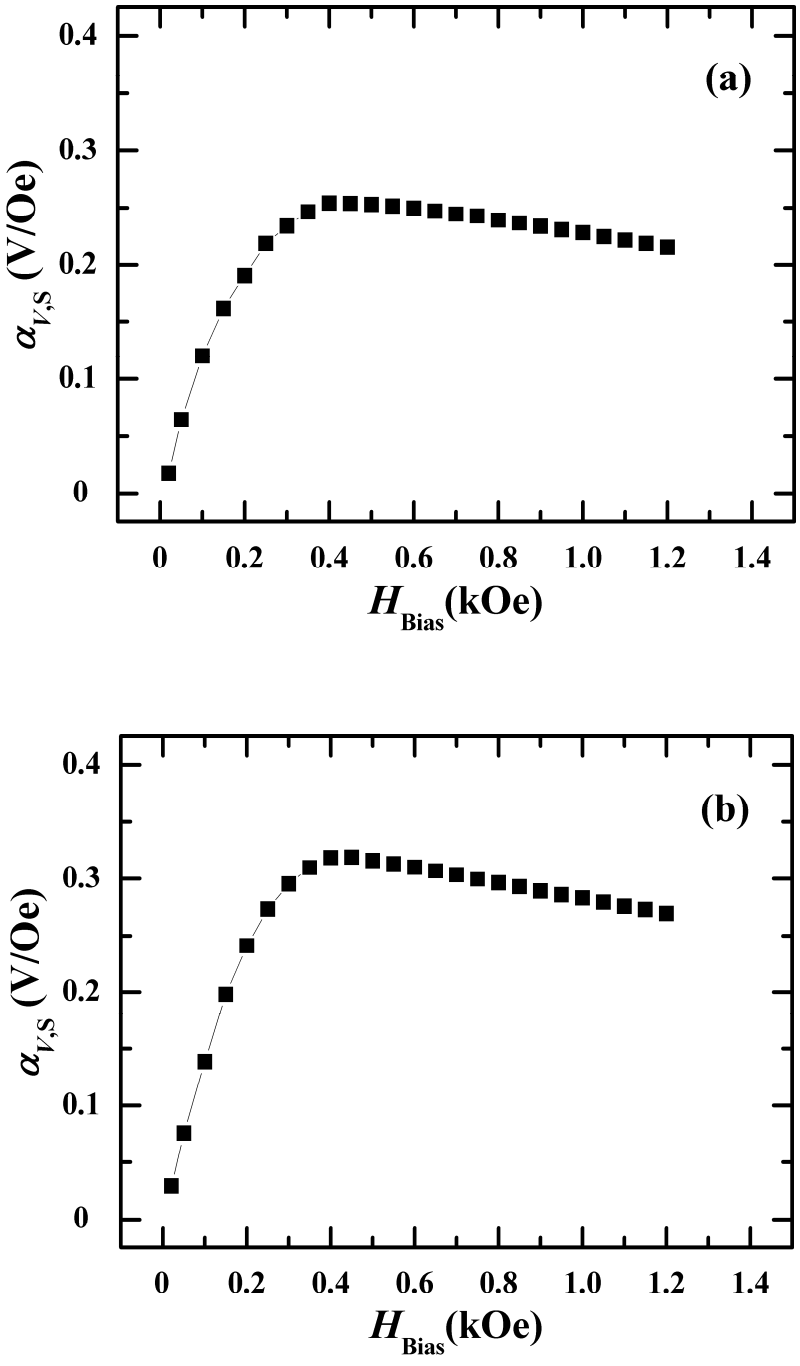

Fig. 3.23 Measured $\alpha_{V,S}$ as a function of H_{Bias} at 50 Hz for the bar-shaped sensing elements with (a) Rosen-type and (b) long-type PMN−PT single-crystal transformers.

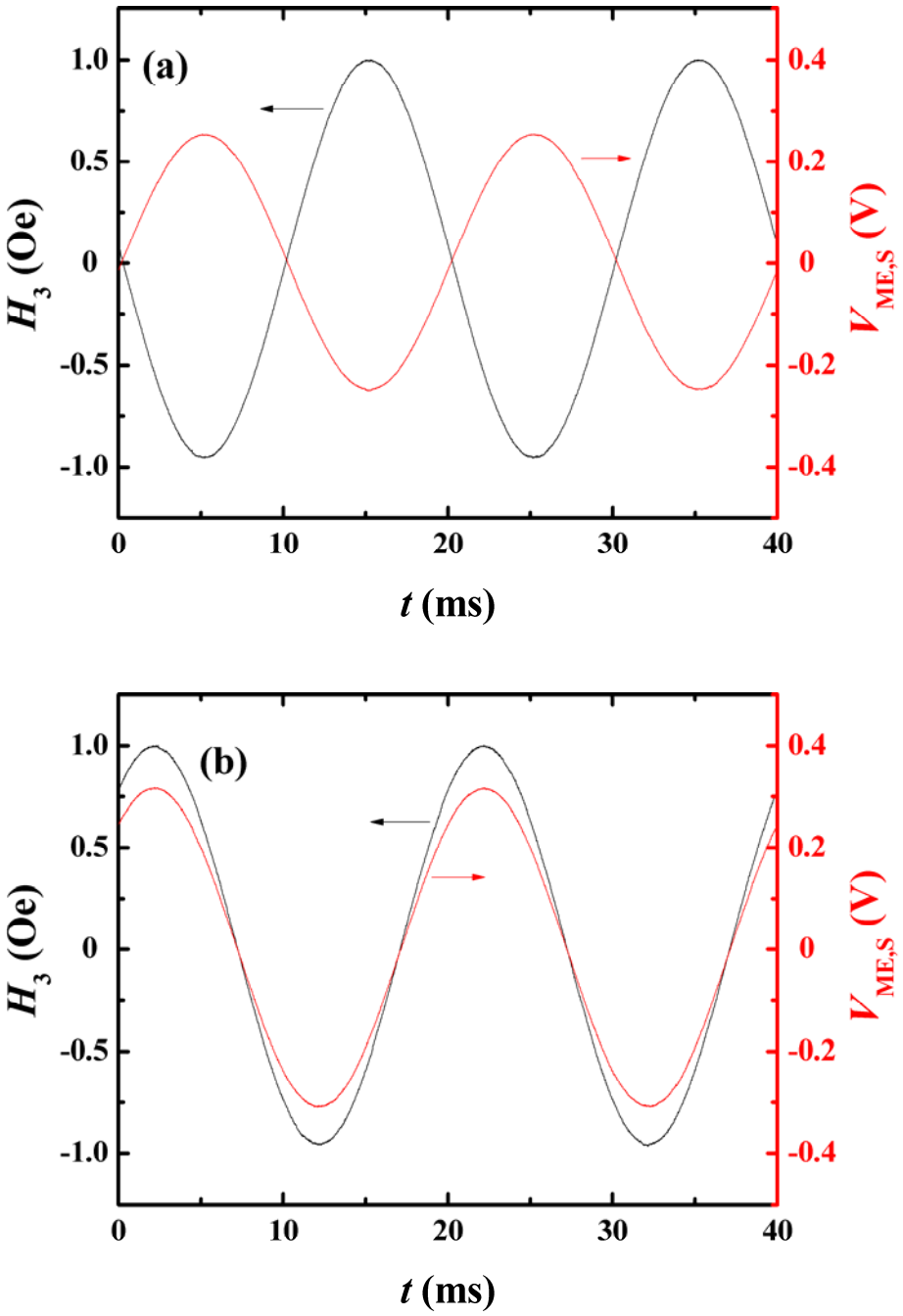

Fig. 3.24 Measured waveforms of $V_{ME,S}$ due to an applied H_3 of 1 Oe peak at an H_{Bias} of 0.4 kOe at 50 Hz for the bar-shaped sensing elements with (a) Rosen-type and (b) long-type PMN−PT single-crystal transformers.

Figures 3.25 and 3.26 plot the measured $\alpha_{V,S}$ and $\alpha_{V,T}$ as a function of f at various H_{Bias} and with an H_3 of 1 Oe peak for the bar-shaped sensing elements with a Rosen-type and a long-type PMN−PT single-crystal transformers, respectively. Both sensing elements show two obvious resonances, corresponding to the half-wave and full-wave resonance modes. In the ME sensing mode, both sensing elements have a reasonably flat response (i.e., the non-resonance region) for frequencies up to ~30 kHz. The largest $\alpha_{V,S}$ is obtained to be ~0.25 and 0.32 V at H_{Bias} = 0.4 kOe in the non-resonance region for the sensing elements with a Rosen-type and a long-type PMN−PT single-crystal transformers, respectively. For the sensing element with a Rosen-type PMN−PT single-crystal transformer (Fig. 3.25), the two resonances in $\alpha_{V,S}$ are detected to be 4.0 and 3.6 V/Oe at 50.5 and 92.2 kHz at H_{Bias} = 0.4 kOe, while the two resonances in $\alpha_{V,T}$ are found to be 13.1 and 15.5 V/Oe at 38.0 and 80.6 kHz at H_{Bias} = 0.4 kOe. For the sensing element with a long-type PMN−PT single-crystal transformer (Fig. 3.26), the two resonances in $\alpha_{V,S}$ are observed to be 5.2 and 3.8 V/Oe at 66.3 and 154.3 kHz at H_{Bias} = 0.4 kOe, while the two resonances in $\alpha_{V,T}$ are found to be 7.6 and 8 V/Oe at 56 and 126 kHz at H_{Bias} = 0.4 kOe. In general, the amplification of $\alpha_{V,T}$ in the sensing element with a Rosen-type PMN−PT transformer is ~2 times larger compared to the sensing element with a long-type PMN−PT transformer because of the different voltage step-up ratios associated with the two transformers as discussed in Section 2.3.2 of Chapter 2.

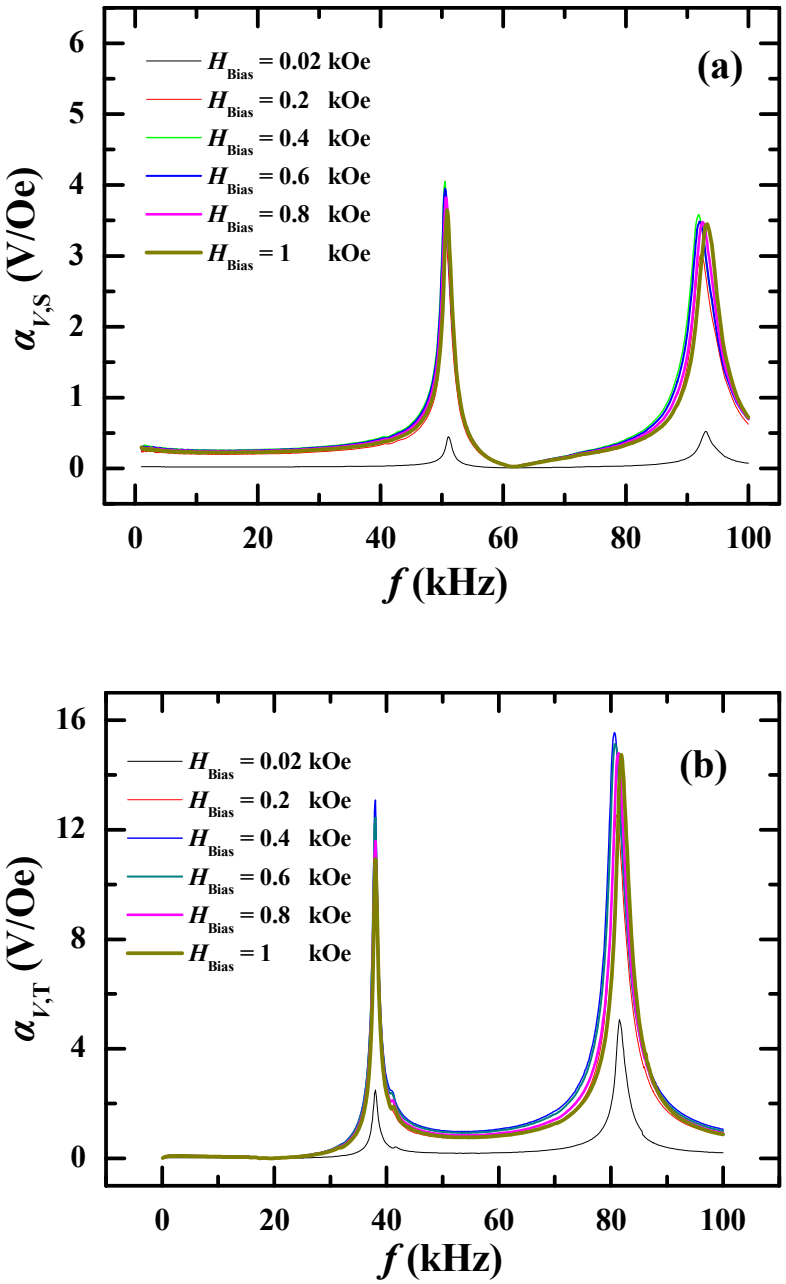

Fig. 3.25 Measured (a) $\alpha_{V,S}$ and (b) $\alpha_{V,T}$ as a function of f at various H_{Bias} and with an H_3 of 1 Oe peak for the bar-shaped sensing elements with Rosen-type PMN−PT single-crystal transformer.

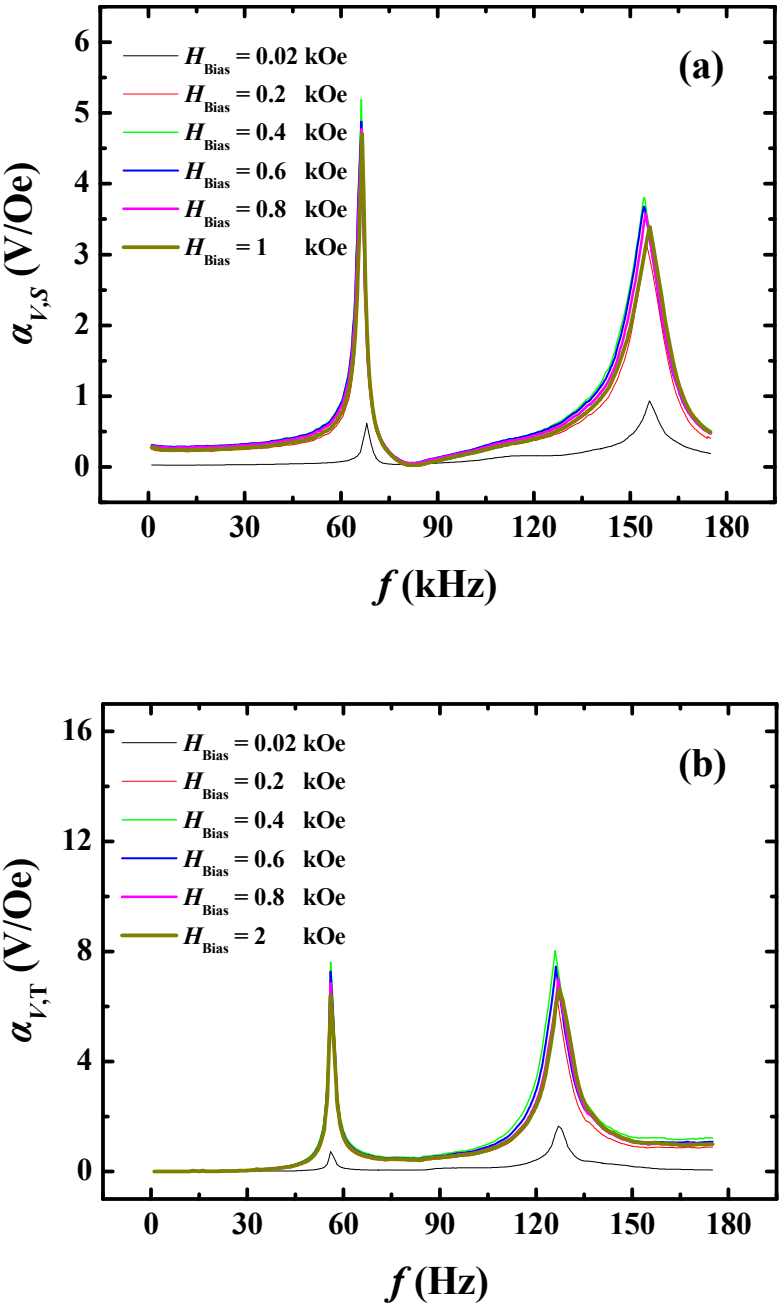

Fig. 3.26 Measured (a) $\alpha_{V,S}$ and (b) $\alpha_{V,T}$ as a function of f at various H_{Bias} and with an H_3 of 1 Oe peak for the bar-shaped sensing element with long-type PMN−PT single-crystal transformer.

Chapter 4

Development of Magnetoelectric Passive Current Sensors

4.1 Introduction

A novel class of passive current sensor with great potential for realizing self-sustainable condition monitoring of electrical assets has been proposed and outline in Chapter 1 based on magnetoelectric (ME) sensing elements. The fabrication, characterization, and physical properties of five different types of magnetostrictive and piezoelectric materials constituting the ME sensing elements have been reported in Chapter 2. The structure, working principles, physical modeling, characterization, and performance of three characteristic types of ME sensing elements have also been documented in Chapter 3.

In this chapter, the plate-shaped and ring-shaped ME sensing elements realized in Chapter 3 are developed into novel surface mount-type and clamp-type ME passive current sensors, respectively. The conceptual design and design requirements of the sensors are stated. The effects of magnetic field biasing, electric field shielding, and/or thermal insulation on the performance of the sensors are studied by magnetic, electric, and/or thermal physical modeling and/or finite element analysis (FEA)

techniques. The fabrication and performance evaluations of the sensors are performed, and summaries of useful performance data are provided for each type of sensors.

4.2 Surface Mount-Type ME Passive Current Sensor

4.2.1 Conceptual Design and Design Requirements

Figure 4.1 shows the conceptual design of the proposed surface mount-type ME passive current sensor. The design basically consists of a plate-shaped ME sensing element magnetically biased by a pair of NdFeB magnet bars in a brass shielding case with inner layers of superwool thermal insulator. This configuration provides an easy and flexible way for installing the sensor and detecting the magnetic fields governed by current-carrying electrical cables or conductors.

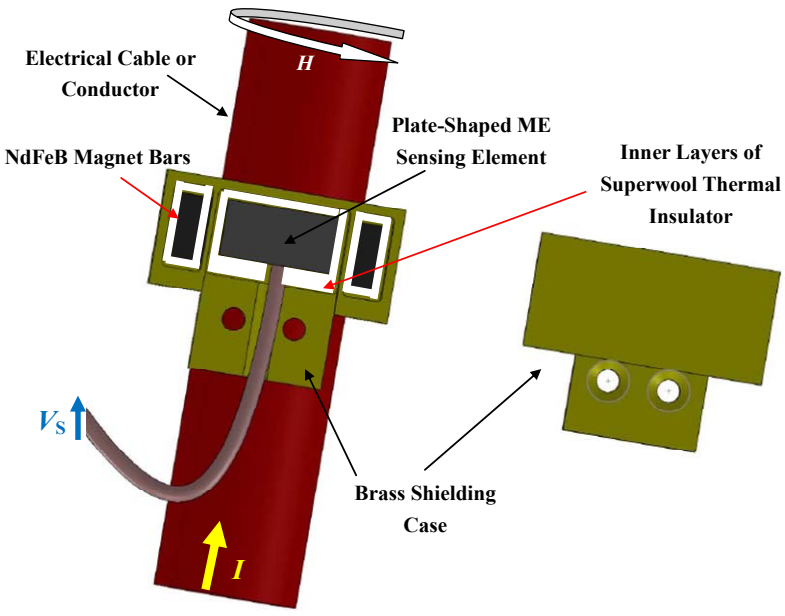

Fig. 4.1 Conceptual design of the proposed surface mount-type ME passive current sensor for detecting magnetic fields governed by current-carrying electrical cables or conductors.

As reported in Chapter 3, the ME voltage coefficient (α_V) and current sensitivity (S_I) of the ME sensing elements depend greatly on the level of magnetic bias field (H_{Bias}), and there exists an optimal H_{Bias} for each type of ME sensing elements. In our proposed design in Fig. 4.1, a pair of NdFeB magnet bars are employed to give an optimal H_{Bias} to the plate-shaped ME sensing element. Moreover, electromagnetic waves in various electrical and electronic devices such as electrical motors, fluorescent lights, radio receivers, computers, etc. are rich in spectral content and generally radiate electromagnetic interference (EMI) or noise to the environment. Hence, electric field shielding is the second important consideration to improve the stability of our magnetic field sensing-based current sensors. In addition, thermal property is the third important consideration in sensor design. A good thermal insulation can extend the thermal stability and hence the working temperature range of the sensors indeed.

To enable the design of the proposed surface mount-type ME passive current sensor in Fig. 4.1, the following design requirements are required:

(1) It should have a pair of magnets to provide an average magnetic bias field (H_{Bias}) of ~0.4 kOe throughout the length of the plate-shaped ME sensing element.

(2) It should have a high electric field shielding effectiveness (S_E) in excess of 40 dB over the operating frequency range of 25 Hz−150 kHz.

(3) It should have good thermal insulation to assure a small deterioration in current sensitivity (S_I) of < 15 % in the working temperature range of 30−60 °C.

(4) It should be ease of installation and mountable on the surfaces of electrical cables or conductors.

(5) It should be compact in size, preferably within 25 × 25 × 10 mm^3.

(6) It should be mechanically strong and light weight (< 25 g).

4.2.2 Effect of Magnetic Field Basing

In our sensor design, NdFeB magnets were selected to provide the required magnetic bias field (H_{Bias}) of ~0.4 kOe to the plate-shaped ME sensing element. NdFeB magnets, short for neodymium-iron-boron magnets, have been commercially available since 1984. The family of NdFeB magnets, which is regarded as an important family of rare earth-based magnets, covers sintered NdFeB magnets and bonded NdFeB magnets according to the different production processes. Sintered NdFeB magnets, which offer the highest energy product [$(BH)_{max}$] compared to any other magnetic materials today, are available in a very wide range of sizes, shapes, and grades. The important material properties of commercial sintered NdFeB magnets are summarized in Table 4.1 [74]. The sintered NdFeB magnets have a giant residual magnetic flux density (B_r) in excess of 1.32 T which makes them capable of providing the required H_{Bias} level with small sizes. The high operating temperature of 120 °C (maximum) ensures a high thermal stability.

Table 4.1 Important material properties of sintered NdFeB magnets provided by China Rare Earth Magnet Ltd. [74].

	Symbol	Value
Residual magnetic flux density (T)	B_r	1.32−1.38
Coercive field (kA/m)	H_c	≥955
Intrinsic coercive field (kA/m)	H_{ci}	≥1353
Maximum energy product (kJ/m^3)	$(BH)_{max}$	318−342
Relative permeability	μ_r	~1.05
Density (kg/m^3)	ρ	7450−7650
Maximum operating temperature (°C)	T_{max}	120

Figure 4.2(a) illustrates the photograph of a disk-shaped sintered NdFeB magnet supplied by China Rare Earth Magnet Ltd. The as-supplied NdFeB magnet disk had a diameter of 15 mm and a thickness of 2 mm. It also had a layer of nickel coating on its surfaces as well as the north (N) and south (S) poles normal to the circular surfaces. Figure 4.2(b) shows the photograph of a bar-shaped sintered NdFeB magnet cut from the as-supplied magnet disk in Fig. 4.2(a) using a wire electrical discharge (WEDM) technique described in Section 2.2.2.1 of Chapter 2. The cut NdFeB magnet bar had a length (l_{Mag}) of 7 mm, a width (w_{Mag}) of 3 mm, and a thickness (t_{Mag}) of 2 mm. Its N and S poles were oriented normal to the rectangular surfaces defined by ($l_{Mag} \cdot w_{Mag}$) so that it has a thickness magnetization.

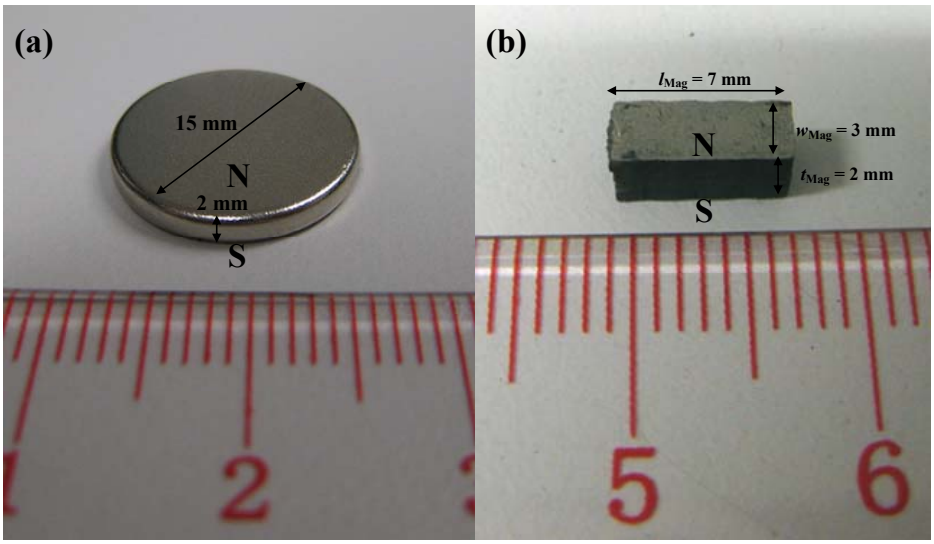

Fig. 4.2 Photographs of (a) an as-supplied sintered NdFeB magnet disk and (b) a NdFeB magnet bar prepared by cutting the as-supplied sintered NdFeB magnet disk in (a). The labels N and S denote the north and south poles of the magnets, respectively.

4.2.2.1 Physical Modeling

Based on the current model for analyzing a pair of magnet bars with uniform thickness magnetization (Fig. 4.3), the expression for the magnetic flux density [$B_{\text{Bias}}(x)$] at a point along the x-axis and with a distance (x) from the centerline towards the magnet bars with a separation $(d/2)$ can be written as [75]

$$B_{\text{Bias}}(x) = \frac{B_r}{\pi}(A - B + C - D), \tag{4.1}$$

$$A = \tan^{-1}\left[\frac{w_{\text{Mag}} l_{\text{Mag}}}{2x_1\sqrt{4x_1^2 + w_{\text{Mag}}^2 + l_{\text{Mag}}^2}}\right],$$

$$B = \tan^{-1}\left[\frac{w_{\text{Mag}} l_{\text{Mag}}}{2(x_1 + t_{\text{Mag}})\cdot\sqrt{4(x_1 + t_{\text{Mag}})^2 + w_{\text{Mag}}^2 + l_{\text{Mag}}^2}}\right],$$

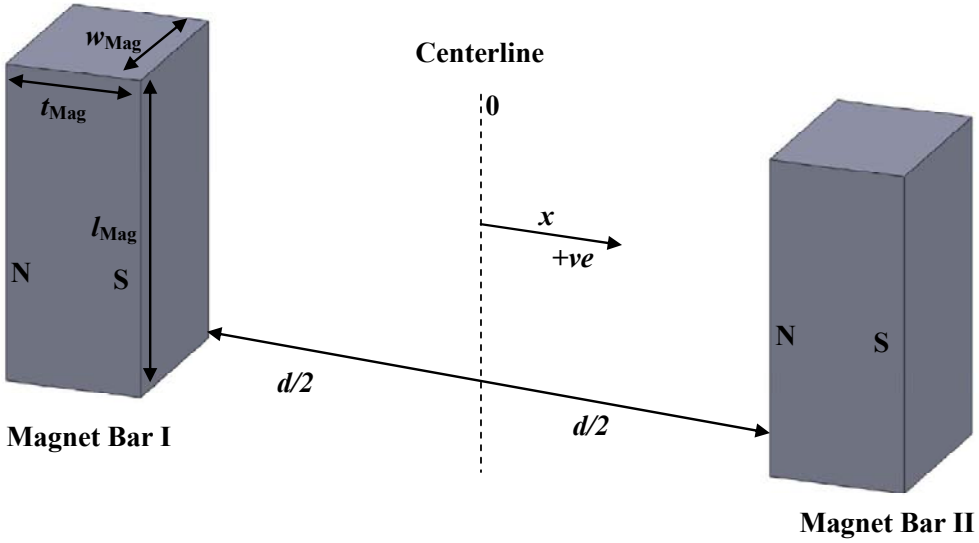

Fig. 4.3 Schematic diagram for the physical modeling of magnetic field distribution governed by a pair of magnet bars (Magnet I and Magnet II) with uniform thickness magnetization.

$$C = \tan^{-1}\left[\frac{w_{\text{Mag}} l_{\text{Mag}}}{2x_2\sqrt{4x_2^2 + w_{\text{Mag}}^2 + l_{\text{Mag}}^2}}\right],$$

$$D = \tan^{-1}\left[\frac{w_{\text{Mag}} l_{\text{Mag}}}{2(x_2 + t_{\text{Mag}})\cdot\sqrt{4(x_2 + t_{\text{Mag}})^2 + w_{\text{Mag}}^2 + l_{\text{Mag}}^2}}\right],$$

where B_r is the residual magnet flux density of the magnet bars; l_{Mag}, w_{Mag} , and t_{Mag} are the length, width, and thickness of the magnet bars, respectively; $x_1 = d/2 + x$ and $x_2 = d/2 - x$ are the separations between the centerline and Magnet Bar I and the centerline and Magnet Bar II, respectively. The corresponding magnetic field [$H_{\text{Bias}}(x)$] is obtained as

$$H_{\text{Bias}}(x) = \frac{B_{\text{Bias}}(x)}{\mu_0 \mu_r}, \tag{4.2}$$

where μ_0 (= $4\pi \times 10^{-7}$ H/m) is the magnetic permeability of free space; μ_r (= 1) is the relative magnetic permeability of the region of measurement (air).

Equations (4.1) and (4.2) state that $H_{\text{Bias}}(x)$ is strongly dependent upon the material (i.e., B_r) and dimensions (i.e., l_{Mag}, w_{Mag}, and t_{Mag}) of the magnet bars as well as the relative separation between the two magnet bars (d). To reduce the size and weight of the resulting current sensors, it is required to have a large Br and hence a large $H_{\text{Bias}(x)}$ using small magnet bars.

Combining Eqs. (4.1) and (4.2), and using the material properties of NdFeB magnets in Table 4.1, H_{Bias} as a function of x is calculated and plotted in Fig. 4.4. The two NdFeB magnet bars: Magnet I and Magnet II are assumed to have the same dimensions of l_{Mag} = 7 mm, w_{Mag} = 3 mm, and t_{Mag} = 2 mm and a relative separation (d) of 17 mm. Figure 4.4 reveals that the maximum H_{Bias} of ~4.3 kOe appears at the NdFeB magnet bars and the minimum H_{Bias} of ~0.2 kOe occurs at the centerline between the two NdFeB magnet bars with a relative separation (d) of 17 mm. As our plate-shaped ME sensing element has a length of 12 mm (Fig. 3.4), the maximum H_{Bias} acting on the sensing element is ~1.1 kOe at x = ±6 mm, and the average H_{Bias} ($H_{\text{Bias,avg}}$) acting on the sensing element is ~0.4 kOe from x = -6 mm to x = 6 mm. This average H_{Bias} fits the optimal H_{Bias} value of 0.4 kOe for the plate-shaped ME sensing element to be used in the surface mount-type ME passive current sensor.

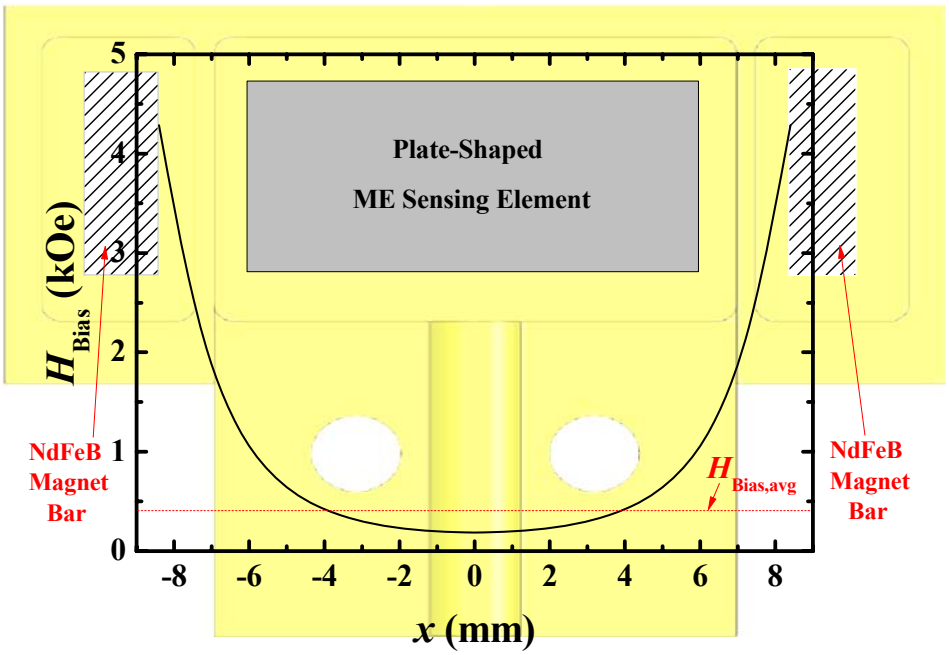

Fig. 4.4 **Calculated H_{Bias} as a function of x for a pair of NdFeB magnet bars with dimensions 7 mm (l_{Mag}) × 3 mm (w_{Mag}) × 2 mm (t_{Mag}) and a relative separation (d) of 17 mm. The plated-shaped ME sensing element is taken to have a length of 12 mm.**

4.2.2.2 Finite Element Analysis

A commercial finite element software package, ANSYS® 10.0 (ANSYS, Inc Pennsylvania, U.S.A), was employed to perform the magnetic finite element analysis (FEA) in order to have an improved insight into the physical modeling of the effect of magnetic field biasing described in Section 4.2.2.1. In ANSYS®, Maxwell's equations were used as the basis for magnetic FEA. Figure 4.5 shows the two-dimensional (2-D) finite element model created for computing the magnetic field distribution governed by a pair of NdFeB magnet bars and sandwiching the plate-shaped ME sensing element. The use of the 2-D model conserves simplicity by reducing the number of

elements required for meshing. The 2-D coupled-field element PLANE 13 was used for meshing the plate-shaped ME sensing element, NdFeB magnet bars, brass shielding case, and air gaps (in the absence of superwool thermal insulator). It is noted that PLANE 13 is defined by four nodes with up to four degrees-of-freedom per node including 2-D magnetic field capability. There were a total of 1694 plane elements and 1778 elements nodes in the model. If the mesh density was coarser, the results were not accurate enough. If the mesh density was much finer, it would increase the computation time. The material properties obtained in Fig. 2.9 and shown in Table 4.1 were used for the plate-shaped ME sensing element and the NdFeB magnet bars, respectively. For the brass shielding case and the air gaps, a relative magnetic permeability (μ_r) of unity was assumed.

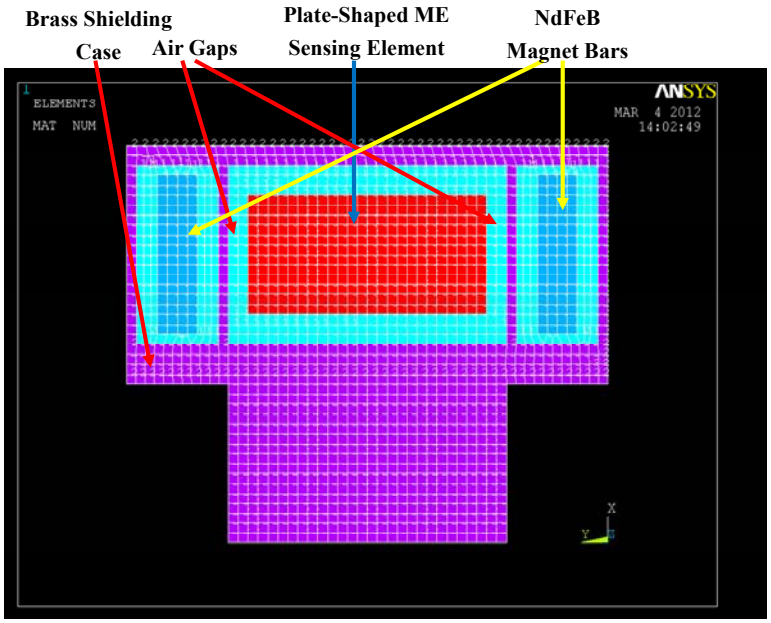

Fig. 4.5 The 2-D finite element model used to compute the magnetic field distribution governed by a pair of NdFeB magnet bars and sandwiching the plate-shaped ME sensing element as in the physical modeling described in Section 4.2.2.1.

Figure 4.6(a) shows the magnetic field vector display obtained from the magnetic FEA in which the arrows indicate the directions of magnetic field while the colors represent the strength of magnetic field. Figure 4.6(b) shows the computed (by FEA) and calculated (by physical modeling) H_{Bias} as a function of x. The calculated values are extracted from Fig. 4.4. It is seen that the computed H_{Bias} agrees well with the calculated H_{Bias}. The computed maximum H_{Bias} near the NdFeB magnet bars is ~4.2 kOe and the computed minimum H_{Bias} at the centerline is ~0.28 kOe. Moreover, the maximum and average H_{Bias} that act on the sensing element are found to be ~1.8 and ~0.4 kOe, respectively.

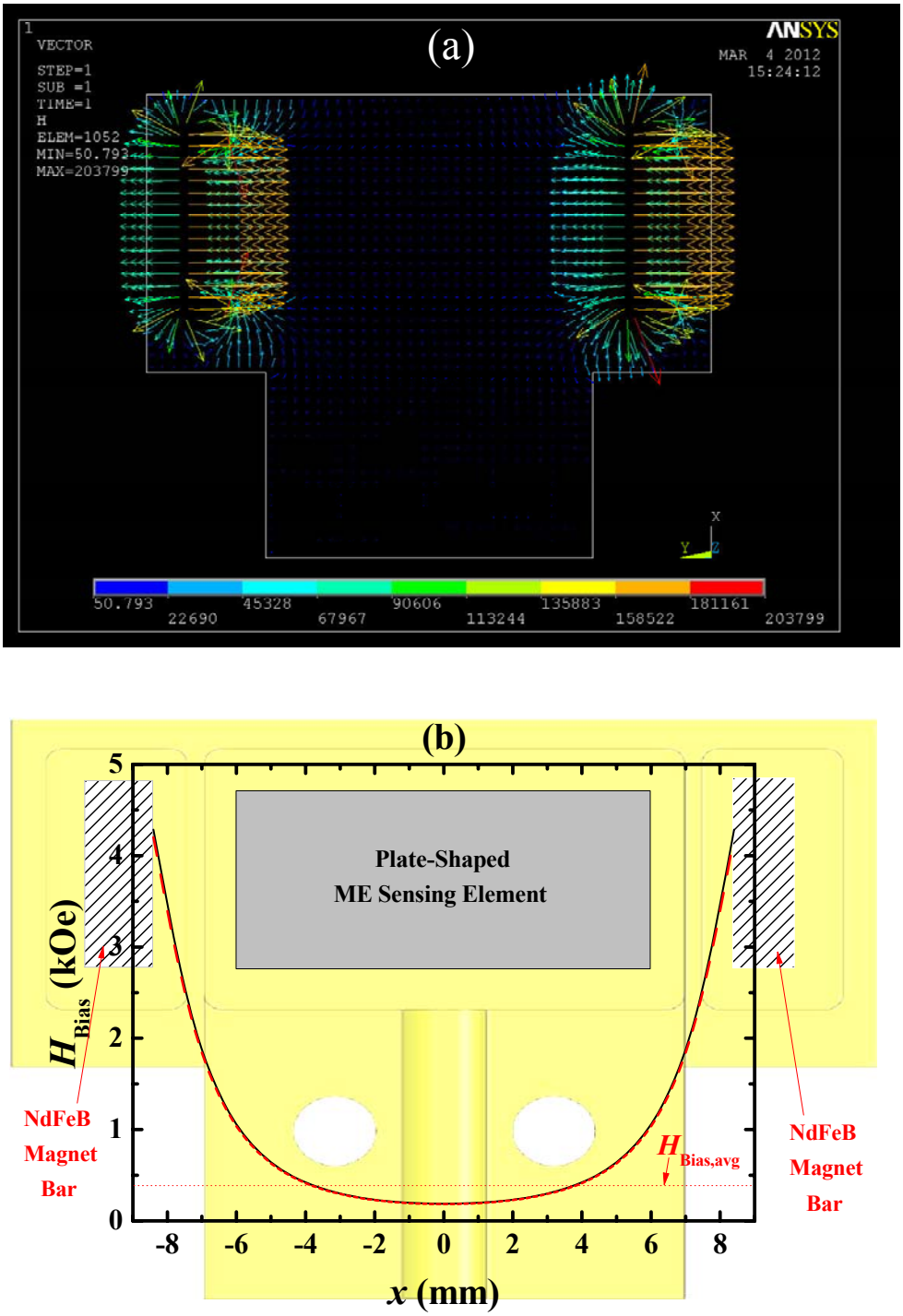

Fig. 4.6 ANSYS FEA results showing (a) the magnetic field vector display and (b) H_{Bias} as a function of x (dash line). The calculated H_{Bias} as a function of x in Fig. 4.4 is also included in (b) (solid line) for comparison.

4.2.3 Effect of Electric Field Shielding

A shield is a metallic partition placed between two regions of space to control the propagation of electromagnetic fields from one region to the other region. A shield may be used to contain electromagnetic fields if it is surrounded by noise sources. This configuration provides protection for susceptible devices and equipment located inside the shield. A shield may also be used to keep electromagnetic radiation out of a region.

Shielding can be specified in terms of the reduction in magnetic and/or electric field strength caused by the shield. It is convenient to express this shielding effectiveness in units of decibel (dB). The shielding effectivenesses for electric fields (S_E) and magnetic fields (S_M) are defined, respectively [76], as

$$S_E = 20\log\frac{E_0}{E_1} \tag{4.3}$$

and

$$S_H = 20\log\frac{H_0}{H_1}, \tag{4.4}$$

where E_0 and H_0 are the incident electric and magnetic field strengths, respectively; and E_1 and H_1 are the electric field and magnetic field strengths of the transmitted wave as it emerges from the shield, respectively. In general, a shielding effectiveness in the range of 0−30 dB is regarded as the lowest level of shielding, while that above 60 dB is considered as a high level of shielding.

4.2.3.1 Physical Modeling

There are two types of loss encountered by an electromagnetic field striking a solid metallic material (i.e., a shield), namely: absorption loss and reflection loss. By considering these two types of loss, the total shielding effectiveness of a shield for electric fields and magnetic fields can be expressed, respectively, as

$$S_E = A_E + R_E \tag{4.5}$$

and

$$S_H = A_H + R_H + B_H\,, \tag{4.6}$$

where A_E and A_H are the absorption losses of the shield for electric fields and magnetic fields, respectively; R_E and R_H are the reflection losses of the shield for electric fields and magnetic fields, respectively; and B_H is the multiple-reflection correction factor of the shield for magnetic fields. It is noted that Eqs. (4.5) and (4.6) can further be interpreted as follows:

(1) When an electric field or a magnetic field passes through a shield, its amplitude decreases exponentially. This decay occurs because of the production of ohmic losses and hence heating in the shield by eddy currents, and this type of loss is known as the absorption loss. The general expressions for A_E and A_H as stated in Eqs. (4.5) and (4.6) can be written, respectively, as

$$A_E = A_H = 131.4t\sqrt{f\mu_{\mathrm{r}}\sigma_{\mathrm{r}}}\,, \tag{4.7}$$

where t is the thickness of the shield; f is the frequency of the electric or magnetic field; μ_r (= μ / μ_0; $\mu_0 = 4\pi\times10^{-7}$ H/m = permeability of free space) is the relative permeability of the shield; and σ_r (= σ / σ_{copper}; $\sigma_{copper} = 5.96\times10^7$ S/m = conductivity of copper) is the relative conductivity of the shield.

(2) Reflection loss is naturally different from absorption loss because it is a function of the ratio of field impedance to shield impedance. An electric field has a higher reflection loss than a magnetic field (i.e., $R_E > R_H$). For our ME passive current sensors, magnetic fields act as the input-determined field source and the detection distance from the source is unknown. Hence, R_H of near field can be assumed to be small (i.e., $R_H \rightarrow 0$), and only R_E is considered as follows:

$$R_H \rightarrow 0 \tag{4.8}$$

and

$$R_E = 322 + 10\log\frac{\sigma_r}{\mu_r f^3 r^2}, \tag{4.9}$$

where r is the distance from the input-determined field source to the shield.

(3) For shielding of magnetic fields, the multiple-reflection correction factor (B_H) can be neglected if the shield is sufficiently thick to provide $A_H > 9$ dB. Otherwise, B_H should be taken into account using

$$B_H = 20\log(1 - e^{-2t/\delta}), \tag{4.10}$$

$$\delta = \sqrt{\frac{2}{\omega \mu_0 \mu_r \sigma_0 \sigma_r}}, \tag{4.11}$$

where t and δ are the thickness and skin depth of the shield, respectively.

Based on the above interpretation, S_E and S_H in Eqs. (4.5) and (4.6) can be written as

$$S_E = A_E + R_E = 131.4t\sqrt{f\mu_r\sigma_r} + \left[322 + 10\log\frac{\sigma_r}{\mu_r f^3 r^2}\right] \tag{4.12}$$

and

$$S_H = A_H + B_H = 131.4t\sqrt{f\mu_r\sigma_r} + 20\log(1 - e^{-2t/\delta}). \tag{4.13}$$

It is clear from Eqs. (4.12) and (4.13) that μ_r and σ_r are the major material parameters in controlling S_E and S_H. Larger μ_r and σ_r lead to larger A_E, A_H, and B_H, while a larger σ_r with a smaller μ_r result in a larger R_E. It should be highlighted that the effects of electric field and magnetic field shielding coexist in a shield indeed. For the proper operation of our ME passive current sensors, a high S_E and a low S_H are required. Hence, a shield of higher σ_r and low μ_r is more desirable. Table 4.2 shows μ_r and σ_r of three common metallic shielding materials: brass, aluminum, and iron. It is seen that both brass and aluminum have higher σ_r and lower μ_r (= 1) compared to iron. Therefore, they may be suitable for use as the shielding case of our current sensors.

Table 4.2 Relative conductivity and relative permeability of three common metallic shielding materials.

Parameter	Symbol	Brass	Aluminum	Iron
Relative Conductivity	σ_r	0.35	0.63	0.17
Relative Permeability	μ_r	1	1	5000

Figure 4.7 shows the S_E–f plots for brass, aluminum, and iron at the same distance from the input-determined field source to the shield (r) of 10 mm but with different shield thicknesses (t) of 0.1, 0.5, 1, and 2 mm. It is observed that S_E increases with increasing t. Nonetheless, a high S_E in excess of 200 dB can be achieved for all the three different shielding materials in the f range of 25 Hz−150 kHz when $t \geq 0.1$ mm. Among them, iron gives the best S_E, while brass and aluminum have comparable values of S_E. This is because iron has an exceptionally high μ_r of 200 which increases significantly the contribution of A_E in S_E in accordance with Eq. (4.12).

Figure 4.8 provides the S_H–f plots for brass, aluminum, and iron with different t of 0.1, 0.5, 1, and 2 mm. Again, S_H increases with increasing t. Also, iron exhibits a significantly high S_H in excess of 60 dB in the f range of 24−150 kHz for $t \geq 0.1$ mm. Brass and aluminum only demonstrate a low S_H generally close to 0 dB for $t \leq 0.1$ mm. By combining the S_E and S_H results in Figs. 4.7 and 4.8, iron shows an excellent shielding performance for both electric and magnetic fields because of the high σ_r (=0.17) and the exceptionally high μ_r (=200). Due to the unity in μ_r, brass and aluminum demonstrate a sufficiently high S_E (>200 dB) and a usefully low S_H (~0 dB) at $t \leq 0.1$ mm for frequencies up to 150 kHz. This makes brass and aluminum, especially brass, very suitable for use as the shielding case in our ME passive current sensors.

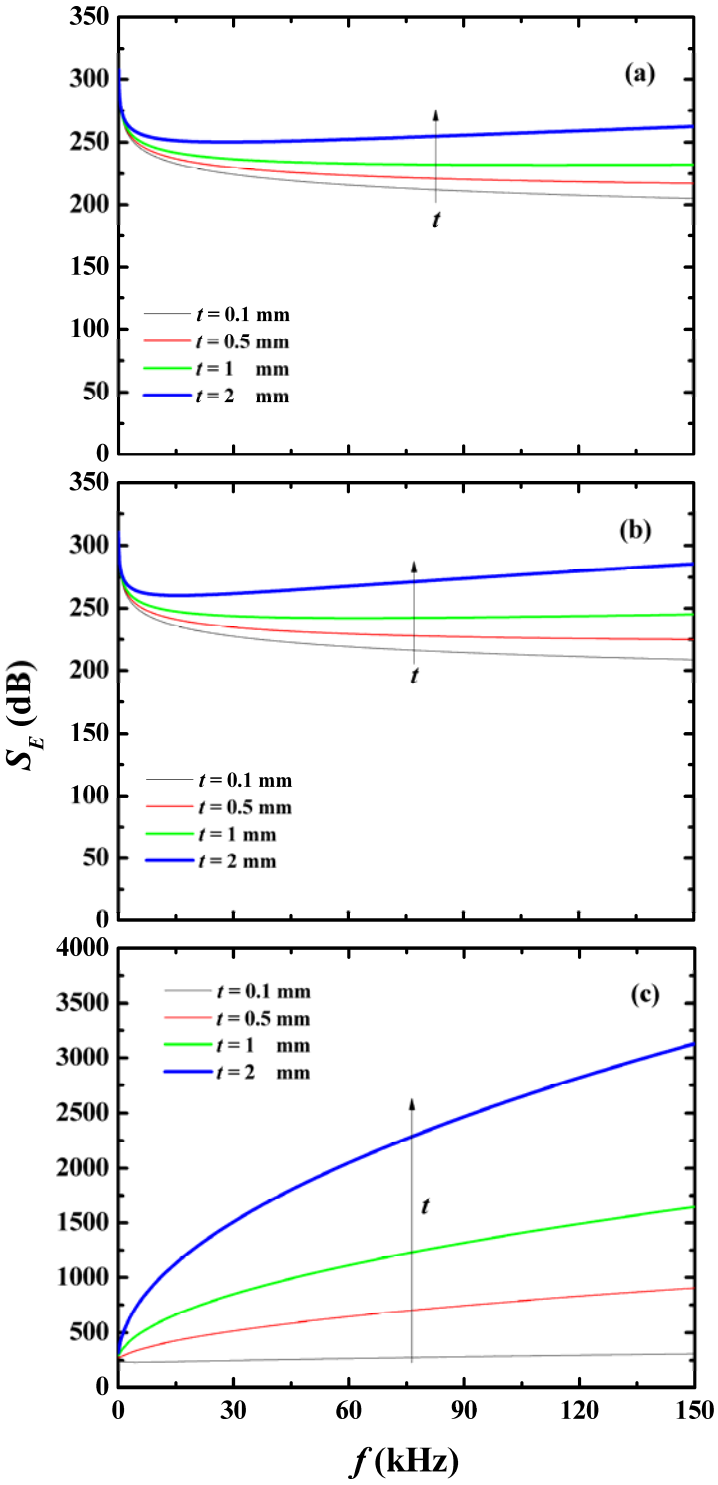

Fig. 4.7 S_E–f plots for (a) brass, (b) aluminum, and (c) iron at the same r of 10 mm but with different t of 0.1, 0.5, 1, and 2 mm.

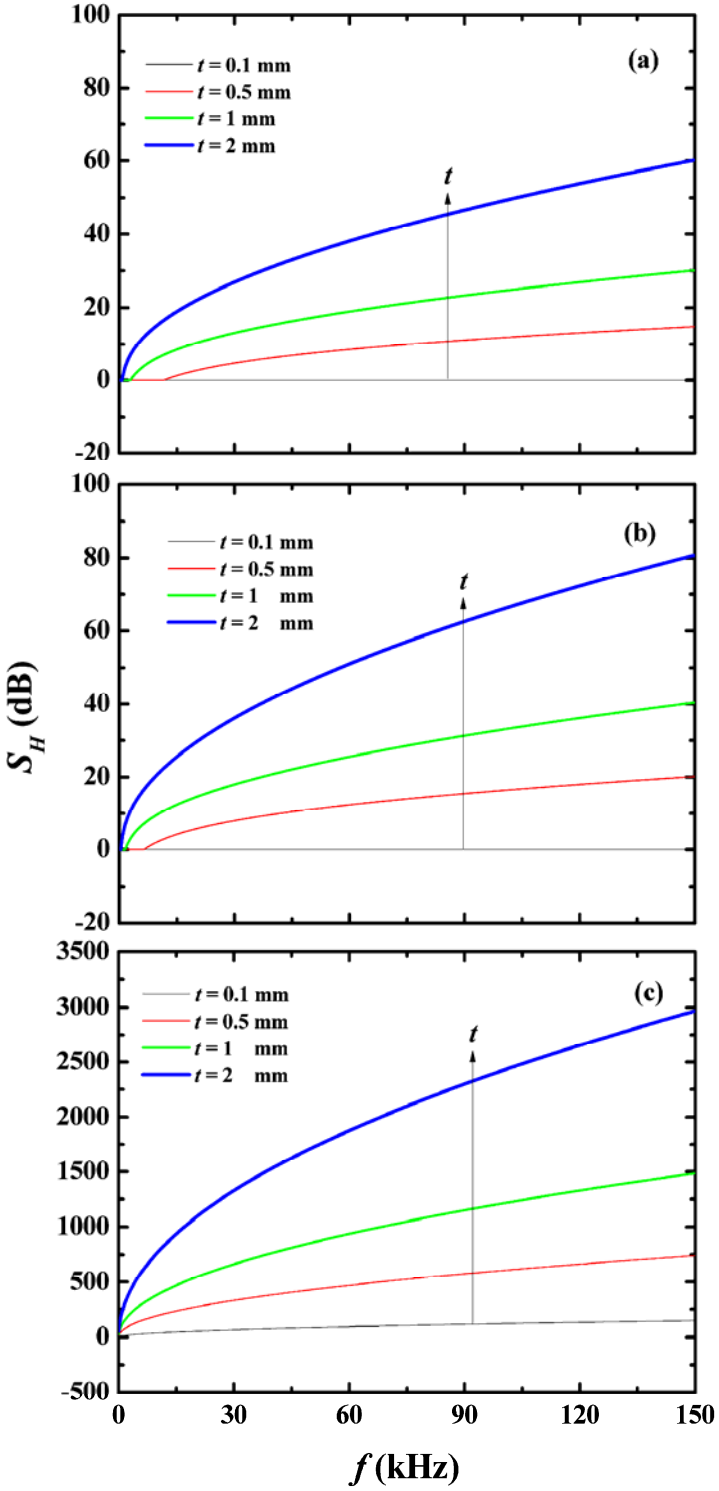

Fig. 4.8 S_H–f plots for (a) brass, (b) aluminum, and (c) iron with different t of 0.1, 0.5, 1, and 2 mm.

4.2.4 Effect of Thermal Insulation

Thermal insulation is another important consideration in the valid operation of the ME passive current sensors. In electrical current sensing, we would like the sensor output signals be solely responded to the applied currents. However, the ME sensing elements and other parts/components used to configure the sensors also respond to changes in temperature. Thus, the effect of working (environmental) temperature on the performance the thermal insulation of the current sensors needs to be studied. Our interests are to understand: (1) the level of deterioration in current sensitivity (S_I) in the desired operating temperature range of 25−60 °C; (2) the maximum operating temperature; and (3) the time required to achieve a thermal equilibrium at a given working temperature.

Since the electric field shielding case of our surface mount-type ME passive current sensor is made of brass in order to achieve a good electric field shielding performance, the thermal conductive nature of brass will deteriorate the thermal stability of the ME sensing element and the NdFeB magnet bars housed inside the brass shielding case and hence the resulting current sensor. It is crucial to introduce a thermal insulator between the brass shielding case and the ME sensing element/NdFeB magnet bars. Among the commercially available thermal insulating materials, superwool 607 is an alkaline earth silicate (AES) fiber-based material and allows superior thermal insulation properties to be achieved in minimal space [77]. Superwool 607 has many attractive features, including low thermal conductivity (0.04 W/m·K), low thermal shrinkage (<2 %), high classification temperature (1300 °C), and

good mechanical strength (>0.45 MPa). These features make superwool 607 a good thermal insulating material. Superwool 607 was used as the thermal insulator in our ME passive current sensors for increasing their thermal stability.

4.2.4.1 Finite Element Analysis

Finite element transient thermal analysis based on ANSYS® 10.0 was performed to compute the time-dependent temperature distributions of the surface mount-type ME passive current sensor. Figure 4.9 illustrates the 2-D finite element model for the current sensor. The element PLANE 55 with a 2-D thermal conduction capability was selected for the finite element model. This element had four element nodes with single degree-of-freedom, i.e., temperature, at each node. There were a total of 2985 plane elements and 3114 element nodes in the finite element model. The thermomechanical properties as tabulated in Table 4.3 were used for the brass shielding case, NdFeB magnet bars, superwool thermal insulator, Terfenol-D alloy plate, and PMN−PT single-crystal plate. The boundary condition applied in the analysis was that the current sensor was subject to two different steady working (environmental) temperatures of 60 and 90 °C in all directions as illustrated in Fig. 4.10.

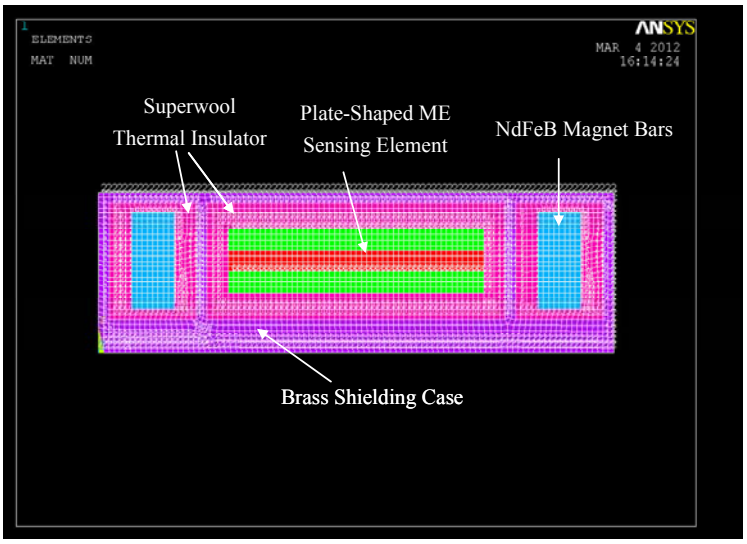

Fig. 4.9 The 2-D finite element model used to compute the time-dependent temperature distributions of the surface mount-type ME passive current sensor.

Table 4.3 Thermomechanical properties of brass shielding case, NdFeB magnet bars, superwool 607 thermal insulator, Terfenol-D alloy plate, and PMN−PT single-crystal plate.

Parameter	Symbol	Brass Shielding Case	Superwool 607 Thermal Insulator	Terfenol-D Alloy Plate	PMN−PT Single-Crystal Plate	NdFeB Magnet Bar
Density (kg/m^3)	ρ	8920	6	8090	7700	7500
Specific Heat capacity (J/kg·°C)	c	385	1357	320	880	444
Thermal Conductivity (W/m·°C)	k	401	0.06	10.5	1.5	1.7

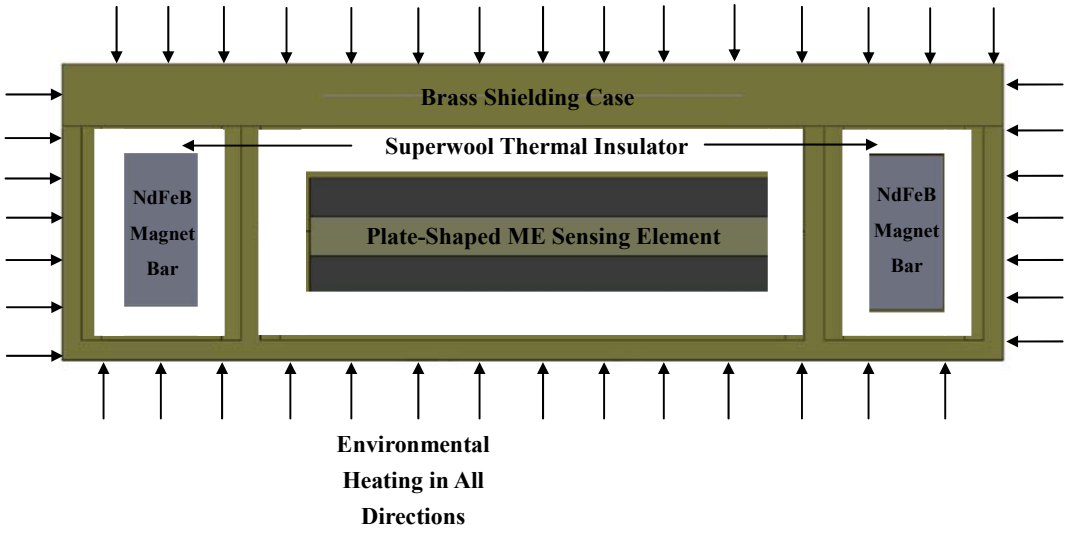

Fig. 4.10 Schematic diagram (end view) showing the boundary conditions applied in the finite element transient thermal analysis of the surface mount-type ME passive current sensor.

Figures 4.11 and 4.12 show the computed time-dependent temperature distributions of the surface mount-type ME passive current sensor when subjected to two different steady working (environmental) temperatures of 60 and 90 °C, respectively, in all directions. It is found that the temperature develops faster in the application of a higher temperature to the current sensor. Because brass is a good thermal conductor (Table 4.3), the heat transfer from the environment to the brass shielding case is relatively faster (~30 s). Both superwool and PMN−PT single-crystal are good thermal insulators in general, so the heat transfer from the brass shielding case to them is relatively slow. The time required for the sensing element to fully reach 60 °C is ~300 s when the applied working temperature is 60 °C (Fig. 4.11). At the increased temperature of 90 °C, the times required for the sensing element to fully reach 60 and 90 °C are 80 and 400 s, respectively.

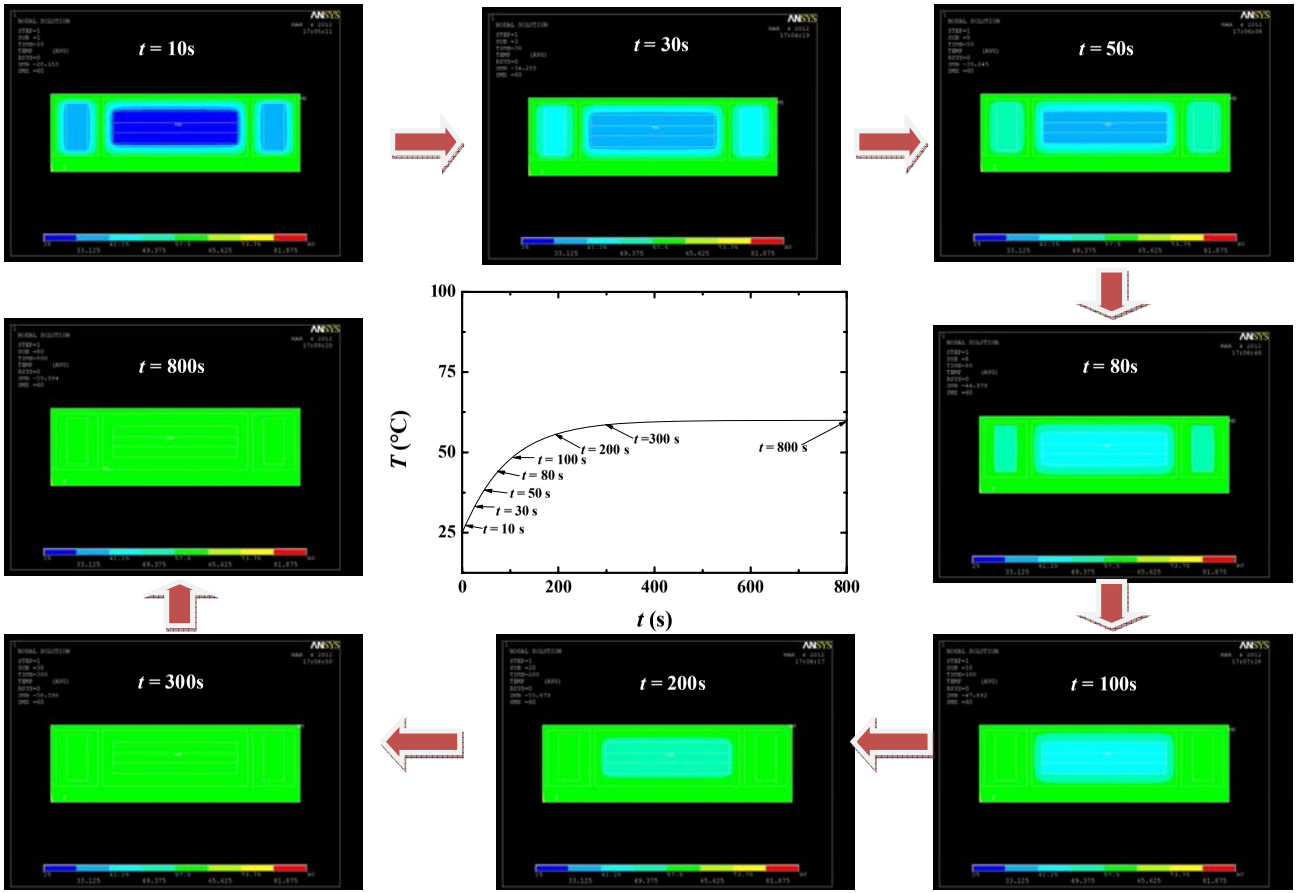

Fig. 4.11 Computed time-dependent temperature distributions of the surface mount-type ME passive current sensor at a steady working (environmental) temperature of 60 °C.

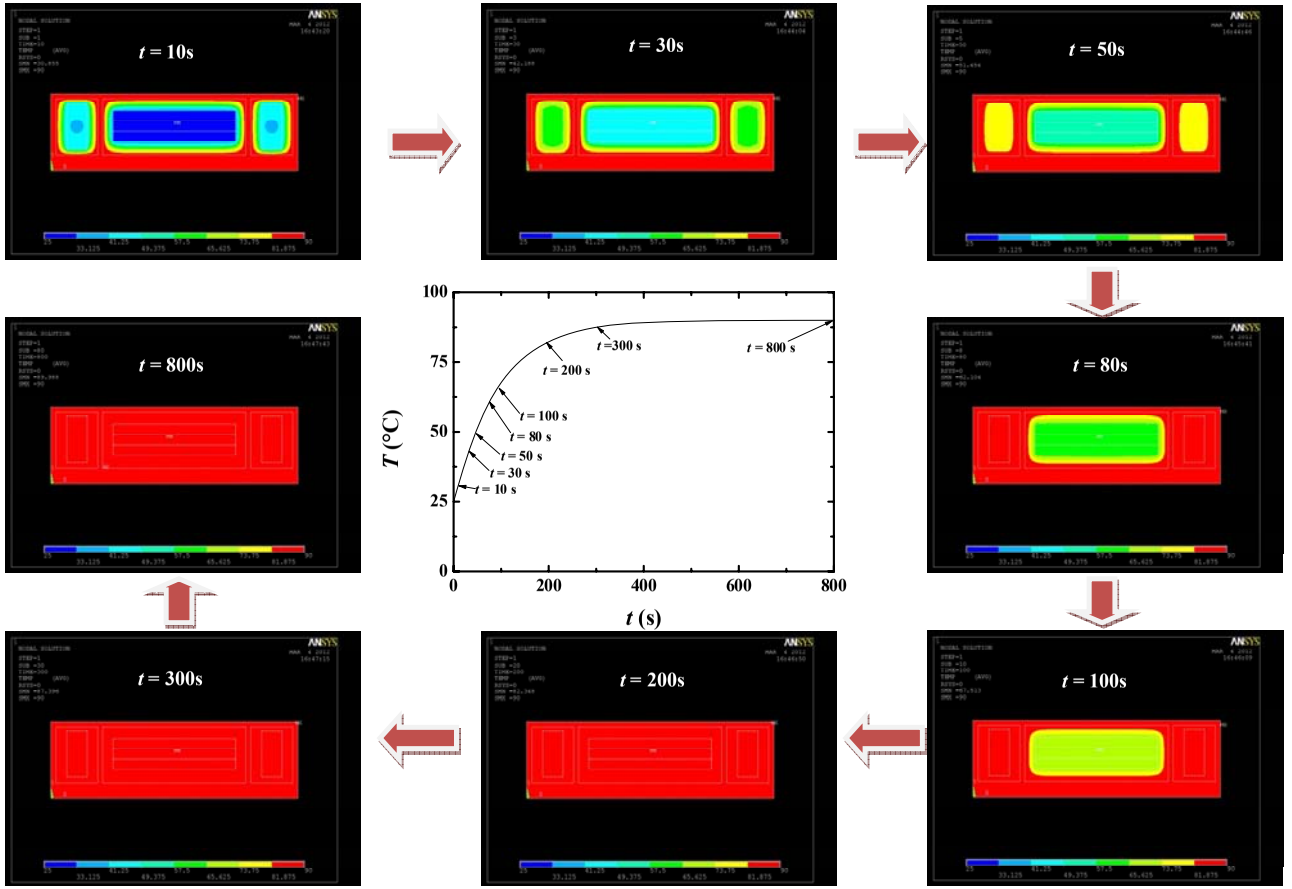

Fig. 4.12 Computed time-dependent temperature distributions of the surface mount-type ME passive current sensor at a steady working (environment) temperature of 90 °C.

4.2.5 Fabrication

Figure 4.13 shows the schematic diagram of the fabrication of the surface mount-type ME passive current sensor. First, the cover and body of the brass shielding case were machined in accordance with the mechanical drawing illustrated in Fig. 4.14. Second, a layer of superwool thermal insulator was applied to the surfaces of the middle and two side slots of the case body. Third, a pair of NdFeB magnet bars, each of dimensions 7 mm (length) × 3 mm (width) × 2 mm (thickness), were placed in the two side slots of the case body, while a plate-shaped ME sensing element with dimensions 12 mm (length) × 6 mm (width) × 3 mm (thickness) was inserted into the middle slot of the case body. Fourth, a 1.5 m long RG179 coaxial cable with a BNC connector, which was pre-connected to the plate-shaped ME sensing element, was made to have a common ground with the case body for electric field shielding and was positioned along the cable slot of the case body. Fifth, the superwool thermal insulator was employed again to fill in the gaps of the slots and to cover the top surfaces of the NdFeB magnet bars and the plate-shaped ME sensing element. Finally, the case body was covered by the case cover and two screws were used to tighten the case. The overall dimensions and weight of the fabricated sensor were found to be 24.2 mm (length) × 20 mm (width) × 6 mm (height) and 20 g, respectively.

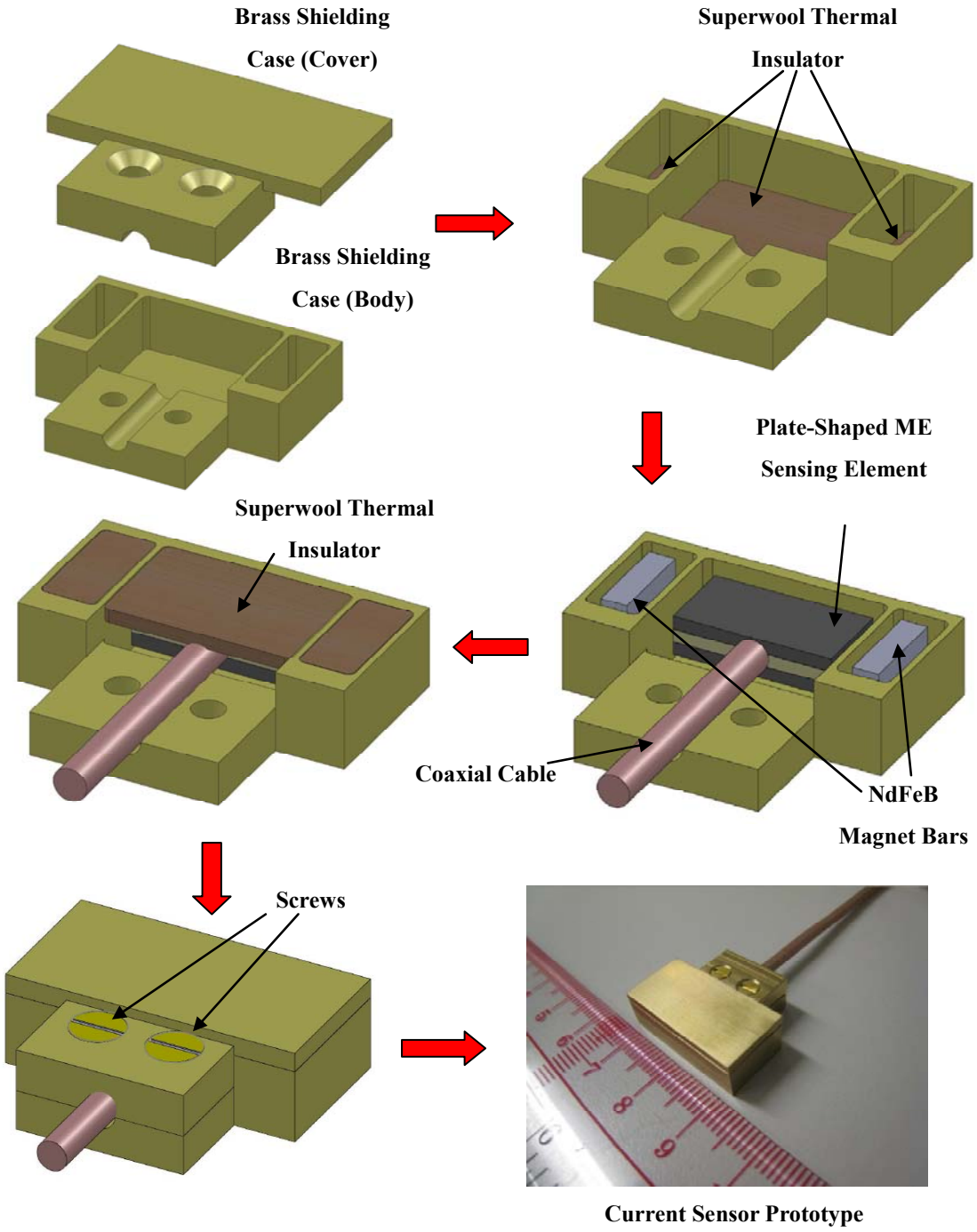

Fig. 4.13 Schematic diagram showing the fabrication of the surface mount-type ME passive current sensor.

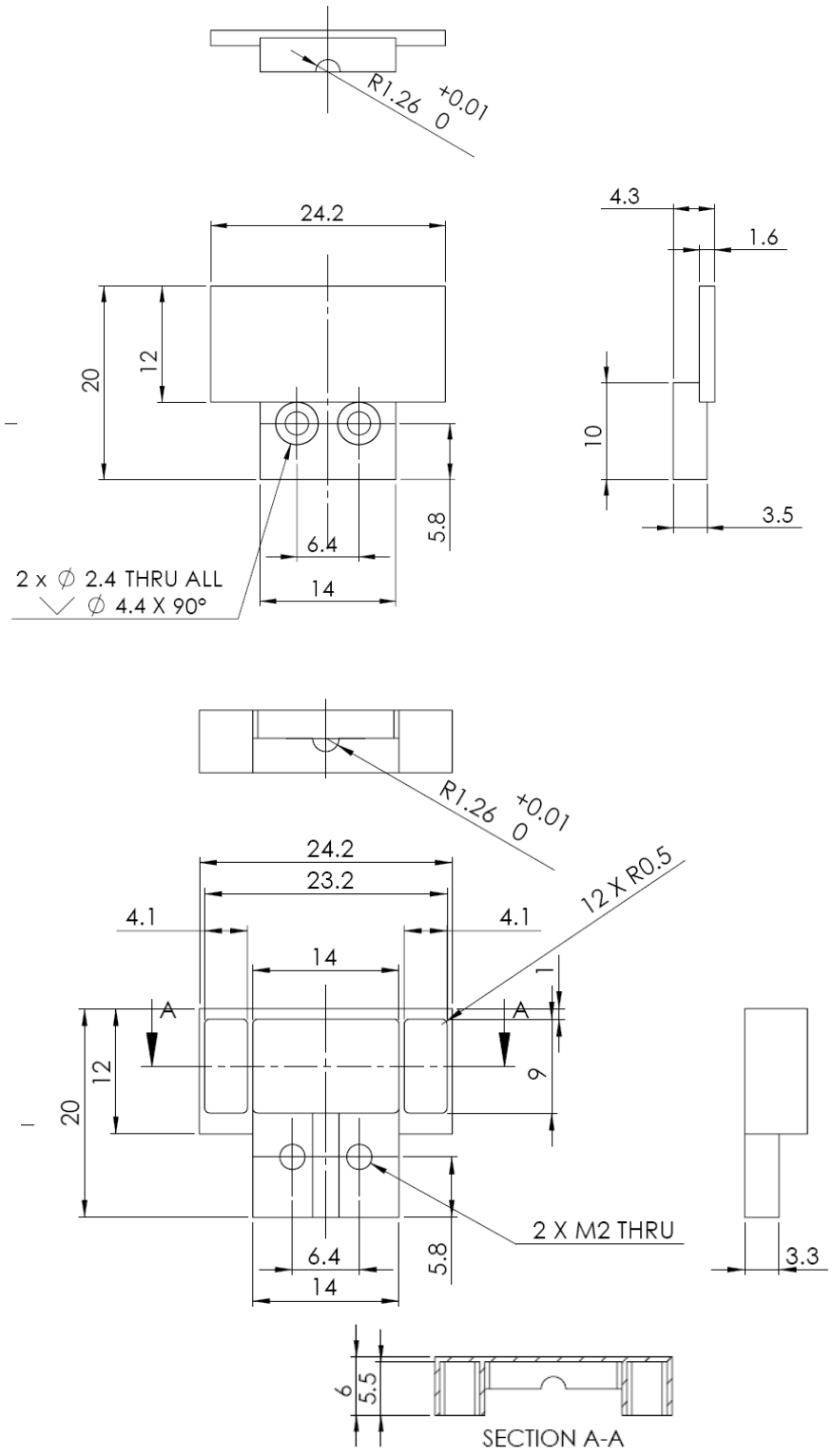

Fig. 4.14 Mechanical drawing for machining the brass shielding case of the surface mount-type ME passive current sensor. All dimensions are in millimeter (mm).

4.2.6 Performance Evaluations

4.2.6.1 Effect of Magnetic Field Basing

The magnetic bias field (H_{Bias}) distribution set up by a pair of NdFeB magnet bars in the surface mount-type ME passive current sensor was measured along the *x*-axis by a Gaussmeter (F. W. Bell 7030) equipped with a transverse Hall-effect probe (STA99-0404) as shown in Fig. 4.15. The exact value of *x* in the range of ±6 mm was confirmed by a laser displacement sensor (Keyence LK-G82) connected to a sensor controller (Keyence LK-G3001).

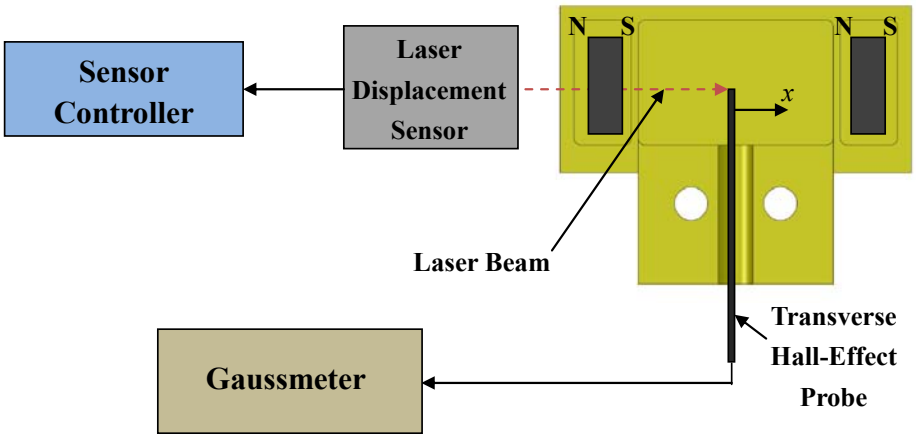

Fig. 4.15 Experimental setup for measuring the magnetic bias field (H_{Bias}) distribution along the *x*-axis and set up by a pair of NdFeB magnet bars in the surface mount-type ME passive current sensor.

Figure 4.16 plots the measured, computed (by FEA), and calculated (by physical modeling) H_{Bias} as a function of x. It is obvious that the results agree well with each other. The agreement confirms the validity of our physical model in Section 4.2.2.1 and our finite element model in Section 4.2.2.2. The experimental result shows that the maximum and minimum H_{Bias} experienced by the plate-shaped ME sensing element are ~1 and ~0.2 kOe, respectively, thus giving an average H_{Bias} ($H_{Bias,avg}$) of ~0.4 kOe throughout the length of the sensing element. This $H_{Bias,avg}$ is capable of assuring the optimal H_{Bias} required by the plated-shaped ME sensing element.

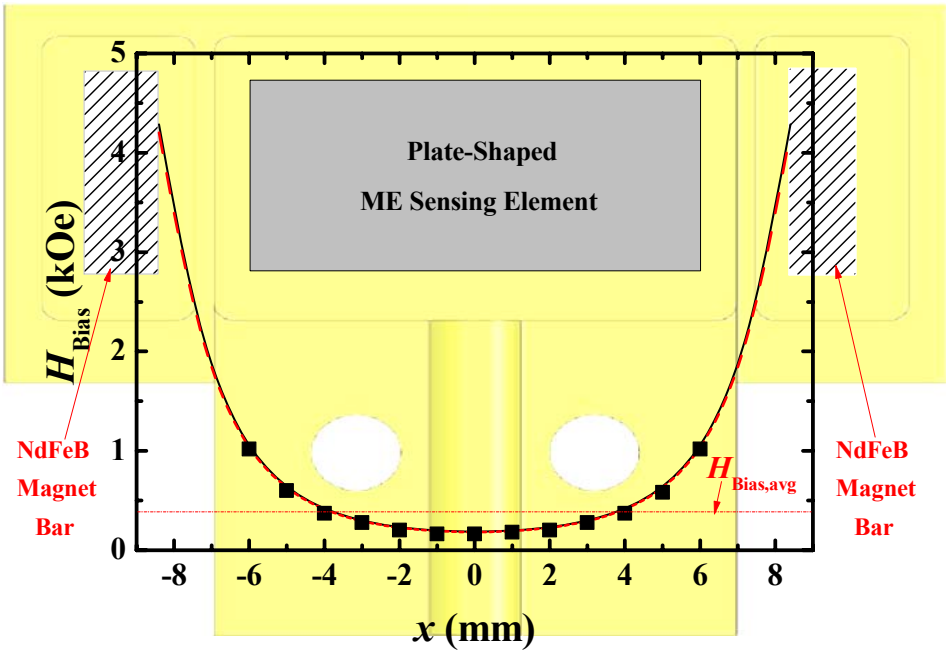

Fig. 4.16 Comparison between the measured (solid square), computed (dash line), and calculated (solid line) H_{Bias} as a function of x for the surface mount-type ME passive current sensor.

4.2.6.2 Effect of Electric Field Shielding

Figure 4.17 illustrates the experimental setup for testing the electric field shielding performance of the surface mount-type ME passive current sensor. A swept sinusoidal voltage (V) of 50 V peak was generated over a prescribed frequency (f) range of 25 Hz−150 kHz by an arbitrary waveform generator (Agilent 33210A) via a constant-voltage supply amplifier (AE Techron 7796HF) and applied to an 1 m long, 3 mm diameter electrical cable terminated with a 10 MΩ resistor load to ground. According to Guass's law, the strength electric field radiation (E_r) can be written as

$$E_r = \frac{V}{2r \ln\left(\frac{d}{2r_C} + \sqrt{\frac{d^2}{2r_C^{\,2}} - 1}\right)}, \tag{4.14}$$

where r is the distance of measurement from the electrical cable (=0.05 m in our case); d is the separation between the live electrical cable and ground electrical cable (=0.1 m in our case) ; r_C is the radius of the electrical cable, respectively. This was to simulate an electric field radiation of strength 114 V/m peak to the surface mount-type ME passive current sensor and its associated plate-shaped ME sensing element placed between the live and ground electrical cables with r = 0.05 m and d = 0.1 m. The signals picked up by the current sensor and the sensing element were measured and sampled by a data acquisition unit (Nation Instruments NBC-2110 and NI-PCI6132) under the control of a computer with a Labview program.

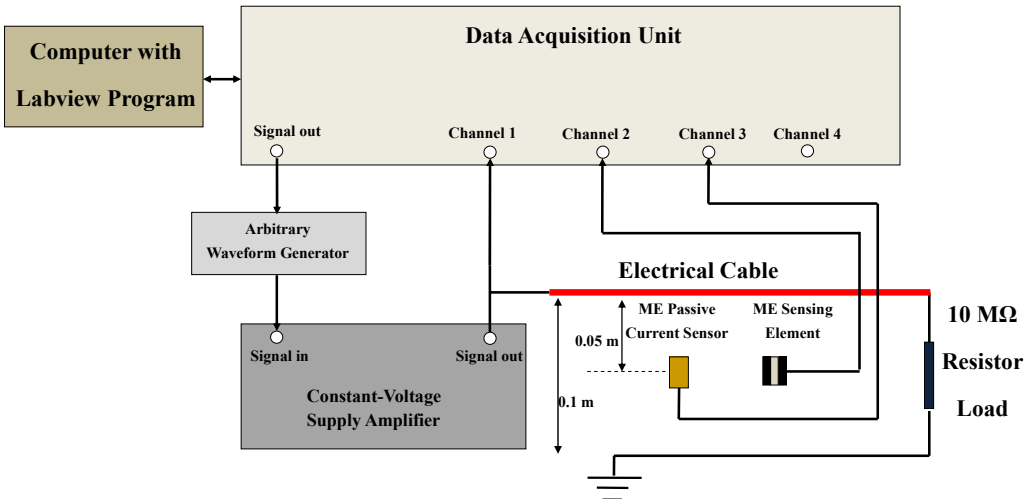

Fig. 4.17 Experiment setup for testing the electric field shielding performance of the surface mount-type ME passive current sensor.

Figure 4.18(a) presents the V_S–f curves of the surface mount-type ME passive current sensor and the associated plate-shaped ME sensing element at an electric field radiation of 114 V/m peak. The sensing element exhibits significant noise with amplitude varying from 5 to 35 mV. Due to the introduction of the brass shielding case, the resulting current sensor demonstrates an essentially low noise of 20−100 μV. Using Eq. (4.3), S_E of the current sensor was determined and plotted in Fig. 4.18(b). It is seen that S_E is in excess of 50 dB in the f range of 25 Hz − 150 kHz, indicating the presence of an effective electric field shielding in the brass shielding case.

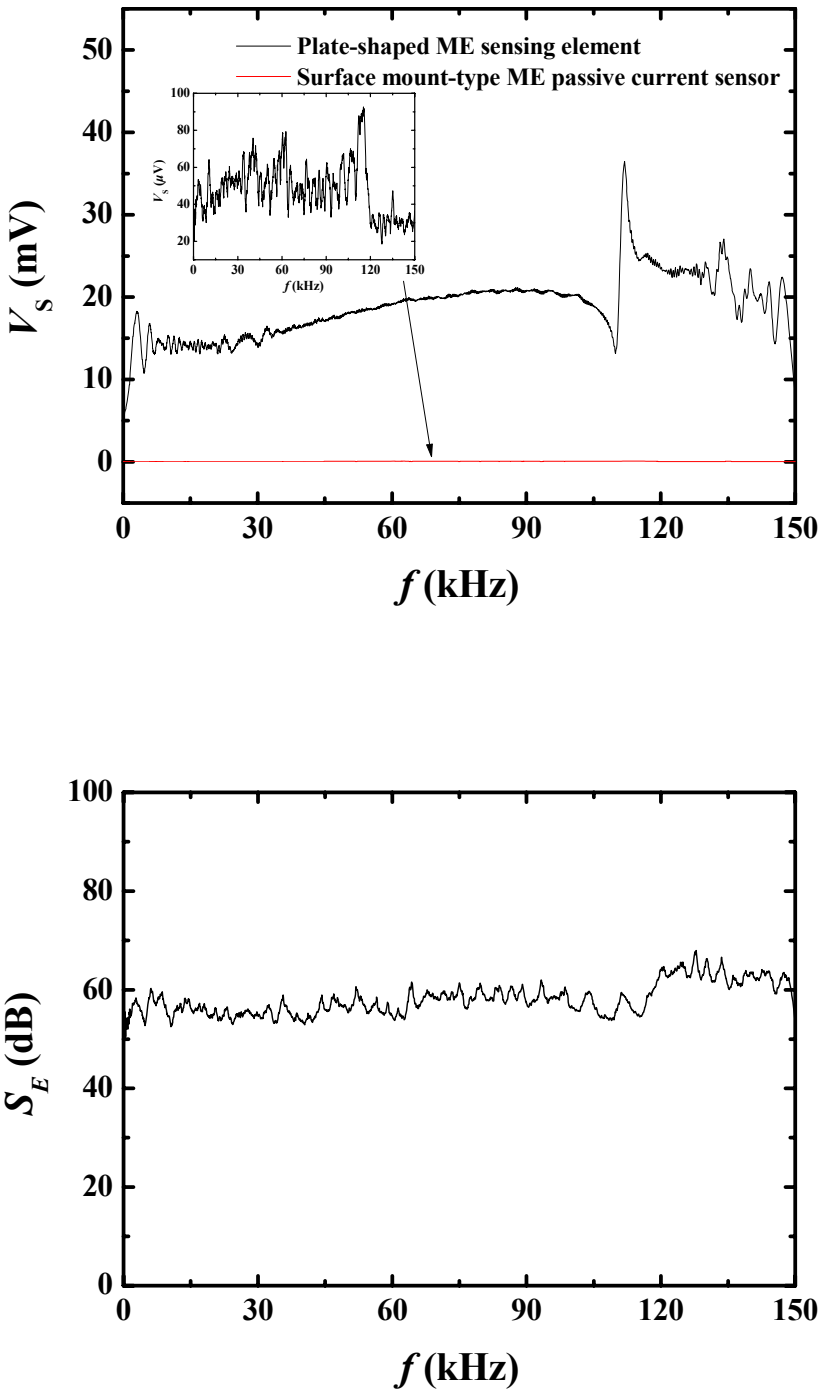

Fig. 4.18 **(a) Measured V_S – f curves of the surface mount-type ME passive current sensor and the plate-shaped sensing element at an electric field radiation of 114 V/m peak. (b) Measured S_E-f of the current sensor.**

4.2.6.3 Effect of Thermal Insulation

Figure 4.19 shows the experimental setup for measuring the thermal insulation performance of the surface mount-type ME passive current sensor. The ME passive current sensor under test was placed in a tube furnace (Carbolite MTF 12/38/400) equipped with a temperature process controller (Eurotherm 3216) and was subject to various temperatures (T) of 30−90 °C. For the quasistatic test, a low-frequency (f = 50 Hz) sinusoidal current (I) in the range of 0.1−3 A peak was generated by an arbitrary waveform generator (Agilent 33210A) via a constant-current supply amplifier (AE Techron 7796HF) to a 3 mm diameter high-temperature electrical cable inserted through the tube furnace and terminated with an 0.47 Ω resistor load to the ground. A swept sinusoidal current (I) of 1 A peak in the prescribed frequency (f) range of 25 Hz−150 kHz was used for the dynamic test. For

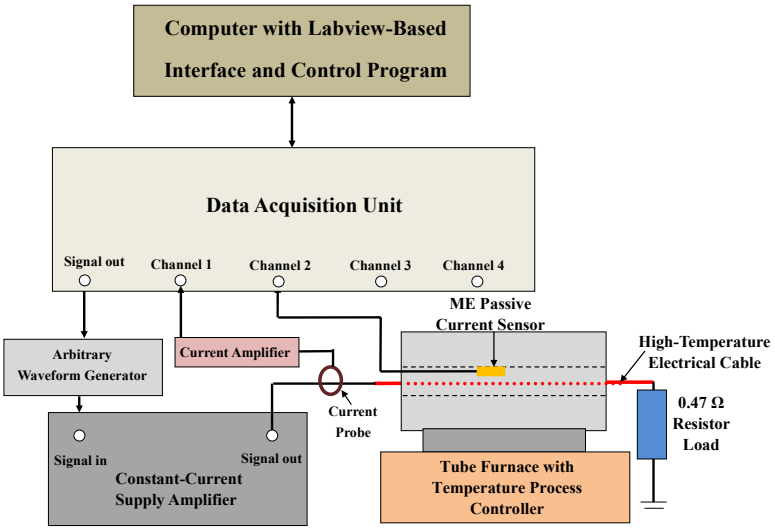

Fig. 4.19 Experiment setup for measuring the thermal insulation performance of the surface mount-type ME passive current sensor.

both tests, a current probe (Hioki 9273) was clamped on the electrical cable to measure the cable currents (I) via a current amplifier (Hioki 3271). The induced voltage (V_S) from the ME passive current sensor was sampled and measured by a data acquisition unit (Nation Instruments NBC-2110 and NI-PCI6132) under the control of a computer with a Labview-based interface and control program.

Figures 4.20(a) illustrates the measured V_S as a function of the applied I at 50 Hz under various T. V_S has a good linear response to I for the whole measured I range at various T. Figure 4.20(b) shows S_I as a function of T at 50 Hz. The values of S_I are obtained from the slopes of the V_S–I plots in Fig. 4.20(a). S_I decreases slightly from ~67 to ~58 mV/A when T is increased from 30 to 60 °C. The decrease is ~13% with the first slope (i.e., temperature compensation coefficient for current sensitivity) of -0.27 mV/A/°C. As T is increased beyond 60 °C, S_I exhibits an obvious decrease with the second slope of -1.92 mV/A/°C. At T = 90 °C, S_I becomes very small, i.e., ~0.57 mV/A. This is a result of the depolarization effect of the PMN−PT single crystal since its T_C is as low as 80 °C [78]. Beyond 80 °C, the piezoelectricity in the PMN−PT single-crystal plate becomes vanish and S_I becomes vanish too. Figures 4.20(c) plots the waveforms of V_S at an applied I of 1 A peak for T = 30, 60, and 80 °C. The V_S waveforms are very stable with 67, 58, and 29 mV peak at T = 30, 60, and 80 °C, respectively. This demonstrates the ability of stable signal conversion from I to V_S in our ME passive current sensor even at T = 80 °C. The fact that V_S shows an opposite phase with I can be explained by the negative sign of the piezoelectric voltage coefficient ($g_{31,p}$) in the PMN−PT single-crystal plate.

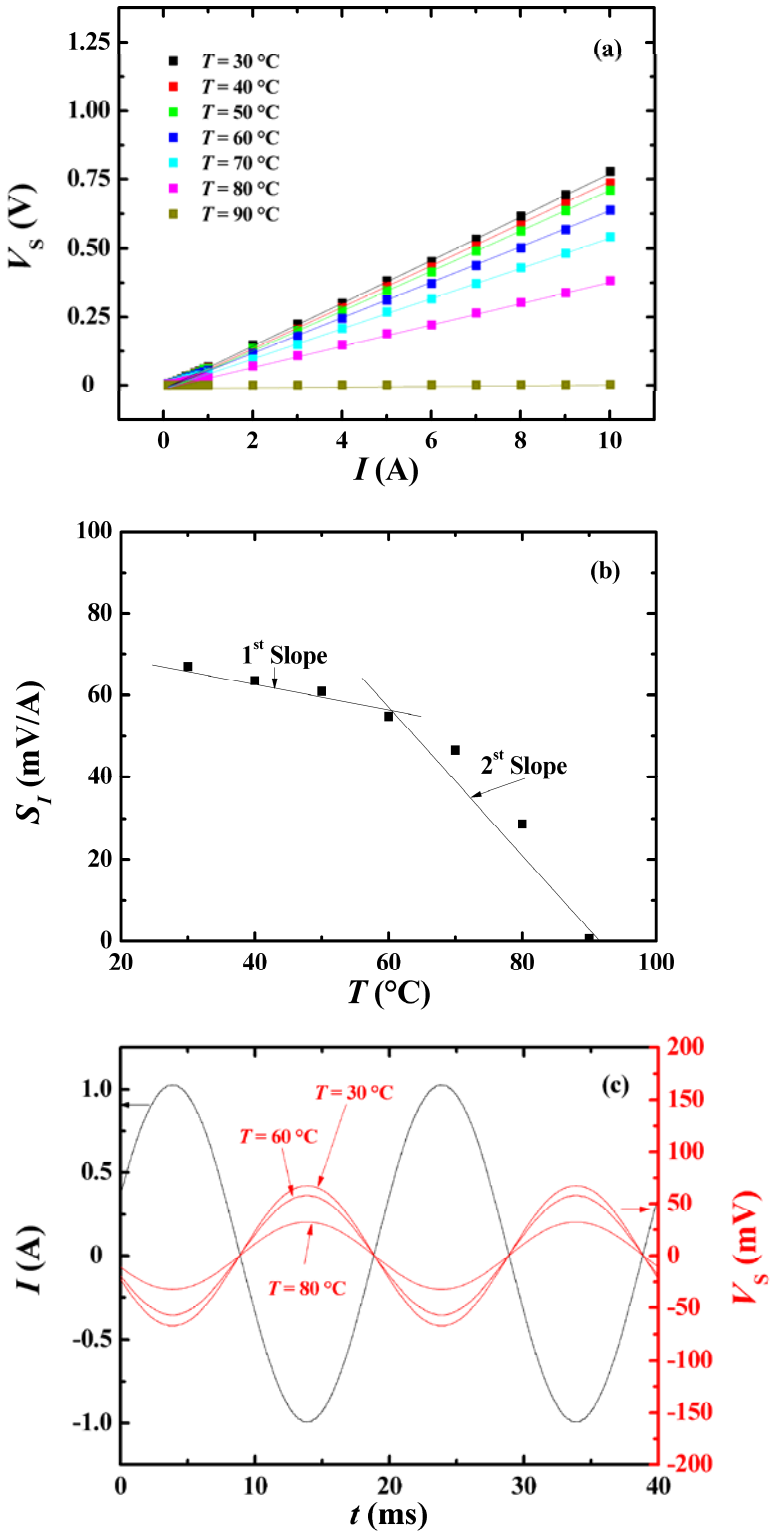

Fig. 4.20 (a) Measured V_S as a function of I at 50 Hz under various T; (b) Measured S_I as a function of T at 50 Hz; (c) Measured V_S waveforms due to an applied I of 1 A peak at 50 Hz for three different T of 30, 60, and 80 °C.

Figure 4.21 shows the measured S_I as a function of f at various T with I = 1 A peak. The largest S_I is observed at T = 30 °C for both the non-resonance and resonance ranges. The non-resonance and resonance (~98 kHz) S_I are found to be ~67 and ~363 mV/A, respectively. The resonance f decreases from 98 to 96.6 kHz when T is increased from 30 to 80 °C.

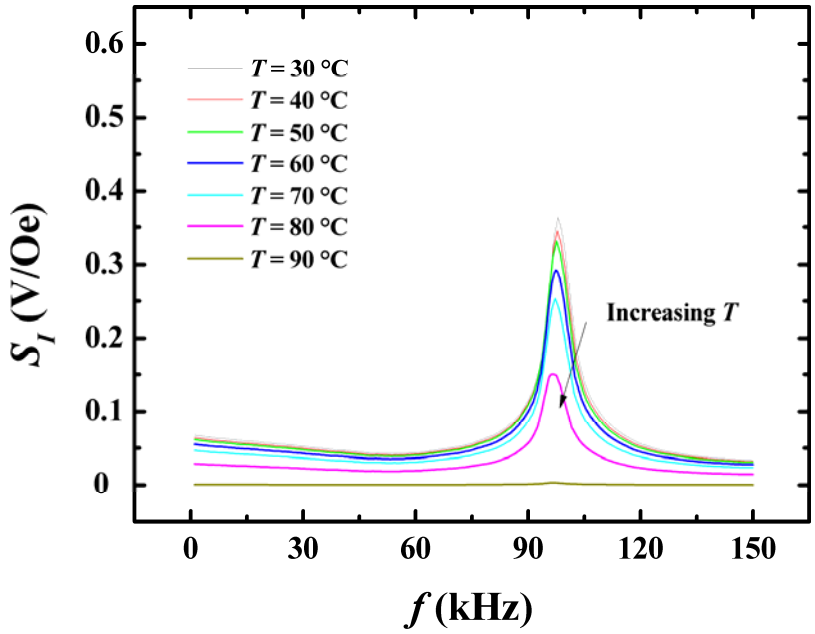

Fig. 4.21 Measured S_I as a function of f at various T for the surface mount-type ME passive current sensor.

4.2.7 Summary of Useful Performance Data

Table 4.4 summarizes the useful performance data of the surface mount-type ME passive current sensor. The current sensor has a wide measurable current range from 0.1 to >10 A, together with a large current sensitivity (S_I) of 67 mV/A, in the frequency range of 25 Hz−60 kHz at 30 °C with a small temperature compensation slope of -0.27mV/A/°C in the temperature range of 30−60 °C. It also has a high electric field shielding effectiveness (S_E) in excess of 50 dB. All these features are realized in a small and light-weight package of 24.2 mm length, 20 mm width, 6 mm height, and 20 g weight.

Table 4.4 Summary of the useful performance data of the surface mount-type ME passive current sensor.

Parameter	Symbol	Value
Measurable Current Range (A)	I	0.1 − >10
Current Sensitivity at 30 °C (mV/A)	S_I	67
Operating Frequency (Hz)	f	25−60,000
Working Temperature (°C)	T_w	30−60
Temperature Compensation Coefficeint for Current Sensitivity at 30−60 °C (mV/A/°C)	T_{comp}	-0.27
Electric Field Shielding Effectiveness (dB)	S_E	>50
Dimensions (mm)	$l \times w \times t$	24.2 x 20 x 6
Weight (g)	W	20

4.3 Clamp-Type ME Passive Current Sensor

4.3.1 Conceptual Design and Design Requirements

Figure 4.22 shows the conceptual design of the proposed clamp-type ME passive current sensor. The design of this current sensor is essentially based on the ring-shaped ME sensing element developed in Section 3.3 of Chapter 3. The current sensor has an open-and-close lock design in the plastic case so that it can clamp on electrical cables or conductors to get access to the complete magnetic field paths governed by the electrical cables or connectors. Accordingly, the ring-shape ME sensing element is separated into two half-rings installed inside the cover and body of the plastic case. When the case cover is closed and locked, the two half-rings apparently form a complete ring.

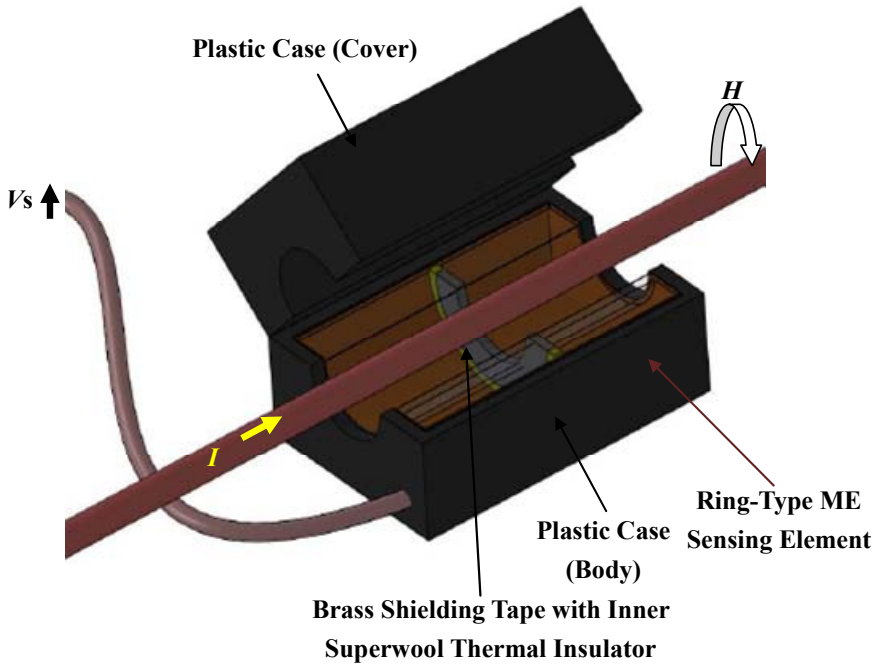

Fig. 4.22 Conceptual design of the proposed clamp-type ME passive current sensor for detecting magnetic fields governed by current-carrying electrical cables or conductors.

It is noted that as the ring-shaped ME sensing element features an internal magnetic biasing provided by the inner Terfenol-D short fiber−NdFeB magnet−epoxy three-phase magnetostrictive composite ring, the study of the effect of magnetic field biasing field as in Section 4.2.2 for the surface mount-type ME passive current sensor is not required. However, the effects of electric field shielding and thermal insulation still need to be considered in this clamp-type ME passive current sensor.

In general, the specifications of the clamp-type ME passive current sensor are set as follows:

(1) It should have a high electric field shielding effectiveness (S_E) in excess of 40 dB over the operating frequency range of 25 Hz −150 kHz.

(2) It should have a high working temperature up to 90 °C with a small deterioration in current sensitivity (S_I) of <25 %.

(3) It should be ease of installation and clampable on electrical cables or conductors.

(4) It should be compact in size, preferably within 40 × 30 × 30 mm^3.

(5) It should be light weight, preferably <45g.

4.3.2 Effect of Electric Field Shielding

According to Eqs. (4.12) and (4.13) in Section 4.2.3, the shielding effectiveness for electric fields (S_E) and that for magnetic fields (S_H) are strongly dependent upon the relative permeability (μ_r) and relative conductivity (σ_r) of the shields. From Fig. 4.7, we know that a high S_E in excess of 200 dB can be obtained in brass, aluminum, and iron shields with thicknesses ≥0.1 mm [Fig. 4.7]. From Fig. 4.8, a usefully small S_H of <10 dB can be achieved in both brass and aluminum shields with thicknesses ≤0.1 mm. Since plastic was used for the case of the clamp-type ME passive current sensor, an additional layer of brass shielding tape of 0.1 mm thickness was employed to provide a good electric field shielding for the current sensor as illustrated in Fig. 4.22.

4.3.3 Effect of Thermal Insulation

ANSYS® 10.0 was used to perform the finite element transient thermal analysis of the clamp-type ME passive current sensor as in Section 4.2.4.1 for the surface mount-type ME passive current sensor. Figure 4.23 shows the 2-D finite element model for computing the time-dependent temperature distributions of our proposed current sensor. The element PLANE 55 with a 2-D thermal conduction capability and consisting of four element nodes with single degree-of-freedom, i.e., temperature, at each node was deployed in the finite element mode. A total of 2194 plane elements and 2316 element nodes were used. The thermomechanical properties as stated in Table 4.5 were employed for the plastic case, superwool 607 thermal insulator, Terfenol-D composite ring, PZT ceramic ring, and NdFeB magnet bars. The brass shielding tape was very thin (0.1 mm thickness) compared with other components, so it was not taken into account in the finite element model. The boundary condition was taken to be an application of a steady working (environmental) temperature of 90 °C in all directions.

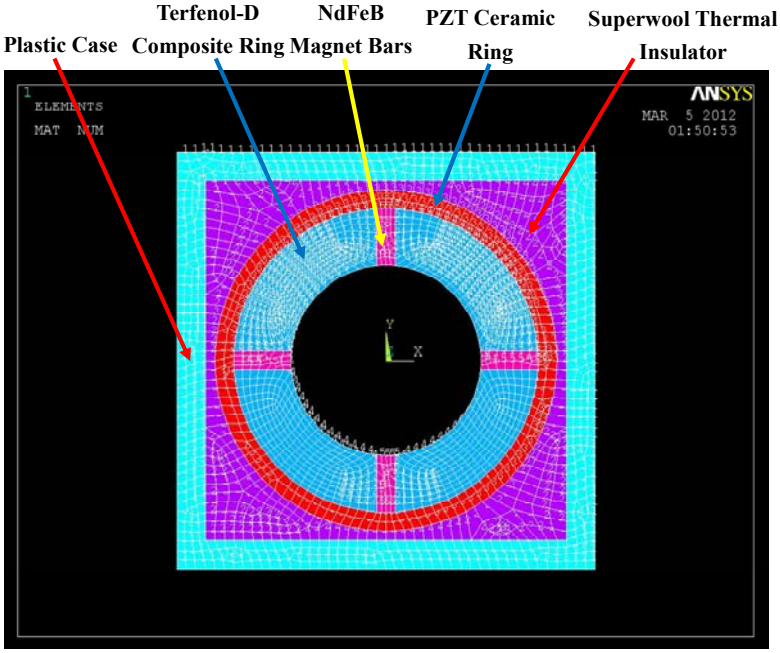

Fig. 4.23 The 2-D finite element model used to compute the time-dependent temperature distributions of the clamp-type ME passive current sensor.

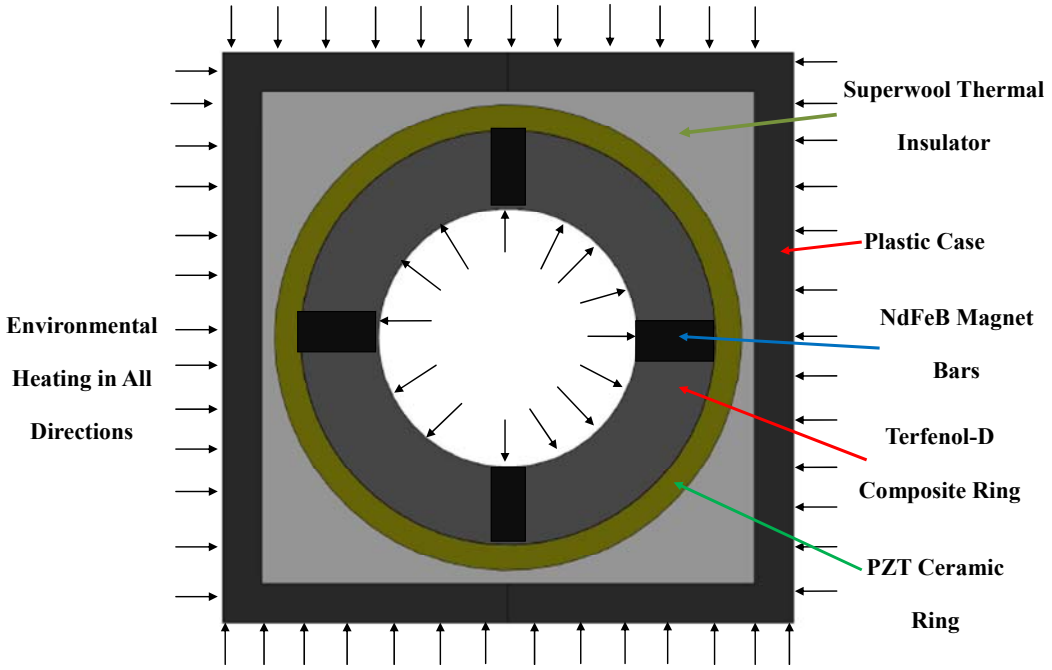

Fig. 4.24 Schematic diagram (end view) showing the boundary condition applied in the finite element transient thermal analysis of the clamp-type ME passive current sensor.

Table 4.5 Thermomechancial properties of plastic case, superwool thermal insulator, Terfenol-D composite ring, PZT ceramic ring, and NdFeB magnet bars.

Parameter	Symbol	Plastic Case	Superwool 607 Thermal Insulator	Terfenol-D Composite Ring	PZT Ceramic Ring	NdFeB Magnet Bar
Density (kg/m^3)	ρ	1.3	6	5310	7700	7500
Specific Heat capacity (J/kg·°C)	c	1200	1357	1100	880	444
Thermal Conductivity (W/m·°C)	k	0.16	0.06	0.19	1.5	1.7

Figure 4.25 illustrates the computed time-dependent temperature distributions of the clamp-type ME passive current sensor in experience of a steady working (environment) temperature of 90 °C in all directions. It is seen that the times required for the ring-shaped ME sensing element to fully reach 60 and 90 °C are ~200 and 800 s, respectively. The temperature development in this clamp-type ME passive current sensor is slower than that in the surface mount-type one as shown Fig. 4.12. The main reason may be due to the increased specific heat capacity in both the plastic case (c = 1200 J/kg·°C) and Terfenol-D composite ring (c = 1100 J/kg·°C) used in the clamp-type design compared to the brass shielding case (c = 385 J/kg·°C) and Terfenol-D alloy plate (c = 320 J/kg·°C) employed in the surface mount-type design.

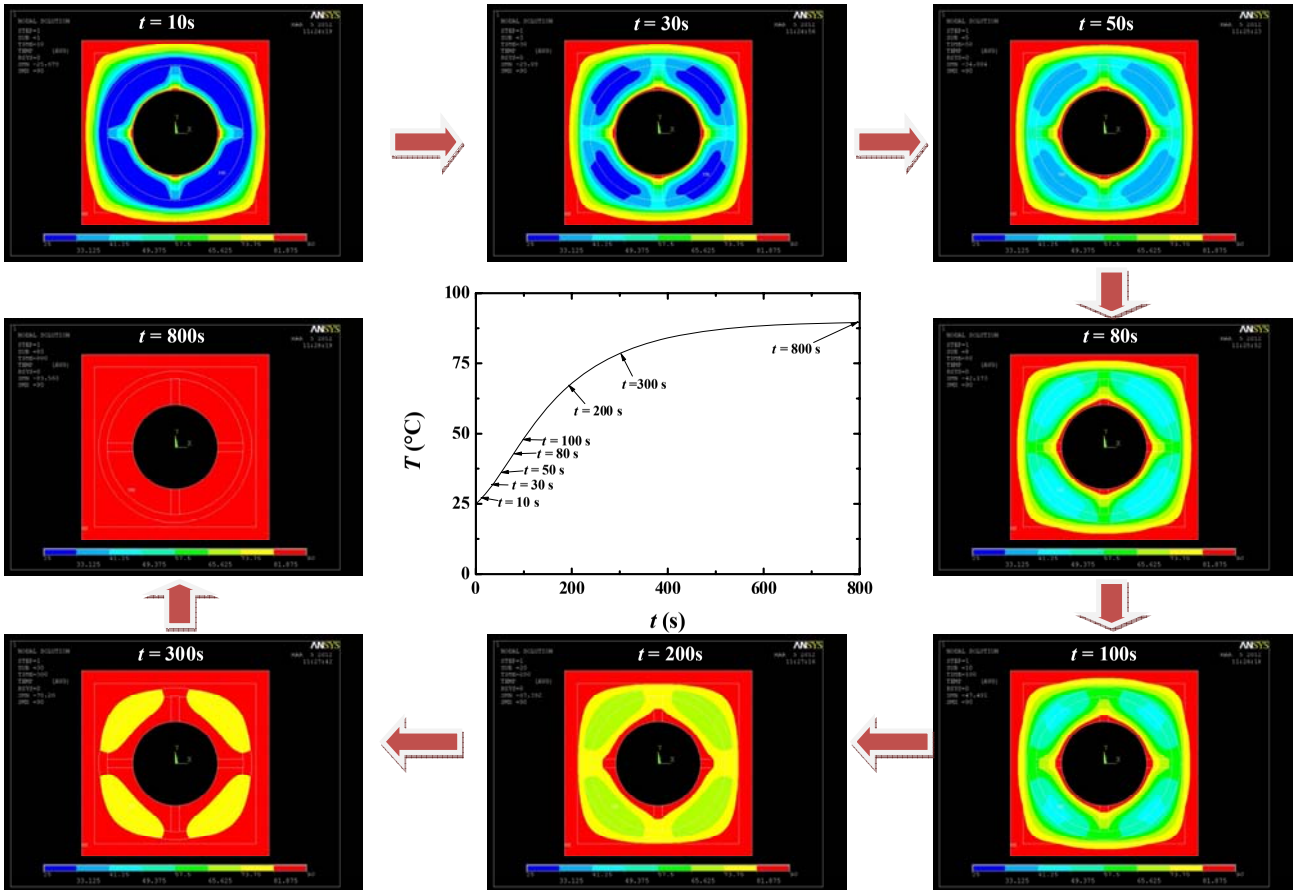

Fig. 4.25 Computed time-dependent temperature distributions of the clamp-type ME passive current sensor at a steady working (environmental) temperature of 90 °C.

4.3.4 Fabrication

Figure 4.26 displays the schematic diagram of the fabrication of the clamp-type ME passive current sensor. First, the plastic case was purchased from the component market and a 3 mm hole was opened inside the body of the case for coaxial cable insertion. Second, a 0.1 mm thick brass shielding tape was glued on the inner surfaces of the cover and body of the plastic case. Third, a layer of superwool thermal insulator was applied to the inner surfaces of the case cover and body. Fourth, a ring-shaped ME sensing element with dimensions of 18 mm outer diameter and 10 mm inner diameter was cut into two half-rings, and a 1.5 m long RG179 coaxial cable with a BNC connector was connected in parallel to the two half-rings for signal output and grounded with the brass shielding tape for electric field shielding. Fifth, while the half-rings and the coaxial cable were positioned suitably in the plastic case, the superwool was applied again to fill in the gaps between the half-rings and the plastic case. Finally, an epoxy was applied to fix any movable parts. The overall dimensions and weight of the fabricated sensor were measured to be 40 mm (length) × 30 mm (width) × 30 mm (height) and 44 g, respectively.

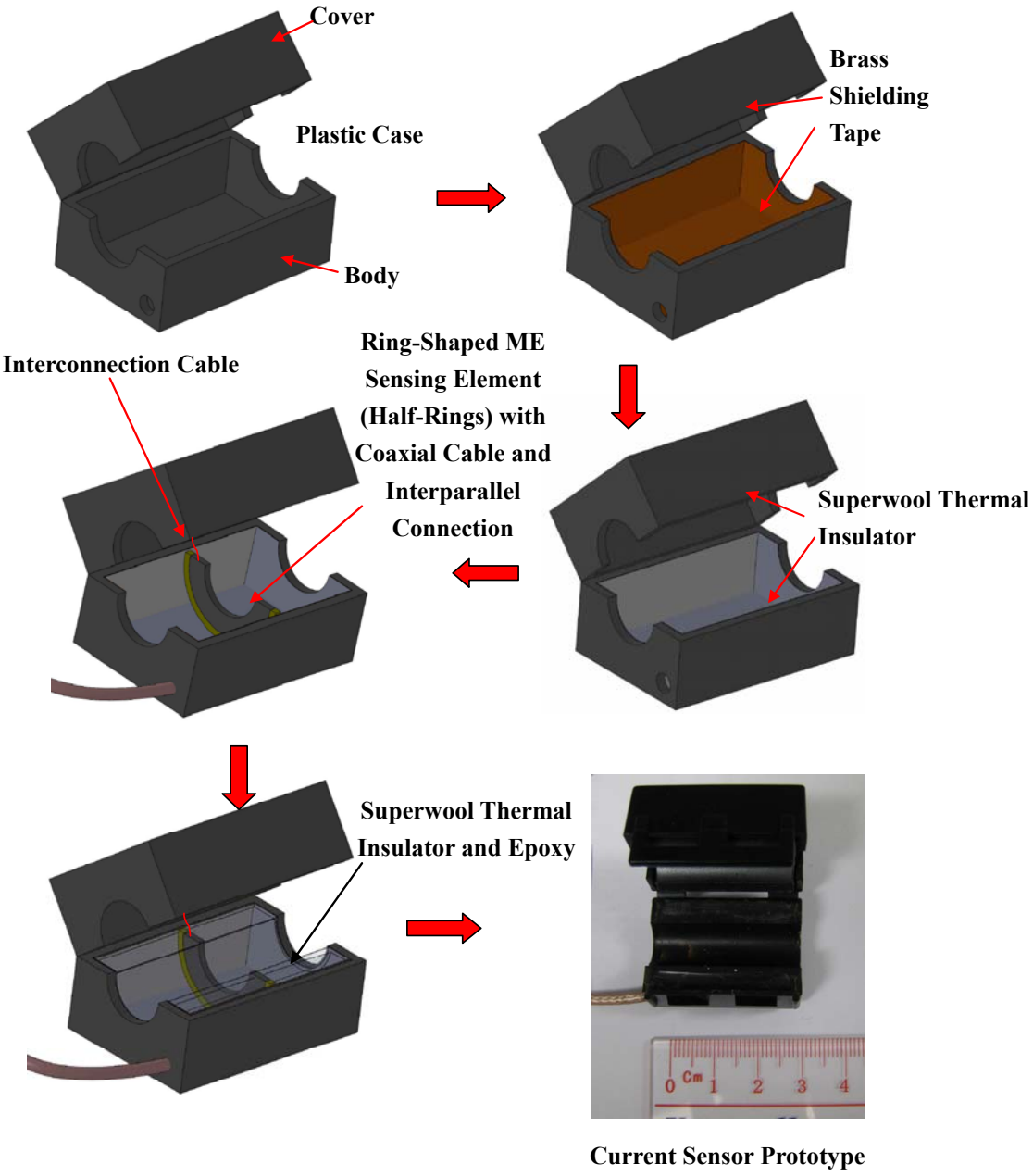

Fig. 4.26 Schematic diagram showing the fabrication of the clamp-type ME passive current sensor.

4.3.5 Characterization

The experimental setups for testing the electric field shielding and thermal insulation performance of the surface mount-type ME passive current sensor shown in Figs. 4.17 and 4.19 were utilized for testing the clamp-type ME passive current sensor. The connections and parameter settings of each equipment in the setups remained unchanged.

4.3.6 Results and Discussion

4.3.6.1 Effect of Electric Field Shielding

Figure 4.27(a) shows the V_S–f curves of the clamp-type ME passive current sensor and the associated ring-type ME sensing element under an electric field radiation of 114 V/m peak. The sensing element produces significant noise with amplitude varying from 3−30 mV. The noise amplitude decreases to 30−150 μV in the current sensor because of the electric field shielding provided by the brass shielding tape. S_E of the current sensor as determined using Eq. (4.12) is plotted in Fig. 4.27(b). It is clear that S_E is higher than 40 dB in the f range of 25 Hz – 150 kHz even though the thickness of brass shielding tape is only 0.1 mm. This is because S_E is mainly dependent upon reflection loss R_E.

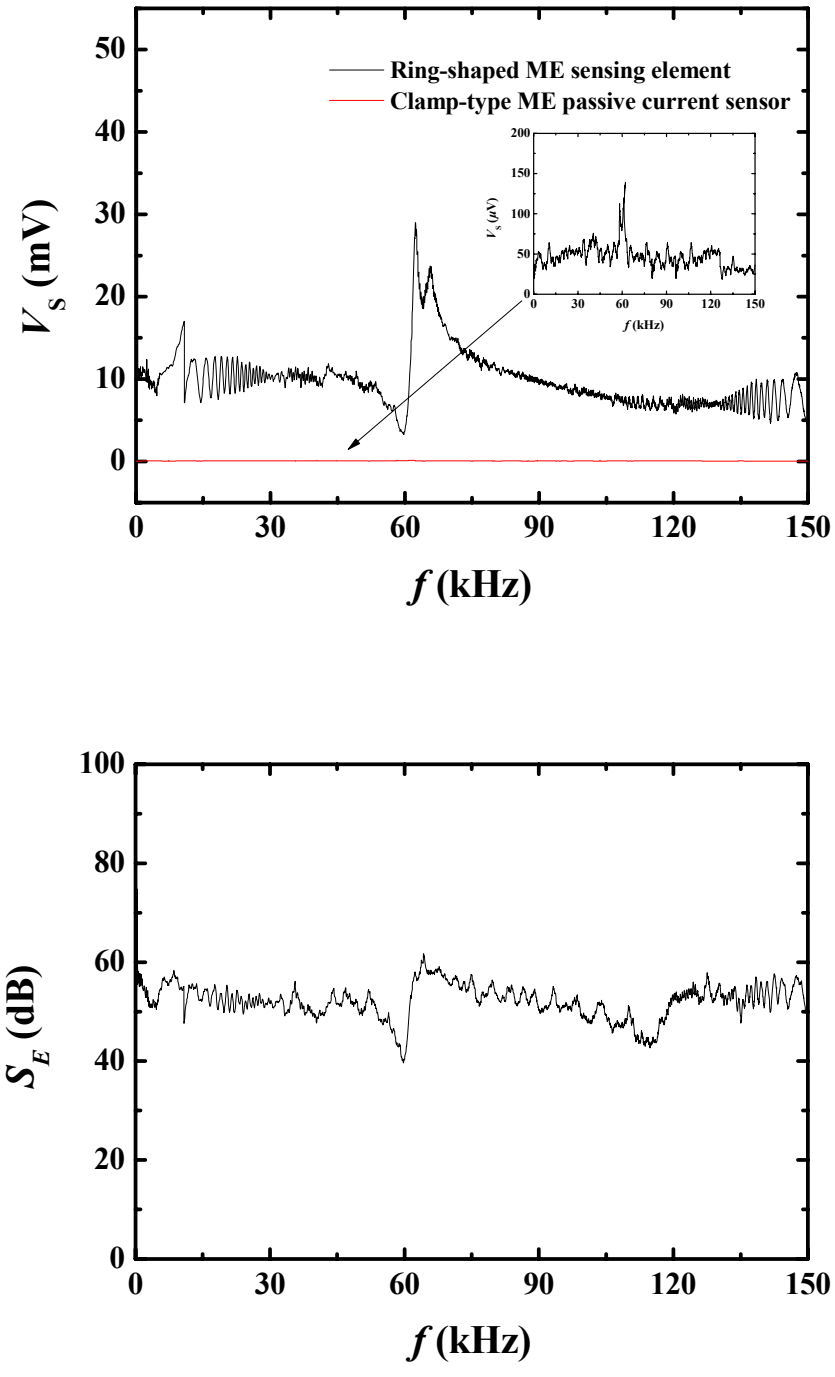

Fig. 4.27 **(a) Measured $V_S - f$ curves of the clamp-type ME passive current sensor and the ring-shaped ME sensing element at an electric field radiation of 114 V/m peak. (b) Measured S_E-f curve of the current sensor.**

4.3.6.2 Effect of Thermal Insulation

Figures 4.28(a) plots the measured V_S as a function of the applied I at 50 Hz under various T for the clamp-type ME passive current sensor. Similar to the surface mount-type one in Fig. 4.18, V_S of this clamp-type sensor has a good linear response to I in the whole measured I range at various T. Figure 4.28(b) shows S_I as a function of T at 50 Hz where the values of S_I are obtained from the slopes of the V_S−I plots in Fig. 4.28(a). S_I decreases slightly from 5.7 to 4.5 mV/A when T is increased from 30 to 90 °C. The decrease is ~21% with a slope of -0.02 mV/A/°C. This slope represents the temperature compensation coefficient for current sensitivity. Comparing to the surface mount-type sensor, this clamp-type sensor can work properly for temperatures as high as 90 °C. Figures 4.28(c) displays the waveforms of V_S at an applied I of 1 A peak for T = 30, 60, and 90 °C. The V_S waveforms are stable with 5.8, 5.2, and 4.5 mV peak at T = 30, 60, and 90 °C, respectively. The fact that V_S shows an opposite phase with I can be explained by the negative sign of the piezoelectric voltage coefficient ($g_{31,p}$) in the PZT ceramic ring of the ring-shaped ME sensing element. This phenomena is the same as the surface mount-type current sensor in Fig. 4.19(c).

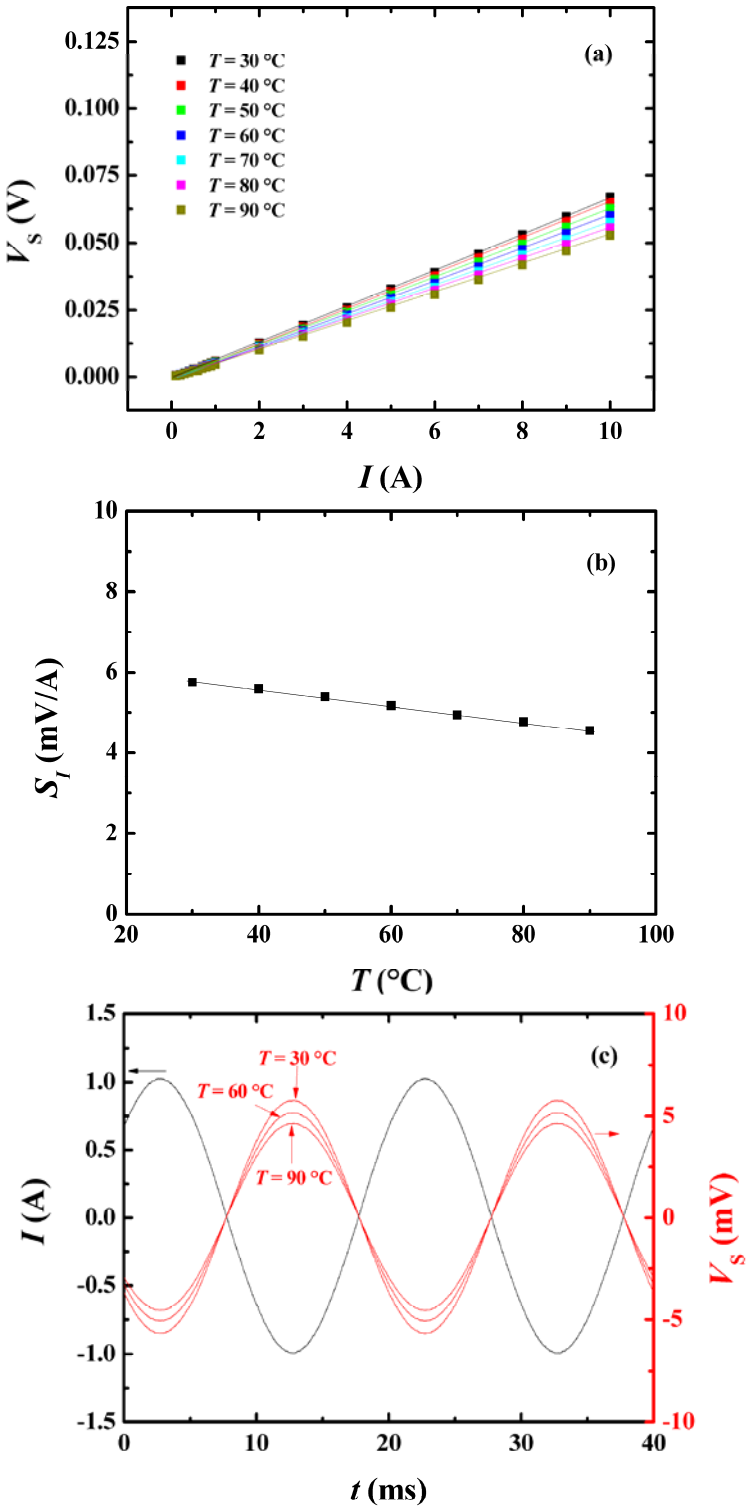

Fig. 4.28 (a) Measured V_S as a function of I at 50 Hz under various T; (b) Measured S_I as a function of T at 50 Hz; (c) Measured V_S waveforms due to an applied I of 1 A peak at 50 Hz for different T of 30, 60, and 90 °C.

4.3.7 Summary of Useful Performance Data

Table 4.6 gives a summary of the useful performance data of the clamp-type ME passive current sensor. The current sensor has a board measurable current range from 0.1 to >10 A and a high current sensitivity (S_I) of 5.8 mV/A at 30 °C with a small temperature compensation slope of -0.02 mV/A/°C in the wide temperature range of 30−90 °C. Besides, it has a high electric field shielding effectiveness (S_E) in excess of >40 dB. In addition, it has a small and light-weight package of 40 mm length, 30 mm width, 30 mm height, and 44 g weight with an open-and-close lock design. .

Table 4.6 Summary of the useful performance data of the clamp-type ME passive current sensor.

Parameter	Symbol	Value
Measurable Current Range (A)	I	0.1 − >10
Current Sensitivity at 30 °C (mV/A)	S_I	5.8
Working Temperature (°C)	T_w	30−90
Temperature Compensation Coefficeint for Current Sensitivity at 30−90 °C (mV/A/°C)	T_{comp}	-0.02
Electric Field Shielding Effectiveness (dB)	S_E	>40
Dimensions (mm)	$l \times w \times t$	40 x 30 x 30
Weight (g)	W	44

Chapter 5

Development of Wireless Communication Units

5.1 Introduction

Based on the plate-shaped and ring-shaped ME sensing elements developed in Chapter 3, surface mount-type and clamp-type ME passive current sensors have been realized with magnetic field biasing, electric field shielding, and thermal insulation capabilities in Chapter 4. In recent years, the concepts of wireless sensors and wireless condition monitors have become popular. As pointed out in Chapter 1, state-of-the-art wireless sensors and wireless condition monitors are mainly based on the integration of active sensors and wireless communication (transmitter and receiver) units as well as the powering of them by power packs or batteries. In fact, the need of powering the active sensors in addition to the wireless communication units as well as the demand for wiring the power cables apart from the signal cables have imposed great challenges on the installation and maintenance of wireless condition monitors. The technological breakthrough in ME passive current sensors in the present study can create a new format for wireless sensors and wireless condition monitors because powering is only required for wireless communication units.

In this chapter, two different types of multichannel wireless communication units are developed and reported to fit with the surface mount-type and clamp-type ME passive current sensors developed in Chapter 4 for applications in electrical assets in Chapter 6. These include: (1) short-range, 4-channel, 2.4 GHz wireless communication unit and (2) long-range, 3-channel, 3G/2G wireless communication unit. For each type of unit, the conceptual design and design requirements are stated, the hardware and software developments are described, the performance evaluation and results are presented, and the useful performance data are summarized.

5.2 Short-Range, 4-Channel, 2.4 GHz Wireless Communication Unit

5.2.1 Conceptual Design and Design Requirements

Figure 5.1 shows the system block diagrams of the single-channel wireless transmitter and the 4-channel wireless receiver in the proposed short-range, 4-channel, 2.4 GHz wireless communication unit. A complete 2.4 GHz wireless communication unit consists of four single-channel wireless transmitters and one 4-channel wireless receiver, all powered by batteries. Each of the four single-channel wireless transmitters is composed of three functional modules, namely: signal conditioning module, central processing module, and wireless transmission module. The 4-channel wireless receiver contains four identical sets of functional modules, namely: wireless receiving module and digital-to-analog (D-A) conversion module.

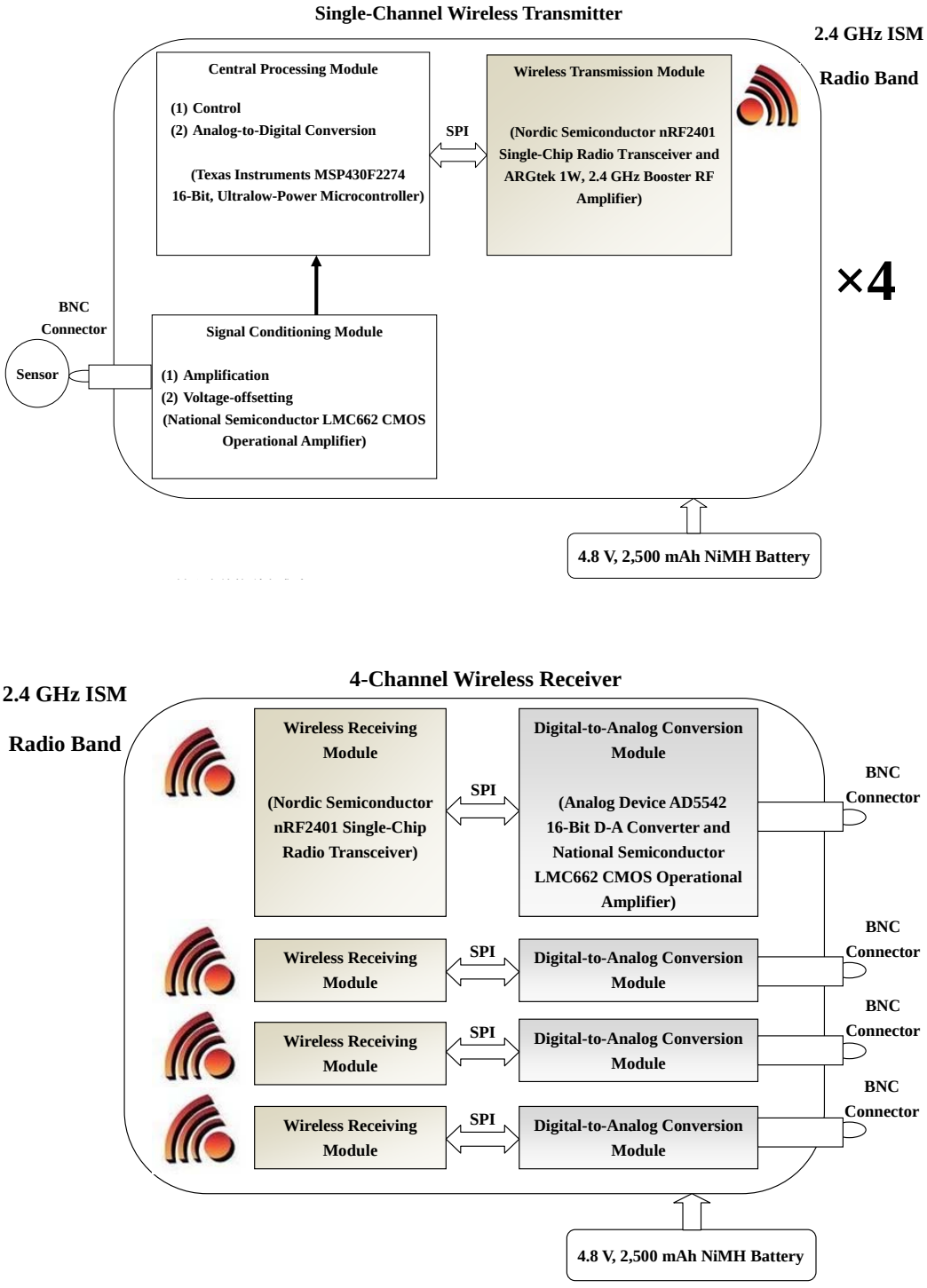

Fig. 5.1 System block diagrams of the single-channel wireless transmitter and the 4-channel wireless receiver in the proposed short-range, 4-channel, 2.4 GHz wireless communication unit.

In operation, each of the four 2.4 GHz communication channels (i.e., each of the four transmitter and receiver pairs) functions at a unique frequency in the 2.4 GHz international industrial, scientific, and medical (ISM) radio band of 2.4000−2.4835 GHz. On the side of the four single-channel wireless transmitters, the current signatures detected by the ME passive current sensors and in form of analog signals are coupled to the inputs of the wireless transmitters through Bayonet Neill–Concelman (BNC) connectors before being transformed into a stable, determined, non-negative analog-signal format by the signal conditioning modules with amplification and dc-offsetting functions. The conditioned analog signals are converted into a usable digital-data format by the central processing modules, each comprising a microcontroller with the desired clock speed and an analog-to-digital (A-D) converter with the preferred A-D conversion resolution and sampling rate. The digital data is transferred to the wireless transmission module through the high-speed serial peripheral interface (SPI) port for wireless data transmission at the predetermined data transmission frequency (in the 2.4 GHz ISM radio band), rate, and power. On the side of the 4-channel wireless receiver, the wireless data received by the wireless receiving module of each communication channel is converted into a usable analog-signal format by its digital-to-analog (D-A) conversion module. The converted analog signals are coupled to the external means through BNC connectors. The operations of each single-channel wireless transmitter and each 4-channel wireless receiver are supported by nickel-metalhydride (NiMH) battery at suitable voltage and current ratings.

The following specifications are required for designing the 2.4 GHz wireless communication unit:

(1) It should be operated in the 2.4 GHz international ISM radio band of 2.4000−2.4835 GHz.

(2) It should provide a sufficiently long communication range up to 300 m.

(3) It should have four signal-input, wireless-communication, and signal-output channels to simultaneously accommodate four ME passive current sensors.

(4) It should use BNC connectors as the signal-input and signal-output connectors.

(5) It should provide a voltage gain of 10 for all signal-input channels.

(6) It should have sufficiently high microcontroller data architecture of 16 bits and clock speed of 16 MHz.

(7) It should have reasonably high A-D conversion resolution of 10 bits and sampling rate of 200 k/s.

(8) It should have a high D-A conversion resolution of 16 bits and a short D-A conversion settling time of about 1 μs.

(9) It should have a high data transmission rate up to 1 Mbps and a short delay time of less than 20 ms between the transmission and reception points.

(10) It should be powered by 4.5–5.5 V, 2,500 mAh NiMH battery (i.e., 4 × AA 1.2 V, 2,500 mAh NiMH battery).

(11) It should have a small operating power of less than 1.5 W to ensure good energy saving with life time longer than 6 h.

5.2.2 Hardware Development

Figure 5.2 illustrates the circuit diagram of the single-channel wireless transmitter used in the 2.4 GHz wireless communication unit and conceptualized in Fig. 5.1(a). There are four single-channel wireless transmitters in a 2.4 GHz wireless communication unit, each consisting of a signal conditioning module, a central processing module, and a wireless transmission module. The main components of the signal conditioning module, central processing module, and wireless transmission module are a National Semiconductor LMC662 CMOS operational amplifier, a Texas Instruments MSP430F2274 16-bit, ultralow-power microcontroller, and a Nordic Semiconductor nRF2401 single-chip radio transceiver with an ARGtek 1 W, 2.4 GHz booster radio frequency (RF) amplifier, respectively. The LMC662 CMOS operational amplifier is configured as an inverting amplifier with a voltage gain of 10 and a dc-offset of 2.5 V. The MSP430F2274 16-bit, ultralow-power microcontroller, which belongs to the MSP430 microcontroller family, not only has 16-bit data architecture and 16 MHz clock speed, but also contains a build-in A-D converter of 10-bit conversion resolution and 200 k/s sampling rate. The 10-bit A-D conversion resolution is sufficient for most 50 Hz-based electrical signal-sensing applications. The 200 k/s A-D sampling rate ensures that each sampling execution only takes 5 μs. The MSP430F2274 16-bit, ultralow-power microcontroller also provides the SPI port and the universal asynchronous receiver and transmitter (UART) port for interface with the wireless transmission module. The SPI port is used in our design. The nRF2401 single-chip radio transceiver is connected with an ARGtek 1 W, 2.4 GHz booster RF

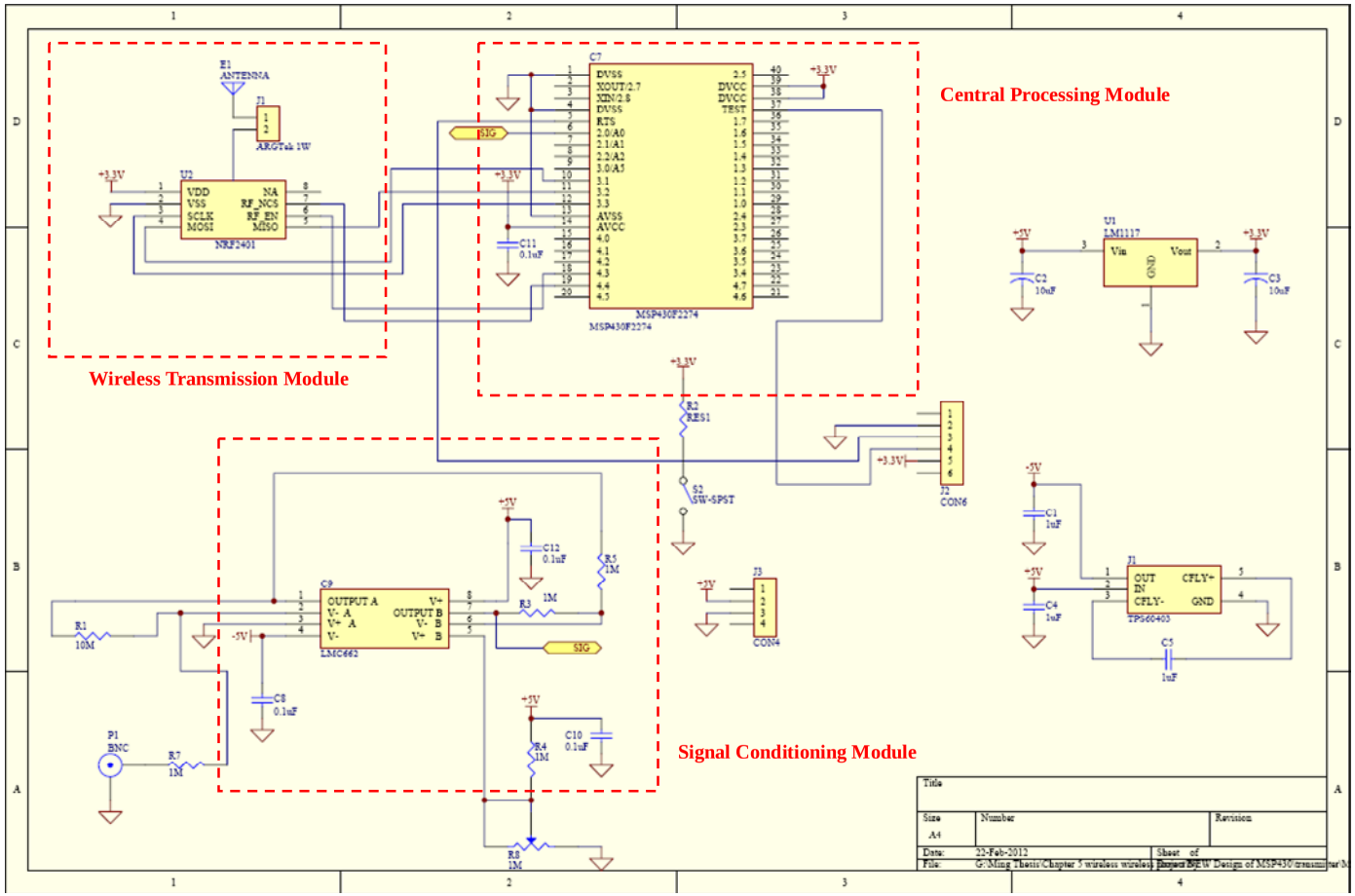

Fig. 5.2 Circuit diagram of the single-channel wireless transmitter in the 2.4 GHz wireless communication unit.

amplifier in the wireless transmission module. The nRF2401 single-chip radio transceiver has a configurable data transmission rate up to 1 Mbps and is operated in the 2.4 GHz international ISM radio band covering the 2.4000−2.4835 GHz frequency range. The ARGtek 1 W, 2.4 GHz booster RF amplifier is designed to amplify and transmit data at the nominal transmission frequency and power of 2.4 GHz and 1 W, respectively.

Figure 5.3 shows the circuit diagram of the 4-channel wireless receiver used in the 2.4 GHz wireless communication unit and conceptualized in Fig. 5.1(b). Four identical sets of single-channel wireless receiver are combined and built to form this 4-channel wireless receiver, each comprising of a wireless receiving module and a D-A conversion module. The main components of the wireless receiving module and the D-A conversion module are a Nordic Semiconductor nRF2401 single-chip radio transceiver and an Analogy Device AD5542 16-bit D-A converter with a National Semiconductor LMC662 COMS operational amplifier. Upon receiving the wireless data (unsigned integer) from the nRF2401 single-chip radio transceiver in the wireless receiving module, the AD5542 16-bit D-A converter converts the integer values to non-negative analog signals before passing them to the LMC662 CMOS operational amplifier to generate bipolar analog signals in the D-A conversion module. The 1 μs D-A conversion settling time ensures that there is enough time for the stabilization of the D-A conversion process. A dc supply voltage of 4.8 V, which is formed by connecting four pieces of AA 1.2 V, 2,500 mAh NiMH battery in series, is employed to energize each single-channel wireless transmitter and the 4-channel wireless

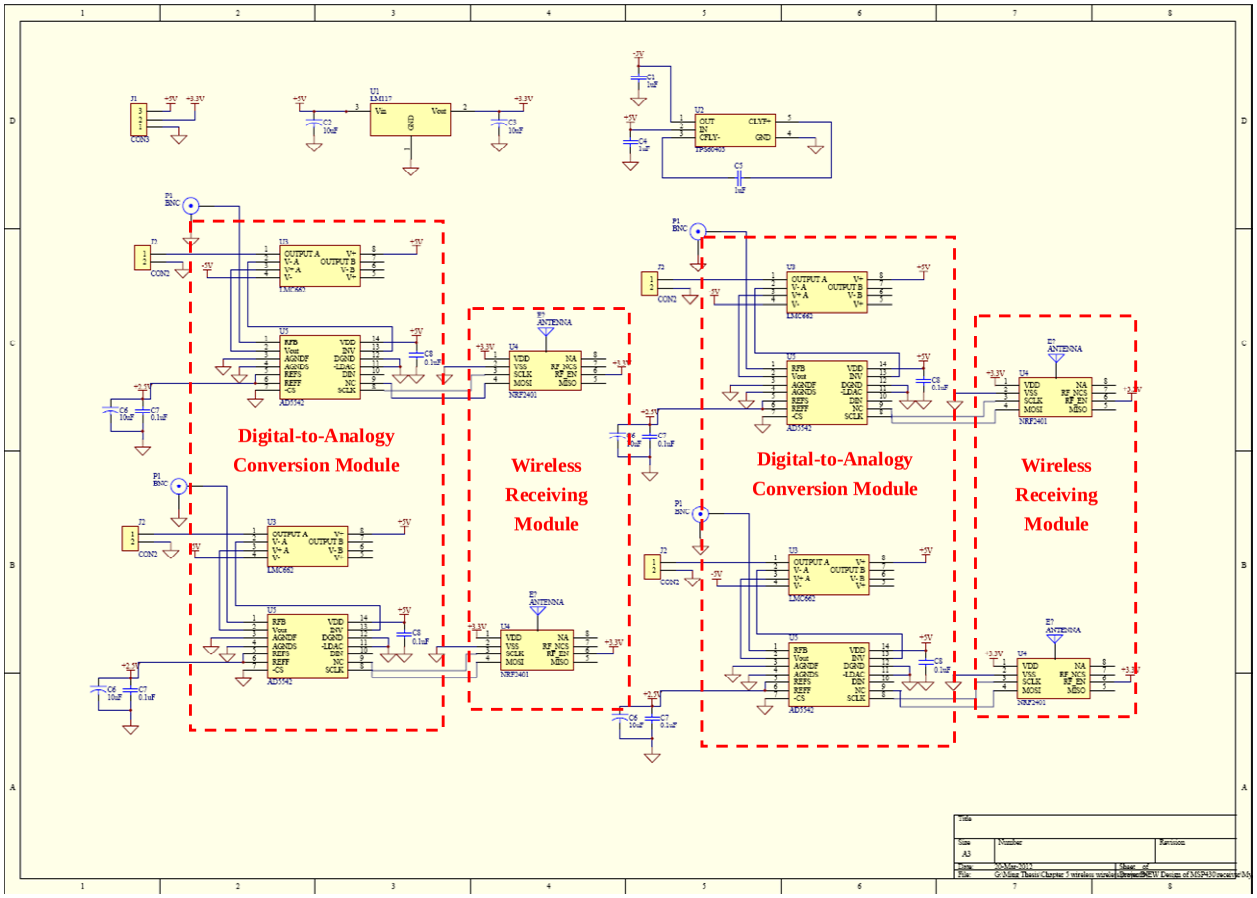

Fig. 5.3 Circuit diagram of the 4-channel wireless receiver in the 2.4 GHz wireless communication unit.

receiver. The current arrangement is expected to have a sufficiently long communication range up to 300 m with a short delay time of less than 20 ms between the transmission and reception points.

Figure 5.4 shows the photographs of the fabricated 2.4 GHz wireless communication unit. They involve the circuit board of the single-channel wireless transmitter [Fig. 5.4(a)], the circuit board of the 4-channel wireless receiver [Fig. 5.4(b)], and the full set of 2.4 GHz wireless communication unit having four single-channel wireless transmitters and one 4-channel wireless receiver [Fig. 5.4(c)].

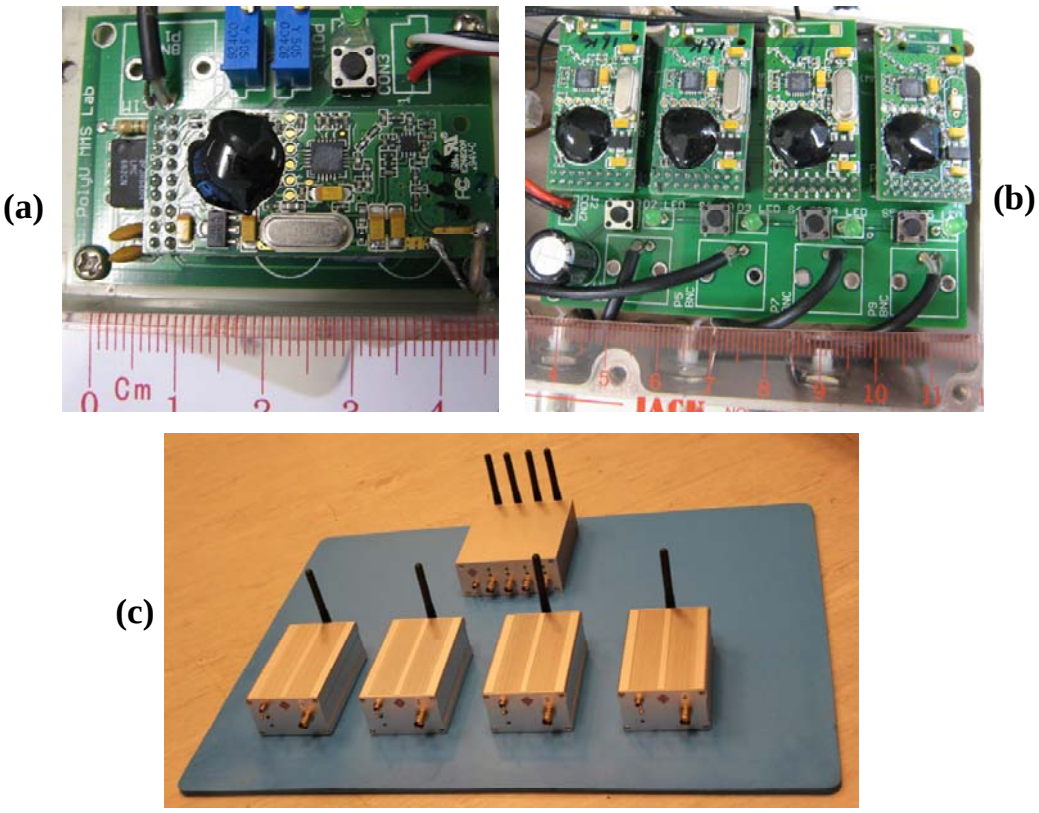

Fig. 5.4 Photographs of the fabricated 2.4 GHz wireless communication unit. (a) circuit board of the single-channel wireless transmitter; (b) circuit board of the 4-channel wireless receiver; and (c) full set of 2.4 GHz wireless communication unit having four single-channel wireless transmitters (the front ones) and one 4-channel wireless receiver (the back one).

5.2.3 Software Development

Figure 5.5 illustrates the flow diagram of the data communication process of the 2.4 GHz wireless communication unit. First, each of the four pairs of wireless transmitter and receiver is powered on and initialized to find and match its own wireless communication channel. If a wireless communication channel is established to form a transmitter and receiver pair, the A-D converter of the MSP430F2274 16-bit, ultralow-power microcontroller in the central processing module of the wireless transmitter starts to operate and converts the non-negative analog signals into digital data. The converted digital data is transmitted to the paired wireless receiver through the 2.4 GHz ISM radio band. In order to allow the wireless transmitter to create and transmit a radio packet, a sampling time interval of 20 μs is set in the program of the central processing module in the wireless transmitter for the A-D converter to decrease the sample rate to 50 ks/s. The ShockBurst^{TM} technology with first-in, first-out (FIFO) organization and manipulation is used to clock and transfer the wireless data [79]. On the wireless receiver side, the digital data is collected and converted back to analog signals by the wireless receiving module and the D-A conversion module, respectively.

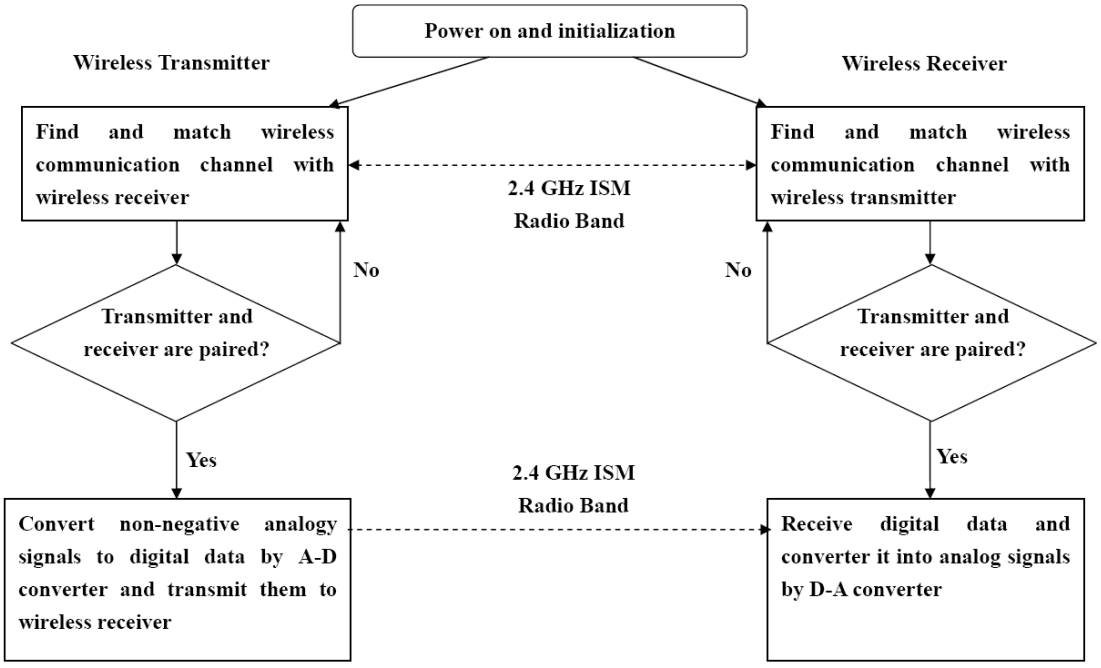

Fig. 5.5 Flow diagram of the communication process of the 2.4 GHz wireless communication unit.

5.2.4 Performance Evaluation

Figure 5.6 shows the experimental setup for the evaluation of the performance of the developed 2.4 GHz wireless communication unit in Fig. 5.4. Two different tests, one with an arbitrary waveform generator as the input and one with an ME passive current sensor as the input, were performed. For the test with arbitrary waveform generator, a sinusoidal voltage (V_T) of 0.1 V peak was generated at three different frequencies (f) of 50, 150, and 250 Hz by an arbitrary waveform generator (Tektronix AFG 3022B) to the BNC signal input of the wireless transmitter. For the test with ME passive current sensor, the surface mount-type ME passive current sensor shown in Fig. 4.12 was placed on a 3 mm diameter electrical cable connected with an 0.47 Ω resistor load to ground and energized by a sinusoidal current (I) of 1 A peak at

50, 150, and 250 Hz through an arbitrary waveform generator (Agilent 33210A) and a constant-current supply amplifier (AE Techron 7796HF). The voltage (V_R) output from the wireless receiver was measured by an oscilloscope (Tektroniz MSO2014). The dc supply voltage of the battery (V_B) was measured continually by a digital voltmeter (UNI-T UT39-C) when the 2.4 GHz wireless communication unit was under continuous operation so as to determine the battery life of the 2.4 GHz wireless communication unit. The wireless communication range (d) was also determined in the Fo Tan depot of MTR Corporation Limited by placing the wireless transmitter and receiver pair at a constant height of 1.5 m with respective to the floor and measuring the wireless signal strength for every 25 m increment in d for 1 min period. The wireless transmission strength (S_W) was determined using

$$S_W = \frac{t_{on}}{t_{meas}} \times 100\%, \tag{3.7}$$

where t_{on} is the time recorded for the signal-strength light-emitting diode (LED) to light up and t_{meas} (=1 min) is the time of measurement.

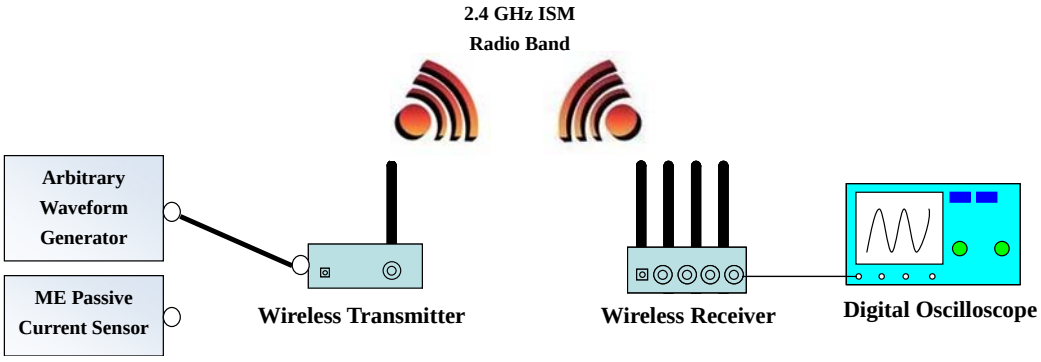

Fig. 5.6 Experimental setup for the evaluation of the performance of the developed 2.4 GHz wireless communication unit in Fig. 5.4.

5.2.5 Results and Discussion

5.2.5.1 Arbitrary Waveform Generator as the Input

Figure 5.7 shows the waveforms of arbitrary waveform generator output voltage (V_T) of 0.1 V peak at three different frequencies (f) of 50, 150, and 250 Hz. The corresponding waveforms output from the wireless receiver (V_R) at a wireless communication range (d) of 5 m are also included. It is seen that there exists a delay time of 14 ms between V_T and V_R in all cases. This delay time is mainly due to the conversion times of A-D and D-A converters as well as the data packet time of the wireless transmitter as stated in Section 5.2.2. Moreover, there is 10-times amplification between V_T and V_R. Nonetheless, the stable and clear V_R indicates the low noise nature of our wireless communication unit.

Figure 5.8 shows the dc supply voltage of battery (V_B) as a function of time (t) for the wireless transmitter. Since the ARGteck 1 W, 2.4 GHz booster RF amplifier was used in the wireless transmitter, the power consumption of the wireless transmitter is much more than the wireless receiver, and the battery life of the wireless transmitter plays the dominant role in the operating life time of the 2.4 GHz wireless communication unit. It is clear that V_B is 5.2 V when four pieces of AA 1.2 V, 2,500 mAh batteries are in the fully charged state. The higher resulting voltage level of 5.2 V compared to 4.8 V is mainly attributed to the use of 1.4 V voltage-mode charging method for the four pieces of AA 1.2 V, 2,500 mAh NiMH battery. After the four batteries are in the fully charged state, each of them is 1.3 V instead of 1.2 V.

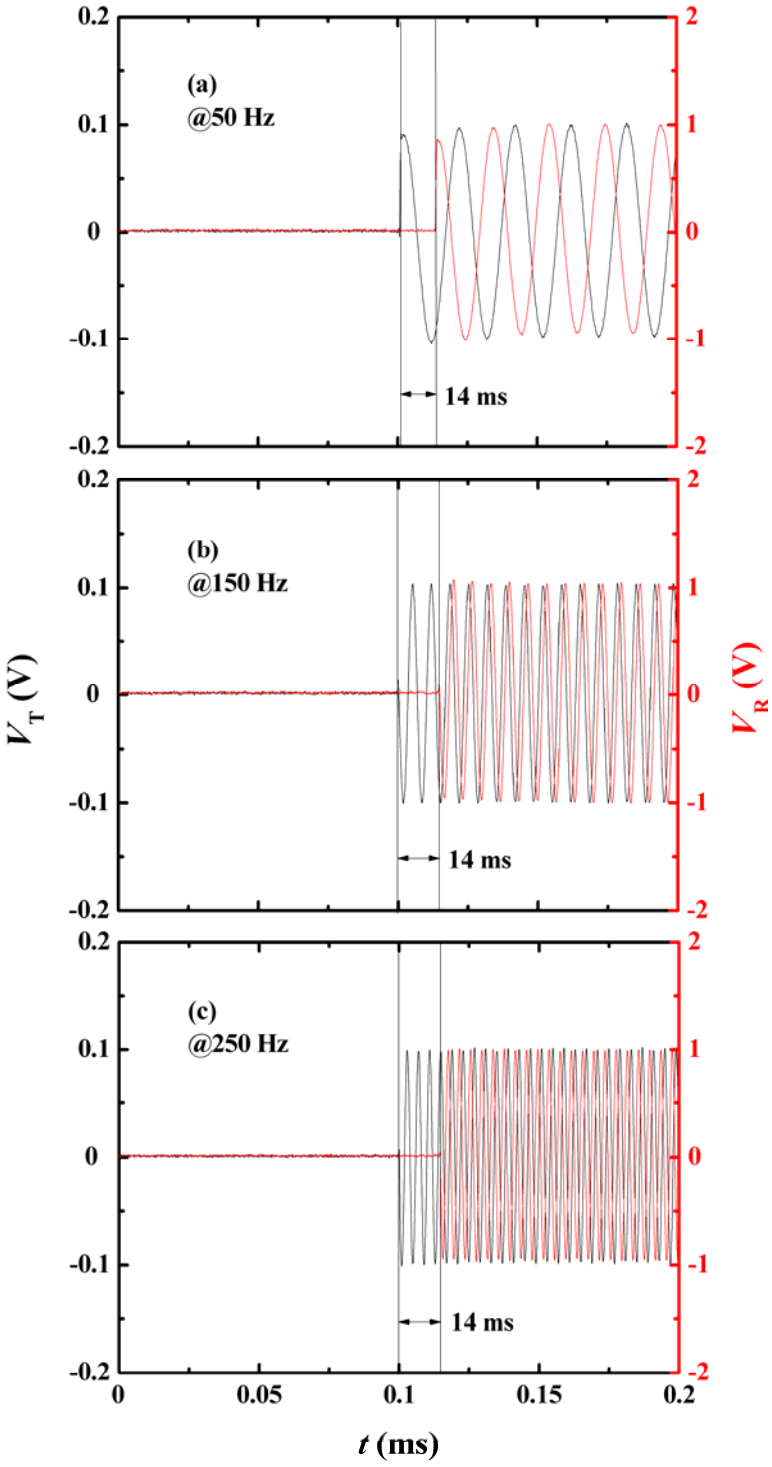

Fig. 5.7 **Waveforms of V_T of 0.1 V peak at three different f of (a) 50, (b) 150, and (c) 250 Hz. The corresponding V_R at d = 5 m are also included.**

Nevertheless, V_B decreases to 4.5 V when the wireless transmitter is operated continuously for 7 h. Since the minimum operating voltage of LMC662 CMOS operational amplifier is 4.5 V, the operating life time of the wireless transmitter and hence the 2.4 GHz wireless communication unit is ~7 h.

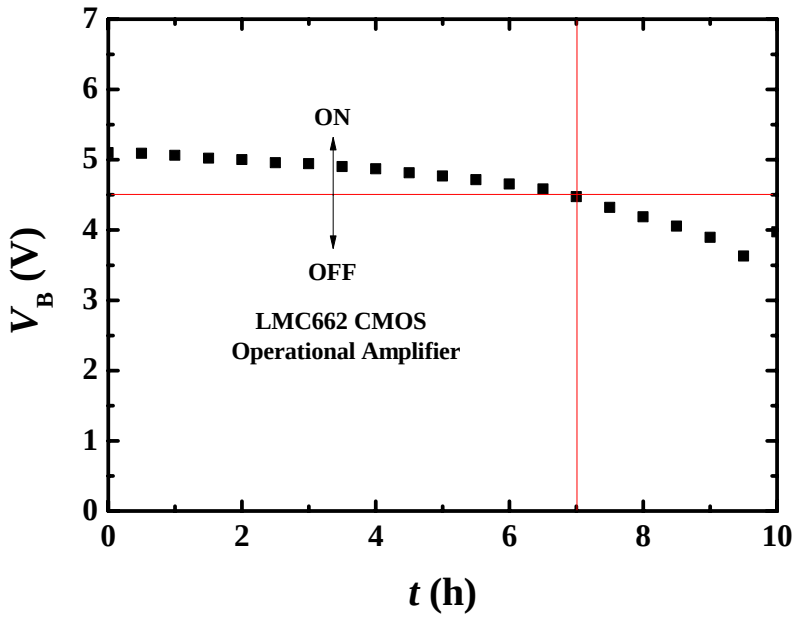

Fig. 5.8 **V_B as a function of t for the wireless transmitter in the 2.4 GHz wireless communication unit.**

Figure 5.9 shows the wireless transmission strength (S_W) as a function of wireless communication range (d) of the 2.4 GHz wireless communication unit. It is found that S_W can be preserved at a high value of ~80 % when d is as large as 300 m. For $d \leq 125$ m, S_W is nearly 100 %. This indicates that the wireless transmitter and receiver have excellent transmission and reception performances, respectively. For 125 m $\leq d \leq$ 200 m, S_W is in the range of 90–100 %, suggesting a good communication performance. For 200 m $\leq d \leq$ 300 m, S_W still maintains reasonably high values of 80–90 %, reflecting an average communication performance. Beyond 300 m, S_W drops below 80 % and the communication performance is classified as poor. Hence, our 2.4 GHz wireless communication unit can provide a long communication range of 300 m.

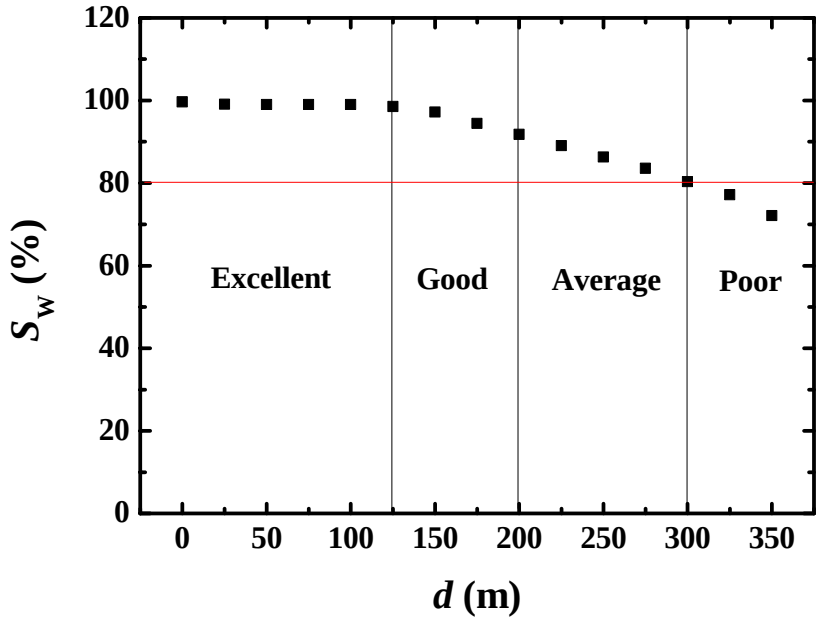

Fig. 5.9 S_W as a function of d of the 2.4 GHz wireless communication unit.

5.2.5.2 ME Passive Current Sensor as the Input

Figure 5.10 plots the waveforms of the wireless receiver output voltage (V_R) due to an applied current (I) of 1 A peak at various frequencies (f) of 50, 150, 250 Hz to the 3 mm diameter electrical cable. In Chapter 4, we found that the current sensitivity (S_I) of the surface mount-type ME passive current sensor is ~67 mV/A. It is seen from Fig. 5.10 that V_R is ~0.67 V due to the ×10 voltage gain present in the wireless transmitter of the 2.4 GHz wireless communication unit as stated in Section 5.22. On the other hand, I and V_R are in an asynchronous state because of the delay time of the 2.4 GHz wireless communication system as reported in Fig. 5.7.

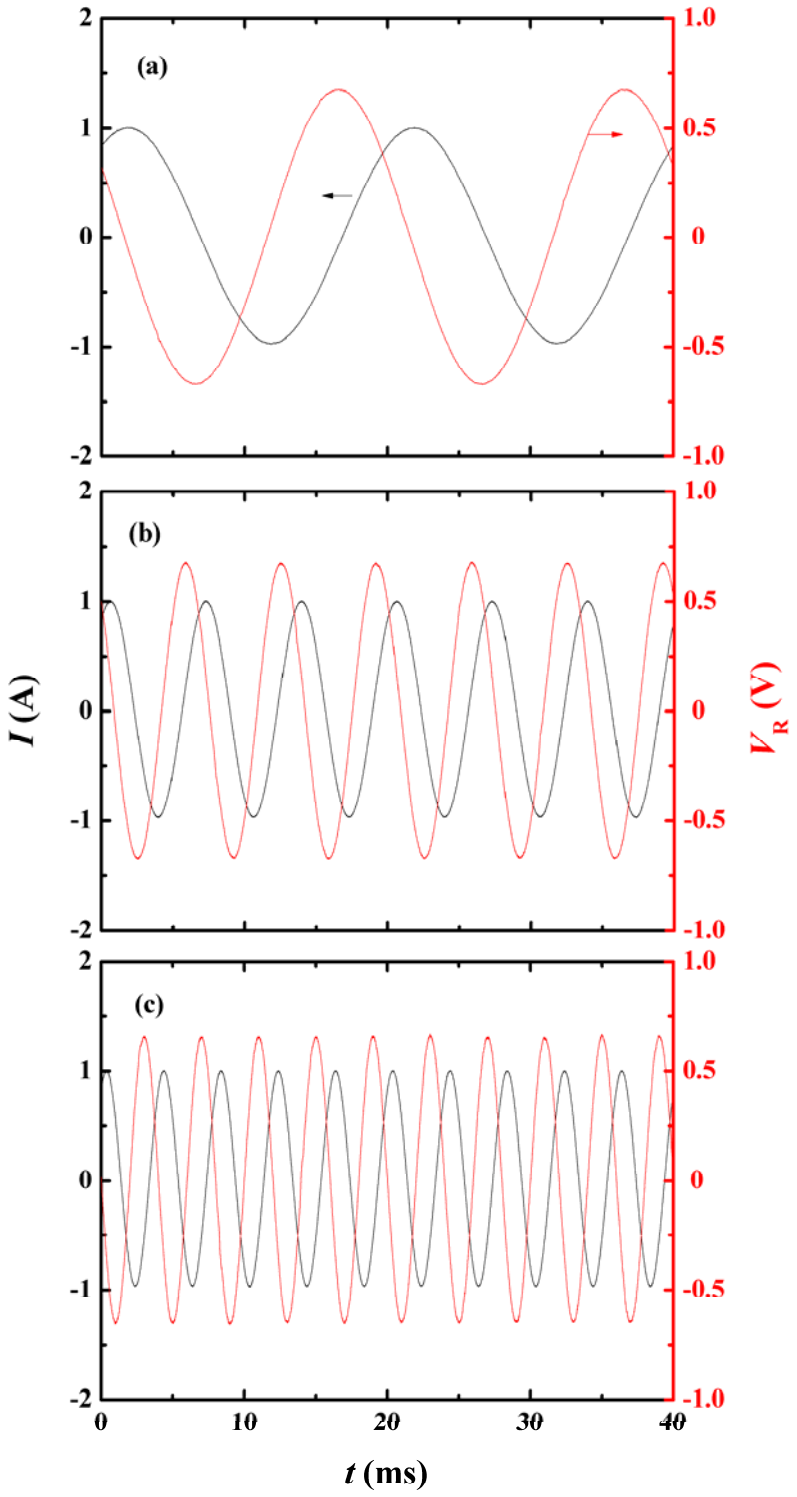

Fig. 5.10 Waveforms of V_R due to an applied I of 1 A peak at three different frequencies (f) of (a) 50, (b) 150, and (c) 250 Hz.

5.2.6 Summary of Useful Performance Data

Table 5.1 summarizes the useful performance data of the short-range, 4-channel, 2.4 GHz wireless communication unit. The wireless communication unit fulfills the 2.4 GHz international ISM radio communication standards with a sufficiently long communication range up to 300 m. Moreover, it has four signal-input, wireless-communication, and signal-output channels, each with BNC connectors, ×10 voltage gain, 16-bit microprocessor data architecture, 16 MHz microcontroller clock speed, 10-bit A-D conversion resolution, 200 k/s A-D sampling rate, 16-bit D-A conversion resolution, 1 μs D-A conversion settling time, 1 Mbps data transmission rate, and 20 ms delay time. In addition, it can be powered continually by 4.5–5.5 V, 2,500 mAh NiMH battery for about 7 h with power consumption of only 1.5 W.

Table 5.1 Summary of useful performance data of the short-range, 4-channel, 2.4 GHz wireless communication unit.

Parameter	Value
Operating frequency	ISM 2.4000−2.4835 GHz
Communication range	≥300 m*
Number of signal-input, wireless-communication, and signal-output channels	4
Voltage gain	×10
Microcontroller	16-bit data architecture, 16 MHz clock speed
A-D converter	10-bit conversion resolution, 200 k/s sampling rate
D-A converter	16-bit conversion resolution, 1μs settling time
Data transmission rate	1 Mbps maximum
Delay time	<20 ms
Supply voltage	4.5–5.5 V
Power	<1.5 W
Continuous operating time	>7 h for 4 × AA 1.2 V, 2,500 mAh NiMH battery
Signal input and output means	BNC connectors

* Test in the Fo Tan depot of MTR Corporation Limited.

5.3 Long-Range, 3-Channel, 3G/2G Wireless Communication Unit

5.3.1 Conceptual Design and Design Requirements

Figure 5.11 shows the system block diagram of the long-range, 3-channel, 3G/2G wireless communication unit. The 3G/2G wireless communication unit is composed of a 3-channel wireless transmitter powered by dc power supply and a personal computer (PC)-based file transfer protocol (FTP) data server with web control interface. The 3-channel wireless transmitter has four functional modules, namely: signal conditioning module, analog-to-digital (A-D) conversion module, central processing module, and wireless transmission module. The data communication between the 3-channel wireless transmitter and the PC-based FTP data server is essentially based on the switchable 3G/2G mobile broadband service provided by a commercial mobile broadband internet service provider (ISP) under the control of the web control interface built in the PC-based FTP data server.

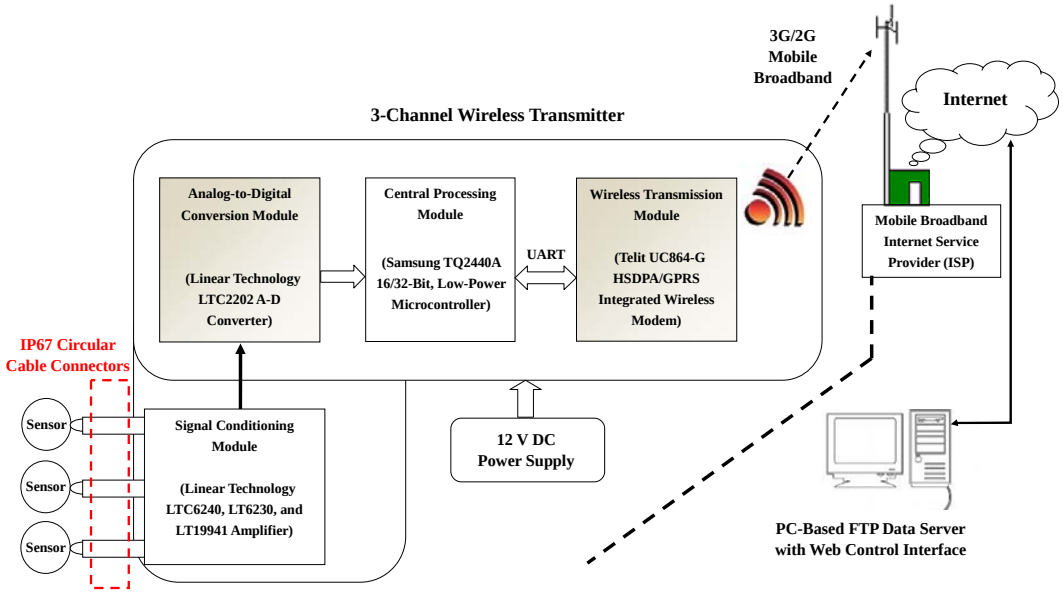

Fig. 5.11 System block diagram of the proposed long-range, 3-channel, 3G/2G wireless communication unit.

It is noted that 3G or 3rd generation mobile telecommunications is a generation of standards for mobile phones and mobile telecommunications services fulfilling the International Mobile Telecommunications–2000 (IMT–2000) specifications by the International Telecommunication Union. The 3G mobile telecommunication technology includes 3G, 2.5G, and 2G functionalities. It not only allows the connection between the wireless world with the internet world, but also provides much faster data transfer rates than the 2.5G and 2G technologies. The 2G systems in use today are capable of transferring data at around 10 kbps in the four frequency bands of 850, 900, 1,800, and 1,900 MHz. The 2.5 G systems have higher data transfer rates of 28.8–144 kbps in the same frequency bands as the 2G systems. The 3G systems provide even faster data transfer rates in excess of 384 kbps in the three frequency bands of 850, 1900, and 2100 MHz [80]. The packet-switched technology is used in the 3G systems to connect mobile terminals to the network all the time. High-speed downlink packet access (HSDPA) is an improved download packet data transfer protocol used for the 3G systems. HSDPA is not just a minor change of the specifications of 3G systems but also a major upgrade that brings clear capacity improvements and much higher data speeds than the existing 3G systems. General packet radio service (GPRS) is a packet-oriented mobile data transfer protocol adopted by the 2G systems.

In operation, the analog signals detected by the ME passive current sensors are coupled to the signal conditioning module of the 3-channel wireless transmitter through BNC-to-IP67 circular cable connectors for the transformation into a stable and

determined analog-signal format in suitable ranges. The conditioned analog signals are converted into a usable digital-data format by the A-D converter in the A-D conversion module with the desired conversion resolution and sampling rate. The converted digital data is stored in random access memory (RAM) of the central processing module and then transferred to the HSDPA/GPRS integrated wireless modem of the wireless transmission module through the universal asynchronous receiver/transmitter (UART) port. The HSDPA/GPRS integrated wireless modem transmits the digital data through the auto-switchable 3G/2G mobile broadband network provided by a commercial mobile broadband ISP to the PC-based FTP data server. With the aid of the web control interface, the received digital data is stored in the hard disk of the PC-based FTP data server and the current signatures are reproduced by the waveform viewer of the web control interface. The important configuration parameters, such as voltage gain, sampling rate, scanning duration, and sleeping interval, can also be configured remotely by the configurator of the web control interface. The operator can control the operation of the 3G/2G wireless communication unit as well as monitor, process, and analyze the current signatures based on the PC-based FTP data server and the web control interface in general.

The following specifications are adopted for the design of the 3G/2G wireless communication unit:

(1) It should be auto-switchable between the 3G and 2G mobile broadband networks/services and supported by the HSDPA and GPRS protocols, respectively.

(2) It should have three signal-input and wireless-communication channels for the accommodation of three ME passive current sensors.

(3) It should use IP67 circular cable connectors as the signal-input connectors.

(4) It should have three selectable voltage gains of 1, 10, and 100 for all signal-input channels.

(5) It should have high microcontroller data architecture of 32 bits and clock speed of 400 MHz with an internal RAM of 64 Mbytes.

(6) It should have a high A-D conversion resolution of 16 bits and a fast A-D sampling rate of 10 M/s.

(7) It should have configurable sampling rate up to 4 MHz, scanning duration up to 2 s, and sleeping interval up to 24 h for data collection.

(8) It should be powered by 12 V dc.

(9) It should have a small operating power of less than 4 W.

5.3.2 Hardware Development

Figure 5.12 shows the circuit diagram of the 3-channel wireless transmitter used in the 3G/2G wireless communication unit and conceptualized in Fig. 5.11. The 3-channel wireless transmitter consists of four functional modules, including a signal conditioning module, an A-D conversion module, a central processing module, and a wireless transmission module. The main components of the signal conditioning module, A-D conversion module, central processing module, and wireless transmission module are Linear Technology LTC6230 and LT6240 CMOS operational amplifiers and LT1994 differential input/output amplifier, a Linear Technology LTC2202 A-D converter, a SAMSUNG S3C2440A 16/32-bit, low-power microcontroller, and a Telit UC864-G HSDPA/GPRS integrated wireless modem, respectively. The LTC6230 and LTC6240 CMOS operational amplifiers are configured as a voltage follower with unity voltage gain and a non-inverting amplifier with three selectable voltage gains of 1, 10, and 100, respectively. The LT1994 is a high-precision, low-noise, low-distortion differential input/output amplifier for driving the LTC2202 A-D converter. The LTC2202 A-D converter has 16-bit A-D conversion resolution and 10 M/s sampling rate to ensure an excellent digitalization of analog signals even at high frequencies and in wide dynamic ranges. The S3C2440A 16/32-bit, low-power microcontroller has the data architecture of 16/32 bits, the maximum clock speed of 400 MHz, an internal RAM of 64 Mbytes, and a fully static design to enable cost- and power-sensitive applications. The S3C2440A microcontroller also provides the SPI and the universal asynchronous receiver and

transmitter (UART) ports for communication with the wireless transmission module. The 32-bit architecture and the UART port are used in the current design. The Telit UC864-G HSDPA/GPRS integrated wireless modem in the wireless transmission module is good for use in the global wireless data transmission because of widely selectable operating frequencies of the 3G (850, 1900, and 2,100 MHz) and 2G (850, 900, 1,800, and 1,900 MHz) systems with the nominal transmission power of 2 W. A dc voltage of 12 V, supplied by a universal dc power supply, is employed to sustain the operation of the 3-channel wireless transmitter.

Figure 5.13 shows the photographs of the fabricated 3-channel wireless transmitter in the circuit-board view [Fig. 5.13(a)] and in the overall view [Fig. 5.13(b)]. The circuit board is housed in a waterproof case which fulfills the International Protection (IP) 67 standards of totally protected against dust and the effect of immersion between 15 cm and 1 m. As IP67 circular cable connectors are used on the 3-channel wireless transmitter side while BNC connectors are employed for the ME passive current sensors, BNC-to-IP67 circular cable connectors are needed in between.

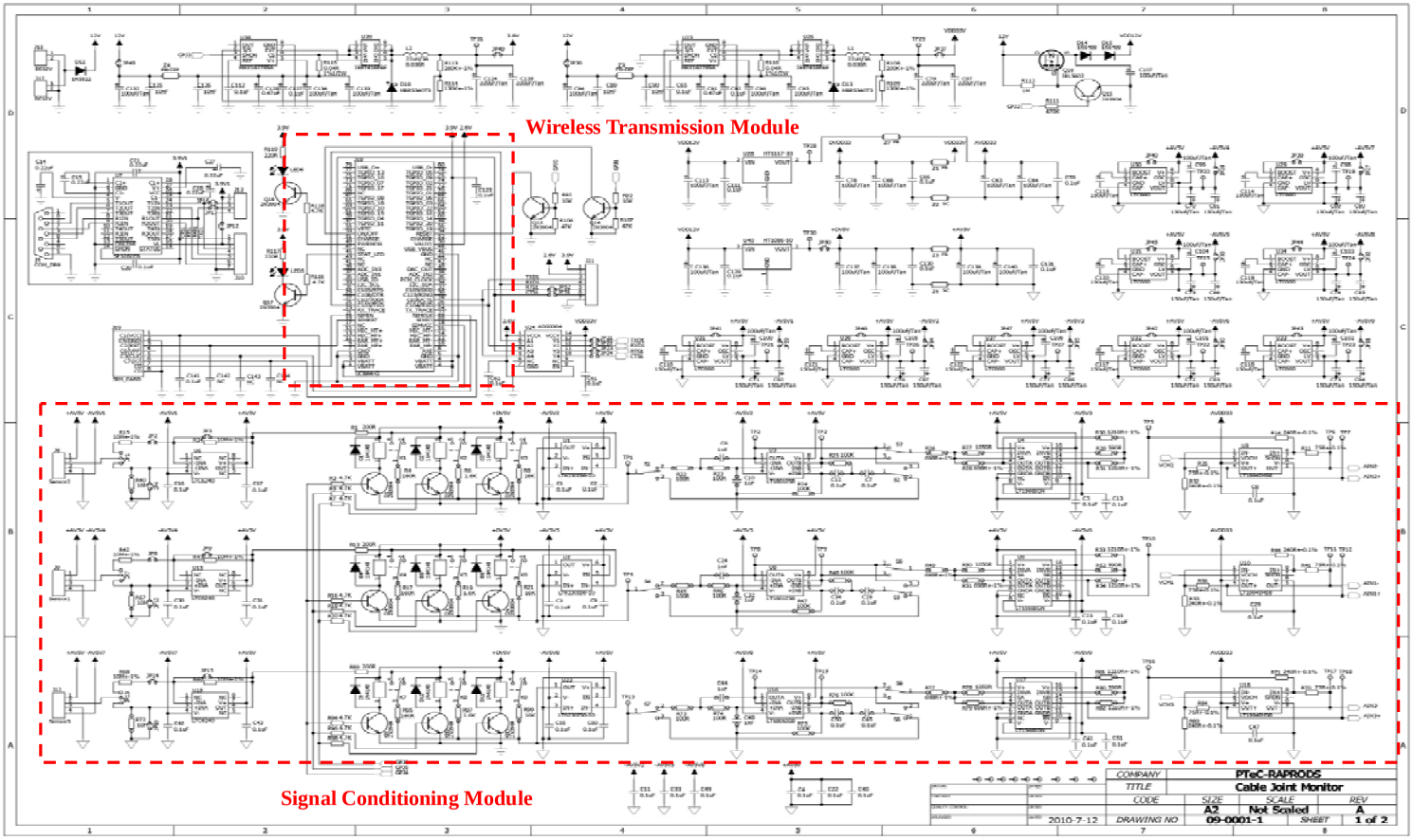

Fig. 5.12(a) Circuit diagram of the signal conditioning module and wireless transmission module in the 3-channel wireless transmitter.

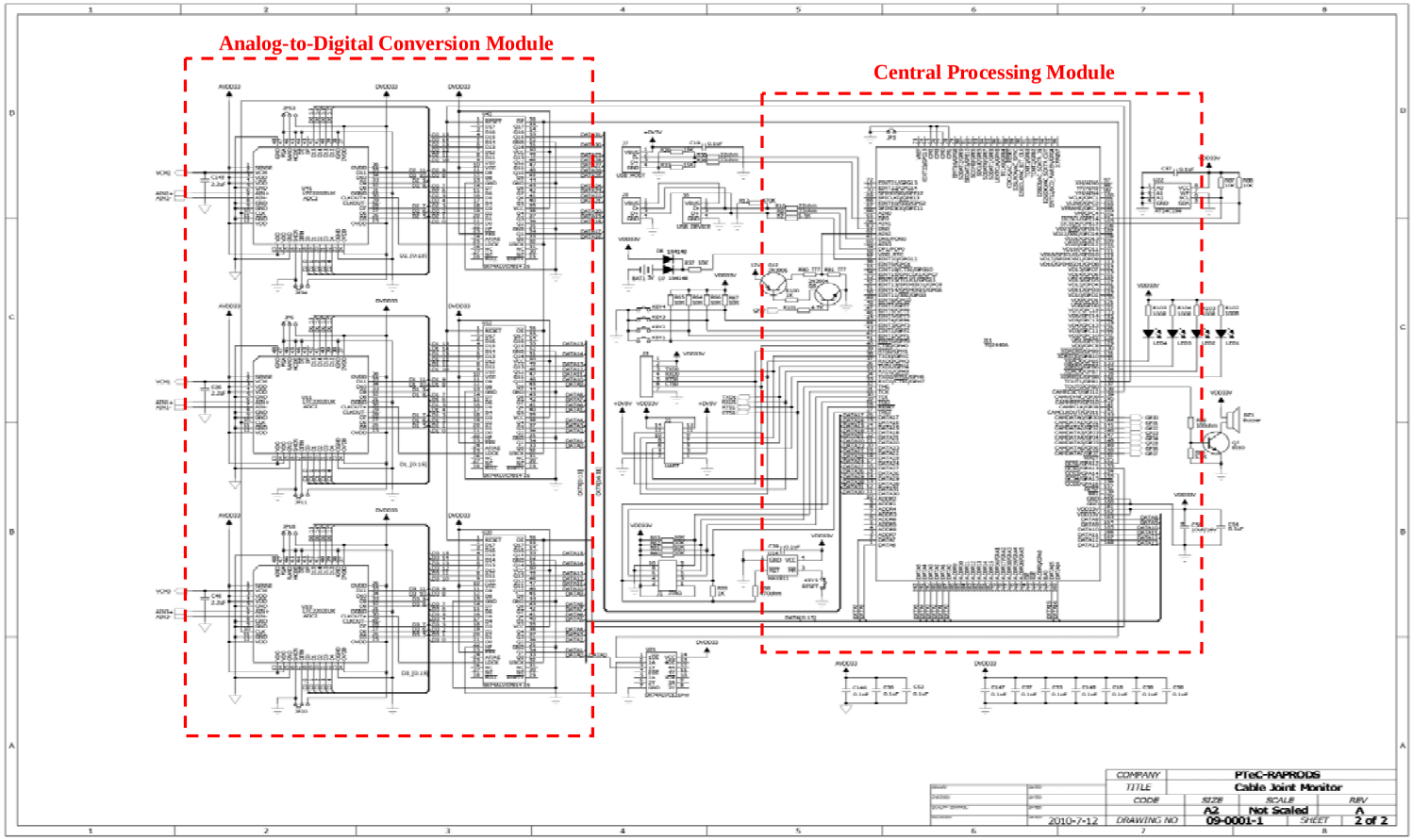

Fig. 5.12(b) Circuit diagram of the analog-to-digital (A-D) conversion module and central processing module in the 3-channel wireless transmitter.

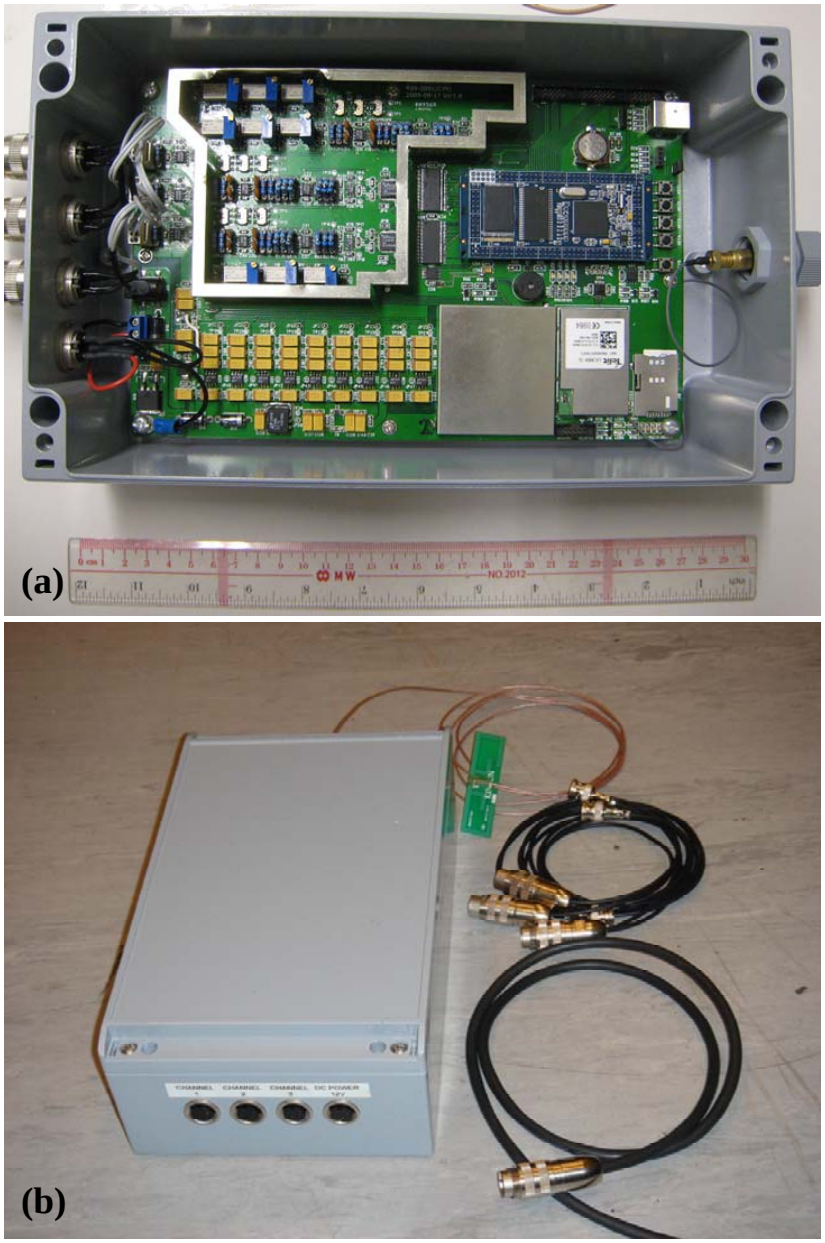

Fig. 5.13 Photographs of the fabricated 3-channel wireless transmitter. (a) Circuit-board view and (b) overall view.

5.3.3 Software Development

Figure 5.14 shows the flow diagram of the data communication process of the 3G/2G wireless communication unit. When the 3-channel wireless transmitter is powered on, it will be initialized using the configuration parameter file pre-stored in the 3-channel wireless transmitter. The configuration parameters preset in the configuration parameter file include ×1 voltage gain, 4 MHz sampling rate, 100 ms scanning duration, and 5 min sleeping interval. The 3-channel wireless transmitter processes the sensor signals and stores the converted digital data in RAM using the preset configuration parameters if no update is available. If the PC-based FTP data server can be login by the 3-channel wireless transmitter, the digital data will be transferred to it through the 3G/2G mobile broadband network/service provided by a commercial mobile broadband ISP (3 mobile band operated by Hutchison Telecommunications Hong Kong Holdings Limited is used in our case). The PC-based FTP data server receives the transmitted digital data and stores it in the root directory of its hard disk. The user can access the sensor signal waveforms and their frequency spectra using the waveform viewer of the web control interface developed by National Instruments Labview 8.6 program. The user can also read and edit the configuration parameter file by the configurator of the web control interface and store the modified configuration parameter file in the root directory of the hard disk in the PC-based FTP data server. If the logon of the PC-based FTP data server is failure, the 3-channel wireless transmitter will perform the re-login operation for at most 5 times. If failure again, the 3-channel wireless transmitter will re-process and re-store the digital data in

RAM. After the PC-based FTP data server has received all the data available in RAM, the modified configuration parameter file will be downloaded from the root directory of the hard disk of the PC-based FTP data server and also updated by the 3-channel wireless transmitter through the 3G/2G mobile broadband network. Finally, the 3-channel wireless transmitter will go to sleep mode according to the sleeping interval defined in the configuration parameter file.

Figure 5.15 shows the configurator and waveform viewer of the web control interface in the 3G/2G wireless communication unit. The web control interface was developed by National Instruments Labview 8.6 program. As illustrated in Fig.5.15(a), the configurator contains four functional controls which allow the operator to remotely configure the operation of the 3G/2G wireless communication unit. These include: voltage gain (×1, ×10, and ×100), sampling rate (1, 2, and 4 MHz), scanning duration (0.1−2 s), sleeping interval (5 mins−24 hour). For the waveform viewer in Fig. 5.15(b), different colors are used to indicate the three different waveforms and frequency spectra due to the three different signal-input and communication channels. The waveform and frequency spectrum files are named and sorted by the date and time of capture for ease of referencing. The files can also be exported as data files in ASCII format for further processing and analysis.

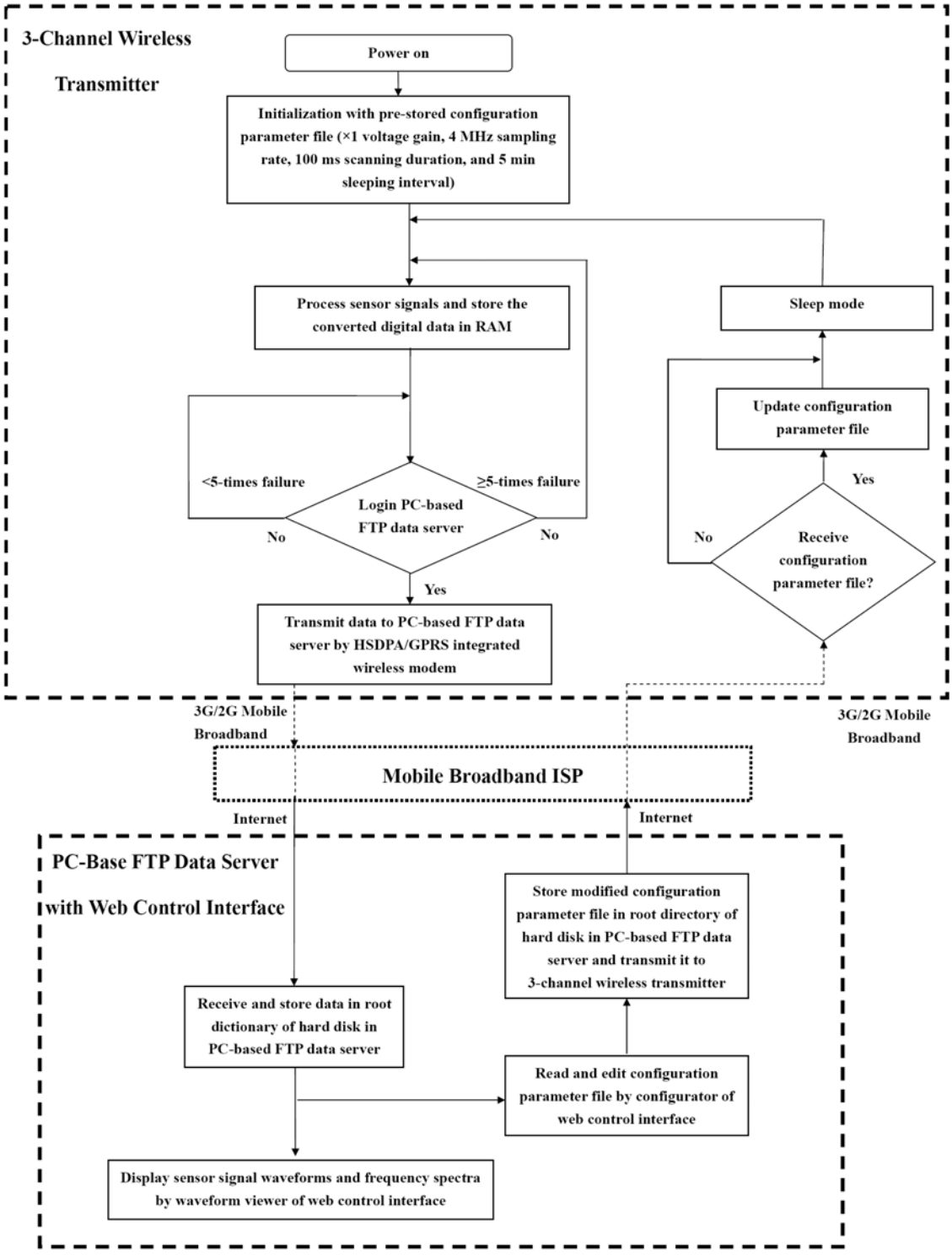

Fig. 5.14 Flow diagram of the data communication process of the 3G/2G wireless communication unit.

(a)

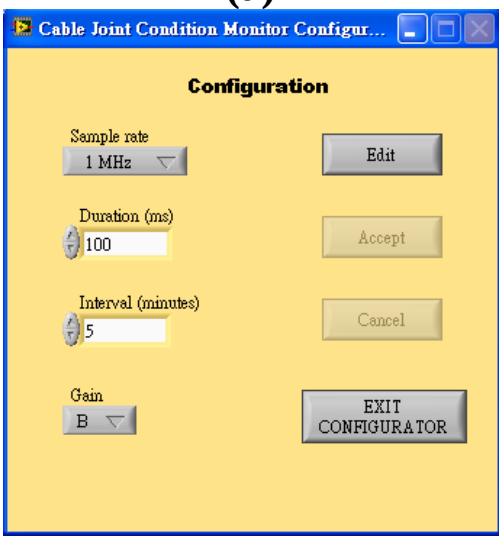

(b)

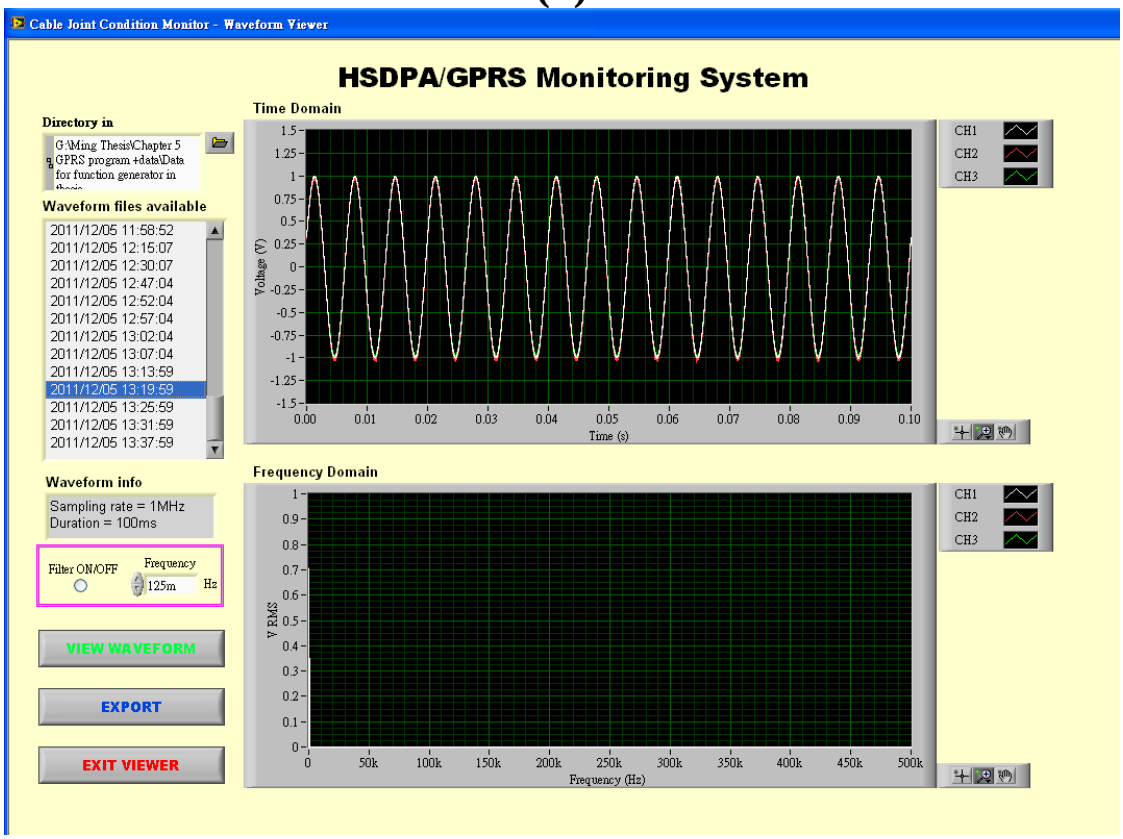

Fig. 5.15 (a) Configurator and (b) waveform viewer of the web control interface in the 3G/2G wireless communication unit.

5.3.4 Performance Evaluation

The performance of the developed 3G/2G wireless communication unit was evaluated in the laboratory environment with arbitrary waveform generator and ME passive current sensor as the signal-input sources, respectively (Fig. 5.16). For the test with arbitrary waveform generator, a sinusoidal voltage of 10 mV peak was generated at three different frequencies (*f*) of 50, 150, and 250 Hz by an arbitrary waveform generator (Agilent 33210A) connected to a signal-input channel of the 3-channel wireless transmitter. For the test with ME passive current sensor, three surface mount-type ME passive current sensors (Fig. 4.13) were placed on a 3 mm diameter electrical cable terminated with an 0.47 Ω resistor load to ground and driven by a sinusoidal current of 1 A peak at three different *f* of 50, 150, and 250 Hz using the arbitrary waveform generator and a constant-current supply amplifier (AE Techron 7796HF). A current probe (Hioki 9273) with a current amplifier (Hioki 3271) was employed to monitor the cable current. The sensor outputs were connected to the three signal-input channels of the 3-channel wireless transmitter via BNC-to-IP67 circular cable connectors. For both tests, the signals received by the PC-based FTP data server were displayed by the waveform viewer of the web control interface in both time and frequency domains.

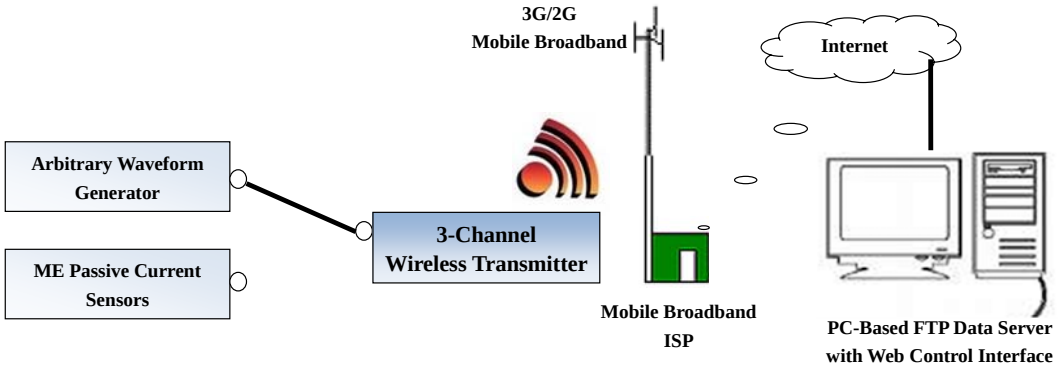

Fig. 5.16 Experimental setup for the evaluation of the performance of the developed 3G/2G wireless communication unit.

5.3.5 Results and Discussion

5.3.5.1 Arbitrary Waveform Generator as the Input

Figure 5.17 shows the received waveforms and their frequency spectra in an application of a sinusoidal voltage of 10 mV peak at three different frequencies (*f*) of 50, 150, and 250 Hz from the arbitrary waveform generator to the 3-channel wireless transmitter. The configuration parameters for the 3-channel wireless transmitter are ×10 voltage gain, 1 MHz sampling rate, 100 ms scanning duration, and 5 min sleeping interval. It is clear that the received waveforms at three different *f* of 50, 150, and 250 Hz are very clear without harmonics and other signal frequencies. The observation is further supported by the single peak located at 50, 150, and 250 Hz, respectively, as seen from their frequency spectra.

f = 50 Hz

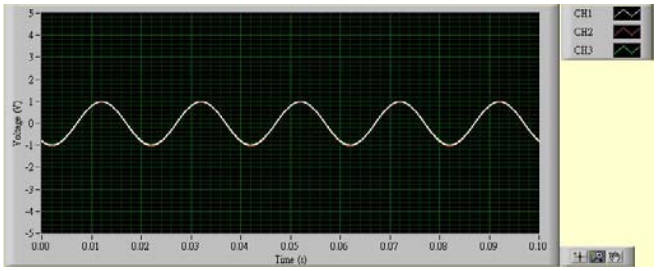

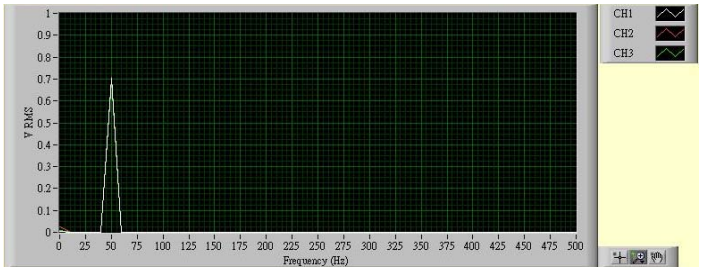

f = 150 Hz

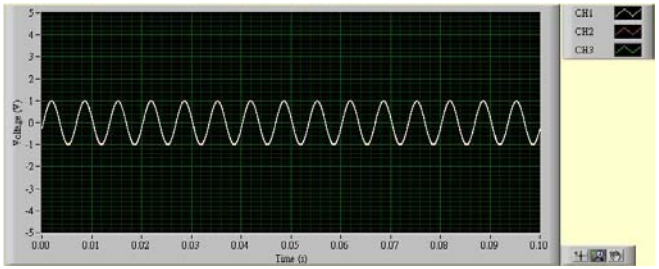

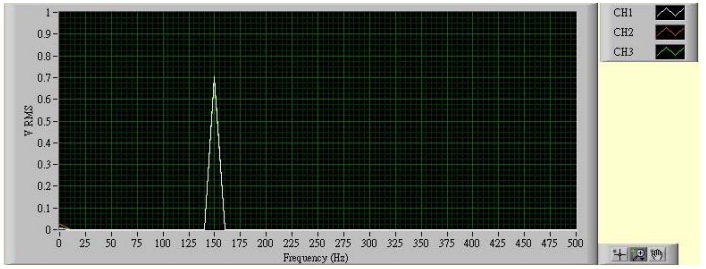

f = 250 Hz

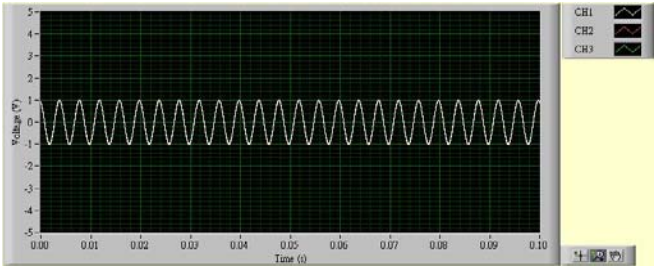

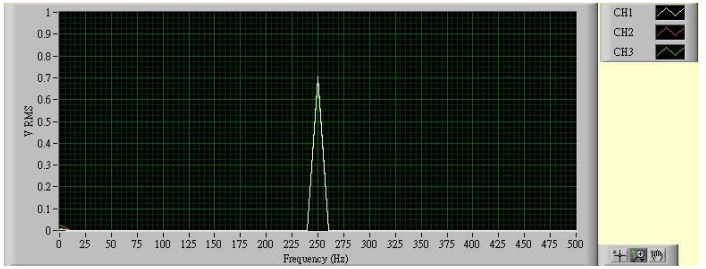

Fig. 5.17 Received waveforms and their frequency spectra at an applied voltage of 10 mV peak for f = 50, 150, and 250 Hz from the arbitrary waveform generator to the 3-channel wireless transmitter. The configuration parameters are ×10 voltage gain, 1 MHz sampling rate, 100 ms scanning duration, and 5 min sleeping interval.

Figure 5.18 displays the waveforms received by the three communication channels in an application of a sinusoidal voltage of 10 mV peak at a frequency of 50 Hz from the arbitrary waveform generator to the three signal-input channels of the 3-channel wireless transmitter with three different voltage gains of ×1, ×10, and ×100. The other configuration parameters such as sampling rate, scanning duration, and sleeping interval remain unchanged. Significant noises are found for the case of unity voltage gain [Fig. 5.18(a)]. The noise level reduces with increasing the voltage gain to ×10 and ×100. These correspond to the voltage levels of 0.1 and 1 V peak, respectively, and suggest the validity of using the ×10 and ×100 voltage gains in practice.

5.3.5.2 ME Passive Current Sensor as the Input

Figure 5.19 shows the waveforms received by the three communication channels at two different voltage gains of ×1 and ×10 when three surface mount-type ME smart passive current sensors are used to detect 1 A peak, 50 Hz cable current. The configuration parameters, including sampling rate, scanning duration, and sleeping interval are set to 1 MHz, 100 ms, and 5 min, respectively. Again, significant noises are detected with ×1 voltage gain [Fig. 5.19(a)]. Fortunately, this problem can be solved by changing the voltage gain to ×10 [Fig. 5.19(b)].

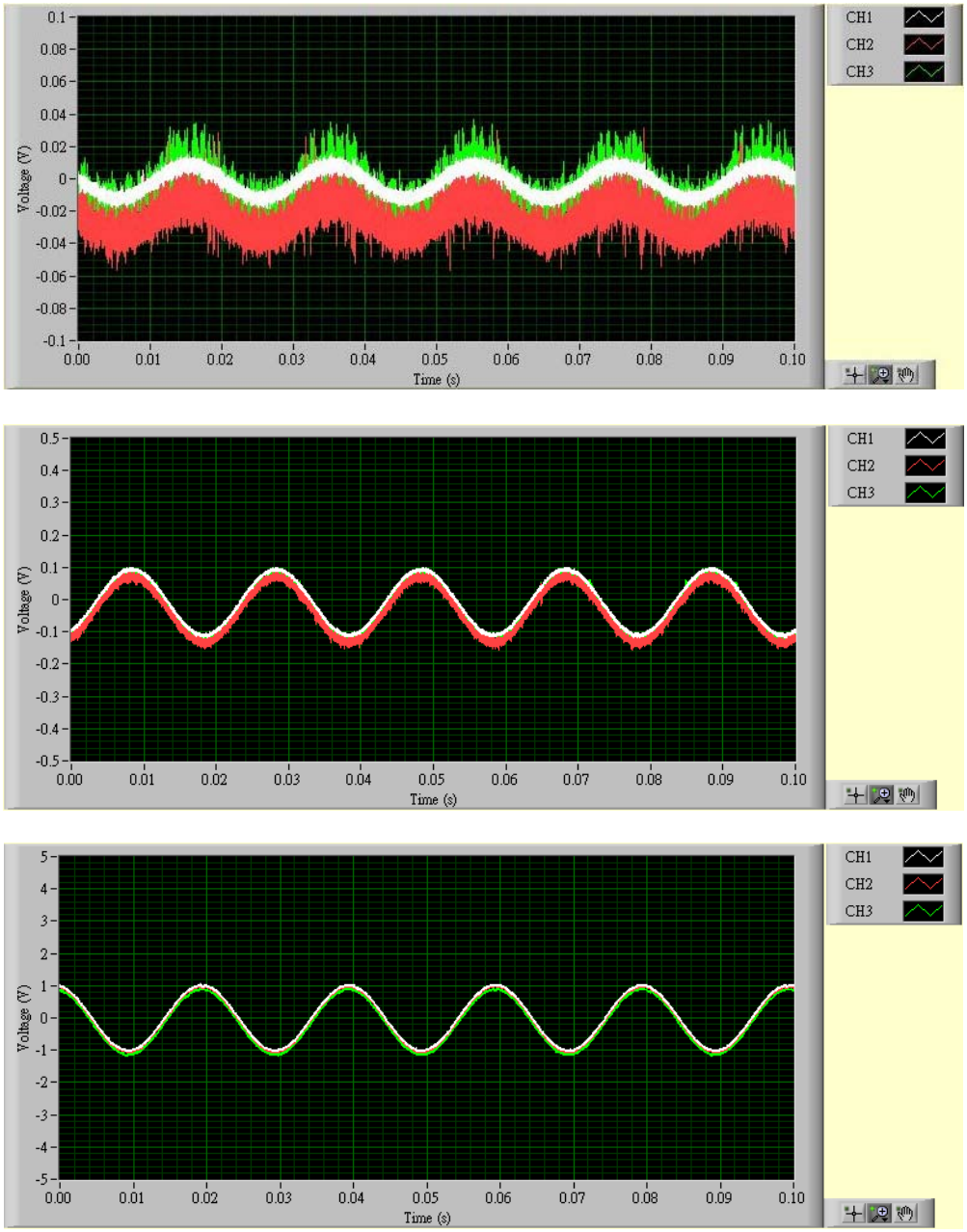

Fig. 5.18 Waveforms received by the three communication channels at an applied voltage of 10 mV peak, 50 Hz frequency from the arbitrary waveform generator to the three signal-input channels of the 3-channel wireless transmitter with three different voltage gains of (a) ×1, (b) ×10, and (c) ×100.

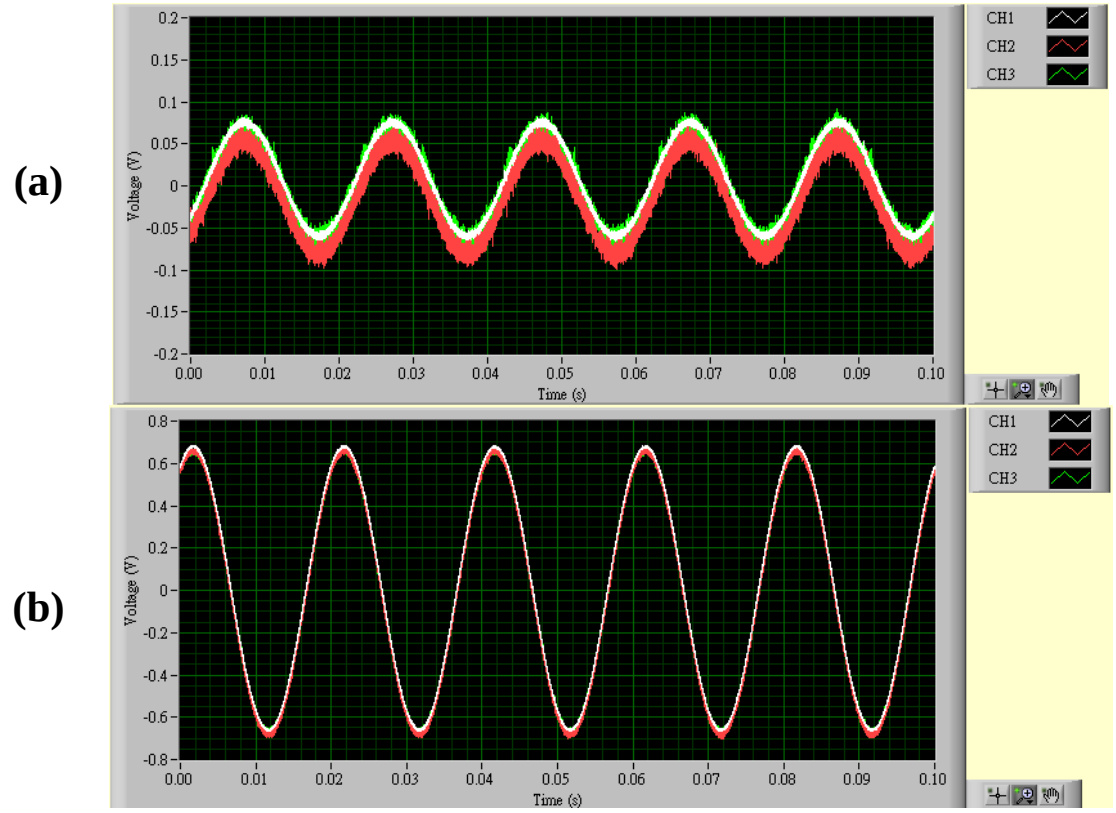

Fig. 5.19 Waveforms received by the three communication channels at two different voltage gains of (a) ×1 and (b) ×10 when three surface mount-type ME passive current sensors are used to detect 1 A peak, 50 Hz cable current.

5.3.5.3 Summary of Useful Performance Data

Table 5.2 shows the summary of useful performance data of the long-range, 3-channel, 3G/2G wireless communication unit. The 3G/2G wireless communication unit is auto-switchable between the 2G and 3G mobile broadband networks/services. It has three signal-input and communication channels to accommodate three ME passive current sensors at the same time. This is specifically designed for monitoring 3-phase currents. IP67 circular cable connectors are used as the signal-input means. The 32-bit data architecture, 400 MHz clock speed, and 64 Mbyte RAM provided by the microcontroller ensures the high-speed control and data storage in the 3-channel

wireless transmitter. The 16-bit A-D conversion resolution and 10 M/s sampling rate in A-D converter makes the high-frequency measurement possible. The selectable voltage gain (×1, ×10, and ×100) provides large measuring ranges and reduces abnormal noises. The configurable sampling rate (≤4 MS/s), scanning duration (0.1–2 s), and sleeping interval (5 min–24 h) increase the application flexibility.

Table 5.2 Summary of the useful performance data of the long-range, 3-channel, 3G/2G wireless communication unit.

Parameter	Value
Network	3G/2G (auto-switchable)
Number of communication channels	3
Signal-input means	IP67 circular cable connector
Voltage gain	×1, ×10, and ×100
Microcontroller	32-bit data architecture, 400 MHz clock speed, 64 Mbytes RAM
A-D converter	16-bit conversion resolution, 10 M/s sampling rate
Data transmission rate	>384 kbps for 3G, 10 kbps for 2G
Sampling rate	≤4 M/s
Scanning duration	0.1–2 s
Sleeping Interval	5 min–24 h
Supply Voltage	12 V dc
Standby Power	<0.3 W
Transmission Power	<4 W

Chapter 6

Wireless Condition Monitoring of Electrical Assets

6.1 Introduction

Novel surface mount-type and clamp-type magnetoelectric (ME) passive current sensors based on plate-shaped and ring-shaped ME sensing elements realized in Chapter 3 have been developed in Chapter 4. A short-range, 4-channel 2.4 GHz wireless communication unit and a long-range, 3-channel HSDPA/GPRS wireless communication unit have also been developed in Chapter 5. Since these ME passive current sensors require no external power supplies to sustain their operation and produce sufficiently large and clear output voltage signals in response to the input currents or magnetic fields over a broad range of frequencies without the strong support by signal conditioners, they can truly serve as autonomous sensors for improved condition monitoring purposes.

In this chapter, the two types of ME passive current sensors are integrated with the two types of wireless communication units to form a new generation class of wireless condition monitor for wireless condition monitoring of three different electrical assets. These include:

(1) Electrical motor drives of the train traction system of a 12-carbin mainline train operated by MTR Corporation Limited and running between Hong Kong and Shenzhen, China;

(2) An ABB 400 V, 1,000 A, 3-phase electrical switchgear for the control, protection, and isolation of electrical machines and equipment and located in the Electrical Machines Laboratory (EF001a) of the Department of Electrical Engineering at PolyU; and

(3) A 220 V, 13 A switching mode power supply for driving electronic equipment.

For each case, the application background is first introduced. The field installation and implementation of the wireless condition monitor are then described. The test results are later disclosed and analyzed. The concluding remarks are provided at the end.

6.2 Monitoring of Electrical Motor Drives of Train Traction System

6.2.1 Application Background

Rail network is a symbol of the rapid development of a country. Mainland China, for example, has recently drawn the world's attention by the construction of the world's longest high-speed rail network. As in January 2011, there are 8,383 km of routes in service, including 2,197 km of routes operating at the maximum speed of about 350 km/h. The entire high-speed rail network will reach 13,073 and 25,000 km by the end of 2011 and 2015, respectively [81]. It is believed that the construction of rail network will directly boost the economic growth in China.

The East Rail Line of MTR Corporation Limited, which came into service in 1910, is the earliest urban public rail line in Hong Kong (Fig. 6.1). The East Rail Line has 34 km of routes covering 14 stations from Hung Hom to Lo Wu and operating at the maximum speed of 120 km/h. It carries an average of 800,000 passengers everyday [82]. The electrical catenary system adopted for the East Rail Line is 25 kV, 50 Hz single-phase ac overhead current collection system, which supplies up to 33 mainline trains per hour per direction. The electricity is taken from CLP Power Hong Kong Limited through 132/25 kV single-phase transformers with open-delta connection. It is then fed into the electrical catenary system for energizing the mainline trains [83]. Table 6.1 shows the specifications of the mainline trains for the East Rail Line. A typical mainland train consists of 12 cabins with the total length of about 285 m. Its maximum service speed is 120 km/h with an acceleration and a deceleration of 2.0 and 3.6 km/h/s, respectively. The train traction system has four sets of dc induction

electrical traction motor (GEC model G315) and thyristor-controlled electrical motor drives situated underneath the 2nd, 5th, 8th, and 11th cabins. Each motor carries 225 kW output power.

Fig. 6.1 The 12-cabin mainline train operated by MTR Corporation Limited in Hong Kong and running between Hong Kong and Shenzhen on the East Rail Line.

Table 6.1 Specifications of the 12-cabin mainline train for the East Rail Line.

Parameter	Value
Number of Carbins	12
Length	285 m
Width	3.1 m
Height	4.7 m
Number of doors per side per cabin	5
Maximum service speed	120 km/h
Acceleration	2.0 km/h/s
Deceleration	3.6 km/h/s
Traction system	4 sets of dc induction traction motor (GEC model G315) and thyistor-controlled electrical motor drive
Power output per motor	225 kW
Electrical system	25 kV, 50 Hz, single-phase ac overhead current collection system

In practice, electrical and mechanical faults are unavoidable in such complicated train traction systems and may become more prominent at high speeds. The faults related to pantographs, control drives, track defects, bogie bearings, gear boxes, and electrical motors have been discussed recently [84,85]. Nevertheless, real-time monitoring of the operating conditions of train traction systems is deemed necessary for train operators to assure a sufficiently high degree of safety, reliability, and availability, especially at high speeds. As mentioned in Chapter 1, wireless condition-monitoring approach has emerged as a flexible alternative to the traditional system-based wired condition-monitoring approach due to the ease of installation, large scalability, and highly distributed nature. It is known that current signatures governed by electrical motor drives of train traction systems are physically valuable to represent the operating conditions of the train traction systems. In addition, current signature analysis is widely acceptable in the community to provide a highly sensitive, flexible, and cost-effective means for monitoring the statuses of electrical machines including motors, generators, alternators, and transformers [86−88]. However, the long train length, tough and complex system connections, critical measuring locations, high-voltage and heavy-current environment, etc. always impose great difficulties when installing wired or state-of-the-art wireless condition monitors involving active current sensors which are often accompanied with the need of power supplies and heavy-duty signal conditioners.

In view of this, we propose in this study to integrate four pieces of surface mount-type ME passive current sensor described in Fig. 4.12 of Chapter 4 with the

short-range, 4-channel 2.4 GHz wireless communication unit presented in Fig. 5.3 of Chapter 5 to form a new generation type of wireless condition monitor for monitoring the electrical motor drives of the train traction system of a 12-carbin mainline train running on the East Rail Line. The field installation and implementation of the four pairs of ME passive current sensor and single-channel wireless transmitter on electrical cables associated with the four electrical motor drives situated underneath the 2nd, 5th, 8th, and 11th cabins of a 12-cabin mainline train is presented, together with the real-time captured, wirelessly monitored current signatures by a 4-channel wireless receiver housed in the driver cabin.

6.2.2 Field Installation and Implementation

Four matched surface mount-type ME pasive current sensors (Fig. 4.12) were integrated with the short-range, 4-channel 2.4 GHz wireless communication unit (Fig. 5.3) to form a wireless condition monitor for electrical motor drives of train traction systems. As shown in Fig. 6.2, four pairs of ME passive current sensor and single-channel wireless transmitter were installed on electrical cables of the four electrical motor drives situated underneath the 2nd, 5th, 8th, and 11th cabins of a 12-cabin mainline train operated by Hong Kong's MTR Corporation Limited and running between Hong Kong and Shenzhen, China on the East Rail Line. A 4-channel wireless receiver was housed in the driver cabin to provide real-time, wireless monitoring of the current signatures of the four electrical motor drives. The train traction system, driven at 25 kV, 50 Hz single-phase ac overhead current collection system, was based on 4 sets of

dc induction electrical traction motor and thyristor-controlled electrical motor drive.

The working principle of the wireless condition monitor is illustrated in Fig. 6.3. A set of four current signatures, governed by the four electrical motor drives of the train traction system, were detected by the four ME passive current sensors, transmitted by the four signal-channel wireless transmitters, received by the 4-channel wireless receiver, and displayed by an oscilloscope (LeCroy WaveRunner 44Xi) in the driver cabin.

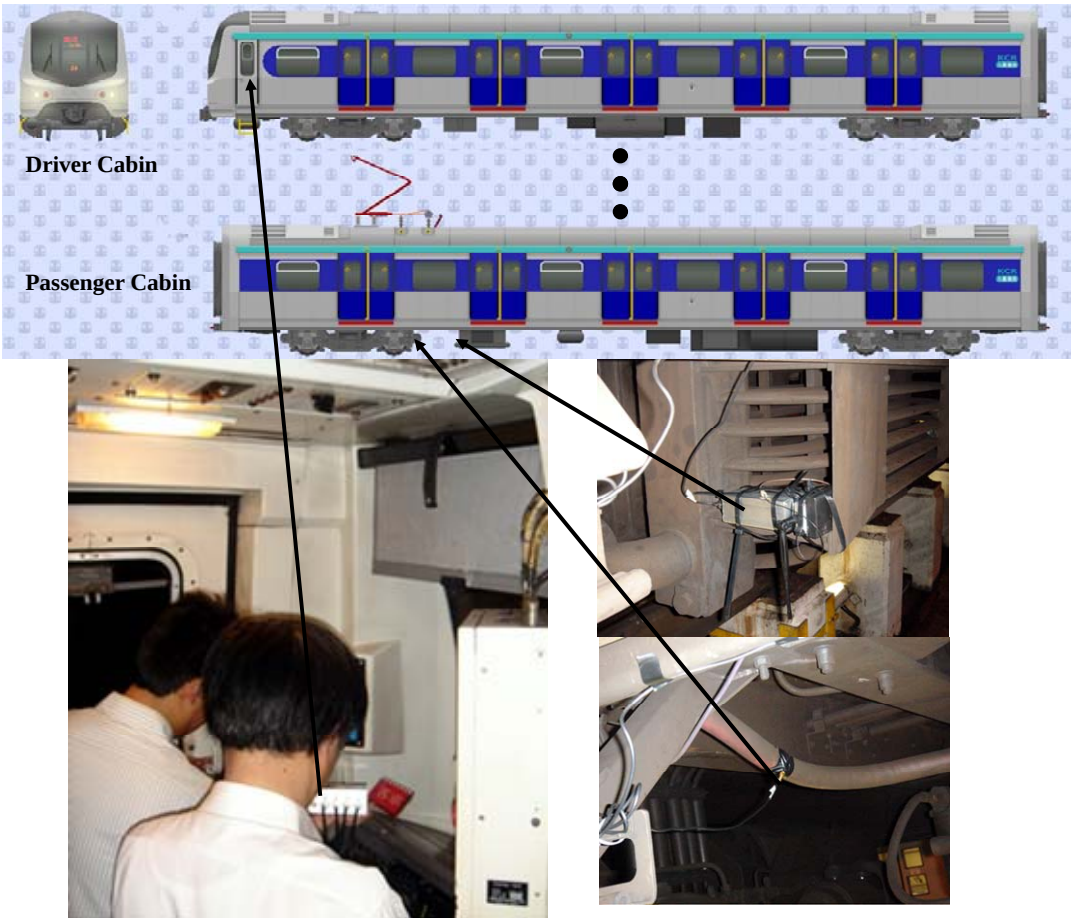

Fig. 6.2 Installation of the surface mount-type ME passive current sensors and the short-range, 4-channel 2.4 GHz wireless communication unit in a 12-cabin mainline train operated by Hong Kong's MTR Corporation Limited and running between Hong Kong and Shenzhen, China on the East Rail Line.

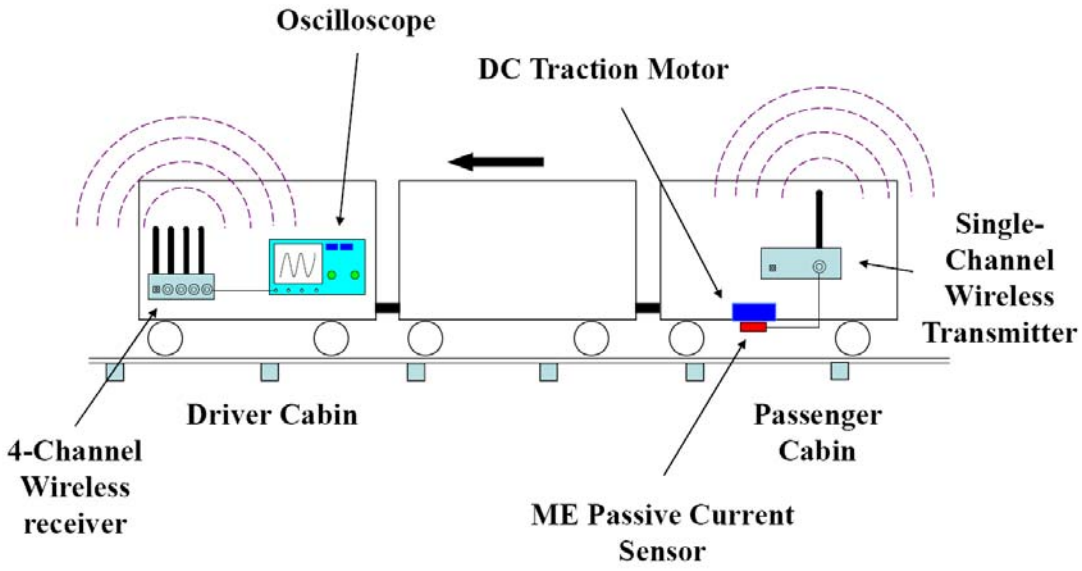

Fig. 6.3 Working principle of the proposed wireless condition monitor in Fig. 6.2.

The ratio of harmonic current (I_k) to fundamental current (I_1) is defined as

$$R_{I_k} = \frac{I_k}{I_1}, \tag{6.1}$$

where $k \neq 1$ is the order of harmonic currents. The total harmonic distortion of current signatures (THD_I), which is an important parameter, i.e., figure-of-merit, used to quantify the level of harmonics in current signatures, was calculated as the square root of the sum of the squares of the root-mean-square (rms) values of harmonic currents (I_k) divided by the rms value of the fundamental current (I_1) [86]:

$$THD_I = \frac{\sqrt{\sum_{k=2}^{15} I_k^2}}{I_1}. \tag{6.2}$$

6.2.3 Results and Analysis

Figures 6.4 and 6.5 show the current signatures acquired by the proposed wireless condition monitor and the distributions of the ratio of harmonic to fundamental currents (R_{Ik}) calculated using Eq. (6.1) when the train traction system is under steady-state and acceleration conditions, respectively. It is clear that the current signatures captured under the acceleration condition are physically different from those acquired under the steady-state condition. The calculated R_{Ik} distributions for harmonic currents up to the 15th order vary from 0.2 to 27 % for all cabins when the train traction system is under steady-state condition (Fig. 6.4). However, the calculated R_{Ik} distributions for harmonic currents have obviously larger variations from 0.3 to 67 % when the train traction system is under acceleration condition (Fig. 6.5). The total harmonic distortion of current signatures (THD_I) as calculated using Eq. (6.2) is found to vary from 34 to 38 % and from 51 to 66 % when the train traction system is under steady-state and acceleration conditions, respectively. This suggests more thermal losses occurred in the overhead lines and transformers when the train traction system is under acceleration condition compared to the steady-state condition [83]. For both conditions, our wireless condition monitor is capable of providing reliable real-time current signatures of all the four electrical motor drives. Hence, train operators can determine whether the train traction systems are running normally or not.

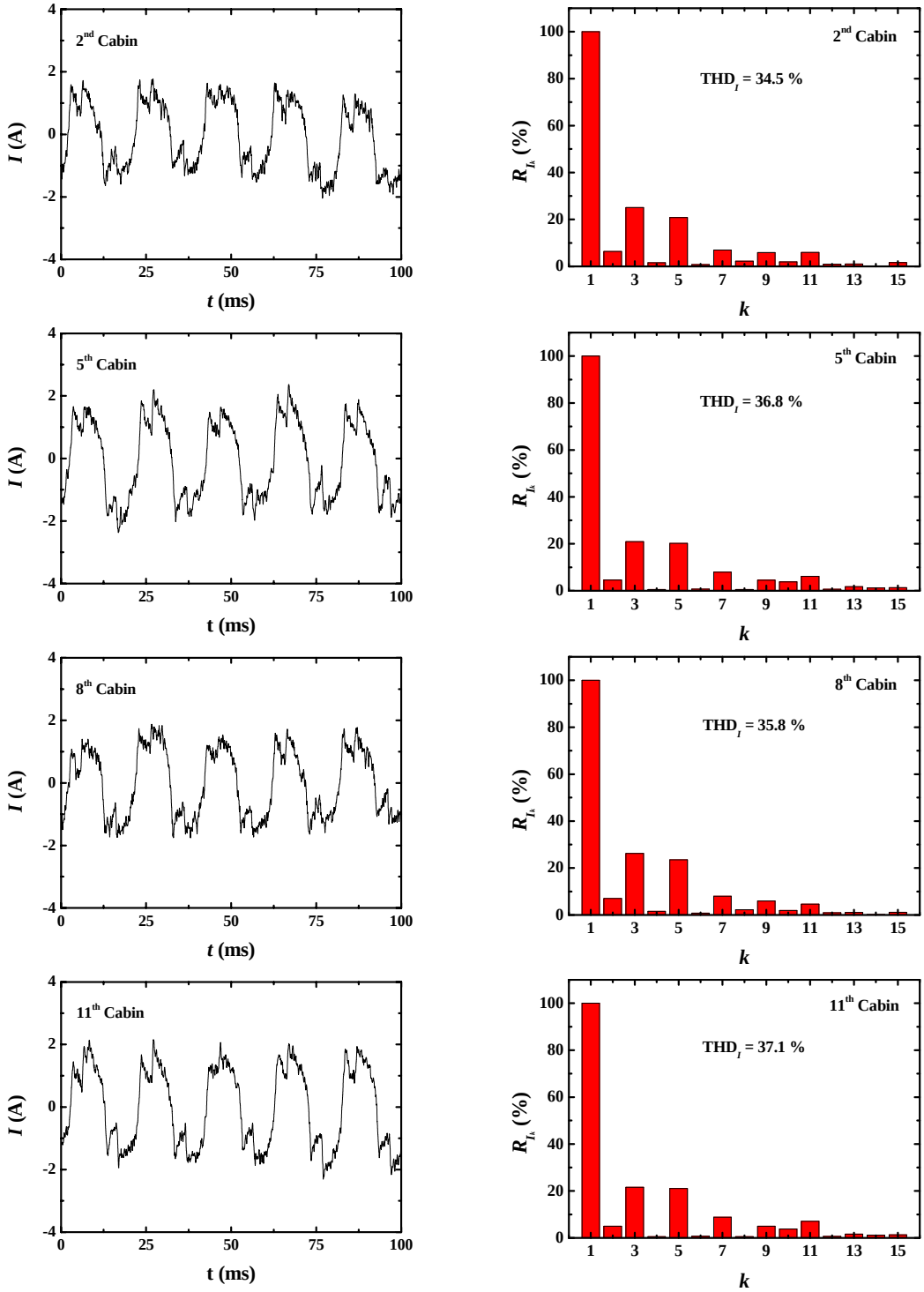

Fig. 6.4 **Current signatures acquired by the proposed wireless condition monitor and distributions of the ratio of harmonic to fundamental currents (R_{Ik}) calculated using Eq. (6.1) when the train traction system is operating under steady-state condition. The total harmonic distortions of current signatures (THD_I) are calculated using Eq. (6.2) and showed.**

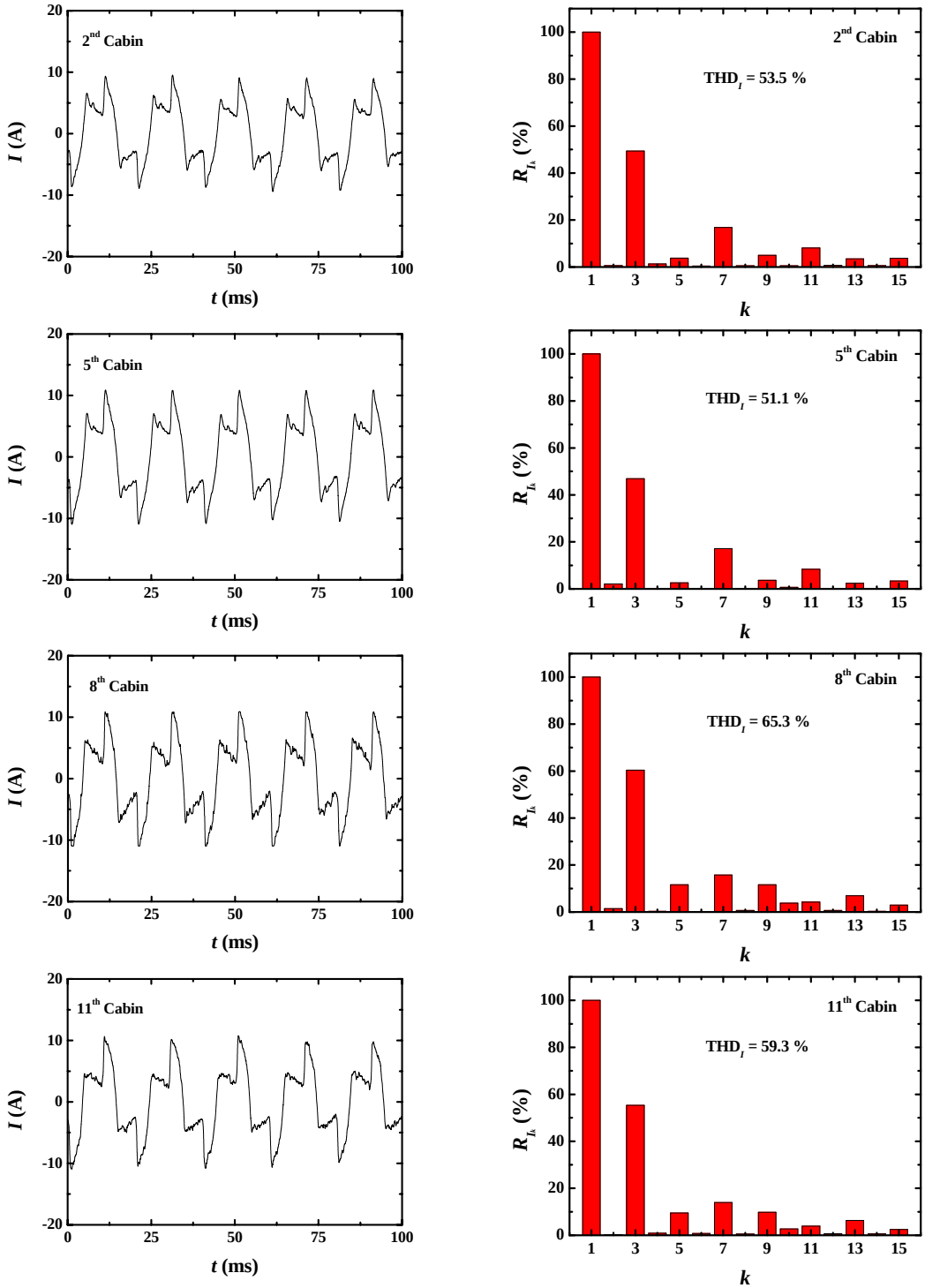

Fig. 6.5 **Current signatures acquired by the proposed wireless condition monitor and distributions of the ratio of harmonic to fundamental currents (R_{Ik}) calculated using Eq. (6.1) when the train traction system is under acceleration condition. The total harmonic distortions of current signatures (THD_I) are calculated using Eq. (6.2) and showed.**

6.2.4 Concluding Remarks

A first new-generation wireless condition monitor has been developed and demonstrated in electrical motor drives of train traction systems by integrating four surface mount-type ME passive current sensors with a short-range, 4-channel 2.4 GHz wireless communication unit to provide real-time, wireless monitoring of the current signatures of the four electrical motor drives situated underneath the 2nd, 5th, 8th, and 11th cabins of a 12-cabin mainline train operated by Hong Kong's MTR Corporation Limited on the East Rail Line. Four pairs of passive current sensors and single-channel wireless transmitters have been installed on electrical cables associated with the four electrical motor drives, while a 4-channel wireless receiver has been housed in the drive cabin. The current signatures were acquired by the wireless condition monitor in both steady-state and acceleration conditions. The distributions of ratio of harmonic to fundamental currents (R_{Ik}) and the total harmonic distortion of current signatures (THD_I) have also been calculated and analyzed. In addition to the magnitude of the current signatures, both R_{Ik} and THD_I obtained in acceleration condition have been found to be much higher than those in steady-state condition. Therefore, the train operators can determine real-time whether the train traction systems are running normally or not by simply noticing the current signatures and their R_{Ik} and THD_I values.

6.3 Monitoring of Electrical Switchgear

6.3.1 Application Background

In electrical power systems, switchgears are the combination of electrical disconnect switches, fuses, and circuit breakers used to control, protect, and isolate electrical equipment. In control, switchgears allow the systems to be split into small sections, making quick restoration of power supplies and clear faults downstream. In protection, switchgears interrupt short-circuit and overload fault currents while maintaining services to unaffected circuits. In isolation, switchgears isolate circuits from power supplies to enhance system availability by allowing more than one source to feed a load. With the rapid development of higher voltages, bigger units, and larger capacities as well as the rapid spread of nobody duty management of electrical systems, the safe and reliable operation of switchgears is becoming more and more important.

Most accidents in switchgears are related to hot temperatures generated by heavy currents in contacts, cables or buses [89]. On-line condition monitoring will identify potential problems which may lead to the damage of switchgears and their connecting systems. Correlations between the monitored currents, loads, and ambient conditions would allow abnormal conditions to be identified and early alarms to notify operation and maintenance personnel of potential problems. Further deterioration from abnormal conditions could lead to a recommendation to suspend the service of the switchgears. Hence, an on-line condition monitoring of the electrical currents in switchgears is not only very important but also challenging because of the existence of high voltages, heavy currents, and strong electromagnetic fields. Hence, our developed

ME passive current sensors are capable of providing a good demonstration to this application.

In this case, three surface mount-type ME passive current sensors (Fig. 4.12) are integrated with a long-range, 3-channel HSDPA/GPRS wireless communication unit (Fig. 5.14) to form a wireless condition monitor for monitoring the current signatures associated with three 380 V, 400 A 3-phase power distribution cables inputted to an ABB 400 V, 1,000 A, 3-phase electrical switchgear installed in the Electrical Machines Laboratory (EF001a) of the Department of Electrical Engineering at PolyU. Figure 6.12 shows the photograph of the 400 V, 1,000 A, 3-phase electrical switchgear made by ABB Xiamem Low Voltage Equipment Co, Ltd. Table 6.2 summarizes the important parameters of the ABB 400 V, 1,000 A, 3-phase electrical switchgear in Fig. 6.12. It has a rated operating voltage of 400 V, a rated operating frequency of 50 Hz for the incoming 380 V, 400 A, 3-phase electrical powers from CLP Power Hong Kong Limited. The high rated main busbar current of 2,000 A and the large rated distribution busbar current of 1,000 A ensure the switchgear in good operation even at the full-load current of 400 A. The high rated main busbar peak withstand current of 165 kA and large rated busbar short-time withstand current of 75 kA provide a high transient current stability in the switchgear.

Fig. 6.6 The 400 V, 1,000 A, 3-phase electrical switchgear made by ABB Xiamen Low Voltage Equipment Co. Ltd. and installed in the Electrical Machines Laboratory (EF001a) of the Department of Electrical Engineering at PolyU.

Table 6.2 Specifications of the ABB 400 V, 1,000 A, 3-phase electrical switchgear shown in Fig. 6.6.

Parameter	Value
Rated operating voltage	400 V
Rated frequency	50 Hz
Rated main busbar current	2,000 A
Rated distribution busbar current	1,000 A
Rated main busbar peak withstand current	165 kA
Rated main busbar short-time withstand current	75 kA

6.3.2 Field Installation and Implementation

Figure 6.7 shows the field installation of three surface mount-type ME passive current sensors (Fig. 4.12) and a long-range, 3-channel HSDPA/GPRS wireless communication unit (Fig. 5.14) in an ABB 400 V, 1,000 A, 3-phase electrical switchgear loaded with electrical machines and equipment and located in the Electrical Machines Laboratory (EF001a) of the Department of Electrical Engineering at PolyU. The three current sensors were mounted on the surfaces of the 380 V, 400 A 3-phase power distribution cables connected from CLP Power Hong Kong Limited. The three output signal coaxial cables from the current sensors were connected to the three input channels, of the wireless communication unit.

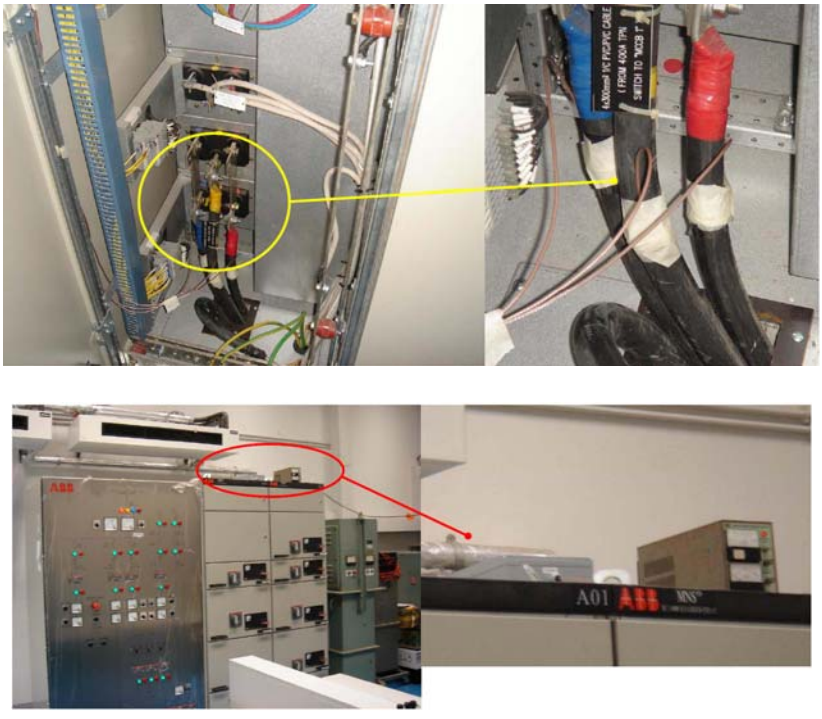

Fig. 6.7 Installation of the surface mount-type ME passive current sensors and the long-range, 3-channel HSDPA/GPRS wireless communication unit in the ABB 400 V, 1,000 A, 3-phase electrical switchgear located in the Electrical Machines Laboratory (EF001a) of the Department of Electrical Engineering at PolyU.

The working principle of the proposed wireless condition monitor for the monitoring of power distribution cables for the electrical switchgear is shown in Fig. 6.8. The three current sensors detected the magnetic fields governed by the currents (*I*) flowing in the 3-phase power distribution cables. The wireless communication unit transmitted the current signature data through the commercial HSDPA/GPRS internet network to the personal computer (PC)-based file transfer protocol (FTP) server located in the operator room (HJ801) of PolyU. In operation, the wireless communication unit was set at 1 MHz sampling rate, 10 times voltage gain, 0.1 s scanning time, and 30 min transmission interval. The current signature data was collected continuously by the PC-based FTP server, stored as a database in the PC, and processed by the PC to give the current waveforms and frequency spectra. The wireless condition monitor has been put in service May 2010. In the present case, data collected in the period from 12 September 2011 (Monday) to 16 September 2011 (Friday) was chosen for presentation since this period covered two electrical machine-related laboratory sessions and the monitored information was able to represent the electricity utilization in the presence and absence of the laboratory sessions in the Electrical Machines Laboratory. Figure 6.9 shows the laboratory timetable of the Electrical Machines Laboratory in the academic year 2011/2012. It is clear that there were two laboratory sessions running from 09:30 to 12:25 on 12 September 2011 (Monday) and from 18:30 to 21:25 on 16 September 2011 (Friday).

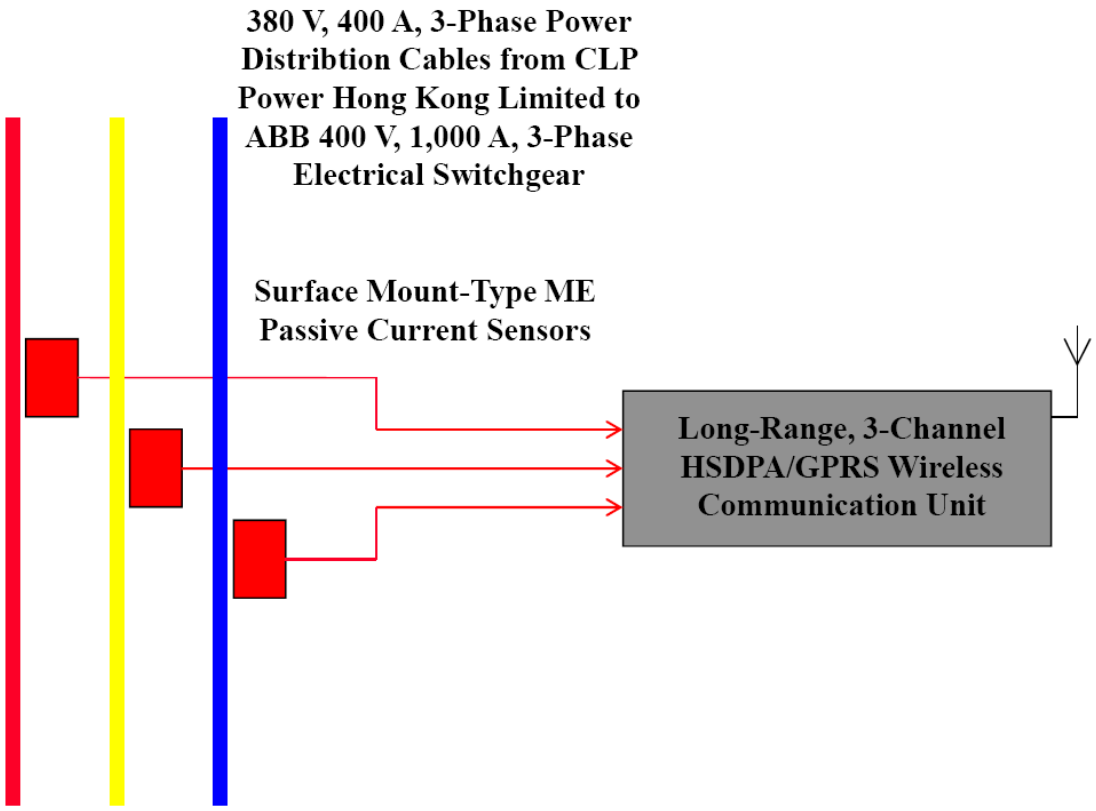

Fig. 6.8 Working principle of the proposed wireless condition monitor in Fig. 6.7.

Lab Timetable
Year : 2011/12 Semester: 1
Department : ELECTRICAL ENGINEERING (41)
Lab : EF001a

	Monday	Tuesday	Wednesday	Thursday	Friday	Saturday
08:30-09:00						
09:00-09:25						
09:30-10:00	EE3731 ELECTROMECHANICAL ENERGY CONVERSION 731S01 [121] LAB001 Start on Wk3 [EF001a] KC Wong					
10:00-10:25						
10:30-11:00						
11:00-11:25						
11:30-12:00						
12:00-12:25						
12:30-13:00						
13:00-13:25						
13:30-14:00						
14:00-14:25						
14:30-15:00						
15:00-15:25						
15:30-16:00						
16:00-16:25						
16:30-17:00						
17:00-17:25						
17:30-18:00						
18:00-18:25						
18:30-19:00					EE3021 ELECTROMECHANICAL ENERGY CONVERSION 021S01 [1111] LAB001 Start on Wk3 [EF001a] KC Wong	
19:00-19:25						
19:30-20:00						
20:00-20:25						
20:30-21:00						
21:00-21:25						
21:30-22:00						
22:00-22:25						

Remark:
Detail lab schedule to be arranged by subject lecturer
Electives
Compulsory
Lab for Compulsory/Electives subject

Fig. 6.9 Laboratory timetable of the Electrical Machines Laboratory (EF001a) in the academic year 2011/12.

6.3.3 Test Results and Analysis

Figure 6.10 shows the monitored rms currents as a function of time session (*T*) for Phases A, B, and C of the electrical switchgear on five consecutive dates from 12 September 2011 (Monday) to 16 September 2011 (Friday). The high current usage is detected on Monday from 10:00 to 12:00 and on Friday from 19:00 to 20:30 due to the running of laboratory lessons on these two days. The highest current usage is found to be 38 A for Phase A, 27 A for Phase B, and 43 A for Phase C at around 11:00 on Monday and to be 31 A for Phase A, 33 A for Phase B, and 46 A for Phase C at around 20:00 on Friday. In other time sessions, the usage of current in the electrical switchgear is ~14 A on average.

Figure 6.11 illustrates the monitored 3-phase current waveforms and the transformed frequency spectra at three different times and dates of 09:23:39 on 12 September 2011 (Monday), 10:53:39 on 12 September 2011 (Monday), and 19:58:03 on 16 September 2011 (Friday), respectively. It is clear that the current usages at 10:53:39 on 12 September 2011 [Fig. 6.11(b)] and at 19:58:03 on 16 September 2011 [Fig. 6.11(c)] are much higher than that of 09:23:39 on 12 September 2011 [Fig. 6.11(a)] because of the holding of laboratory lessons. In rest time of 09:23:29 on 12 September 2011 [Fig. 6.11(a)], the harmonic currents are slightly larger than the laboratory times [Figs. 6.11(b) and (c)]. It may be caused by the connection of dirty loads to the 3-phase supplies in the laboratory by researchers. In the laboratory lessons, an imbalance of use of 3-phase current occurs due to the operation of different

electrical motors and generators at the same time, including three-phase and single-phase ac motors and generators.

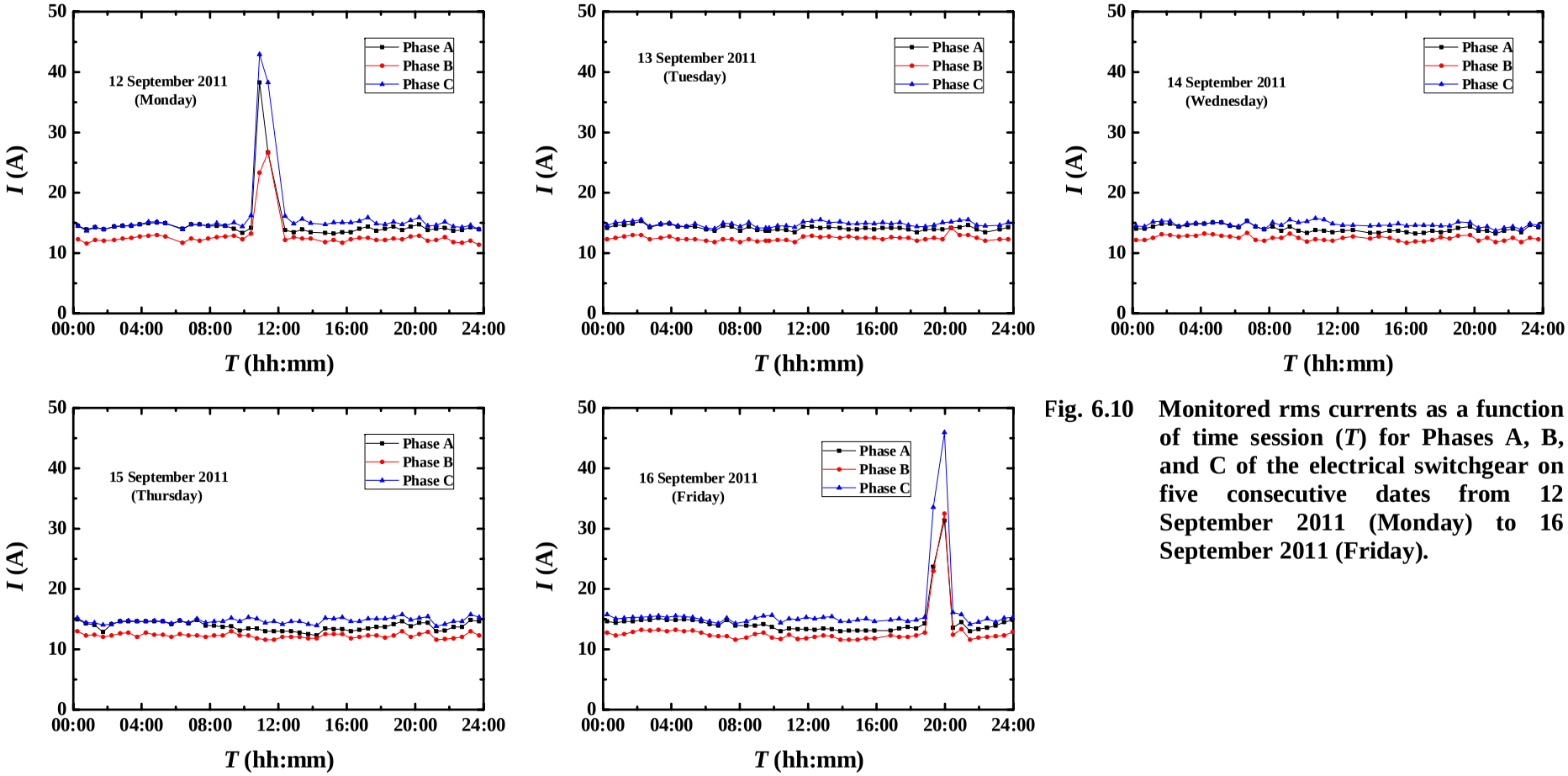

Fig. 6.10 **Monitored rms currents as a function of time session (*T*) for Phases A, B, and C of the electrical switchgear on five consecutive dates from 12 September 2011 (Monday) to 16 September 2011 (Friday).**

(a)

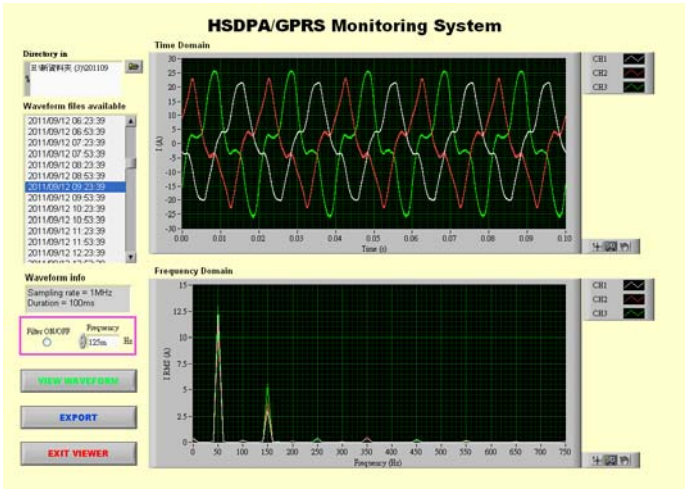

(b)

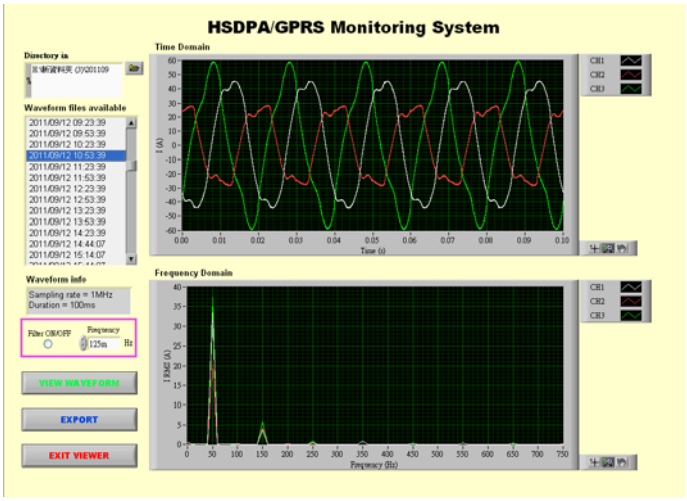

(c)

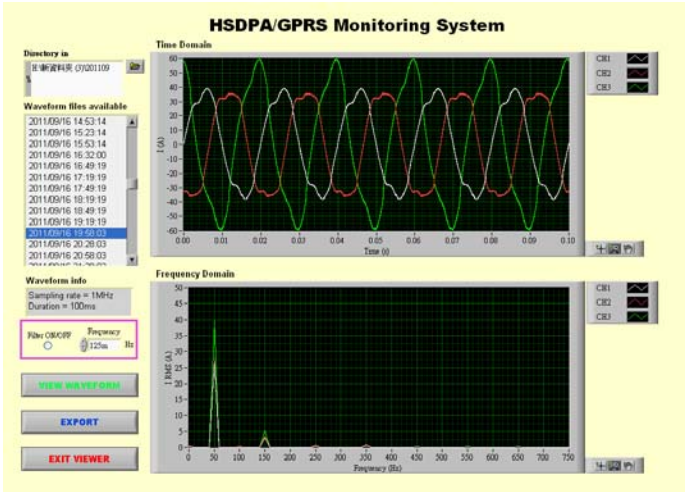

Fig. 6.11 Monitored 3-phase current waveforms and the transformed frequency spectra at three different times and dates: (a) 09:23:39 on 12 September 2011, (b) 10:53:39 on 12 September 2011, and (c) 19:58:03 on 16 September 2011.

6.3.4 Concluding Remarks

A second new-generation wireless condition monitor has been realized and applied for electrical switchgear using three surface mount-type ME passive current sensors and a long-range, 3-channel HSDPA/GPRS wireless communication unit to provide real-time, wireless monitoring of 3-phase currents of the three power distribution cables associated with the ABB 400 V, 1,000 A, 3-phase electrical switchgear installed in the Electrical Machines Laboratory (EF001a) of the Department of Electrical Engineering at PolyU. The wireless condition monitor has been deployed in the electrical switchgear since May 2010. During the report period of 12 September 2011 (Monday) –16 September 2011 (Friday), the electricity utilization in the presence and absence of laboratory lessons has been investigated and the current usage has been found to be as high as 27–46 A and as low as 14 A when a laboratory session was and was not running, respectively. Hence, the proposed wireless condition monitor can provide remote monitoring of the conditions of the electrical switchgear.

6.4 Monitoring of Switching Mode Power Supply

6.4.1 Application Background

Switching mode power supplies are a major class of electronic power supplies which incorporates a switching regulator to ensure an efficient conversion and transfer of electrical power from a source to a load with regulated output voltage and current characteristics. Compared to traditional linear power supplies, the switching mode power supplies are smaller and lighter due to the elimination of isolation and voltage-scaling transformers. Unlike linear power supplies, the switching regulator of switching mode power supplies switch continually between low-dissipation, full-on and full-off states by spending very little time in the high-dissipation transitions in order to minimize waste of energy. Voltage regulation is achieved by varying the ratio of on-to-off time. In contrast, linear power supplies regulate the output voltages by continually dissipating power in power transistors. Nonetheless, this suggests that switching mode power supplies generally have lower power dissipation and high efficiencies than the linear power supplies. While switching mode power supplies have many advantages, their configurations are more complicated. Moreover, the high-frequency switching often induces EMI, harmonics, ripples, etc. to their own circuits and other equipment, while simple designs can cause poor power factors.

Therefore, a third type of wireless condition monitor comprising a clamp-type ME passive current sensor (Fig. 4.3) and a short-range, 4-channel 2.4 GHz wireless communication unit (Fig. 5.3) are formed to monitor the current signatures associated with a 220 V 13 A switching mode power supply used for driving a personal computer

(PC). Similar to the previous two cases, the field installation and implementation of the wireless condition monitor are presented; the test results are analyzed; and concluding remakes are provided.

6.4.2 Field Installation and Implementation

The installation and implementation in this case is relatively simple as compared with the previous two cases involving electrical motor drives of the train traction system (Section 6.2) and electrical switchgear (Section 6.3). As shown in Fig. 6.12, the clamp-type ME passive current sensor as reported in Fig. 4.25 was clamped on an electrical cable of the 220V, 13 A switching power supply of a PC and the signal output from the current sensor was directed to the input of the single-channel wireless transmitter as described in Fig. 5.3. The switching mode power supply was rated at 300 W power with ±12, ±5, and +3.3 V multi-voltage outputs. The four-channel wireless receiver was connected with an oscilloscope (Tektronix MSO 2014) to provide real-time wireless monitoring and recording of the current signatures of the switching mode power supply.

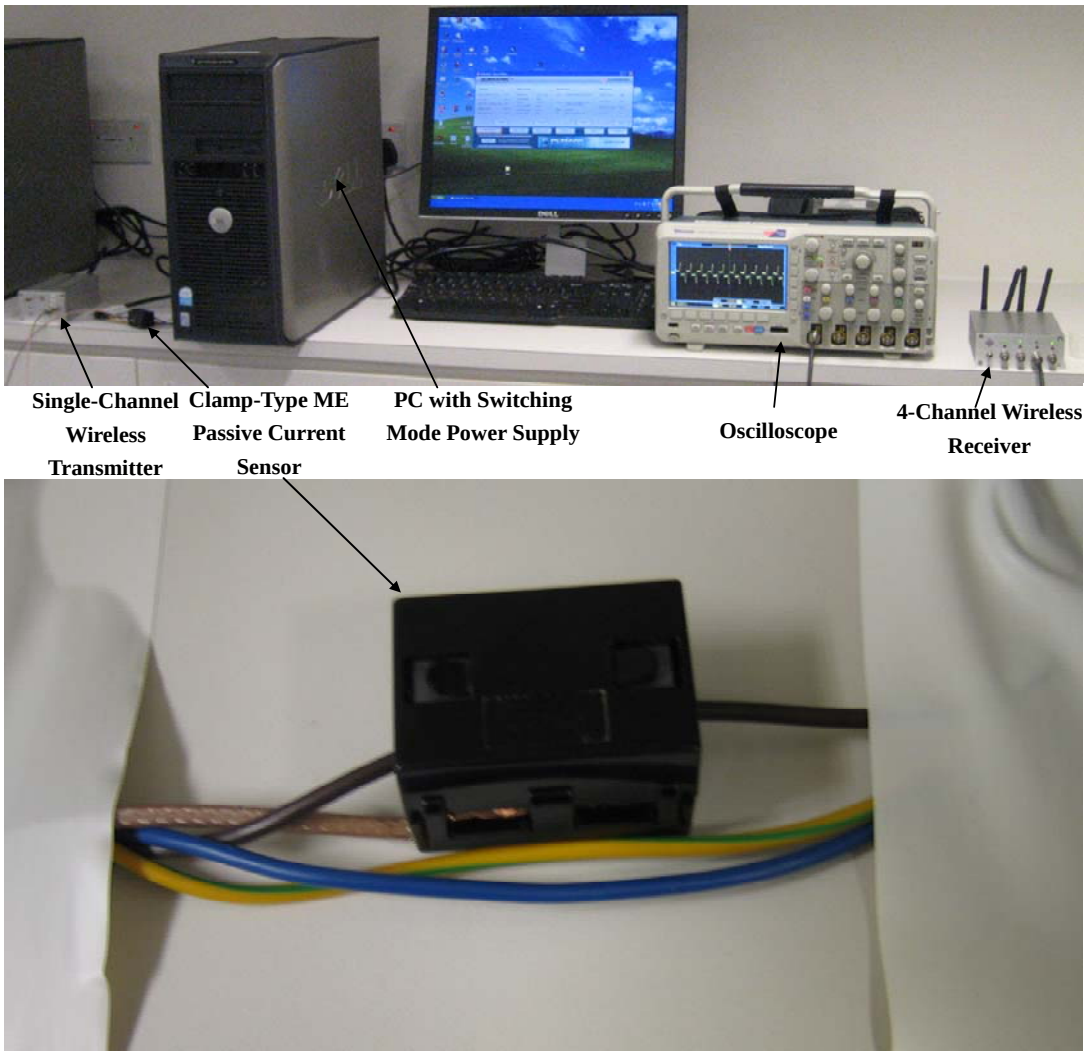

Fig. 6.12 Installation of the clamp-type ME passive current sensor and the short-range, 4-channel wireless communication unit in a 220 V, 13 A switching mode power supply for PC.

6.4.3 Test Results and Analysis

Figure 6.13 shows the current signatures acquired by the proposed wireless condition monitor and the distributions of the ratio of harmonic to fundamental currents (R_{Ik}) calculated using Eq. (6.1) when the switching mode power supply of the PC is in the idle (i.e., sleep mode) and processing conditions. The total harmonic distortion of the current signatures (THD_I) is calculated using Eq. (6.2) and showed in the same plots of R_{Ik}. It is found that the currents supplied by the switching mode power supply are ~0.65 and ~ 0.95 A rms when the PC is in the idle and processing conditions, respectively. There are some even harmonics in the idle condition, but only odd harmonics are present in the processing condition. It may be due to the asymmetrical current signatures in the idle condition to reduce the efficiency of the switching mode power supply. The corresponding THD_I values are found to be 99.9 and 94.2 % for the idle and processing conditions, respectively.

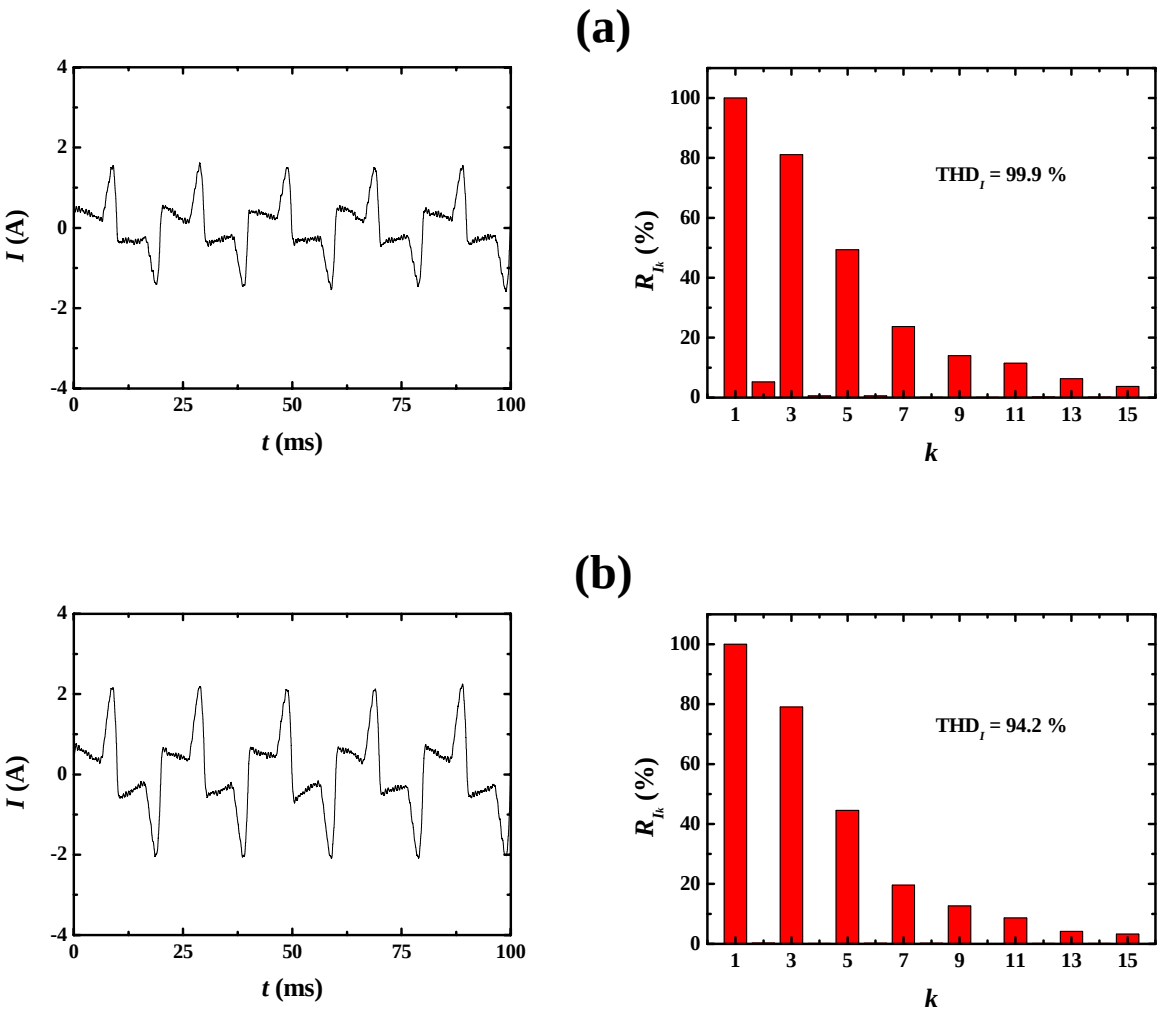

Fig. 6.13 Current signatures acquired by the proposed wireless condition monitor and distributions of the ratio of harmonic to fundamental currents (R_{Ik}) calculated using Eq. (6.1) when the switching mode power supply of PC is in (a) idle and (b) processing conditions. The total harmonic distortion of current signatures (THD_I) is calculated using Eq. (6.2) and showed.

6.3.4 Concluding Remarks

A third new-generation wireless condition monitor has been formed and showed up to monitor the currents of a switching mode power supply of a PC based on a clamp-type ME passive current sensor and a short-range, 2.4 GHz wireless communication unit. The current signatures collected by the wireless condition monitor when the PC is the idle and processing conditions have been compared and analyzed using R_{Ik} and THD_I. Only even harmonics of R_{Ik} have been observed in the idle condition, causing THD_I to be higher in the processing condition (i.e., 94.2 %) compared to the idle condition (i.e., 99.9 %). Therefore, it is practically viable to use the developed wireless condition monitor for real-time, wireless monitoring of electronic equipment and systems.

Chapter 7

Conclusions and Suggestions for Future Work

7.1 Conclusions

The rapid development in modern electrical asserts such as smart electric grids, renewable energy systems, high-speed and intercity railways, electric vehicles, intelligent buildings, telecommunication systems, etc. in recent years has greatly increased the concerns and demands about real-time monitoring of the operating conditions of the assets for performance optimization, utilization maximization, safety enhancement, and reliability improvement. Traditional “wired condition monitors” for electrical assets involve the deployment of active current sensors (e.g., Hall sensors, Rogowski coils, etc.) in multiple locations (nodes) and the connections between the active sensors and their power supplies, signal conditioners, and base station (network) through power and signal cables/wires. These wired condition monitors are not only complicated and expensive in terms of installation and maintenance, but also suffer from applications having large spatial sizes, tough and complex arrangements, critical measuring locations, high-voltage and heavy-current environments, etc. By contrast, state-of-the-art “wireless condition monitors”, which usually integrate active current sensors with wireless communication (transmitter and receiver) units, all powered by power packs or batteries, have emerged as a flexible alternative to the traditional wired

condition monitors due to the ease of installation, large scalability, and highly distributed nature. However, the need for powering the active sensors with limited battery life through power cables still constrains their applicability.

In this thesis, we have aimed at developing a new generation of wireless condition monitors consisting of novel surface mount-type or clamp-type magnetoelectric (ME) passive (power supply-free) current sensors and 2.4 GHz or 3G/2G multichannel wireless communication units for an improved real-time wireless monitoring of the current signatures governed by electrical assets. Three representative types of electrical assets have been identified and implemented with the new generation wireless condition monitors. These include: (1) electrical motor drives of train traction systems; (2) 400 V, 1,000 A, 3-phase electrical switchgears; and (3) 220 V, 13 A switching mode power supplies.

First, five different types of magnetostrictive and piezoelectric materials which constitute the ME sensing elements in the ME passive current sensors have been studied in the three aspects of fabrication, characterization, and physical properties. The materials include: $Tb_{0.3}Dy_{0.7}Fe_{1.92}$ (Terfenol-D) alloy plates and Terfenol-D short-bar–epoxy composite plates on the magnetostrictive side and $0.7Pb(Mg_{1/3}Nb_{2/3})O_3$–$0.3PbTiO_3$ (PMN–PT) single-crystal plates/bars, PMN–PT single-crystal transformers, and PZT ceramic rings on the piezoelectric side. The quasistatic and dynamic magnetic, magnetomechanical, and elastic properties of Terfenol-D alloy plates and Terfenol-D short-bar–epoxy composite plates have been evaluated at zero prestress condition. The dielectric, electromechanical, and elastic properties of PMN–PT

single-crystal plates/bars have been investigated according to the resonance method stated in the ANSI/IEEE standard. The frequency dependence of step-up voltage ratio of PMN–PT single-crystal transformers has also been determined. The acquired physical properties have been served as the fundamental material properties for development of ME sensing elements and the subsequent ME passive current sensors.

Second, three characteristic types of ME sensing elements have been developed through the exploration of their structures, working principles, physical modeling, fabrication, characterization, and performance. The ME sensing elements include: (1) plate-shaped sensing elements with a PMN–PT piezoelectric single-crystal plate having a thickness polarization sandwiched between two Terfenol-D magnetostrictive alloy plates having a length magnetization; (2) ring-shaped sensing elements with an inner Terfenol-D short-bar–NdFeB magnet–epoxy three-phase magnetostrictive composite ring having a circumferential magnetization and an internal magnetic biasing concentric to an outer PZT piezoelectric ceramic ring having a wall-thickness polarization; and (3) bar-shaped sensing elements with a Rosen-type or long-type PMN–PT piezoelectric single-crystal transformer with its input part sandwiched between two Terfenol-D magnetostrictive alloy plates having a length magnetization. Physical models for describing the working principles of the sensing elements and for predicting their ME voltage coefficients (α_V) under different combinations of dimensions and material properties have been established and confirmed by experimental investigations. It has been found that the maximum α_V of the plate-shaped, ring-shaped, and bar-shaped sensing elements are about 280, 21.6,

and 320 mV/Oe at non-resonance, and 3.2, 0.3, and 15.5 V/Oe at resonance, respectively. In addition, the plate-shaped and ring-shaped sensing elements are suitable for broadband nonresonance sensing, while the bar-shaped sensing elements incorporating piezoelectric transformers for amplification of ME voltages are good for narrowband resonance sensing with increased sensitivity.

Third, two novel types of ME passive current sensors, namely: (1) surface mount-type current sensors and (2) clamp-type current sensors, both with magnetic field biasing, electric field shielding, and thermal insulation capabilities, have been conceptualized based on the plate-shaped and ring-shaped ME sensing elements, respectively, and their design requirements have been stated in accordance with application needs. Magnetic, electric, and/or thermal physical modeling and/or finite element analysis (FEA) techniques have been applied to investigate the effects of magnetic field biasing, electric field shielding, and/or thermal insulation on the performance of the current sensors. The fabrication and performance evaluations of the current sensors have been performed and summaries of useful performance data have been provided.

Fourth, two different types of multichannel wireless communication units, including a short-range, 4-channel, 2.4 GHz unit and a long-range, 3-channel, 3G/2G unit, have been developed for integration with the developed ME passive current sensors. The conceptual design and design requirements as well as the hardware and software developments of the two units have been described. The performance of the two units have been evaluated in the laboratory environment using direct signals

generated by an arbitrary waveform generator and indirect signals detected by the ME passive current sensors.

Finally, three distinct sets of wireless condition monitors have been formed for use in three different field tests. In the first field test, four surface mount-type current sensors have been integrated with the 2.4 GHz wireless communication unit for monitoring the electrical motor drives of the train traction system of a 12-cabin mainline train operated by MTR Corporation Limited and running between Hong Kong and Shenzhen, China on the East Rail Line. Four pairs of current sensors and wireless transmitters have been installed on electrical cables associated with the four electrical motor drives of the train traction system situated underneath the 2^{nd}, 5^{th}, 8^{th}, and 11^{th} cabins of the train, while the wireless receiver has been housed in the driver cabin to provide real-time wireless monitoring of the current signatures of the four electrical motor drives. The real-time current signatures, ratio of harmonic current to fundamental current (R_{Ik}) spectra, and total harmonic distortion of current signatures (THD_I) under steady-state and acceleration conditions have been captured, analyzed, and discussed. In the second field test, three surface mount-type current sensors have been used with the 3G/2G wireless communication unit for monitoring an ABB 400 V, 1,000 A, 3-phase electrical switchgear located in the Electrical Machines Laboratory (EF001a) of the Department of Electrical Engineering at PolyU. The wirelessly transmitted 3-phase current signature data has been remotely accessed, processed, monitored, and controlled by a personal computer (PC)-based file transfer protocol (FTP) server with a web-based user control interface located in the Multifunctional

Materials and Systems Laboratory (HJ801–HJ803) of PolyU. The current usage of Phases A, B, and C of the electrical switchgear in the period from 12 September 2011 (Monday) to 16 September 2011 (Friday) has been collected, stored, and analyzed. The results have been compared with the laboratory timetable and utilization with good agreements. In the third field test, a clamp-type current sensor has been combined with the 2.4 GHz wireless communication unit for monitoring a 220 V, 13 A switching mode power supply used for driving PC. The current usage of the PC under idle and processing states have been assessed and analyzed by evaluating its real-time current signatures and the resulting R_{Ik} and THD_I.

7.2 Suggestions for Future Work

7.2.1 Self-Powered Wireless Condition Monitors

In this study, ME passive current sensors based on the magnetoelectric effect have been successfully developed and demonstrated to alleviate the powering and wiring problems intrinsic in state-of-art active current sensors and their wireless condition monitors [Fig. 1.4(b)]. On the one hand the ME passive current sensors can truly function as autonomous current sensors for improved current monitoring purposes, and on the other hand they can be configured and used as passive energy converters to convert magnetic (or electromagnetic) energy radiated from current-carrying cables or conductors into electrical energy in energy harvesters for the subsequent energization of wireless communication units in replacement of power packs or batteries [Fig. 1.4(c)]. Accordingly, self-powered wireless condition monitors

can be realized by combining the dual-functionality of current sensing and energy conversion/harvesting of the ME passive current sensors. Therefore, the ME energy harvesting technology is a worth topic for further study.

7.2.2 DC Magnetoelectric Current Sensors

The ME passive current sensors reported in this thesis are essentially "ac" ME passive current sensors whereby an ac applied electric current or magnetic field induces an ac electric voltage on the basis of the mechanically mediated magnetostrictive and piezoelectric effects in the constituent material phases of the ME sensing elements. As a result, these sensors fall short of any dc or quasi-dc applications such as sensing of electric currents or magnetic fields in dc electrical machines and electric vehicles as well as detection of magnetic field anomalies.

Figure 7.1 shows a promising type of "dc" ME current sensor invented during the course of the present study [90]. The operation of the sensor is based on the direct-coupling of Lorentz force generated from a pair of electrically connected aluminum strips under an applied dc magnetic field and a reference ac electric current to the

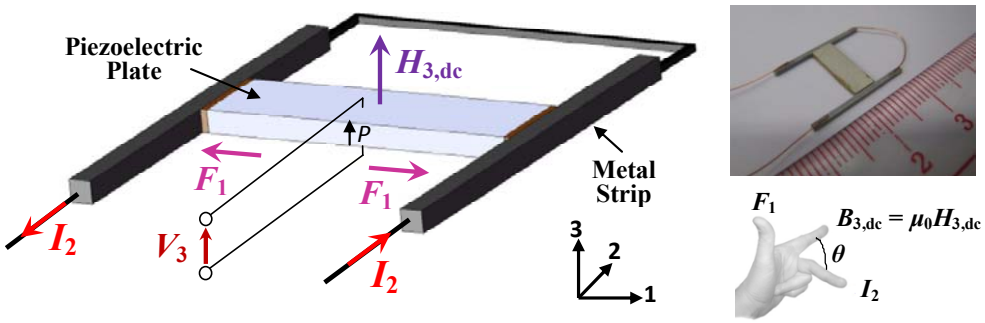

Fig. 7.1 Schematic diagram and photograph of the proposed dc ME current sensor.

sandwiched PMN–PT piezoelectric single-crystal plate so as to produce a piezoelectric voltage with amplitude linearly proportional to the applied dc magnetic field and with both amplitude and frequency directly controllable by the reference ac electric current. This dc ME current sensor only needs a less-demanding reference ac electric current to produce the dc measuring function.

7.2.3 Magnetostrictive-Fiber Bragg Grating (MS–FBG) Current Sensors

The ME passive current sensors in the present study are capable of providing real-time current measurements with single measuring point. To obtain multiple-point measurements, wireless sensor nodes and networks are required. Alternatively, by combining magnetostrictive materials and fiber Bragg gratings (FBGs), a novel class of current sensors, known as magnetostrictive–fiber Bragg grating (MS–FBG) current sensors, can be realized and shown in Fig. 7.2 [91]. In the proposed design, the magnetostrictive materials function as a magnetic actuator with magnetostrictive strain as the output, while the FBGs operate as a strain sensor with the magnetostrictive

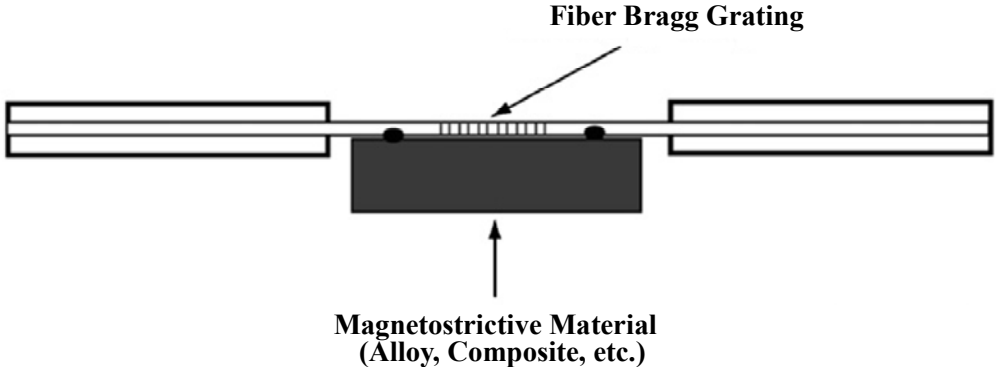

Fig. 7.2 Schematic diagram of the MS−FBG current sensor.

strain from the magnetostrictive materials as the input. Compared to conventional non-optical current sensors such as Hall-effect sensors and reluctance coils, this type of MS–FBG current sensors features a high level of immunity to electromagnetic interference (EMI), a great potential for large-scale multiplexing, and a large capability for self-reference.

Appendix A

Electrical Equivalent Circuits of Piezoelectric Plates and Magnetoelectric Laminates

A.1 Electrical Equivalent Circuit of Piezoelectric Plates

The piezoelectric effect in a piezoelectric plate having a length polarization (P) along the z-direction and operating in the length (or the 33-) mode can be depicted by an electrical equivalent circuit approach. Consider the piezoelectric plate with the length-polarized configuration and arranged in the Cartesian coordinate system as shown in Fig. A.1. Since the length (l_p) is much larger than the width (w_p) and the thickness (t_p), the length mode is regarded as the fundamental operating mode in the piezoelectric plate.

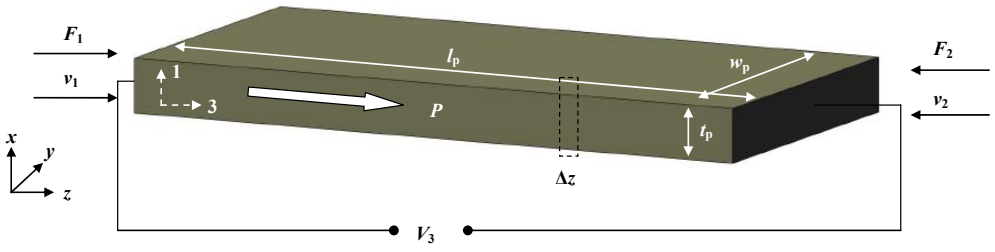

Fig. A.1 Schematic diagram of a piezoelectric plate having a length polarization (P) and operating in the length mode.

The constitutive equations for the piezoelectric plate are given by

$$S_{3,\mathrm{p}} = s_{33}^{D} T_{3,\mathrm{p}} + g_{33,\mathrm{p}} D_3 , \tag{A.1}$$

$$E_3 = -g_{33,\mathrm{p}} T_{3,\mathrm{p}} + \beta_{33}^{T} D_3 , \tag{A.2}$$

where D_3 and E_3 are the dielectric displacement and electric field along the length (or the *z*-) direction, respectively; $S_{3,\mathrm{p}}$ and $T_{3,\mathrm{p}}$ are the strain and stress along the length direction, respectively; β_{33}^{T}, $g_{33,\mathrm{p}}$, and s_{33}^{D} are the dielectric impermittivity at constant stress, the piezoelectric voltage coefficient, and the elastic compliance at constant dielectric displacement, respectively.

According to the Newton's second law of motion, the wave equation is expressed as

$$\frac{\partial^2 \zeta}{\partial t^2} = (v_3^D)^2 \frac{\partial^2 \zeta}{\partial z^2} , \tag{A.3}$$

where $v_3^D = \sqrt{\rho_p s_{33}^D}$ is the longitudinal wave velocity and ζ is the longitudinal displacement. Under harmonic oscillation, Eq. (A.3) is simplified as

$$\frac{\partial^2 \zeta}{\partial z^2} + k^2 \zeta = 0 , \tag{A.4}$$

where $k = \omega / v_3^D$ is the wave number and ω is the angular frequency. The general solution of Eq. (A.4) can be written as

$$\zeta = A \sin kz + B \cos kz . \tag{A.5}$$

The face velocities ($\dot{\zeta}$) of the piezoelectric plate at the boundaries $z = 0$ and $z = l_{\mathrm{p}}$ are expressed, respectively, as

$$\dot{\zeta}\,|_{z=0} = j\omega B = v_1 \tag{A.6}$$

and

$$\dot{\zeta}\,|_{z=l_p} = j\omega(A\sin kl_p + B\cos kl_p) = -v_2\,. \tag{A.7}$$

The two variables A and B are resolved as

$$A = -(\frac{v_1\cos kl_p}{\sin kl_p} + \frac{v_2}{\sin kl_p})\frac{1}{j\omega} \tag{A.8}$$

and

$$B = \frac{v_1}{j\omega}\,. \tag{A.9}$$

ζ, $S_{3,p}$ ($=\partial\zeta/\partial z$), and $T_{3,p}$ are determined to be

$$\zeta = -\frac{1}{j\omega}\left[(\frac{v_1\cos kl_p}{\sin kl_p} + \frac{v_2}{\sin kl_p})\sin kz - v_1\cos kz\right], \tag{A.10}$$

$$S_{3,p} = \frac{\partial\zeta}{\partial z} = -\frac{k}{j\omega}\left[(\frac{v_1\cos kl_p}{\sin kl_p} + \frac{v_2}{\sin kl_p})\cos kz - v_1\sin kz\right], \tag{A.11}$$

and

$$T_{3,p} = \frac{1}{s_{33}^D}\left(S_{3,p} - g_{33,p}D_3\right) = -\frac{k}{j\omega s_{33}^D}\left[(\frac{v_1\cos kl_p}{\sin kl_p} + \frac{v_2}{\sin kl_p})\cos kz + v_1\sin kz\right] - \frac{g_{33,p}}{s_{33}^D}D_3\,. \tag{A.12}$$

The forces (F_1 and F_2) acting on the two end faces of the piezoelectric plate are related to $T_{3,p}$ as

$$F_1 = -A_pT_{3,p}\,|_{z=0} = \frac{A_pk}{j\omega s_{33}^D}(\frac{v_1\cos kl_p}{\sin kl_p} + \frac{v_2}{\sin kl_p}) + \frac{g_{33,p}A_p}{s_{33}^D}D_3\,, \tag{A.13}$$

$$F_2 = -A_pT_{3,p}\,|_{z=l_p} = \frac{A_pk}{j\omega s_{33}^D}(\frac{v_1}{\sin kl_p} + \frac{v_2\cos kl_p}{\sin kl_p}) + \frac{g_{33,p}A_p}{s_{33}^D}D_3\,, \tag{A.14}$$

where $A_p = w_p\ t_p$ is the cross-sectional area of the piezoelectric plate. The coupling current (I_3) passing through the electrodes is

$$I_3 = j\omega A_p D_3 . \tag{A.15}$$

The output voltage (V_3) of the piezoelectric plate along the length direction is

$$V_3 = \int_0^l E_3 dz = \frac{g_{33,p}}{j\omega s_{33}^D}(v_1 + v_2) + \frac{1}{j\omega C_0} I_3 . \tag{A.16}$$

By combining Eqs. (A.13), (A.14), and (A16), the total equations for the piezoelectric plate can be written as

$$F_1 = (Z_1 + Z_2 + Z_{C0})v_1 + Z_2 v_2 + NV_3 , \tag{A.17}$$

$$F_2 = Z_2 v_1 + (Z_1 + Z_2 + Z_{C0})v_2 + NV_3 , \tag{A.18}$$

$$I_3 = j\omega C_0 V_3 - N(v_1 + v_2) , \tag{A.19}$$

where

$$C_0 = \frac{A_p}{l_p}\varepsilon_{33}^T(1-k_{33}^2) = \frac{A_p}{l_p}\varepsilon_{33}^S , \quad Z_0 = \rho_p A_p v_3^D , \quad Z_{C_0} = -\frac{N^2}{j\omega C_0} , \quad Z_1 = jZ_0 \tan\frac{kl_p}{2} ,$$
$$Z_2 = \frac{Z_0}{j\sin kl_p} \text{ and } N = \frac{g_{33,p}C_0}{s_{33}^D} = \frac{A_p d_{33,p}}{l_p s_{33}^E} .$$

Using Eqs. (A.17)−(A.19), the electrical equivalent circuit of the length-polarized piezoelectric plate is constructed as depicted in Fig. A.2. The transformer is assumed to be lossless and represents the conversion of mechanical energy into electrical energy with the transformation factor N.

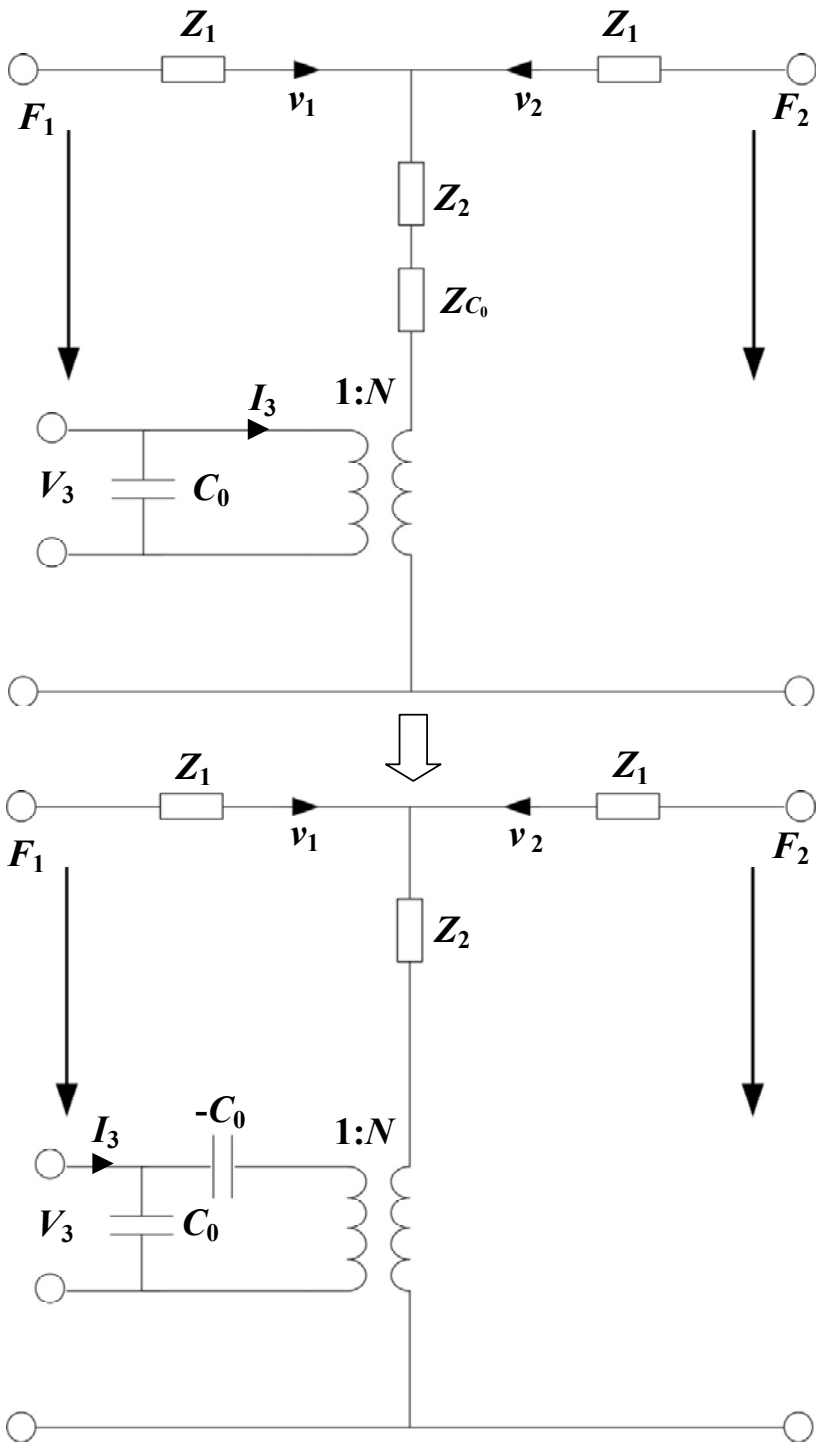

Fig. A.2 Electrical Equivalent circuit of a length-polarized piezoelectric plate operating in length mode.

A.2 Electrical Equivalent Circuits of Magnetoelectric Laminates

A.2.1 *L*−*T* Magnetoelectric Laminated Composites

The magnetoelectric (ME) effect in a *L*−*T* ME laminated composite having a length magnetization (*M*) along the *z*-direction and a thickness polarization (*P*) along the *x*-direction can be arranged in the Cartesian coordinate system as shown in Fig. A.3. When an ac magnetic field (H_3) is applied along the length (or the 3-) direction of the magnetostrictive material phase of the composite, an ac magnetostrictive strain ($S_{3,m}$) is induced in the length direction of the magnetostrictive material phase due to the magnetostrictive effect. This $S_{3,m}$ is mechanically coupled to the sandwich piezoelectric material phase, giving rise to an ac piezoelectric voltage (V'_3) across the thickness of the piezoelectric material phase in the 3-direction due to the piezoelectric effect. This mechanically mediated magnetostrictive and piezoelectric effect is said to be an extrinsic ME effect in the composite.

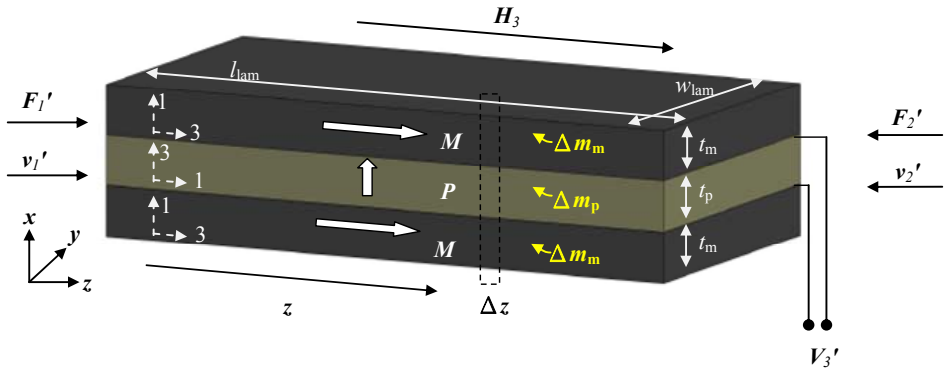

Fig. A.3 Schematic diagram of a *L*−*T* ME laminated composite having a length magnetization (*M*) and a thickness polarization (*P*).

For the length-magnetized magnetostrictive material phase operating in the length (or the 33-) mode, the piezomagnetic constitutive equations are expressed as

$$S_{3,\mathrm{m}} = s_{33}^{H} T_{3,\mathrm{m}} + d_{33,\mathrm{m}} H_3 , \tag{A.20}$$

$$B_3 = d_{33,\mathrm{m}} T_{3,\mathrm{m}} + \mu_{33}^{T} H_3 , \tag{A.21}$$

where H_3 and B_3 are the magnetic field and magnetic flux density along the length (or the 3-) direction, respectively; $S_{3,\mathrm{m}}$ and $T_{3,\mathrm{m}}$ are the strain and stress along the length direction, respectively; and μ_{33}^{T} is the magnetic permeability at constant stress, $d_{33,\mathrm{m}}$ is the piezomagnetic strain coefficient; and s_{33}^{H} is the elastic compliance coefficient at constant magnetic field strength. For the thickness-polarized piezoelectric material phase operating in the transverse (or the 31-) mode, the piezoelectric constitutive equations are given by

$$S_{1,\mathrm{p}} = s_{11}^{E} T_{1,\mathrm{p}} + d_{31,\mathrm{p}} E_3 , \tag{A.22}$$

$$D_3 = d_{31,\mathrm{p}} T_{1,\mathrm{p}} + \varepsilon_{33}^{T} E_3 . \tag{A.23}$$

where E_3 and D_3 are the electric field and electric displacement along the thickness (or the 3-) direction, respectively; $S_{1,\mathrm{p}}$ and $T_{1,\mathrm{p}}$ are the mechanical strain and stress along the length (or the 1-) direction, respectively; ε_{33}^{T} is the dielectric permittivity at constant stress; $d_{31,\mathrm{p}}$ is the piezoelectric strain coefficient; and s_{11}^{E} is the elastic compliance coefficient at constant electric field strength.

According to Newton's second law of motion, the equation of motion that couples the piezomagnetic and piezoelectric constitutive equations can be written as

$$(\Delta m_{\mathrm{p}} + 2\Delta m_{\mathrm{m}})\frac{\partial^2 \zeta}{\partial t^2} = \Delta T_{1,\mathrm{p}}(A_{\mathrm{p}}) + \Delta T_{3,\mathrm{m}}(2A_{\mathrm{m}}), \tag{A.24}$$

where $\Delta m_{\mathrm{m}} = \rho_{\mathrm{m}} A_{\mathrm{m}} \Delta x$ and $\Delta m_{\mathrm{p}} = \rho_{\mathrm{p}} A_{\mathrm{p}} \Delta x$ are the masses of the magnetostrictive and piezoelectric material phases, respectively; and ρ_{m} and ρ_{p} are the densities of the magnetostrictive and piezoelectric material phases, respectively. Because of the lamination configuration, the total cross-sectional area of the composite (A_{lam}) is

$$A_{\mathrm{lam}} = A_{\mathrm{p}} + 2A_{\mathrm{m}} = t_{\mathrm{lam}} w_{\mathrm{lam}}, \tag{A.25}$$

where A_{m} and A_{p} are the cross-sectional areas of the magnetostrictive and piezoelectric material phases, respectively; t_{m} and t_{p} are the thicknesses of the magnetostrictive and piezoelectric material phases, respectively; $t_{\mathrm{lam}} = t_{\mathrm{p}} + 2\ t_{\mathrm{m}}$ and w_{lam} are the thickness and width of the composite, respectively. Combining Eqs. (A.24) and (A.25), we have

$$\overline{\rho}\frac{\partial^2 \zeta}{\partial t^2} = n\frac{\partial T_{3,\mathrm{m}}}{\partial x} + (1-n)\frac{\partial T_{1,\mathrm{p}}}{\partial x},\ (0 < n < 1), \tag{A.26}$$

where $n = 2A_{\mathrm{m}} / A_{\mathrm{lam}} = 2t_{\mathrm{m}} / t_{\mathrm{lam}}$ is the thickness ratio of the magnetostrictive material phase to the composite; and $\overline{\rho} = \dfrac{\rho_{\mathrm{p}} A_{\mathrm{p}} + \rho_{\mathrm{m}}(2A_{\mathrm{m}})}{A_{\mathrm{lam}}}$ is the average mass density of the composite. The wave equation can be described by

$$\frac{\partial^2 \zeta}{\partial t^2} = \overline{v_1^D}^2 \frac{\partial^2 \zeta}{\partial x^2}, \tag{A.27}$$

where $\overline{v_1^D} = \sqrt{\left(\dfrac{n}{s_{33}^H} + \dfrac{1-n}{s_{11}^E}\right) \Big/ \overline{\rho}}$ is the effective wave velocity. Under harmonic oscillation, Eq. (A.27) is simplified as

$$\frac{\partial^2 \zeta}{\partial x^2} + k^2 \zeta = 0, \tag{A.28}$$

where $k = \omega / \overline{v_1^D}$ is the wave number and ω is the angular frequency. The general solution of Eq. (A.28) can be written as

$$\zeta = A \sin kx + B \cos kx. \tag{A.29}$$

The face velocities ($\dot{\zeta}$) of the composite at the boundaries z = 0 and $z = l_{\text{lam}}$ are expressed as

$$\dot{\zeta}|_{z=0} = j\omega B = v_1^{'} \tag{A.30}$$

and

$$\dot{\zeta}|_{z=l_{\text{lam}}} = j\omega(A \sin kl_{\text{lam}} + B \cos kl_{\text{lam}}) = -v_2^{'}. \tag{A.31}$$

The two variables A and B are resolved as

$$A = -(\frac{v_1^{'} \cos kl_{\text{lam}}}{\sin kl_{\text{lam}}} + \frac{v_2^{'}}{\sin kl_{\text{lam}}}) \frac{1}{j\omega}. \tag{A.32}$$

and

$$B = \frac{v_1^{'}}{j\omega}. \tag{A.33}$$

ζ, $S_{1,\text{p}}$, $T_{1,\text{p}}$, and $T_{3,\text{m}}$ are determined to be

$$\zeta = -\frac{1}{j\omega}\left[(\frac{v_1^{'} \cos kl_{\text{lam}}}{\sin kl_{\text{lam}}} + \frac{v_2^{'}}{\sin kl_{\text{lam}}}) \sin kx - v_1 \cos kx\right], \tag{A.34}$$

$$S_{1,\text{p}} = \frac{\partial \zeta}{\partial x} = -\frac{k}{j\omega}\left[(\frac{v_1^{'} \cos kl_{\text{lam}}}{\sin kl_{\text{lam}}} + \frac{v_2^{'}}{\sin kl_{\text{lam}}}) \cos kx - v_1 \sin kx\right], \tag{A.35}$$

$$T_{1,\mathrm{p}} = \frac{1}{s_{11}^{E}}\left(S_{1,\mathrm{p}} - d_{31,\mathrm{p}}E_3\right) = -\frac{k}{j\omega s_{11}^{E}}\left[\left(\frac{v_1^{'}\cos kl_{\mathrm{lam}}}{\sin kl_{\mathrm{lam}}} + \frac{v_2^{'}}{\sin kl}\right)\cos kx - v_1\sin kx\right] - \frac{d_{31,\mathrm{p}}}{s_{11}^{E}}E_3\,, \tag{A.36}$$

and

$$T_{3,\mathrm{m}} = \frac{1}{s_{33}^{H}}\left(S_{3,\mathrm{m}} - d_{33,\mathrm{m}}H_3\right) = -\frac{k}{j\omega s_{33}^{H}}\left[\left(\frac{v_1^{'}\cos kl_{\mathrm{lam}}}{\sin kl_{\mathrm{lam}}} + \frac{v_2^{'}}{\sin kl_{\mathrm{lam}}}\right)\cos kx - v_1\sin kx\right] - \frac{d_{33,\mathrm{m}}}{s_{33}^{H}}H_3\,. \tag{A.37}$$

The forces ($F_1^{'}$ and $F_2^{'}$) acting on the two end faces of the composite are related to $T_{1,\mathrm{p}}$ and $T_{3,\mathrm{m}}$ as

$$F_1^{'} = -A_{\mathrm{p}}T_{1,\mathrm{p}}\,|_{x=0} - 2A_mT_{3,\mathrm{m}}\,|_{x=0} \tag{A.38}$$

and

$$F_2^{'} = -A_{\mathrm{p}}T_{1,\mathrm{p}}\,|_{x=l_{\mathrm{lam}}} - 2A_mT_{3,\mathrm{m}}\,|_{x=l_{\mathrm{lam}}} \tag{A.39}$$

where $A_{\mathrm{p}} = w_{\mathrm{p}}\times t_{\mathrm{p}}$ and $A_{\mathrm{m}} = w_{\mathrm{m}}\times t_{\mathrm{m}}$ is the cross-sectional area of the piezoelectric and magnetostrictive plate, respectively. Let $\overline{\rho v_1^{D}} = \left(\frac{n}{s_{33}^{H}} + \frac{1-n}{s_{11}^{E}}\right)\Big/ v_1^{D}$ and use the geometric formula $\frac{1}{\tan\alpha} = \frac{1}{\sin\alpha} - \tan\frac{\alpha}{2}$, Eqs. (A.36) and (A.37) become

$$F_1^{'} = \left(\frac{A_{\mathrm{p}}}{s_{11}^{E}} + \frac{2A_{\mathrm{m}}}{s_{33}^{H}}\right)\frac{v_2^{'} + v_1^{'}\cos kl_{\mathrm{lam}}}{j\bar{v}\sin kl_{\mathrm{lam}}} + \frac{A_{\mathrm{p}}d_{31,\mathrm{p}}}{s_{11}^{E}}E_3 + 2A_m\frac{d_{33,\mathrm{m}}}{s_{33}^{H}}H_3 \tag{A.40}$$

and

$$F_2^{'} = \left(\frac{A_{\mathrm{p}}}{s_{11}^{E}} + \frac{2A_{\mathrm{m}}}{s_{33}^{H}}\right)\frac{v_2^{'}\cos kl_{\mathrm{lam}} + v_1^{'}}{j\bar{v}\sin kl_{\mathrm{lam}}} + \frac{A_{\mathrm{p}}d_{31,\mathrm{p}}}{s_{11}^{E}}E_3 + 2A_m\frac{d_{33,\mathrm{m}}}{s_{33}^{H}}H_3\,. \tag{A.41}$$

The coupling current ($I_3^{'}$) passing through the electrodes is

$$I_3^{'} = j\omega l_{lam} w_{lam} \left(\varepsilon_{33}^{T} - \frac{d_{31,\mathrm{p}}^2}{s_{11}^{E}} \right) E_3 - \frac{w_{lam} d_{31,\mathrm{p}}}{s_{11}^{E}} (v_1^{'} + v_2^{'}) . \tag{A.42}$$

By combining Eqs. (A.38), (A.39), and (A.40), the total equations for the $L-T$ ME laminated composite with a length magnetization and a thickness polarization can be written as

$$F_1^{'} = (Z_1^{'} + Z_2^{'} + Z_{C0}^{'}) v_1^{'} + Z_2^{'} v_2^{'} + \varphi_p V_3^{'} + \varphi_m H_3 , \tag{A.43}$$

$$F_2^{'} = Z_2^{'} v_1 + (Z_1^{'} + Z_2^{'} + Z_{C0}^{'}) v_2^{'} + \varphi_p V_3^{'} + \varphi_m H_3 , \tag{A.44}$$

$$I_3^{'} = j\omega_0 C_0^{'} V_3^{'} - v_1^{'} \varphi_p - v_2^{'} \varphi_p , \tag{A.45}$$

where

$$C_0^{'} = \frac{w_{lam} l_{\mathrm{lam}}}{t_p} (\varepsilon_{33}^{T} - \frac{d_{31}^2}{s_{11}^{E}}) = \frac{w_{lam} l_{\mathrm{lam}}}{t_p} (\varepsilon_{33}^{T} - k_{31}^2) = \frac{w_{lam} l_{\mathrm{lam}}}{t_p} \varepsilon_{33}^{S} , \quad Z_0^{'} = \overline{\rho} \overline{v_1^{D}} A_{\mathrm{lam}} , \quad Z_{C0}^{'} = 0$$

$$Z_1^{'} = j Z_0^{'} \tan \frac{k l_{\mathrm{lam}}}{2} , \quad Z_2^{'} = \frac{Z_0^{'}}{j \sin k l_{\mathrm{lam}}} , \quad \varphi_m = 2 A_m \frac{d_{33,\mathrm{m}}}{s_{33}^{H}} , \text{ and } \quad \varphi_p = \frac{w_p d_{31,\mathrm{p}}}{s_{11}^{E}} .$$

Using Eqs. (A.43)−(A.45), the electrical equivalent circuit of the $L-T$ ME laminated composite is constructed as depicted in Fig. A.4. The transformers are assumed to be lossless and represent the conversions of the magnetic energy into mechanical energy and of the mechanical energy into electrical energy with the transformation factors φ_{m} and φ_{p}, respectively.

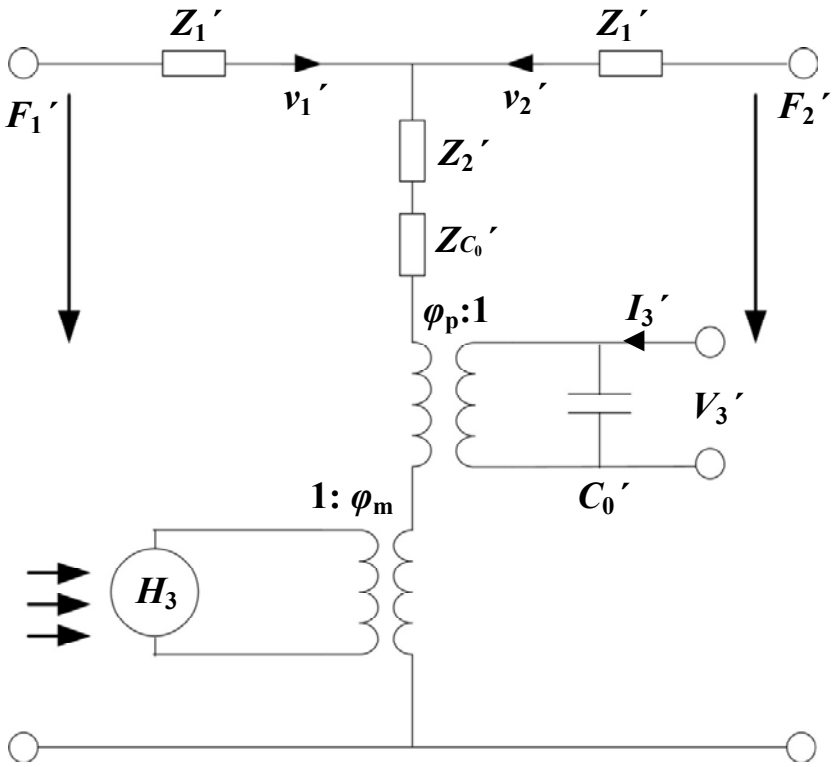

Fig. A.4 Electrical equivalent circuit of a $L-T$ ME laminated composite.

A.2.2 *L*−*L* Magnetoelectric Laminated Composites

The magnetoelectric (ME) effect in a *L*−*L* ME laminated composite having length magnetization (*M*) and a length polarization (*P*), both along the *z*-direction, can be arranged in Cartesian coordinate system as shown in Fig. A.5. When an ac magnetic field (H_3) is applied along the length (or the 3-) direction of the magnetostrictive material phase of the composite, an ac magnetostrictive ($S_{3,m}$) is induced in the length direction of the magnetostrictive material phase due to the magnetostrictive effect. This $S_{3,m}$ is mechanically coupled to the sandwiched piezoelectric material phase, resulting in an ac piezoelectric voltage (V_3') across the length of the piezoelectric material phase in 3-direction due to the piezoelectric effect. This is a mechanically medicated extrinsic magnetoelectric effect in the composite as a result of the product effect of the magnetostrictive effect in the magnetostrictive material phase and piezoelectric in the piezoelectric material phase.

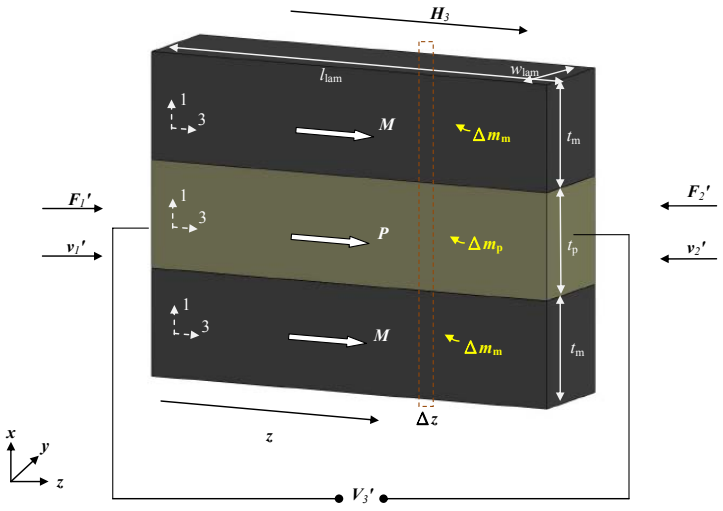

Fig. A.5 Schematic diagram of a *L*−*L* laminated composite having a length magnetization (*M*) and a length polarization (*P*).

For the length-magnetized magnetostrictive material phase operating in the length (or the 33-) mode, the piezomagnetic constitutive equations are given as

$$S_{3,\mathrm{m}} = s_{33}^{H} T_{3,\mathrm{m}} + d_{33,\mathrm{m}} H_3 , \tag{A.46}$$

$$B_3 = d_{33,\mathrm{m}} T_{3,\mathrm{m}} + \mu_{33}^{T} H_3 , \tag{A.47}$$

where H_3 and B_3 are the magnetic field and magnetic flux density along the length (or the 3-) direction, respectively; $S_{3,\mathrm{m}}$ and $T_{3,\mathrm{m}}$ are the strain and stress along the length direction, respectively; and μ_{33}^{T} is the magnetic permeability at constant stress; $d_{33,\mathrm{m}}$ is the piezomagnetic strain coefficient; s_{33}^{H} is the elastic compliance coefficient at constant magnetic field strength. For the length-polarized piezoelectric material phase operating in the length (or the 33-) mode, the piezoelectric constitutive equations are expressed given by

$$S_{3,\mathrm{p}} = s_{33}^{D} T_{3,\mathrm{p}} + g_{33,\mathrm{p}} D_3 , \tag{A.48}$$

$$E_3 = -g_{33,\mathrm{p}} T_{3,\mathrm{p}} + \beta_{33}^{T} D_3 , \tag{A.49}$$

where E_3 and D_3 are the electric field and electric displacement along the length (or the 3-) direction, respectively; $S_{3,\mathrm{p}}$ and $T_{3,\mathrm{p}}$ are the mechanical strain and stress along the length (or the 3-) direction, respectively; β_{33}^{T}, is the dielectric impermittivity at constant stress; $g_{33,\mathrm{p}}$ is the piezoelectric voltage coefficient; and s_{33}^{D} is the elastic compliance coefficient at constant electric displacement.

According to the Newton's second law of motion, the equation of motion that couples the piezomagnetic and piezoelectric constitutive equations can be written as

$$(\Delta m_{\mathrm{p}} + 2\Delta m_{\mathrm{m}})\frac{\partial^2 \zeta}{\partial t^2} = \Delta T_{3,\mathrm{p}}(A_{\mathrm{p}}) + \Delta T_{3,\mathrm{m}}(2A_{\mathrm{m}}), \tag{A.50}$$

where $\Delta m_{\mathrm{m}} = \rho_{\mathrm{m}} A_{\mathrm{m}} \Delta x$ and $\Delta m_{\mathrm{p}} = \rho_{\mathrm{p}} A_{\mathrm{p}} \Delta x$ are the masses of the magnetostrictive and piezoelectric material phases, respectively; ρ_{m} and ρ_{p} are the densities of the magnetostrictive and piezoelectric material phases, respectively. Because of the lamination configuration, the total cross-sectional area of the composite (A_{lam}) is

$$A_{\mathrm{lam}} = A_{\mathrm{p}} + 2A_{\mathrm{m}} = t_{\mathrm{lam}} w_{\mathrm{lam}}, \tag{A.51}$$

where A_{m} and A_{p} are the cross-sectional areas of the magnetostrictive and piezoelectric material phases, respectively; t_{m} and t_{p} are the thicknesses of the magnetostrictive and piezoelectric material phases, respectively. $t_{\mathrm{lam}} = t_{\mathrm{p}} + 2t_{\mathrm{m}}$ and w_{lam} are the thickness and width of the composite, respectively. Combining Eqs. (A.50) and (A.51), we have

$$\bar{\rho}\frac{\partial^2 \xi}{\partial t^2} = n\frac{\partial T_{3,\mathrm{m}}}{\partial z} + (1-n)\frac{\partial T_{3,\mathrm{p}}}{\partial z}, \ (0 < n < 1), \tag{A.52}$$

where $n = 2A_{\mathrm{m}} / A_{\mathrm{lam}} = 2t_{\mathrm{m}} / t_{\mathrm{lam}}$ is the thickness ratio of the magnetostrictive material phase to the composite; and $\bar{\rho} = \dfrac{\rho_{\mathrm{p}} A_{\mathrm{p}} + \rho_{\mathrm{m}}(2A_{\mathrm{m}})}{A_{\mathrm{lam}}}$ is the average mass density of the composite. The wave equation can be described by

$$\frac{\partial^2 \zeta}{\partial t^2} = \overline{v_3^D}^2 \frac{\partial^2 \zeta}{\partial z^2}, \tag{A.53}$$

where $\overline{v_3^D} = \sqrt{\left(\dfrac{n}{s_{33}^H} + \dfrac{1-n}{s_{33}^D}\right) \Big/ \bar{\rho}}$ is the effective wave velocity. Under harmonic oscillation, Eq. (A.53) is simplified as

$$\frac{\partial^2 \zeta}{\partial z^2} + k^2 \zeta = 0\,, \tag{A.54}$$

where $k = \omega / \overline{v_3^D}$ is the wave number and ω is the angular frequency. The general solution of Eq. (A.54) can be written as

$$\zeta = A \sin kz + B \cos kz\,. \tag{A.55}$$

The face velocity ($\dot{\zeta}$) of the composite at the boundaries z = 0 and $z = l_{\text{lam}}$ are expressed as

$$\dot{\zeta}\,|_{z=0} = j\omega B = v_1^{'} \tag{A.56}$$

and

$$\dot{\zeta}\,|_{z=l_{\text{lam}}} = j\omega(A \sin kl_{\text{lam}} + B \cos kl_{\text{lam}}) = -v_2^{'}\,. \tag{A.57}$$

The two variable A and B are resolved as

$$A = -(\frac{v_1^{'} \cos kl_{\text{lam}}}{\sin kl_{\text{lam}}} + \frac{v_2^{'}}{\sin kl_{\text{lam}}}) \frac{1}{j\omega} \tag{A.58}$$

and

$$B = \frac{v_1^{'}}{j\omega}\,. \tag{A.59}$$

ζ, $S_{3,\text{p}}$, $T_{3,\text{p}}$, and $T_{3,\text{m}}$ are determined to be

$$\zeta = -\frac{1}{j\omega}\left[(\frac{v_1^{'} \cos kl_{\text{lam}}}{\sin kl_{\text{lam}}} + \frac{v_2^{'}}{\sin kl_{\text{lam}}}) \sin kz - v_1^{'} \cos kz\right], \tag{A.60}$$

$$S_3 = \frac{\partial \zeta}{\partial z} = -\frac{k}{j\omega}\left[(\frac{v_1^{'} \cos kl_{\text{lam}}}{\sin kl_{\text{lam}}} + \frac{v_2^{'}}{\sin kl_{\text{lam}}}) \cos kz - v_1^{'} \sin kz\right], \tag{A.61}$$

$$T_{3,\mathrm{p}} = \frac{1}{s_{33}^{D}}\left(S_{3,\mathrm{p}} - g_{33,\mathrm{p}} D_3\right) = -\frac{k}{j\omega s_{33}^{D}}\left[\left(\frac{v_1^{'}\cos kl_{\mathrm{lam}}}{\sin kl_{\mathrm{lam}}} + \frac{v_2^{'}}{\sin kl_{\mathrm{lam}}}\right)\cos kz - v_1^{'}\sin kz\right] - \frac{g_{33,\mathrm{p}}}{s_{33}^{D}} D_3 \tag{A.62}$$

and

$$T_{3,\mathrm{m}} = \frac{1}{s_{33}^{H}}\left(S_{3,\mathrm{m}} - d_{33,\mathrm{m}} H_3\right) = -\frac{k}{j\omega s_{33}^{H}}\left[\left(\frac{v_1^{'}\cos kl_{\mathrm{lam}}}{\sin kl_{\mathrm{lam}}} + \frac{v_2^{'}}{\sin kl_{\mathrm{lam}}}\right)\cos kx - v_1 \sin kx\right] - \frac{d_{33,\mathrm{m}}}{s_{33}^{H}} H \tag{A.63}$$

.

The forces ($F_1^{'}$ and $F_2^{'}$) acting on the two end faces of the composite are related to $T_{1,\mathrm{p}}$ and $T_{3,\mathrm{m}}$ as

$$F_1 = -A_{\mathrm{p}} T_{3,\mathrm{p}}\,|_{z=0} - 2A_{\mathrm{m}} T_{3,\mathrm{m}}\,|_{z=0} \tag{A.64}$$

and

$$F_2 = -A_{\mathrm{p}} T_{3,\mathrm{p}}\,|_{z=l_{\mathrm{lam}}} - 2A_{\mathrm{m}} T_{3,\mathrm{m}}\,|_{z=l_{\mathrm{lam}}}. \tag{A.65}$$

Let $\overline{\rho v_3^{D}} = \left(\frac{n}{s_{33}^{H}} + \frac{1-n}{s_{33}^{D}}\right) \Big/ \overline{v_3^{D}}$ and use the geometric $\frac{1}{\tan\alpha} = \frac{1}{\sin\alpha} - \tan\frac{\alpha}{2}$, Eqs. (A.64) and (A.65) become

$$F_1^{'} = \left(\frac{A_{\mathrm{p}}}{s_{33}^{D}} + \frac{2A_{\mathrm{m}}}{s_{33}^{H}}\right)\frac{v_2^{'} + v_1^{'}\cos kl_{\mathrm{lam}}}{j\bar{v}\sin kl_{\mathrm{lam}}} + \frac{A_{\mathrm{p}} g_{33,\mathrm{p}}}{s_{33}^{D}} D_3 + 2A_m \frac{d_{33,\mathrm{m}}}{s_{33}^{H}} H_3 \tag{A.66}$$

and

$$F_2^{'} = \left(\frac{A_{\mathrm{p}}}{s_{33}^{D}} + \frac{2A_{\mathrm{m}}}{s_{33}^{H}}\right)\frac{v_2^{'}\cos kl_{\mathrm{lam}} + v_1^{'}}{j\bar{v}\sin kl_{\mathrm{lam}}} + \frac{A_{\mathrm{p}} g_{33,\mathrm{p}}}{s_{33}^{D}} D_3 + 2A_{\mathrm{m}} \frac{d_{33,\mathrm{m}}}{s_{33}^{H}} H_3. \tag{A.67}$$

The coupling current ($I_3^{'}$) passing through the electrodes is

$$I_3^{'} = j\omega A_{\mathrm{p}} D_3 \tag{A.68}$$

The voltage output of the piezoelectric material phase of the composite along the length direction is

$$V_3^{'} = \int_0^{l_{\text{lam}}} E_3 dz = \frac{g_{33}^{p}}{j\omega s_{33}^{D}}(v_1^{'} + v_2^{'}) + \frac{1}{j\omega\left[\dfrac{w_{\text{lam}} t_p}{l_{\text{lam}}}\varepsilon_{33}^{T}(1-k_{33}^{2})\right]} I_3^{'}. \tag{A.69}$$

By combining Eqs. A.66), (A.67), and (A.69), the total equations for the $L-L$ ME laminated composite with a length magnetization and a length polarization can be written as

$$F_1^{'} = (Z_1^{'} + Z_2^{'} + Z_{C0}^{'})v_1^{'} + Z_2^{'}v_2^{'} + \varphi_p V_3^{'} + \varphi_m H_3, \tag{A.70}$$

$$F_2^{'} = Z_2^{'}v_1 + (Z_1^{'} + Z_2^{'} + Z_{C0}^{'})v_2^{'} + \varphi_p V_3^{'} + \varphi_m H_3, \tag{A.71}$$

$$I_3^{'} = j\omega_0 C_0^{'} V_3^{'} - v_1^{'}\varphi_p - v_2^{'}\varphi_p, \tag{A.72}$$

where

$$C_0^{'} = \frac{w_{\text{lam}} t_p}{l_{\text{lam}}}\varepsilon_{33}^{T}(1-k_{33}^{2}) = \frac{w_{\text{lam}} t_p}{l_{\text{lam}}}\varepsilon_{33}^{S},\ Z_0^{'} = \overline{\rho}\,\overline{v_3^{D}} A_{\text{lam}},\ Z_{C0}^{'} = -\frac{\varphi_p^2}{j\omega C_0^{'}},$$

$$Z_1^{'} = j\overline{\rho}\,\overline{v_3^{D}} A_{\text{lam}} \tan\frac{kl_{\text{lam}}}{2},\ Z_2^{'} = \frac{\overline{\rho}\,\overline{v_3^{D}} A_{lam}}{j\sin kl_{\text{lam}}},\ \varphi_m = 2A_m \frac{d_{33}^{m}}{s_{33}^{H}}, \text{ and } \varphi_p = \frac{g_{33}^{p} C_0^{'}}{s_{33}^{D}}.$$

Using the Eqs. (A.70) − (A.72), the electrical equivalent circuit of the $L-L$ laminated composite is constructed as depicted in Fig. A.6. The transformers are assumed to be lossless and represents the conversion of the magnetic energy into mechanical energy and of the mechanical energy into electrical energy with the transformation factors φ_{m} and φ_{p}, respectively.

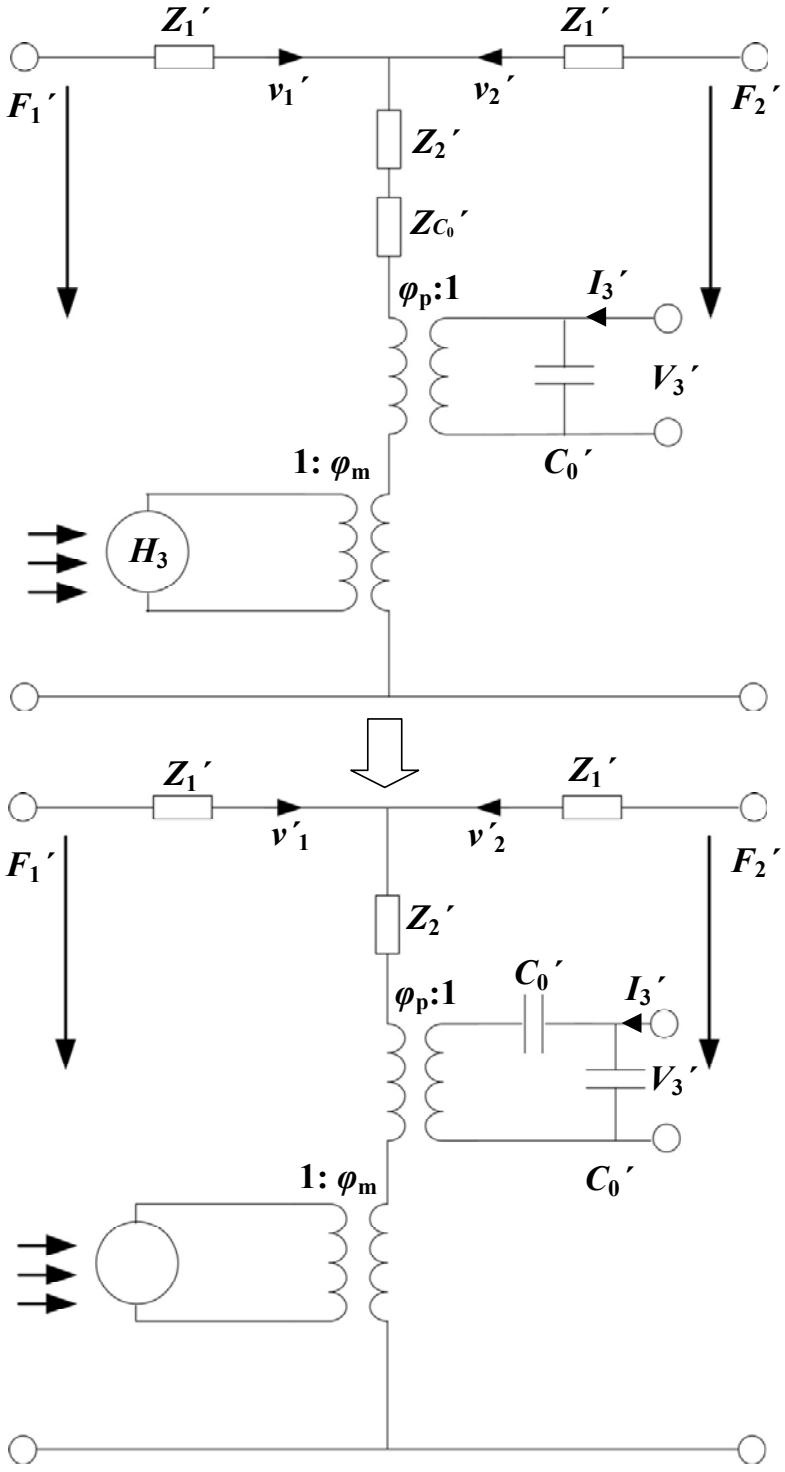

Fig. A.6 Electrical equivalent circuit of a *L*−*L* ME laminated composite plate.

List of References

[1] J. E. Amadi-Echensu, K. Brown, R. Willett, and J. Mathew, *Definitions, Concepts and Scope of Engineering Asset Management*, Springer, London, 2011.

[2] G. Montanari, "Envisaging Links between Fundamental Research in Electrical Insulation and Electrical Asset Management", *IEEE Electrical Insulation Magazine*, Vol. 24, Issue 6, pp. 7–21, 2008.

[3] P. Cawley, "Non-destructive Testing–Current Capabilities and Future Directions", *Journal of Materials: Design and Applications*, Vol. 215, No. 4 pp. 213–223, 2001.

[4] S. Pierce, "Condition Monitoring of Electrical Asset", http://www.sirfrt.com.au /Nationalforum/07ELNF/Presentations/3-Steve%20Pierce_AGL_Torrens_%20 Isl.pdf.

[5] P. Kiameh, *Electrical Equipment Handbook: Troubleshooting and Maintenance*, McGraw-Hill, New York, 2003.

[6] "Electrical and Electronics Engineers, except Computer", *Occupational Outlook Handbook*, 2005, http://classic-web.archive.org/web/20050713014728 /http://www.bls.gov/oco/ocos031.htm.

[7] Y. Han and Y. H. Song, "Condition Monitoring Techniques for Electrical Equipment－A Literature Survey", *IEEE Transaction on Power Delivery*, Vol. 18, pp. 4–12, 2003.

[8] B. K. N. Rao, *Handbook of Condition Monitoring*, Elsevier Advanced Technology, London, 1996.

[9] R. Barron, *Engineering Condition Monitoring: Practice, Method and Applications*, Longman, London, 1996.

[10] J. G. Webster, *Electrical Measurement Signal Processing and Displays*, CRC Press, New York, 2004.

[11] E. Ramsden, *Hall-Effect Sensors: Theory and Applications*, 2nd Edition, Elsevier, Burlington, 2006.

[12] Melexis Microelectronic Integrated System, http://www.melexis.com.

[13] Murata, http://www.murata-ps.com.

[14] PEM Power Electronic Measurement Ltd, http://www.pemuk.com.

[15] RC-Electronic, http://www.rc-electronics-usa.com.

[16] M. Fiebig, "Revival of the Magnetoelectric Effect", *Journal of Physics D: Applied Physics*, Vol. 38, pp. R135–152, 2005.

[17] W. C. Röntgen, "Ueber Die Durch Bewegung Eines im Homogenen Electrischen Felde Befindlichen Dielectricums Hervorgerufene Electrodynamische Kraft", *Annalen der Physik*, Vol. 35, pp. 264–270, 1888.

[18] P. Curie, "Sur la Symetrie Dans les Phenomenes Physiques", *Journal of Physics*, Vol. 3e se, pp. 393–415, 1894.

[19] D. N. Astrov, "Magnetoelectric Effect in Antiferromagnetics", *Soviet Physics JETP*, Vol. 11, No. 3, pp. 708–709, 1960.

[20] D. N. Astrov, "Magnetoelectric Effect in Chromium Oxide", *Soviet Physics JETP*, Vol. 13, No. 4, pp. 729–733, 1961.

[21] Web of Knowledge, http://isi10.isiknowledge.com/.

[22] J. V. D. Boomgaard, D. R. Terrell, R. A. J. Born, and H. F. J. I. Giller, "An In situ Grown Eutectic Magnetoelectric Composite Materials: Part 1 Composition and Unidirectional Solidification", *Journal of Materials Science*, Vol. 9, pp. 1705–1709, 1974.

[23] J. Ryu, S. Priya, A. V. Carazo, K. Uchino, and H. E. Kim, "Effect of the Magnetostrictive Layer on Magnetoelectric Properties in Lead Zirconate Titanate/Terfenol-D Laminate Composites", *Journal of American Ceramic Society*, Vol. 84, pp. 2905–2908, 2001.

[24] J. Ryu, A. V. Carazo, K. Uchino, and H. E. Kim, "Magnetoelectric Properties in Piezoelectric and Magnetostrictive Laminate Composites", *Japanese Journal of Applied Physics*, Vol. 40, pp. 4948–4951, 2001.

[25] V. J. Folen, G.T. Rado, and E. W. Stalder, "Anistotropy of the Magnetoelectric Effect in Cr_2O_3", *Physical Review Letters*, Vol. 6, pp. 607–608, 1961.

[26] S. Foner and M. Hanabusa, "Magnetoelectric Effects in Cr_2O_3 and $(Cr_2O_3)_{0.8}(Al_2O_3)_{0.2}$", *Journal of Applied Physics*, Vol. 34, pp. 1246–1248, 1963.

[27] S. Shtrikman and D. Treves, "Observation of the Magnetoelectric Effect in Cr_2O_3 Powders", *Physical Review*, Vol. 130, pp. 986–988, 1963.

[28] G. T. Rado, "Observation and Possible Mechanisms of Magnetoelectric Effects in a Ferromagnet", *Physical Review Letters,* Vol. 13, pp. 335–337, 1964.

[29] R. Hornreich, "The Magnetoelectric Effect: Some Likely Candidates", *Solid State Communication*, Vol.**7**, pp. 1081–1088, 1969.

[30] W, Eerenstein, N. D. Mathur, and J. F. Scott, "Multiferroic and Magnetoelectric Materials" *Nature*, Vol. 442, pp. 759–765, 2006.

[31] B. D. H. Tellegen, "The Gyrator, a New Electric Network Element", *Philips Research Reports*, Vol. 3, pp. 81–101, 1948.

[32] A. M. J. G. Run, D. R. Terrell, and J. H. Scholing, "An in situ Grown Eutectic Magnetoelectric Composite Material: Part 2 Physical Properties", *Journal of Materials Science*, Vol. 9, pp. 1710–1714, 1974.

[33] J. Boomgaard, A. M. J. G. Run, and J. Suchtelen, "Magnetoelectricity in Piezoelectric–Magnetostrictive Composites", *Ferroelectrics*, Vol. 10, pp. 295–298, 1976.

[34] J. Boomgaard, A. M. J. G. Run, and J. Suchtelen, "Piezoelectric-Piezomagnetic Composites with Magnetoelectric Effect", *Ferroelectrics*, Vol. 14, pp.727–729, 1976.

[35] J. Boomgaard and R. A. J. Born, "A Sintered Magnetoelectric Composite Material $BaTiO_3$–Ni(Co, Mn)Fe_2O_4", *Journal of Material Science*, Vol. 13, pp.1538–1548, 1978.

[36] I. H. Ismailzade, R. M. Ismailov, A. I. Alekperov, and F. M. Salaev, "Magnetoelectric Investigation of the System $BiFeO_3$–$Pb(Fe_{0.5}Nb_{0.5})O_3$", *Physics Status Solidi (a)*, Vol. 57, pp. 99–101, 1980.

[37] I. H. Ismailzade, R. M. Ismailov, A. I. Alekperov, and F. M. Salaev, "Investigation of the Magnetoelectric Effect in Solid Solutions of the Systems $BiFeO_3$–$BaTiO_3$ and $BiFeO_3$–PbTiO3", *Physics Status Solidi (a)*, Vol. 68, pp.81–84, 1981.

[38] I. Bunget and V. Raetchi, "Magnetoelectric Effect in the Heterogeneous System NiZn Ferrite–PZT Ceramic", *Physics Status Solidi*, Vol. 63, pp. 55–59, 1981.

[39] I. Bunget and V. Raetchi, "Dynamic Magnetoelectric Effect in the Composite System of Ni-Zn Ferrite–PZT Ceramics", *Review Forum Physics*, Vol. 27, pp. 401–408, 1982.

[40] R. Rottenbacher, H. J. Oel, and G. Tomandel, "Ferroelectrics Ferromagnetics", *Ceramics International*, Vol. 7, pp.106–108, 1981.

[41] A. E. Gelysin and V. M. Laletin, "Effect of a Magnetic Field on the Resonant Frequency of a Composite Ferrite–Piezoelectric Ceramic", *Soviet Technical Physics Letters*, Vol. 14, No. 10, pp. 758–761, 1988.

[42] S. Priya, R. Islam, S. X. Dong, and D. Viehland, "Recent Advancements in Magnetoelectric Particulate and Laminate Composites", *Journal of Electroceramics*, Vol. 19, pp. 147–164, 2007.

[43] S. X. Dong, J. F. Li, and D. Viehland, "Ultrahigh Magnetic Field Sensitivity in Laminates of Terfenol-D and $Pb(Mg_{1/3}Nb_{2/3})O_3$–$PbTiO_3$ Crystals", *Applied Physics Letters*, Vol. 83, pp. 2265–2267, 2003.

[44] S. X. Dong, J. F. Li, and D. Viehland, "A Longitudinal–Longitudinal mode Terfenol-D/$Pb(Mg_{1/3}Nb_{2/3})O_3$–$PbTiO_3$ Laminate Composites", *Applied Physics Letters*, Vol. 85, pp. 5305–5306, 2004.

[45] K. Mori, and M. Wuttig, "Magnetoelectric Coupling in Terfenol-D /polyvinylidenedifluoride Composites", *Applied Physics Letters*, Vol. 81, Article 100, 2002.

[46] J. Ryu, S. Priya, K. Uchino, H. E. Kim, and D. Viehland, "High Magnetoelectric Properties of $0.68Pb(Mg_{1/3}Nb_{2/3})O_3$–$0.32PbTiO_3$ Single Crystal and Terfenol-D Laminate Composites", *Journal of the Korean Ceramic Society*, Vol. 39, pp. 813–817, 2002.

[47] S. X. Dong, J. Zhai, F. Bai, J. F. Li, D. Viehland, "Push-Pull Mode Magnetostrictive/Piezoelectric Laminate Composite with an Enhanced Magnetoelectric Voltage Coefficient", *Applied Physic Letters*, Vol. 87, Article 062502, 2005.

[48] J. G. Wan, Z. Y. Li, Y. Wang, M. Zeng, G. H. Wang, and J. M. Liu, "Strong Flexural Resonant Magnetoelectric Effect in Terfenol-D/Epoxy-$Pb(Zr,Ti)O_3$ Bilayer", *Applied Physic Letters*, Vol. 86, Article 202504, 2005.

[49] L. Li and X. M. Chen, "Magnetoelectric Characteristics of a Dual-Mode Magnetostrictive/Piezoelectric Bilayered Composite", *Applied Physic Letters*, Vol. 92, Article 072903, 2008.

[50] S. X. Dong, J. Y. Zhai, Z. P. Xing, J. F. Li, and D. Viehland, "Extremely Low Frequency Response of Magnetoelectric Multilayer Composites", *Applied Physics Letters*, Vol. 86, Article 102901, 2005.

[51] S. X. Dong, J. F. Li, and D. Viehland, "Characterization of Magnetoelectric Laminate Composites Operated in Longitudinal–Transverse and Transverse–Transverse Modes, *Journal of Applied Physics*, Vol. 95, pp. 2625–2630, 2004.

[52] Y. J. Wang, S. W. Or, H. L. W. Chan, X. Y. Zhao, and H. S. Luo, "Enhanced Magnetoelectric Effect in Longitudinal–Transverse Mode Terfenol-D/ $Pb(Mg_{1/3}Nb_{2/3})O_3$–$PbTiO_3$ Laminate Composites with Optimal Crystal Cut", *Journal of Applied Physics*, Vol. 103, Article 124511, 2008.

[53] N. Nersessian, S. W. Or, and G. P. Carman, "Magnetoelectric Behavior of Terfenol-D Composite and Lead Zirconate Titanate Ceramic Laminates", *IEEE Transactions on Magnetics*, Vol. 40, No. 4, pp. 2646–2648, 2004.

[54] S. X. Dong, J. Y. Zhai, J. F. Li, and D. Viehland , "Enhanced Magnetoelectric Effect in Three-phase $MnZnFe_2O_4/Tb_{1-x}Dy_xFe_{2-y}/Pb(Zr,Ti)O_3$ Composites", *Journal of Applied Physic*, Vol. 100, Article 124108, 2006.

[55] Y. J. Wang, S. W. Or, H. L. W. Chan, X. Y. Zhao, and H. S. Luo, "Giant Magnetoelectric Effect in Mechanically Clamped Heterostructures of Magnetostrictive Alloy and Piezoelectric Crystal-alloy Cymbal" *Applied Physic Letters*, Vol. 93, Article 213504, 2008.

[56] D. Viehland, S. X. Dong, and J. F. Li, "Magnetoelectric Magnet Field Sensor with Longitudinally Biased Magnetostrictive Layer", *United States Patent*, Patent No. US 7023206 B2, 2006.

[57] S. W. Or and H. L. W. Chan-Wong, "Magnetoelectric Devices and Methods of Using Same." *United States Patent*, Patent No. US 7199495 B2, 2007.

[58] S. W. Or and H. L. W. Chan-Wong, "Magnetoelectric Devices and Methods of Using Same." *United States Patent*, Patent No. US 7298060 B2, 2007.

[59] Y. J. Wang, X. Y. Zhao, W. N. Di, H. S. Luo, and S. W. Or, "Magnetoelectric Voltage Gain Effect in a Long-type Magnetostrictive/Piezoelectric Heterostructure", *Applied Physic Letters*, Vol. 95, Article 143503, 2009.

[60] G. Engdahl, *Handbook of Giant Magnetostrictive Materials*, Academic Press, New York, 2000.

[61] Inner Mongolia Baotou Rare Earth Research Institute, China, http://www.brire.com/index.asp.

[62] Electrical Discharge Machining, http://en.wikipedia.org/wiki/Electrical_discharge_machining.

[63] Araldite LY564/Aradur2954 Data Sheet, from, retrieved March 2004, http://www.huntsman.com/advanced%5Fmaterials/.

[64] T. A. Duenas and G. P. Carman, "Experimental results for magnetostrictive composites" *Symposium on Adaptive Structures and Material Systems Proceedings*, Vol. 57, pp. 63–67, 1998.

[65] S. W. Or, N. Nersessian, and G. P. Carman, "Dynamic Magnetomechanical Behavior of Terfenol-D/Epoxy 1-3 Particulate Composites", *IEEE Transactions on Magnetics*, Vol. 40, pp.71−77, 2004.

[66] B. Noheda, D. E. Cox, and G. Shirane, "Phase Diagram of the Ferroelectric Relaxor (1-x)PbMg1/3Nb2/3O3-xPbTiO3", *Physical Review B*, Vol.66, Article: 054104, 2002.

[67] C. B. DiAntonio, F. A. Williams Jr., S. M. Pilgrim, W. A. Schulze, C. Feng, and Z. Yin, "Characterization Study of the Growth and Electromechanical Properties of 67PMN–33PT Single Crystals", *Proceedings of the 13th IEEE International Symposium on Applications of Ferroelectrics*, Nara, Japan, pp. 431–434, 2002.

[68] H. S. Luo, G. H. Xu, H. Q. Xu, P. C. Wang, and Z. W. Yin, "Compositional Homogeneity and Electric Properties of Lead Magnesium Niobate Titanate Single Crystals Grown by a Modified Bridgman Technique", *Japanese Journal of Applied Physics*, Vol. 39 (Part 1), pp. 5581−5585, 2000.

[69] IEEE Standard on Piezoelectricity, ANS/IEEE Std 176/1987.

[70] C. A. Rosen, "Ceramic Transformers and Filters", *Proceedings of the Electronic Components Symposium*, pp. 205−211, 1956.

[71] C. A. Rosen, K. A. Fish, and H. C. Rothenberg, "Electromechanical Transducer", *United States Patent*, Patent No. US 2830274, 1958.

[72] F. F. Wang, W. Z. Shi, Y. X. Tang, X. M. Chen, T. Wang, and H. S. Luo, " A longitudinal (1-x)Pb(Mg1/3Nb2/3O3−xPbTiO3 single-crystal piezoelectric transformer", *Applied Physics A-Materials Science and Processing*, Vol. 100, pp. 1231−1236, 2010.

[73] T. Ikeda, *Fundamentals of Piezoelectric*, Oxford University Press, New York, 1990.

[74] China Rare Earth Magnet Ltd, http://www.permanentmagnet.com/.

[75] E. P. Furlani, *Permanent Magnet and Electromechanical Devices: Materials, Analysis, and Applications*, Academic Press, San Diego, 2001.

[76] H. W. Ott, *Electricmagnetic Compatibility Engineering*, A John Wiley and Sons, New York, 2009.

[77] Superwool, http://www.goodfellow.com/larger-quantities/ceramics/superwool-607-ht/.

[78] J. Chen, D. Zhou, F. F. Wang, L. H. Luo, B. Ren, Y. T. Lin, W. N. Di, C. Chen, X. Y. Zhao, Z. M. Pan, D. Lin, and H. S. Luo, "Temperature Dependence of Transverse and Shear Mode Properties for 0.71Pb(Mg1/3Nb2/3)O3−0.29PbTiO3 single crystal with the optimal orientation", *Journal of Physics D: Applied Physics*, Vol. 42, Article: 035415, 2009.

[79] Product Specification of Nordic Semicondctor nRF2401.

[80] B. Furht, S. A. Ahson, *HSDPA/HSUPA Handbook*, CRC Press, New York, 2011.

[81] M.X. Bi, " *High-speed Rail Broadens Range of Options for China's New Year Travel*", http://news.xinhuanet.com/english2010/china/2011-02/04/c_13719070.htm.

[82] T. K. Ho, "Railway Engineering Research in Hong Kong", *International Symposium in Transportation Science and Engineering for Global Chinese Scholars*, Beijing, China, 27−30 August 2003.

[83] Z. M. Ye, E. W. C. Lo, K. H. Yuen, P. Tang, S. G. Ye, "A Study of Current Hormonics of Electrical Traction Power Supply System", *31st IEEE Annual Power Electronics Specialists Conference*, Vol. 3, pp. 1149–1152, 2000.

[84] M. Winterling, E. Tuinman, and W. Deleror, "Fault Analysis of Electromechanical Traction Drives", *8th International Conference on Electrical Machines and Drives*, pp. 248−252, 1997.

[85] C. O'Donnel, R. Palacin, and J. Ronsinski, "Pantograph damage and wear monitoring system", *The Institution of Engineering and Technology Conference on Railway Condition Monitoring*, pp. 178−181, 29−30 November, 2006.

[86] M Popescu, A. Bitoleanu, and M. Dobriceanu, "Harmonic Current Reduction in Railway System", *Wseas Transitions on System*, Vol.7, Issue 7, pp. 689−698, July 2008.

[87] W. T. Thomson and M. Fenger, "Case histories of current signature to detect faults in induction motor drives", *IEEE IEMDC'03 IEEE International Electric Machines and Drives Conference*, Vol. 1–3, pp1459–1465, 2003.

[88] J. Royo, F. J. Arcega, "Machine current signature analysis as a way for fault detection in squirrel cage wind generators", *IEEE International Symposium on Diagnostics for Electric Machines, Power Electronics and Drives*, pp. 269–272, 2007.

[89] A. Livshitz, B. Bukengolts, B. H. Chudnovsky, B. A. Chudnovsky, " On-line Temperature Monitoring of Power Distribution Equipment", *Industry Applications Society 52nd Annual Petroleum and Chemical Industry Conference Book Series: Record of Conference Papers-Petroleum and Chemical Industry Conference*, pp. 223–231, 2005

[90] C. M. Leung, S. W. Or, and S. L. Ho, "DC Magnetoelectric Sensor Based on Direct Coupling of Lorentz Force Effect in Aluminum Strip with Transverse Piezoelectric Effect in 0.7Pb(Mg1/3Nb2/3)O3–0.3PbTiO3 single-crystal plate", *Journal of Applied Physics*, Vol. 107, Issue 9, Article Number 09E702, 2010.

[91] H. L. Liu, S. W. Or, and H. Y. Tam, "Magnetostrictive Composite–Fiber Bragg Grating (MC–FBG) Magnetic Field Sensor", *Sensors and Actuators A: Physical*, Vol. 173, pp. 122–126, 2012.